Exploring the Multifunctional Potential of the Cell-Penetrating Peptide sC18: Drug Delivery, Organelle Targeting, and Antimicrobial Activity

Inaugural-Dissertation

zur

Erlangung des Doktorgrades

der Mathematisch-Naturwissenschaftlichen Fakultät

der Universität zu Köln

vorgelegt von

Joshua Christian Grabeck

aus Bergisch Gladbach

angenommen 2025

Begutachtung:

Prof. Dr. Ines Neundorf

Prof. Dr. Jan Riemer

Die im Rahmen der vorliegenden Arbeit durchgeführten Experimente und Untersuchungen wurden im Zeitraum von Oktober 2021 bis Februar 2025 am Institut für Biochemie der Universität zu Köln unter der Anleitung von Frau Prof. Dr. Ines Neundorf durchgeführt.

Abstract

The study and application of peptides have transformed clinical research, offering innovative approaches to combat cancer, organelle-specific diseases, and bacterial antibiotic resistance. This work focuses on developing, characterizing, and designing the cell-penetrating peptide sC18 and its variants to improve drug delivery to cancer cells, achieve organelle-specific targeting, and improve antimicrobial properties.

In the first study, three variants of sC18 were developed to improve its efficacy as a carrier for the anti-cancer drug Doxorubicin. By optimizing the amphipathic structure or net charge, some of them showed enhanced cytotoxicity towards cancer cells while sparing healthy cells. Peptide-drug conjugates (PDCs) containing Doxorubicin were developed, with the peptide sC18ΔE in particular proving to be the most promising candidate for future studies.

Then, sC18 variants bearing peroxisomal targeting sequences were investigated regarding their ability to be transported into the peroxisome via the cellular peroxisomal import machinery. The uptake efficiency varied depending on the utilized PTS and CPP. Moreover, peptides PX1 and PX9 showed high internalization efficiency and good biocompatibility in MCF-7 cells and might enhance the level of Pex5, a major peroxisomal receptor protein. However, colocalization with peroxisomes remained limited. Thus, further optimization is needed to investigate the developed peptides' targeting efficiency and therapeutic relevance.

Finally, the peptide sC18*R,L, was further developed regarding its antimicrobial potential, and several new derivatives were created and biologically tested. The chemical modification using a triazolyl bridge in the peptide RL-8 increased the activity against both Gram-positive and Gram-negative bacteria and improved the peptide stability against proteolytic degradation. In particular, the triazolyl-bridged peptide 8B showed significantly increased bacterial membrane disruption with low cytotoxicity in human cells, making it a potential candidate for combating resistant pathogens. This peptide was further modified in a retro-inverso manner, which increased its antimicrobial activity further.

This work highlights the versatility of sC18 peptides in addressing pressing challenges in drug delivery, organelle-specific targeting, and antimicrobial resistance. Future studies could provide novel insights to improve these peptides for clinical applications.

Zusammenfassung

Die Erforschung und Anwendung von Peptiden hat die klinische Forschung verändert und bietet innovative Ansätze zur Bekämpfung von Krebs, organellenspezifischen Krankheiten und bakterieller Antibiotikaresistenz. Diese Arbeit konzentriert sich auf die Entwicklung, Charakterisierung und das Design des zellpenetrierenden Peptids sC18 und seiner Varianten, um die Medikamentenabgabe an Krebszellen zu verbessern, eine organellenspezifische Zielansteuerung zu erreichen und die antimikrobiellen Eigenschaften zu verbessern.

In der ersten Studie wurden drei Varianten von sC18 untersucht, um deren Wirksamkeit als Träger für das Krebsmedikament Doxorubicin zu verbessern. Durch Optimierung der amphipathischen Struktur oder der Nettoladung zeigten einige von ihnen eine gesteigerte Zytotoxizität gegenüber Krebszellen, während gesunde Zellen verschont blieben. Peptid-Wirkstoff-Konjugate, die Doxorubicin enthalten, wurden entwickelt, wobei sich das PDC bestehend aus sC18ΔE , als der vielversprechendste Kandidat für künftige Studien erwies.

Anschließend wurden sC18-Varianten mit peroxisomalen Zielsequenzen auf ihre Fähigkeit untersucht, über die peroxisomale Importmaschinerie in das Peroxisom transportiert zu werden. Die Aufnahmeeffizienz variierte in Abhängigkeit von den verwendeten Signalsequenzen und der Peptide. Die Peptide PX1 und PX9 zeigten eine hohe Internalisierungseffizienz und gute Biokompatibilität in MCF-7 Zellen und erhöhten das Proteinlevel von Pex5, einem wichtigen peroxisomalen Rezeptorprotein. Die Kolokalisierung der PX-Peptide mit Peroxisomen blieb jedoch gering. Weitere Optimierungen sind erforderlich, um die Zielgenauigkeit und therapeutische Relevanz der entwickelten Peptide zu steigern.

Schließlich wurde das Peptid sC18*R,L hinsichtlich seines antimikrobiellen Potenzials weiterentwickelt, und es wurden neue Derivate synthetisiert und biologisch getestet. Die Modifikation mit einer Triazolylbrücke im Peptid RL-8 verbesserte die Stabilität des Peptids gegen proteolytischen Abbau und erhöhte die Aktivität gegen grampositive, sowie gramnegative Bakterien. Insbesondere das triazolylverbrückte Peptid 8B zeigte eine deutlich erhöhte Membranlysierung bei geringer Zytotoxizität in menschlichen Zellen, was es zu einem potenziellen Kandidaten für die Bekämpfung resistenter Krankheitserreger macht. Die viel versprechenden Peptide wurden in retro-inverser Weise synthetisiert, was deren antimikrobielle Aktivität weiter erhöhte.

Diese Arbeit unterstreicht die Vielseitigkeit von sC18-Peptiden bei der Bewältigung von Herausforderungen im Bereich der Arzneimittelverabreichung, der organellen-spezifischen Ausrichtung und der antimikrobiellen Resistenz. Zukünftige Studien könnten neue Erkenntnisse zur weiteren Verbesserung dieser Peptide für klinische Anwendungen liefern.

Table of contents

1. Introduction

1.1 Architecture and functionality of eukaryotic membranes

A biological membrane is essential for all kingdoms of life. It is a selective barrier separating the intracellular components from the extracellular environment.[1] It plays a crucial role in maintaining cellular integrity, regulating the import and export of substances, facilitating communication through various signaling pathways, and supporting essential cellular processes like energy production, cell division, and molecule transport.[2] The structure of the membranes differs from organism to organism and is always unique depending on its composition. However, the eukaryotic membrane consists primarily of a lipid bilayer with embedded proteins and provides fluidity and stability, allowing the organism to adapt dynamically to environmental needs.[3] The lipid bilayer is built by phospholipids, glycolipids, and sterols, see Fig. 1.[4]

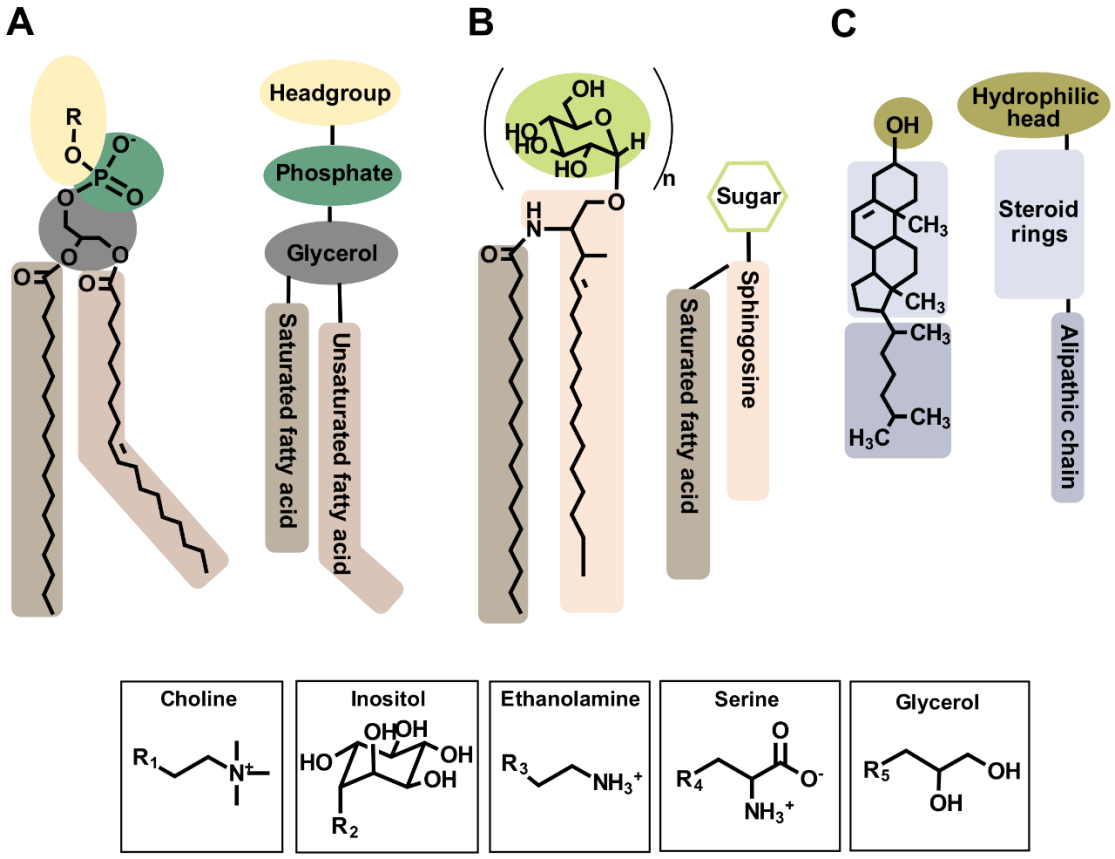

Figure 1. Schematic overview of the three main types of lipids within membranes. (**A**) Phospholipids with prominent headgroups: choline, inositol, ethanolamine, serine, and glycerol. (**B**) Schematic glycosphingolipid, exemplified by glucosylceramide with an attached C18 fatty acid chain. (**C**) The most abundant sterol group in mammalian cells is Cholesterol. Adapted from Hilton, K.L.F.; Manwani, C. et al. [4–6]

However, the headgroup and the hydrophobic tail exhibit different structures and properties.[7,8] The cellular membrane mainly consists of phospholipids, as shown in Fig. 1A,

which possess two fatty acid chains, either saturated or unsaturated. They are linked by a glycerol connected to a phosphate group bound to the hydrophilic headgroup. The headgroup can be divided into five prominent representatives: choline, inositol, ethanolamine, serine, and glycerol.[9,10] Another phospholipid type called sphingophospholipid consists of one fatty acid chain linked by sphingosine (structure like a fatty acid chain) instead of glycerol.[11] A further group of molecules in the cellular membrane are the glycolipids. These also contain fatty acids bound either by glycerol or sphingosine, but they have a directly attached sugar residue instead of a phosphate group. Hereby, the number and type of sugars varies for each glycolipid.[12] Lastly, the sterols represent a group of molecules within the membrane consisting of a hydrophilic head (often a hydroxy group) followed by steroid rings and an aliphatic chain. The sterol commonly found in mammalian cells is cholesterol.[13] Sterols are essential for forming liquid-ordered (Lo) membrane states, also described as lipid "rafts," which play a crucial role in essential biological processes.[14] In contrast, the small polar headgroups of phosphatidylethanolamine confer greater fluidity and lower surface packing density and pressure to phosphatidylethanolamine-rich regions, referred to as liquid-disordered (Ld) microdomains.[15] The uneven distribution of lipid heterogeneity can be stable or temporary. Transient membrane microdomains, such as lipid rafts, are contrasted by stable membrane microdomains, which are defined by tight junctions.

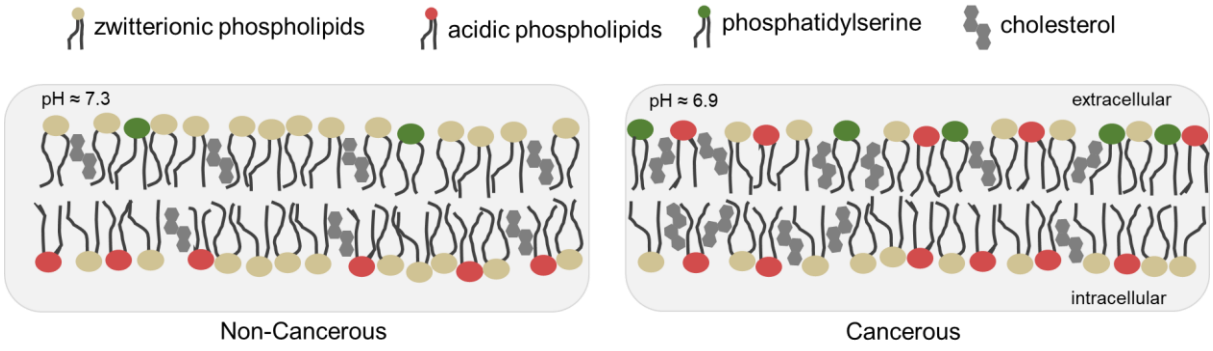

Figure 2. Comparison of cell membrane compositions in non-cancerous and cancerous cells. The asymmetrical distribution of zwitterionic phospholipids, acidic phospholipids, phosphatidylserine, and cholesterol is shown. The extracellular pH changes are also highlighted. Adapted from Neundorf, I. et al. [16]

All these components and properties are not symmetrically distributed, resulting in two different properties in both leaflets. Notably, membranes are unique, and the lipid composition differs depending on the organism.[8] In mammalian cell membranes, the composition of the bilayer varies significantly due to the distribution of lipid types.[17] On the one hand, the outer leaflet, exposed to the extracellular environment, consists mainly of phosphatidylcholine, glycolipids, and sphingomyelin. On the other hand, phospholipids, like phosphatidylserine and phosphatidylethanolamine, are primarily found in the inner leaflet.[3,4,18]

Interestingly, the membrane of cancerous eukaryotes differs from that of non-cancerous eukaryotes. As shown in Fig. 2 and described above, acidic phospholipids in healthy mammalian cells are predominantly found in the inner leaflet, while in cancer cells, they are partially located in the outer leaflet. The phosphatidylserine concentration is significantly enriched in the outer leaflet.[19] This change in lipid composition is typically caused by the misfunction of two ATP-driven pumps, flippases, and floppases. A collapse of this machinery leads to phospholipid rearrangement in the outer leaflet, which is known as phospholipid scrambling. It occurs in both apoptosis and cancer. [20–22] This dysfunction shifts the pH from 7.3 to 6.9, altering the microenvironment of cancer cells towards more acidic conditions.[23] Further, the more acidic tumor micro-environment is mainly caused by hypoxia and elevated lactate production resulting from enhanced glycolysis in cancer cells to ensure proper cell metabolism.[24] Another aspect is the increased cholesterol levels in the cancerous membrane, which leads to higher fluidity that enhances membrane-protein movement and accelerates cell migration. Simultaneously, lipid rafts are increased to maintain high oncogenic signaling. All these differences promote proliferation, migration, and resistance to common therapies.[25,26]

Notably, all these differences can act as biomarkers in the compositions of cancerous membranes, which can be utilized for targeted cancer therapy.[27–29] As cancer remains one of the leading causes of death worldwide, the discovery of new cancer drugs and treatments is crucial to the continued fight against cancer.

1.2 Architecture and functionality of prokaryotic membranes

Also, in prokaryotes, the membrane lipids are essential structural and functional components. They are responsible for membrane organization, cell recognition, membrane fluidity, energy storage, cell signaling, and more.[30,31] However, the types of phospholipids vary depending on the bacterial species. Instead of phosphatidylcholine, as in eukaryotic membranes, phosphatidylethanolamine, phosphatidylglycerol, and cardiolipin are the most abundant phospholipids.[32] Generally, the asymmetrical distribution of the phospholipids in bacteria is widely unknown.[33] Interestingly, in contrast to eukaryotic membranes, the overall structure of bacterial membranes is cholesterol-free. Due to the absence of cholesterol, the membrane fluidity is destabilized, and some bacteria substitute the cholesterol with sterol-like hopanoid, which supports membrane stabilization. These hopanoid structures were mainly found in gram-negative bacteria.[34,35] Bacteria without hopanoid within their cell wall showed that lacking this sterol-like structure increases antibiotic sensitivity. However, the mechanism of how hopanoid supports antibiotic resistance is not fully understood.[36] Furthermore, many proteins, like efflux pumps and aquaporins, are embedded in the membrane. Additionally,

enzymes responsible for ATP synthesis and metabolic processes are located within the bilayer.[37]

Generally, bacterial envelopes can be divided into two main categories: Gram-positive and Gram-negative shown in Fig. 3. They differ in structure and functionality, which is essential for understanding their pathogenesis and further developing treatments against bacteria.[38,39]

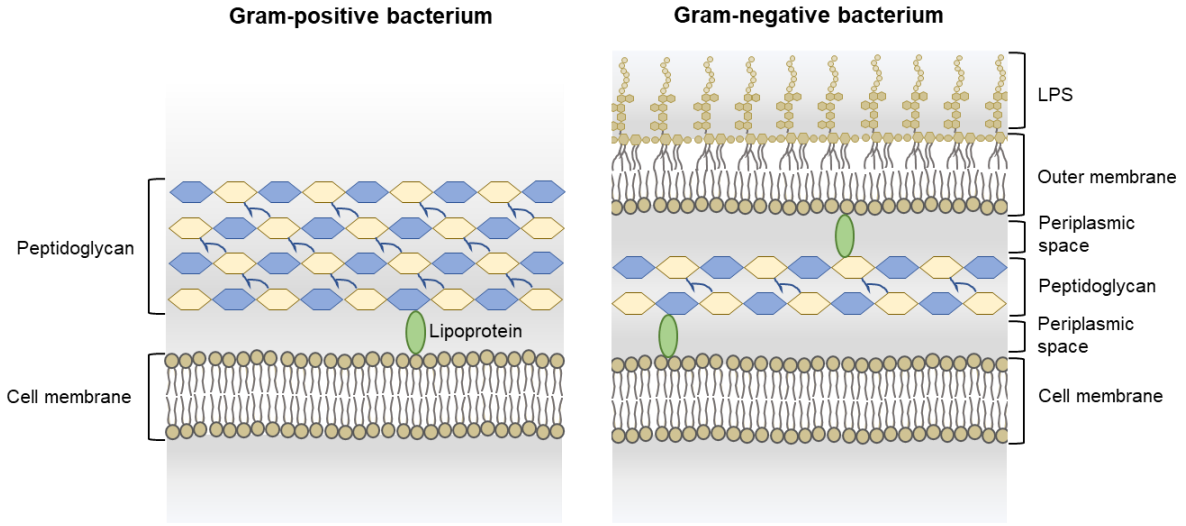

Figure 3. Structural comparison of Gram-negative and Gram-positive bacterial cell envelopes. Differences in peptidoglycan layer thickness, membrane proteins in periplasmic space, outer membrane presence, and associated components, like lipopolysaccharides (LPS), are highlighted. Adapted from Lithgow, T.; Stubenrauch, C.J. et al. [39]

Gram-positive bacteria consist of a thick peptidoglycan layer between 30 and 100 nm thick, which makes up most of the cell wall.[40] The peptidoglycan layer enables gram staining developed by Hans Christian Gram.[41] Wall teichoic or lipoteichoic acids are found on top of the peptidoglycan layer, increasing its negative charge.[42] These are valuable tools to help maintain cell wall integrity, regulate ion transport, facilitate adhesion, and play a role in immune response and cell division. Between the cell membrane and the peptidoglycan layer, there is also a small periplasmic space in which lipoproteins are present.[43] In the years of rising antibiotic resistance, prominent examples of these species have been listed in the ESKAPE group. Some bacteria of the **ES**KAPE group are Gram-positive, like ***E****nterococcus faecium* and ***S****taphylococcus aureus*. These bacteria are highly pathogenic and resistant to many antibiotics, which represents a major challenge to modern medicine.[44]

In contrast, Gram-negative bacteria bear a dual membrane envelope from an outer and cell membrane.[45] The outer membrane holds asymmetrical phospholipids in the inner leaflet and on its outer leaflet lipopolysaccharides (LPS). These LPS support and protect the membrane integrity and act as endotoxins. It, therefore, plays an important role in the development of drugs, as it increases the negative charge of bacteria through phosphate groups.[46]

Underneath the outer membrane, the peptidoglycan layer is surrounded by a periplasmic space with lipoproteins, and the adjacent inner membrane is composed of a phospholipid bilayer. Gram-negative bacteria are generally intrinsically resistant to many classes of antibiotics due to their dual membranes and increased number of efflux pumps.[47] Prominent members of the Gram-negative bacteria from the ES**KAPE** group are ***K****lebsiella pneumoniae*, ***A****cinetobacter baumannii*, ***P****seudomonas aeruginosa,* and ***E****nterobacter species.*[44] As bacteria rapidly develop multidrug resistance and the discovery of new antibiotics is declining, it is essential to focus on developing alternative treatments for bacterial infections.[48]

1.3 Peptides in biomedical research

Peptides play a crucial role in biomedical research due to their advantages over conventional treatments. During the last decades, the interest in peptides from a therapeutic perspective has risen, and many obstacles have been overcome. Significant advancements have been made since the introduction of peptide therapeutics in 1921 with the extraction of insulin. Starting with the development of solid-phase peptide synthesis (SPPS) and identifying products using high-performance liquid chromatography (HPLC) and mass spectrometry (MS).[49,50] The journey of peptides used as therapeutics started with insulin, the first peptide drug for diabetes patients, in 1921.[51] Insulin was initially obtained as an animal extract and can now be recombinantly expressed and produced.[52] During the 20th century, several peptides were discovered and used as therapeutics. The following Tab. 1 lists the early discovered peptides and their introduction into the clinic.

Current research is intensively trying to chemically modify natural peptides to overcome proteolytic degradation and improve oral delivery and selectivity. Thanks to this research, more peptides have entered the clinical phase in recent decades.[53] The first synthetic peptides in the clinical application were Oxytocin, Vasopressin, and Leuprorelin.[54–56]

Simultaneously, peptides with antimicrobial properties were discovered. These low-molecular-weight peptides play a crucial role in the innate immune system and were used for further modification to circumvent the rising antibiotic resistance.[57–59]. Besides their antibacterial properties, the peptides also revealed antiviral and anticancer activity.[60] Interestingly, the rising field of peptides in clinical application is complemented by cell-penetrating peptides (CPP), able to overcome the cellular membrane or to target specific cellular sites by additional organelle-targeting moieties called cell-targeting peptides (CTP). [61]

Table 1. Names, origin, and first clinical application of peptides

Peptide	Origin	Clinical application
Insulin [51]	Canine and Bovine pancreas	1920s
Adrenocorticotropic hormone (ACTH) [62]	Bovine and porcine pituitary glands	1950s
Calcitonin [63]	Salmon ultimobranchial gland	1971
Oxytocin [64]	Synthetic	1962
Vasopressin [65]	Synthetic	1962
Leuprorelin [66]	Synthetic analog of gonadorelin	1984

To date, 80 peptides are U.S. Food and Drug Administration (FDA) approved and available for therapy.[67] The number of peptides in clinical development and undergoing preclinical studies is increasing.[68] To date, peptides have been developed as therapeutic agents for various conditions, such as microbial infections and cancer.

In particular, CPPs are under investigation as drug delivery systems for anti-cancer, antimicrobial, and antiviral treatments, which will be highlighted in the next chapters. [69,70]

1.4 Cell-penetrating peptides and their application to overcome cell membranes

Cell-penetrating peptides (CPPs) are usually small peptides ranging from 4-40 amino acids that can translocate the plasma membrane without destroying the membrane integrity.[71–73] Within the class of CPPs, they can be discriminated into three categories. These categories are cationic, amphipathic, and hydrophobic CPPs that underlie different physiochemical characteristics and properties. [74,75] In detail, cationic CPPs are the most commonly used CPPs and consist of a high number of positively charged amino acids under physiological conditions. Primarily, peptides rich in arginine and lysine are recognized as CPPs, while the sequence order and location are crucial for internalization efficacy.[76] Cationic peptides use charge-driven uptake by electrostatic interaction between their positive charge and the negatively charged headgroups of acidic phospholipids or glycolipids.[77] The best-known example of this category is the TAT peptide derived from the trans-activator of transcription protein, discovered in 1988.[78] This sequence is derived from Human Immunodeficiency Virus Type-1 (HIV-1), which contains multiple arginine residues, resulting in a high positive charge. This peptide can translocate and deliver cargoes like oligonucleotides, proteins, nanoparticles, and small molecular drugs into cells.[79–81] Several years later, a new peptide was discovered that could internalize into cells. This peptide, Penetratin, was derived from a

homeoprotein of *Drosophila melanogaster*.[82] Both peptides were further modified and truncated, resulting in adapted sequences of the TAT peptide and Penetratin listed in Tab. 2.[83]

Table 2. Name, sequence, origin, and category of prominent CPPs.

Name	Sequence	Origin	Category
TAT_{45-57} [78]	GRKKRRQRRRPPQ	HIV-1	cationic
Penetratin [82]	RQIKIWFQNRRMKWKK	Antennapedia *Drosophila melanogaster*	cationic
Pep-1 [84]	KETWWETWWTEWSQPKKKRKV	HIV-reverse transcriptase SV40 T-antigen	primary amphipathic
pVEC [85]	LLIILRRRIRKQAHAHSK	Vascular endothelial cadherin	primary amphipathic
sC18 [86]	GLRKRLRKFRNKIKEK	CAP18	secondary amphipathic
CADY [87]	GLWRALWRLLRSLWRLLWRA	JTS-1	secondary amphipathic
$Bac7_{1-16}$ [88]	RRIRPRPPRLPRPRPR	cathelicidin-derived bovine neutrophils	proline-rich amphipathic

The second category, amphipathic CPPs, comprises peptides that include positive amino acids like arginine and lysine and a nonpolar region with hydrophobic amino acids such as leucine, isoleucine, valine, or alanine. Amphiphilic CPPs can be divided into primary, secondary, and proline-rich amphipathic CPPs. [89] On the one hand, primary amphipathic peptides consist of both a hydrophobic domain and a hydrophilic domain, allowing them to interact with the plasma membrane's hydrophobic lipid tails and hydrophilic headgroups.[90] The most prominent peptides of this class are pVEC and Pep-1.[84,85]

On the other hand, the secondary amphipathic peptides form α-helix or β-sheet structures upon interaction with the plasma membrane.[91] The hydrophobic- and cationic amino acids are distributed within the sequence.[92] A prominent peptide of this class developed and discovered in our group is sC18 and its derivatives with anti-cancer, antimicrobial, and delivery properties.[86,93–97] Another well-studied secondary amphipathic CPP is CADY.[87] The last class of amphipathic peptides contains a proline pyrrolidine template and can build two

secondary structures: polyproline I (PPI) and polyproline II (PPII). The best-known peptide of this class is Bac7.[88,98]

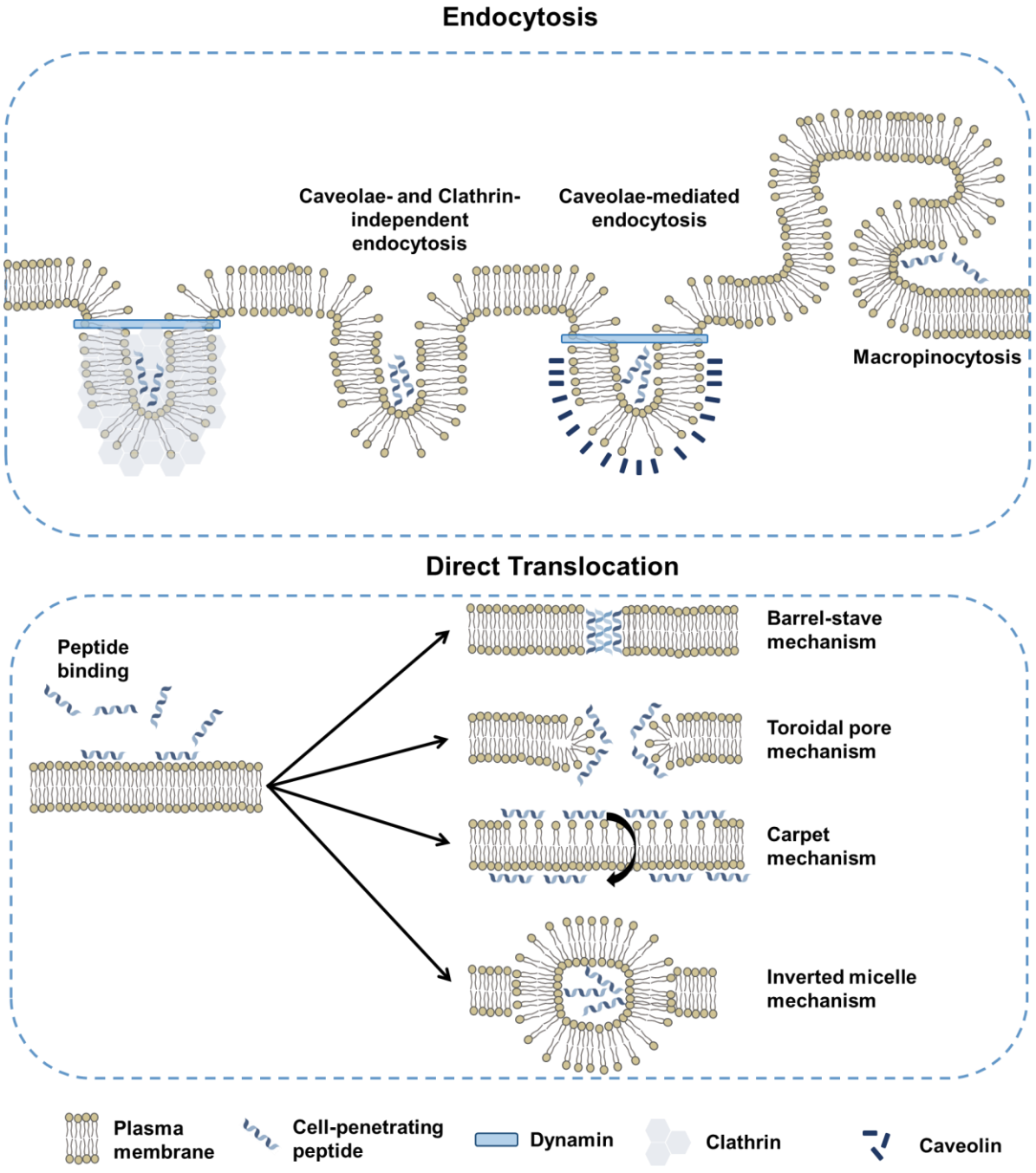

Figure 4. The uptake mechanism of CPPs is differentiated into (A) energy-dependent endocytic models and (B) energy-independent direct translocation models, adapted from Tabujew I, Lelle M, Peneva K, et al.[99]

An important goal is to understand the uptake mechanism of these peptides to enhance their properties through further modification and optimization. All CPPs mentioned and known are able to overcome the cellular membrane. However, the uptake mechanisms are not fully understood. Previous studies extensively investigated the uptake mechanism and the theory

behind internalization.[73,100,101] The differences in the physicochemical properties, net charge, secondary structure, and other characteristics of CPPs influence the potential and efficiency of cellular internalization by different mechanisms. Nowadays, the uptake mechanisms can be categorized into two main routes. First, in energy-dependent vesicular mechanism (endocytosis) and second, the energy-independent (direct translocation) internalization across the cell membrane, as shown in Fig. 4. [102,103] It is known that CPPs in higher concentrations lead to direct translocation, whereby CPPs carrying cargoes prefer an endocytic-dependent uptake mechanism. [104,105] The endocytic uptake is energy-dependent and further divided into four sub-mechanisms: clathrin-dependent, caveolae-mediated, clathrin-, caveolae-independent uptake, and macropinocytosis. Except for macropinocytosis, in which a protrusion of the membrane occurs, the other mechanisms correspond to an invagination of the membrane.[106] It is assumed that the primary uptake of CPPs is endocytic. Therefore, it is important to remember that the peptides must be released from the endosome or early lysosome to reach their intracellular target or efficient drug release.[107,108]

Four major models are provided for the energy-independent uptake mechanism of CPPs: the barrel-stave, toroidal pore, carpet, and inverted micelle mechanisms. These mechanisms are mainly initiated by the electrostatic interaction of the cationic amino acids of the CPPs with the negatively charged headgroups of phospholipids, like phosphatidylserine phosphatidylglycerol, heparin sulfate, and glycosaminoglycan.[109,110] Notably, the interaction of the basic amino acids can be discriminated, as lysine residues have been shown to form monodentate hydrogen bonds. In contrast, arginine residues can form bidentate hydrogen bonds that support the destabilization of the membrane and, at the same time, reinforce the folding of the peptide at the plasma membrane, resulting in a positive curvature. These differences are provided by ammonium-(lysine) and guanidium-(arginine) groups.[111,112] The peptides can transiently destabilize and translocate the membrane by pore formation, divided into a barrel-stave and toroidal model.[113] The main difference between both models is the orientation of the peptide. In the barrel-stave model, the peptides build a ring formation due to hydrophobic residues interacting with the lipid tails of the phospholipids, and the polar residues are directed toward themselves.[114] Instead, the toroidal model describes that the peptides are embedded in the membrane due to the interaction of the basic amino acids of the CPPs with the polar head groups of the phospholipids. [115] The carpet mechanism is another uptake possibility in which the peptide accumulates on the cell membrane, as described for pore formation. When the carpet-like structure is formed, the electrostatic interactions lead to membrane rearrangement, a higher fluidity, and a temporary thinning of the overall membrane structure. High accumulation of the

peptides reduces membrane surface tension, leading to spontaneous membrane translocation.[116,117] Another mechanism is the inverted micelle formation, in which the CPPs interact with the cell membrane due to both electrostatic and hydrophobic parts, which affect the supramolecular organization of the phospholipids and leads to encapsulation of the CPPs into inverse micelles followed by cytosolic release. [83,118]

In summary, the diverse physicochemical properties and structural characteristics of CPPs influence their ability to internalize through energy-dependent and energy-independent translocation mechanisms. Optimizing these pathways, particularly membrane interaction, is crucial for enhancing the efficiency of CPPs as drug delivery tools or medical applications. Interestingly, the endosomal release occurs in the same manner as the cellular membrane penetration achieved by disrupting the endosomal membrane through electrostatic interactions, membrane destabilization, or pore formation, allowing the CPPs and their cargo to enter the cytosol. Exemplary additional modifications for improved endosomal release include endosomal escape domains (EEDs) and pH-sensitive peptides. They are able to facilitate escape from the endosome. [119–122] The translocation of eukaryotic membranes offers numerous opportunities for targeted treatments of diseases.

1.5 Antimicrobial peptides

The worldwide increase in antibiotic resistance by bacteria must be urgently addressed. In the following chapter, antimicrobial peptides (AMPs) will be discussed in detail to combat this growing problem.[123]

Generally, AMPs are low molecular weight oligopeptides naturally derived from plants, animals, and humans.[124] Within the host, they play a major role in the innate immune response and exhibit antimicrobial activity. These peptides typically range from 10-60 amino acids in length, and the majority are cationic, meaning they carry a positive net charge.[125] In addition to the majority of AMPs being cationic, there are also a few anionic AMPs that have been identified. Anionic peptides are less common but still play a role in antimicrobial defense mechanisms.[126,127] Interestingly, the uptake mechanism for these peptides into the cells is also not fully understood.

AMPs can be discriminated by mode of action in targeting intracellular targets or membrane perturbation. On the one hand, the intracellular targets of these peptides affect protein biosynthesis, disrupting DNA replication, enzyme inhibition, or interfering with signaling pathways.[128–130] On the other hand, the uptake and perturbation mechanisms of AMPs are responsible for their antimicrobial activity. However, it is suggested that AMPs use direct penetration and translocation mechanisms described in Fig. 4.[131] The uptake efficacy and

mechanism are based on their conserved amphipathic character. Due to their physicochemical properties, AMPs can interact with bacterial membranes through electrostatic interactions, forming ionic pores or transient gaps that lead to membrane collapse and, ultimately, bacterial death.[132] The mechanisms for overcoming the membrane can be further discriminated into transmembrane pore formation (barrel stave or toroidal model) and non-pore mechanisms such as carpet-like models. In addition to the above-mentioned mechanisms, AMPs mostly use the induction of a negative Gaussian curve (NGC), which is responsible for the peptides disrupting the membrane. The efficacy of NGCs depends on lipid composition as the interaction with the negatively charged phosphatidylglycerol and cardiolipin is increased.[133,134] In general, the lipid composition of bacteria differs greatly from that of eukaryotes.[135]

Table 3. Name, sequence, classification, and origin of prominent known antimicrobial peptides.

Name	Sequence	Classification	Origin
Human β-defensin-1 [136]	DHYNCVSSGGQCLYSACPIFTKIQG TCYRGKAKCCK	Source	human
C18 [137]	GLRKRLRKFRNKIKEKLKKI	Source	rabbit
M2 AH [138]	FKCIYRFFEHGLKRG	Activity (anti-viral),	influenza virus
Bac5 [139]	RFRPPIRRPPIRPPFYP	Amino acids-rich species	bovine
LL-37 [140]	LLGDFFRKSKEKIGKEFKRIVQRIKD FLRNLVPRTES	Structure (α-helical)	human
Gomesin [141]	ZCRRLCYKQRCVTYCRGR	Structure (β-sheet)	spider

The classification of AMPs can be divided into four subgroups dependent on activity (antibacterial-, antiviral-activity, etc.), source (mammalian, insect, etc.), structure (α-helix, β-sheet, etc.), and amino acid-rich composition (tryptophan, proline, etc.). Some examples of these AMPs are listed in Tab. 3. In the past decade, naturally derived antimicrobial peptides (AMPs) have been optimized, and synthetic versions have been developed.[142] These improvements focused on reducing the size of AMPs while enhancing their bioavailability and stability, making them more attractive and practical for therapeutic and clinical use.[143–145] First, the size reduction is interesting as the production costs are much lower.[144] Second, the biggest disadvantage of AMPs in medical applications is their low stability, which has been increased by using unnatural D-amino acids or side chain modification of amino acids, thus significantly prolonging the half-life.[145,146] Lastly, since bioavailability is essential for

biomedical applications and further substitution of antibiotics, AMPs were modified to increase such bioavailability. However, the relationship between AMP properties, such as positive net charge, amphipathicity, hydrophobicity, and helicity, and their antimicrobial activity and toxicity towards mammalian or red-blood cells remains unclear and individual. Standard optimization strategies often involve modifying peptide amphipathicity by adding polar or nonpolar residues to increase selectivity. Given the unpredictable nature of AMP optimization, it is essential to simultaneously conduct both antimicrobial and toxicity tests on eukaryotic and red blood cells to assess effectiveness and safety.[147]

1.6 Peptide-drug conjugates

To date, cancer is the third most common cause of death worldwide, and the trend is rising. Therefore, research in cancer drug development is more focused on this topic. However, standard chemotherapeutics often cannot distinguish between healthy and cancerous cells, leading to high off-target effects.[148] Therefore, antibody-drug conjugates (ADCs) were focused on minimizing off-target effects and increasing drug efficacy. However, besides the advances, ADCs showed low retention time in the blood combined with stability issues in the bloodstream, low penetration capacity into the tumor microenvironment, low payload efficacy, immunogenicity, and unusual off-target toxicity. Furthermore, the production costs are very high and unlikely to be established in broad clinical applications. [149,150]

An emerging approach called peptide-drug conjugate (PDC) was developed to address these issues. PDCs have a lower molecular weight, can penetrate the microenvironment, offer improved delivery efficiency, and are less expensive than ADCs.[151] PDCs comprise cell targeting/penetrating peptides, a linker, and a cytotoxic cargo. The primary function of peptides in conjugates is to enable penetration into the tumor microenvironment through the known mechanism of action (Fig. 4). To achieve this, CPPs are discovered and then further modified to enhance selectivity for tumor cells. For example, chimeric peptides combine a CPP component with a cell-targeting moiety, such as the iRGD motif. This motif interacts with the overexpressed αVβ3-integrin receptor on the surface of multiple tumor types.[152] This dual-function design enhances tumor specificity and improves the ability of the therapeutic agent to reach and affect cancer cells selectively. Another prominent tumor-targeting motif is $GE_{11,}$ which targets the epidermal growth factor receptor (EGFR). This growth factor receptor is also known to be overexpressed in several tumors. [153] In the following Tab. 4 other tumor-homing peptides are listed.

Three linkers were mainly used to couple the drug with the CPP/CTP to incorporate an anti-cancer drug, depending on drug release, stability, selectivity, and overall drug efficacy. The first linkers used are non-cleavable, such as succinyl-maleimide linkers. Due to the non-

cleavable property, the active drug is released after the degradation of the whole PDC. Off-targets and systemic cytotoxic activity are highly reduced. When the drug is linked at the non-active site, it could also be active while bound to the CPP.[154] The maleimide moiety of the linker is coupled by a Thiol-Michael addition, which is a reversible reaction. For example, high levels of glutathione could trigger a retro Michael addition.[155]

Table 4. Name, sequence, and target of prominent targeting sequences.

Name	Sequence	Target
iRGD [152]	CRGDRGPDC	Integrin $\alpha V\beta_3$
GE_{11} [156]	YHWYGYTPQNVI	EGFR
PL3 [157]	AGRGRLVR	Tenascin-C
CREKA [158]	CREKA	fibrin-fibronectin complex

Another group of linkers can be acid-sensitive or enzyme-sensitive, meaning they are cleavable under specific conditions. The oxime-bearing bifunctional linkers, for example, represent an acid-sensitive linker. This linkage is favorable for enhancing the stability of the PDC in the extracellular environment under physiological pH. Therefore, premature drug release resists within the bloodstream. However, it gets cleaved in the tumor environment due to a dropped pH value (pH <5.5). Therefore, it enhances the precision of drug binding to specific sites, minimizing further off-target effects.[159] Stimuli-responsive linkers are a rapidly emerging area of research today. One notable type is ROS-responsive linkers, which contain thioketals that undergo cleavage in response to reactive oxygen species (ROS). Since ROS levels are elevated in tumors, these linkers allow the selective release of anti-cancer drugs directly within the tumor.[160]

All these properties must be compatible with the coupled drug to enable efficient cancer treatment. Famous drugs used in PDCs are Paclitaxel, Gemcitabine, or Doxorubicin, depicted in Fig. 5. These chemotherapeutics are used in clinics to beat cancer but show high systemic cytotoxic effects and several off-targets.[161] In detail, Gemcitabine functions by acting as a cytidine analog. After phosphorylation, it is converted into the active form, gemcitabine triphosphate, which gets incorporated into DNA. This incorporation disrupts DNA synthesis and translation, ultimately leading to cell death.[162] Another example is Paclitaxel, which stabilizes microtubules and inhibits their depolymerization, disrupting the mitotic spindle's normal function. This results in cell cycle arrest in the *G2/M* phase, which initiates apoptotic pathways and controls cell death. Also, this mechanism is non-selective and shows many off-target effects in chemotherapy.[163]

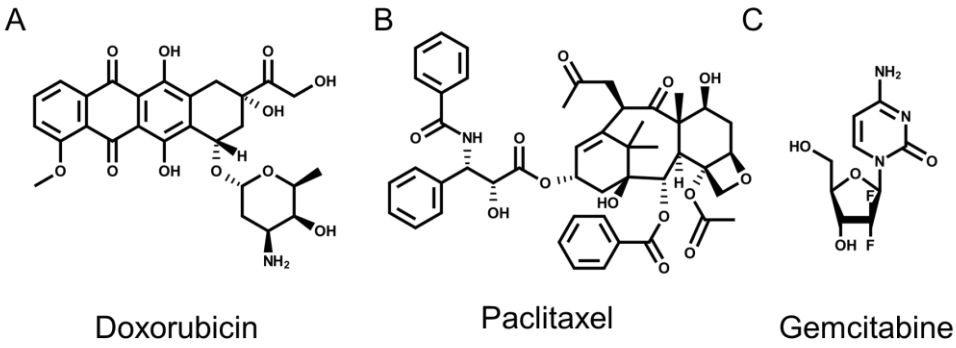

Figure 5. Chemical structures of the prominent drugs (A) Doxorubicin, (B) Paclitaxel, and (C) Gemcitabine used in drug conjugation. [162–164]

Doxorubicin, a well-known chemotherapeutic drug, is an anthracycline antibiotic derived from *Streptomyces peucetius*.[165] Doxorubicin primarily affects intercalating DNA, which disrupts the DNA replication process. Another function is the inhibition of Topoisomerase II, a crucial enzyme breaking down the supercoiled structure, which leads to DNA double-strand breaks. The further stabilization of Topoisomerase II prevents destabilization after DNA double-strand breaks.[164] In addition, the high systemic cytotoxic effect results from generating reactive oxygen species (ROS) produced by the radicals. ROS are responsible for several pathway activations, and overproduction leads, for example, to lipid peroxidation, resulting in loss of cell membrane integrity and, ultimately, in cell death.[166]

In summary, cancer remains one of the leading causes of death worldwide, and significant research efforts are being made to improve drug efficacy and reduce off-target effects in cancer therapy. Conventional treatments lack selectivity, leading to significant side effects, and ADCs also have limitations, including short residence time, low tumor penetration, and stability issues in the bloodstream. Therefore, promising PDCs have been developed as an alternative, offering better penetration of the tumor microenvironment, higher delivery efficiency, and lower costs.

1.7 Subcellular targeting peptides

Besides cancer, numerous other diseases are the focus of current research, many of which require precise targeting of specific organelles within the cell. The next chapter will explore this crucial aspect of targeting organelles in more detail.

Subcellular targeting peptides can reach specific subcellular compartments or organelles after passing the plasma membrane. In the last decades, development research has focused on this topic to generate drugs that can directly treat mostly rare misfunctions in metabolic pathways.[61,75] Several organelles within the cell are involved in key metabolite mechanisms. To target these organelles or metabolite mechanisms within specific organelles,

the cell's own machinery is used by adding signal or targeting sequences to the CPP. The cells have their own sorting system, including receptors located on the target organelles or in the cytosol, which recognize proteins or CPPs containing specific signal- or targeting sequences and facilitate their transport to the correct destination.[167] Various organelles, such as the endomembrane, are passed during this transport. In total, this process is critically observed and checked by cellular monitoring. It starts with recognition of the signal sequence, which can be introduced differently, such as *N*-, *C*-terminal, or within the sequence.[168] Often, the process ends with cleaving off the signal sequence from the cargo/CPP. In organelle-specific drug delivery, CPPs serve as a valuable tool for overcoming the plasma membrane, and following the signal sequence aids in directing non-specific drugs to the appropriate region. As a result, the efficiency of the drug is improved.

For example, the nuclear import is mediated through the nuclear pore complex by an energy-dependent transport supported by the nuclear localization signal (NLS). NLS binds to importin α, subsequently binding importin β, initiating the uptake through the nuclear pore complex (NPC) into the nucleus. The NLSs are generally short 5-16 basic amino acid sequences.[169] Typical examples are the large T antigen of simian virus 40 with PKKKRKV or the nucleoplasmin protein of Xenopus with the sequence KRPAATKKAGQAKKKK.[169,170] Genetic disorders initiate many diseases like cancer as a result of damage or abnormalities in the DNA. Therefore, the nucleus is very interesting for targeted drug delivery mediated by peptides.

To date, mitochondria are the primary intracellular target in drug delivery and are well investigated. Mitochondrial dysfunction leads, among others, to age-related, neurodegenerative, and metabolic diseases.[171,172] Notably, this organelle consists of two phospholipid bilayers separated by the intermembrane space for mitochondrial importation. Due to its autonomous function, mitochondria also have their own genome (mtDNA) hosting 37 genes.[173] However, many proteins are still translated in the cytosol and must be transported into mitochondria. Mitochondrial uptake is mainly facilitated by the mitochondrial targeting sequence (MTS), which is recognized by the translocase outer membrane (TOM).[174] Commonly known MTSs are, for example, from the proteins malate dehydrogenase 2 (MLSLRPSLRKGLVAAKPSGQ) or aldehyde dehydrogenase 5 (LSRTAAAPNSRIFTR).[175] Generally, the signal sequence can vary in length and sequence but conserves the basic amino acids and the α-helix properties supporting the uptake through the negatively charged mitochondrial inner membrane potential. However, after recognition by TOM, the protein bearing the MTS is finally transported into the mitochondrial matrix by translocase inner membrane 23 (TIM23). With the help of the mitochondrial processing peptidase (MPP), the signal sequence is cleaved off, and the folding of the imported protein

starts. In the last decades, many drugs or treatment methods have been developed using direct targeting of mitochondria, which offers increased treatment efficacy and reduced off-target effects.[176]

Another organelle of great interest for targeting is the peroxisome, which is essential for crucial metabolic pathways. Dysfunction of the peroxisomal enzymes results in a high accumulation of toxic metabolites or upregulated synthesis of ether lipids. For example, upregulated ether lipid synthesis is mainly found in aggressive cancer cells.[177] Another prominent disease derived from peroxisome is the Zellweger Spectrum Disorder (ZSD), in which an inability to import peroxisomal proteins occurs, resulting in impaired fatty acid metabolism or ether lipid synthesis.[178,179] To combat such diseases, the complex import machinery of the peroxisome is of great interest. In total, 31 peroxins are known to be involved in the biogenesis of peroxisomes.[180] All peroxisomal proteins involved in metabolic activities must be transported into the peroxisomal matrix recognized by peroxisomal targeting sequences (PTSs).[181,182] In comparison to mitochondria, no known proteins were translated in peroxisome. To date, three different PTSs are known. PTS-1 is a *C*-terminal located sequence, while PTS-2 is *N*-terminally located. Lastly, PTS3 is randomly located independent of PTS1 and PTS2, underlying the import mechanisms of PTS1. Still, there is no known consensus sequence for PTS3.[183]

In detail, the most common form of PTS1 consists of the three amino acids SKL at the *C*-terminus, whereas some variations in the sequence are possible. The sequence can vary, such as S/A/C-K/R/H-L/A/M.[184] Some working groups have also identified elongated PTS1, like PGNAKL, which showed a higher binding affinity to the receptor Pex5.[185] However, the *N*-terminally located PTS2 is a nonapeptide with the consensus motif [R/K]-[L/V/I/Q]-X-X-[L/V/I/H/Q]-[L/S/G/A/K]-X-[H/Q]-[L/A/F].[186] The PTS2 is generally less efficient than the PTS1 pathway for peroxisomal import.[187]

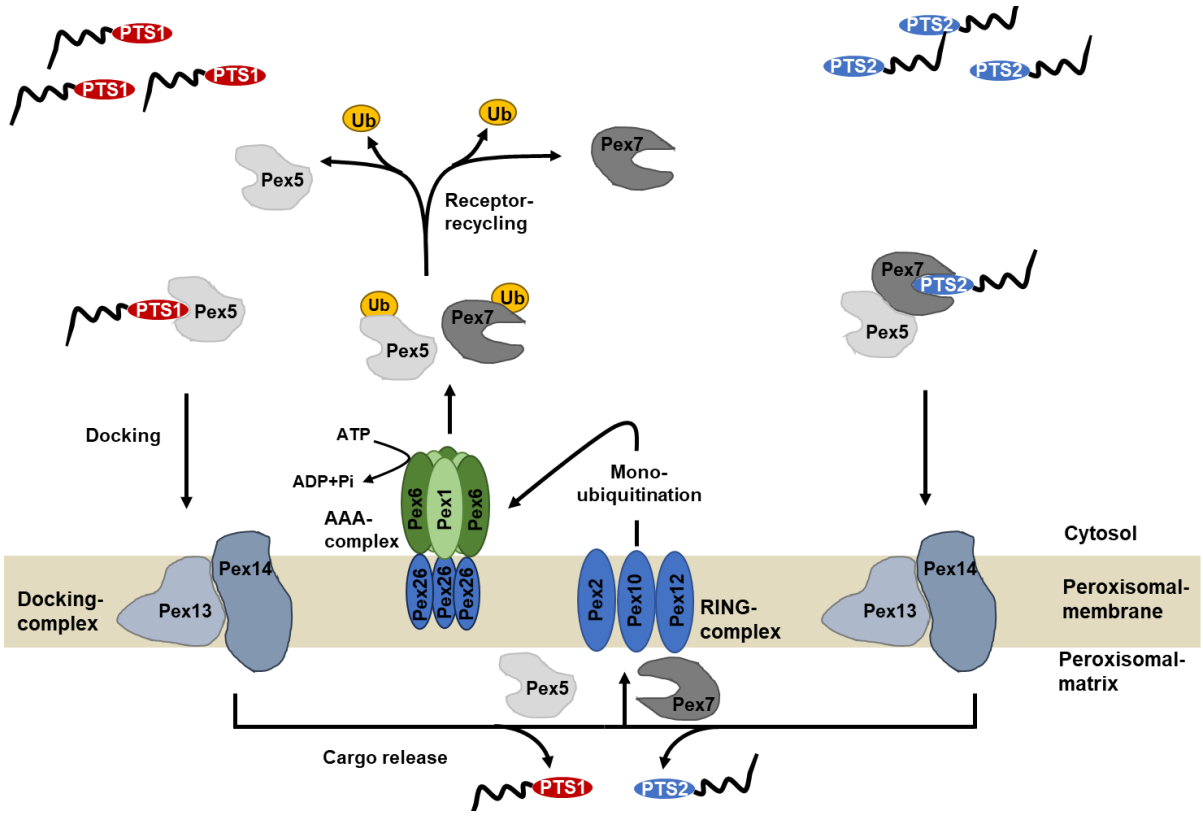

Figure 6. Schematic representation of peroxisomal uptake mechanisms for PTS1 and PTS2. Peroxisomal targeting signals (PTS) uptake follows distinct but related pathways. PTS1 is recognized in the cytosol by the receptor protein Pex5, which mediates its transport to the docking complex formed by Pex13 and Pex14 at the peroxisomal membrane. Following translocation into the peroxisomal lumen, Pex5 is embedded in the peroxisomal membrane, undergoing either mono- or polyubiquitination. Mono-ubiquitinated Pex5 is extracted from the membrane by the hexameric AAA ATPase complex through ATP hydrolysis. Subsequently, the receptor is recycled in the cytosol by deubiquitinating enzymes. For PTS2, a similar pathway is employed, with the key difference being the cytosolic recognition of the PTS2 signal by Pex7. Pex7 interacts with the long isoform of Pex5, facilitating the subsequent steps of the import cycle. Adapted from Gao Y, Skowyra M, et al. [188]

The import mechanism of PTS1 and PTS2 is detailed in Fig. 6. Pex5, an import receptor, recognizes proteins with *C*-terminal PTS1. After recognition of PTS1, the cargo is shuttled towards the peroxisomal membrane. The docking complex comprising Pex13 and Pex14 interacts with the cargo-loaded Pex5. Afterward, the cargo with Pex5 is imported through a transient pore into the peroxisomal matrix built by Pex13.[189] After import, the peroxisomal membrane proteins Pex2/Pex10/Pex12, forming the RING-finger complex, recognize Pex5. Following, the receptor gets ubiquitinated.[190] Hereby, the Pex2 protein is responsible for polyubiquitination facilitated by Ubc4, whereas Pex10/Pex12 are responsible for mono ubiquitination facilitated by UbcH5a/b/c.[191] The recycling of the receptor is dependent on the ubiquitination status. Mono-ubiquitinated receptors are recycled, and poly-ubiquitinated receptors are degraded by proteasomal enzymes.[192] After ubiquitination, the Pex5 protein is shuttled through the membrane by the ATPase Pex1 and Pex6 using ATP as an energy donor. The heterohexameric AAA^{+}-ATPase can unfold Pex5 by threading them through a central pore in a continuous, processive manner. During this process, the cargo of Pex5 is

released in the matrix.[193] Mono-ubiquitin of Pex5 is removed in the cytosol by de-ubiquitinating enzymes (DUBs) and recycled for the uptake machinery.[194]

Unlike PTS1, the PTS2 signal is recognized by the Pex7 receptor. This uptake is based on the same mechanism as for PTS1 and differs only for the Pex5 and Pex7 receptors. Interestingly, Pex7 does not translocate to the docking complex. Instead, the receptor binds to the long isoform of Pex5 (Pex5L), gets shuttled to the docking complex, and is imported into the peroxisomal matrix through Pex13.[195] The export and recycling mechanism is the same as for Pex5.

To conclude, developing organelle-targeted peptides offers precise therapeutic options that modulate subcellular processes within the target. The drug's effect is localized to the correct organelle, enhancing its efficacy and minimizing off-target effects. The benefits of organelle-targeted therapies make it possible to treat the cause of the disease mechanisms instead of treating symptoms.

1.8 The CPP sC18 and its development

In 2009, CPP sC18, which is derived from the antimicrobial protein cathelicidin CAP18 found in rabbit neutrophils, was described. It is able to bind and inhibit LPS.[86] This peptide may be potent in antimicrobial activity, as LPS is on the surface of the envelope of Gram-negative bacteria. This peptide is from the *C*-terminal part of C18 (aa 106-121) of CAP18, in Fig. 7.

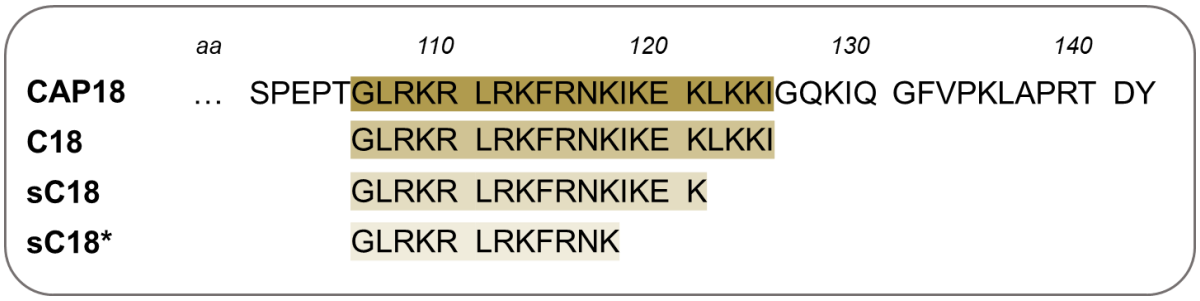

Figure 7. The CPP sC18 is derived from the C-terminal region of the cationic antimicrobial protein CAP18 (Uniprot: P25230, 18 kDa). The *C*-terminal region, termed C18 (aa 106–125), was truncated to form sC18, which adopts an alpha-helical structure in membrane environments. Further deletion of the last four amino acids yielded the variant sC18*.

As described in the previous chapter about CPP, sC18 is classified as secondary amphipathic CPP because it forms a secondary structure upon membrane interaction. The CPP sC18 was investigated in terms of its antimicrobial and anti-cancer properties.[93,96,196] Further studies analyzed the peptide's capacity as a carrier for delivering small molecules, and the peptide was also used to target subcellular organelles.[197,198] Sequence truncation resulted in the peptide sC18. However, ongoing discovery and clarification of the peptide led to an additional shortening of the sequence by four more amino acids. This new peptide was named sC18*.

To increase the net charge of sC18 further, the peptide was newly designed as a dimer ($sC18_2$). This peptide already showed higher uptake efficacy and, due to increased net charge, also a certain tumor selectivity.[199,200] To enhance its therapeutic efficacy, sC18 was also used for either direct or co-incubated drug delivery. Small molecules' inability to overcome the cellular membrane is a major challenge. However, since sC18 can traverse the membrane via mainly endocytic mechanism and additional direct penetration, it is favored as a drug carrier. Co-incubation of $sC18_2$ with Actinomycin D, acting as a chemotherapeutic drug, revealed high efficacy in transportation. Therefore, the anti-cancerous activity was highly increased.[200] Additional conjugation of sC18 with thiosemicarbazone-platinum complexes was investigated, which are known for their anti-proliferative activity, making them promising alternatives to the commonly used chemotherapeutic agent cisplatin. Due to their low bioavailability and limited cellular uptake, conjugation to bioactive peptides, like sC18, offered an effective strategy to enhance delivery. Notably, this sC18-based system demonstrated high stability and low cytotoxicity, likely due to the peptide's properties, making it a strong candidate for clinical application in late-stage radiolabeling approaches.[201] Further studies from Feni et al. started to use a variant of sC18 for generating PDC.[198] As the peptide is conjugated to daunorubicin via the lysine side chain, the peptide was further modified by incorporating a targeting sequence (RGD-motif) for $\alpha V\beta_3$ integrin-expressing cells. Due to this modification, the PDC showed enhanced toxic effects in $\alpha V\beta_3$ integrin-expressing cells.[198]

Another study showed that sC18 variants with organelle-targeting motifs can target cellular receptors. By incorporating signal sequences, studies have also revealed the possibility of targeting subcellular organelles. For targeting the nucleus, sC18 or its shortened version, sC18*, was fused with N50 or NrTP sequences. After fusion with the signal sequences, the observed cytotoxicity remained low, even though the peptides were taken up highly into the nucleus. Co-incubation of sC18*-N50 or sC18*-NrTP with the cytostatic drug Doxorubicin revealed that the drug was shuttled more efficiently into the nucleus.[197] In another study, sC18 was fused to MTS, which led to mitochondrial uptake and highly enhanced the activity of the cytostatic drug after covalent conjugation with chlorambucil.[175] In addition to subcellular targeting, our group recently reported the design and analysis of cell-permeable CaaX peptides consisting of the CPP sC18* bearing the CaaX-motif derived from Ras proteins. Through this modification, the intracellular prenylation machinery was targeted and influenced.[94]

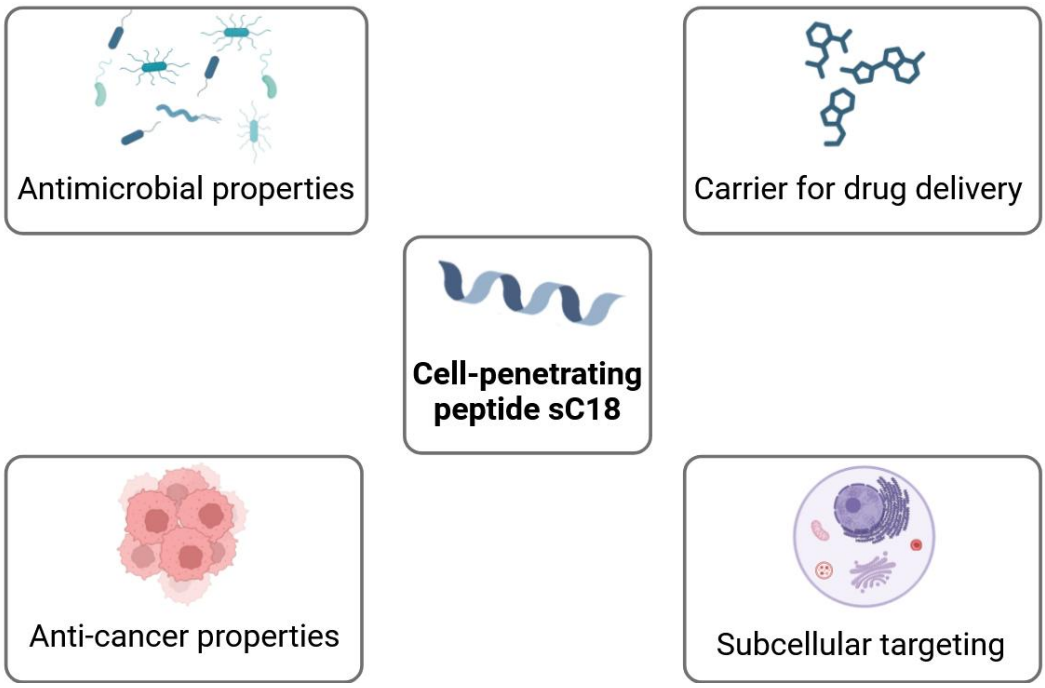

Figure 8. The CPP sC18 and its diverse applications, including antimicrobial activity, anti-cancer properties, drug delivery, and subcellular targeting capabilities. Image created with Biorender®.

As the peptides demonstrated anti-cancer activity, they are likely also to exhibit antimicrobial effects because the membranes of bacteria are predominantly negatively charged, similar to cancerous cells. Interestingly, the peptide sC18 showed nearly no antimicrobial activity, although derived from an antimicrobial protein. To further increase the activity towards bacteria, imidazolium salt conjugates were generated. These conjugates showed antimicrobial activity in low micromolar ranges in multi-resistant bacteria. However, the study revealed that the peptide was not responsible for the activity.[196] Subsequent studies aimed to increase the antimicrobial properties of the peptide itself by amino acid exchanges. Thus, amino acid substitutions were analyzed, and three critical amino acids (Arg10, Glu15, and Lys16) for antimicrobial activity were identified. In particular, the amino acids in direct proximity to the hydrophobic side, Arg10, and Lys16, are favorable for hydrophobic amino acid exchanges. Therefore, phenylalanine and additional fluorinated phenylalanine were incorporated into the sequence. Through these modifications, the overall antimicrobial activity was greatly increased.[93] A worldwide problem is that bacterial biofilm accumulates on the surface of clinical material, resulting in wound infection. Therefore, bifunctional chimeric peptides were developed by fusing an improved sC18 variant with additional titanium-binding sequences. These peptides showed high activity in solution and on titanium surfaces. Due to their ease of synthesis and handling, these peptides offer a promising alternative for preventing bacterial biofilm formation.[93,202]

In summary, all these studies showed that the activity and mode of action of sC18 depend on its modifications and incorporation with drugs, signaling sequences, or protein motifs. As a CPP, sC18 has demonstrated versatile capabilities, including antimicrobial properties, delivery of small-molecule drugs, anti-cancer effects, and targeted intracellular delivery, as shown in Fig. 8. The primary challenge is the rapid proteolytic degradation of peptides. To address this, peptides can be modified by incorporating unnatural building blocks, such as D-amino acids or triazolyl bridges. These modifications prevent proteases from recognizing cleavage sites, significantly limiting peptide degradation.[145]

1.9 Objectives

Cancer is still one of the major causes of death worldwide, and research is focusing on cancer therapy mediated by cell-selective targeting to circumvent high side effects. In addition to the well-known cancer disease, rarer diseases have become a focus of current research. Peroxisomal-related diseases have not yet been fully understood, and the treatment of these diseases has so far been mostly symptom-oriented. Besides diseases related to cancer or organelle-specific malfunctions in eukaryotes, several bacterial strains have started to resist common antibiotics. Current research in bacterial treatments is being greatly expanded to investigate and develop antimicrobial substances to fight the antimicrobial resistance crisis. In this work, variants of sC18 will be developed to address these topics and to support the current research:

1. sC18 variants and their property of transporting Doxorubicin

In the first part of this work, the question arose of whether the peptide sequence of sC18 can be improved to be used as a vehicle for an anti-cancer drug. To answer this question, the sequence of sC18 will be modified to improve cellular internalization and selectivity. Finally, the promising variants will be investigated as PDCs to improve the efficacy and selectivity of the anti-cancer drug Doxorubicin.

2. sC18 variants and the property to target subcellular organelles

In previous studies, the peptides sC18* and sC18*R,L have shown the ability to translocate the plasma membrane through endocytic and direct penetration processes. In this study, the question arose of whether these properties could be used for intracellular targeting, specifically, the peroxisome. Therefore, chimeric peptides will be designed with peroxisomal targeting sequences. These peptides are hypothesized to internalize into cells, and the peroxisomal import machinery is used to reach the peroxisome. This might present a novel approach for targeted drug delivery for peroxisomal-related diseases.

3. Tailoring sC18* variants with antimicrobial activity

Given the antimicrobial and lytic properties of sC18* derivatives, the last study aims to further optimize their activity against bacteria, especially pathogenic ones. Therefore, it should be investigated whether increasing the number of hydrophobic or basic amino acids of sC18* influences the overall antimicrobial activity. Moreover, it is hypothesized that stabilized secondary structure and proteolytic resistance might influence antimicrobial activity. To address this, a triazolyl-bridge will be introduced to reveal if intramolecular chemical modifications could stabilize the secondary structure and enhance proteolytic stability. Additionally, incorporating D-amino acids and reversing the sequence should increase proteolytic resistance further.

2. Material and methods

2.1 Amino acids and resins

All N^{α}-Fmoc protected amino acids and the Rink amide resin were purchased from IRIS Biotech (Marktredwitz, Germany). The preloaded Wang resins and the TentaGel™ S RAM were bought from Merck (Darmstadt, Germany).

2.2 Chemicals

All chemicals, disposables, and reagents were obtained from Carl Roth (Karlsruhe, Germany), Jena Bioscience (Jena, Germany), Merck (Darmstadt, Germany), Sarstedt (Nümbrecht, Germany), and VWR (Darmstadt, Germany) unless otherwise stated.

2.3 Lipids

All lipids used in this study are shown in Tab. 5. All lipids were purchased from Avanti Polar Lipids, Inc. (Alabaster, USA). DOPE, labelled with Atto550, was purchased from Atto Tec (Siegen, Germany).

Table 5. List of used lipids and their abbreviation.

Lipids	Abbreviations
1,2-dioleoyl-sn-glycero-3-[phospho-rac-(1- glycerol)]	DOPG
1,2-dioleoyl-sn-glycero-3- phosphoethanolamine	DOPE
1,2-dioleoyl-sn-glycero-3-phosphocholine	DOPC
1,2-dioleoyl-sn-glycero-3- phosphoethanolamine with Atto 550	Atto550-DOPE

2.4 Figure creation

All figures and tables were generated using BioRender, Microsoft PowerPoint, ChemDraw, Pymol, or Origin.

2.5 Data storage

All primary data are stored on the servers Sofs2 of the Regionales Rechenzentrum der Universität zu Köln (RRZK) and can be viewed on request.

2.6 Equipment

Balances	FA-210-4i, Faust (Klettau, Germany)
	LA 124i, VWR (Darmstadt, Germany)
Cell culture clean bench	Herasafe HS12, Thermo Scientific (Waltham, Massachusetts, USA)
Centrifuges	Heraeus Pico 17, Thermo Scientific (Waltham, Massachusetts, USA)
	Heraeus Multifuge X1R, Thermo Scientific (Waltham, Massachusetts, USA)
	Centrifuge 5147 R, Eppendorf (Hamburg, Germany)
	Centrifuge 5417 C, Eppendorf (Hamburg, Germany)
	MIKRO 22 R, Hettich (Tuttlingen, Germany)
CO_2-incubator	CB Series, Binder (Tuttlingen, Germany)
Concentrator	SpeedVac Savant SC210A and RVT5105 Refrigerated Vaport Trap VLP80 Vacuum Pump, Thermo Scientific (Waltham, Massachusetts, USA)
Electrophoresis power supply	EPS 600, Pharmacia Biotech (Stockholm, Sweden)
	Model 1000/500, Bio-Rad Laboratories (Hercules, California, USA)
ESI mass spectrometer	LTQ XL, Thermo Scientific ((Waltham, Massachusetts, USA)
Flow cytometer	Guava® easyCyte, Merck (Darmstadt, Germany)
Haemocytometer	Neubauer improved, superior Marienfeld (Lauda-Königshofen, Germany)
Heating block	Thermomixer compact, Eppendorf (Hamburg, Germany)
HPLC (analytical)	Hewlett Packard Series 1100, Agilent (Waldbronn, Germany) column: CC 125/4.6 NUCLEODUR 100-5 C18ec, Macherey-Nagel (Düren, Germany)

HPLC (preparative)	Elite LaChrom, Hitachi (Chiyoda, Japan); Autosampler L-2200, Pump L-2130, Diode Array Detector L-2455 and Fraction Collector FoxyR1, Teledyne ISCO (Lincoln, Nebraska, USA) column: VP 250/16 NUCLEODUR 100-5 C18ec, Macherey Nagel (Lincoln, Nebraska, USA)
Imaging system	ChemiDoc™ (BioRad)
LC-MS	LC: Hewlett-Packard Series 1100 (Agilent) MS: LTQ-XL, Thermo Scientific (Waltham, Massachusetts, USA) columns: Aeris™ 3.6 µm PEPTIDE XB-C18 100 Å, Phenomenex (Aschaffenburg, Germany) EC 125/4.6 NUCLEODUR 100-5 C18ec, Macherey-Nagel (Düren, Germany)
Lyophilizer	Alpha 2-4 LDplus, Christ (Osterode am Harz, Germany)
Magnetic stirrer	RET basic, IKA®-Werke GmbH & Co. KG (Staufen im Breisgau, Germany)
	VMS-C7, VWR Advanced (Darmstadt, Germany)
Microscope	Keyence BZ-X810, objective: 60x immersion oil objective (Osaka, Japan)
	UltraView VoX spinning disk confocal microscope, objective: Plan-Apo Tirf 60x/1,49 Oil DIC objective, Perkin Elmer (Waltham Massachusetts, USA)
Multipipette	Multipipette M4, Eppendorf (Hamburg, Germany)
NanoDrop	NanoDrop™ TM 1000 Spectrophotometer, Thermo Scientific (Waltham, Massachusetts, USA)
pH-meter	761 Calimatic, Knick International (Berlin, Germany)
Pipettes	Eppendorf (Hamburg, Germany)
Pipetting aid	NeoLab (Heidelberg, Germany)
Plate reader	Infinite M200, Tecan (Männedorf, Switzerland)
Rotary shaker	KL-2, Edmund Bühler GmbH (Bodelshausen, Germany)
	Swip, Edmund Bühler GmbH (Bodelshausen, Germany)

SDS-PAGE system	Mini-PROTEANT® Tetra Cell, Bio-Rad Laboratories (Hercules, California, USA)
Semi-Dry blotting system	kuro Gel, VWR (Darmstadt, Germany)
Spectrophotometer	Pharo 300, Spectroquant®, Merck (Darmstadt, Germany)
Synthesis robot	Syro I, MultiSynTech (Bochum, Germany)
	PurePep® Chorus, Gyros Protein (Uppsala, Sweden)
	Liberty Blue 2.0, CEM (Kamp-Lintfort, Germany)
TEM	JEM-2100 Plus Transmission Electron Microscope, JEOL (Akishima, Japan)
Thermocycler	Professional TRIO Thermocycler, Biometra (Jena, Germany)
Ultramicrotome	Leica Microsystem, UC6 equipped with a diamond knife (Biel, Switzerland)
Vacuum pump	VWR (Darmstadt, Germany), vacuubrand (Wertheim, Germany)
Vortex	Vortex-Genie 2, Scientific Industries, Inc. (Bohemia, New York, USA)
	JK MS2 Minishaker, IKA®-Werke GmbH & Co. KG (Staufen im Breisgau, Germany)
Water bath	SW22, Julabo (Seelbach, Germany)

2.7 Solid phase peptide Synthesis (SPPS)

All peptides used in this work were synthesized using manual or automated solid-phase peptide synthesis (SPPS), as described in chapter 2.7.1. The used amino acids were N_{α}-protected by Fmoc or Boc, and trifunctional side chains were further protected with acid-labile or base-labile protecting groups working with an orthogonal protecting group strategy.

2.7.1 Automated SPPS

By using automated SPPS, peptides were synthesized in a parallel way. Primarily, the peptides were synthesized with the Syro I peptide synthesizer, whereas the triazolyl-bridged and retro inverso peptides were synthesized with the PurePep® Chorus. The Fmoc/tBu protecting group strategy was used with both automated synthesizers. The synthesis was performed in an open polypropylene reaction vessel equipped with a Teflon frit. Rink amide or Wang-resin was swollen in DMF for up to 15 min to enable a successful coupling efficiency. Then, the following steps depicted in Fig. 9 were performed for the complete sequence.

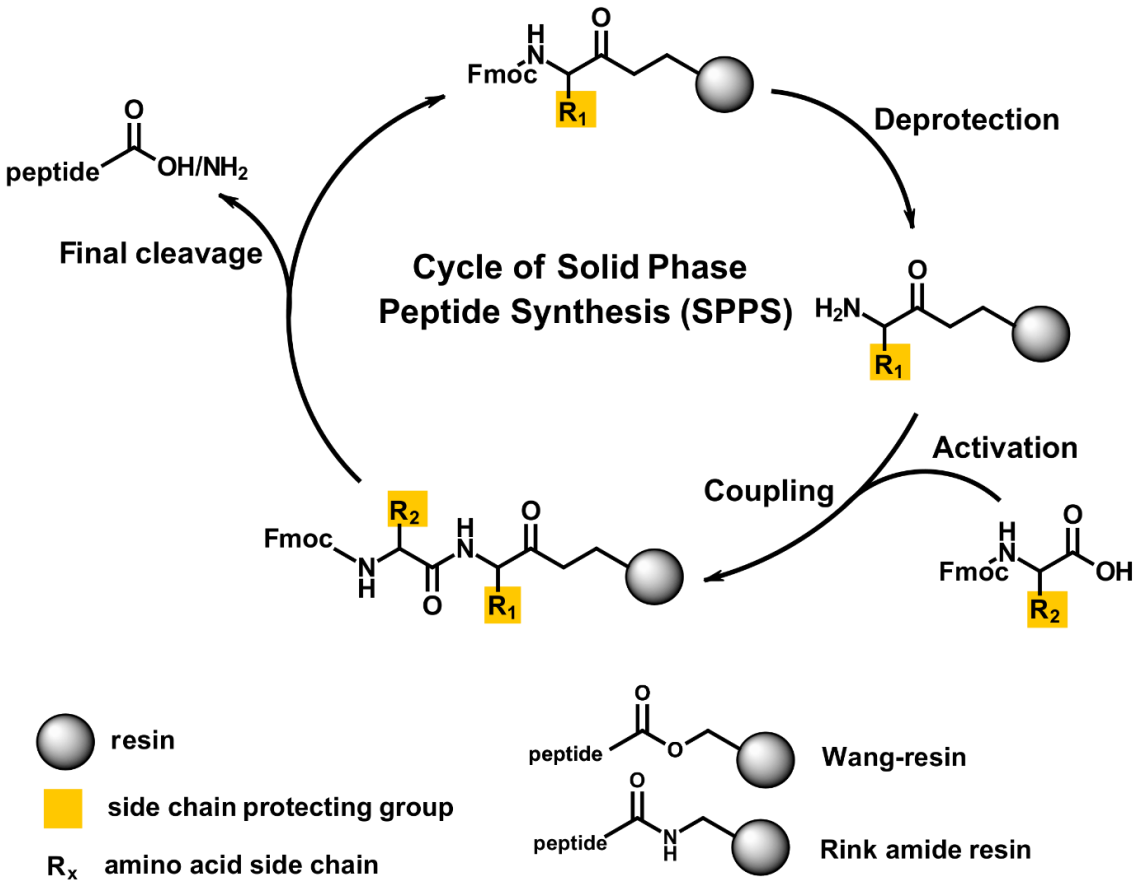

Figure 9. Cycle overview of Solid Phase Peptide Synthesis. First, the resin was deprotected, followed by activation and coupling of the amino acid. This coupling step was repeated twice. This represents one cycle for one amino acid and will be repeated as often as necessary. Finally, the resin was cleaved off after the final Fmoc deprotection.

The cleavage of the N_α-protecting group (Fmoc) was achieved using 40 % piperidine in DMF for 2 min and 20 % piperidine in DMF for 10 min. Afterward, the resins were washed four times with 600 µl DMF and incubated with 300 µl of the Fmoc-protected amino acid to be coupled next, 50 µl 2.4 M DIC in DMF, and 50 µl 2.4 M Oxyma in DMF for 40 min. The coupling step was repeated after washing twice with 800 µl DMF to enhance the coupling efficiency. After the final Fmoc-deprotection, resins were washed four times with 600 µl DMF and then manually washed five times with 1 ml each of DCM, MeOH, and Et_2O. Afterward, the resins were dried.

2.7.2 Manual coupling

Special or expensive amino acids and complicated coupling steps were performed manually. First, the resin was swollen in DMF for 15 min. After discarding the DMF, 8 eq. of the appropriate amino acid and 8 eq. of Oxyma Pure were added to the resin, whereby 8 eq. of DIC were directly added into the solution. The vessel was shaken overnight (o/n) at room temperature. The coupling was repeated after washing eight times with 1 mL DMF. This time, the reactants were added to the resin with 2 eq. of the appropriate amino acid and 2 eq. of HATU. Finally, 2 eq. of DIPEA were added into the solution and shaken for 2 h at rt. The resin was washed with DMF, DCM, MeOH, and Et_2O five times and dried under the fume hood or with the SpeedVac.

2.7.3 Manual Fmoc-deprotection

The resin was swollen for at least 15 min in 1 mL DMF. Afterward, the solvent was removed, and 500 µL of 20 % piperidine in DMF was added and shaken for 20 min at rt. The reaction mixture was removed, and the cleavage was repeated once. The resin was then washed five times with DMF, DCM, MeOH, and Et_2O and afterward air-dried under the fume hood or in the SpeedVac.

2.7.4 Manual Boc protection

First, the resin was swollen in DCM for 15 min. After discarding the DCM, 10 eq. of di-*tert*-butyl-dicarbonat and 1 eq. of DIPEA in 500 µl DCM were added to the resin. The vessel was shaken 2 h at rt. The coupling was repeated after washing five times with 1 mL DCM. The resin was washed with DCM, MeOH, and Et_2O five times and dried under the fume hood or with the SpeedVac. A Kaiser test proved the success of the reaction.

2.7.5 Dde cleavage

Before removing the Dde protecting group, the resin was swollen in DMF under shaking conditions for 15 min. The cleavage solution contains 2 % hydrazine in DMF and was added

to the resin for 10 min. To check the successful deprotecting, the cleavage solution was collected and photometrically analyzed at a wavelength of 301 nm (absorption of the Dde protection group). The cleavage step was repeated until the absorbance at 301 nm is <0.1. Afterward, the resin was washed with DCM, MeOH, and Et_2O five times each. Et_2O and subsequently dried under the fume hood or with the SpeedVac.

2.7.6 Peptide drug-conjugate synthesis

As peptide drug-conjugates (PDCs), the sC18-variants were conjugated via a succinyl maleimide (SMP) linker with the anti-cancer drug Doxorubicin (Dox). The first step was to couple Dox with SMP by the catalytic activity of triethanolamine (TEA). Dox, SMP, and TEA were dissolved in DMF with a molar ratio of 1.1:1:2 and reacted in the dark for at least 3 h under stirring conditions. The coupling process was monitored by thin-layer chromatography (TLC) using chloroform, methanol, and ammonia in a ratio of 70:30:3 (v/v/v). Afterward, the Dox-SMP complex was precipitated in Et_2O o/n at -20 °C. The solution was then centrifuged at 5000 x g for 5 min at 4 °C, and the product was resuspended again in 10 mL Et_2O. This washing step was repeated five times. The pellet was dried under the hood. Then, the complex conjugation of DOX-SMP with C-sC18 was prepared by a Michael addition reaction between the thiol group from the cysteine and maleimide moiety of SMP. Therefore, the synthesized peptide and the DOX-SMP conjugate were dissolved in DMF and subsequently mixed in a molar ratio of 1:2. The reaction was performed in the dark at rt for 48 h under shaking conditions and monitored by TLC as described before. Afterward, the solution was transferred to a dialysis tube (MWCO: 1000 Da) and dialyzed against 500 mL of DMF, which was replaced every 6 h to eliminate the unreacted DOX-SMP complex. After 48 h of dialysis, the reaction was concentrated and precipitated as described for the Dox-SMP conjugate. Preparative RP-HPLC further purified the product. Finally, the conjugates were analyzed by HPLC/ESI-MS. For further assays, conjugates were stored in 1 mM stocks dissolved in MilliQ water at -20 °C.

2.7.7 Manual click reaction

All peptides with a triazolyl-bridge were synthesized at the University of Florence. The synthesis was performed on Tentagel S RAM by automated high-efficiency solid phase peptide synthesis with the PurePep® Chorus synthesizer, following the Fmoc/*t*Bu-strategy. The click reaction of the peptides was performed on resin after the entire peptide had been synthesized. The resin was incubated with 1.2 eq. of CuBr and 1.5 eq. of sodium ascorbate, 5 eq. of DIPEA, and 5 eq. of 2.6 lutidine in DMSO:DMF (1:2, v/v) at 55 °C. An infrared scan checked the efficacy to determine whether free azide moieties were left. Purification of the peptides was performed by RP-HPLC on an alliance chromatography equipped with a BEH C18 column. Peptides were finally analyzed by analytical ESI-MS.

2.7.8 5(6)-carboxyfluorescein labeling

Some peptides were labelled with 5(6)-carboxyfluorescein (CF) to visualize peptides in cellular assays. After swelling the resin in 1 mL DMF for 15 min, it was shaken with 8 eq. of each CF, Oxyma, and DIC in DMF overnight at rt. This coupling step was repeated after five washing steps with 1 mL DMF with 2 eq. each of CF, HATU, and DIPEA in DMF (total volume: 300 µL) for 2 h. Afterward, the resin was washed five times with 1 mL of DMF, DCM, MeOH, and Et_2O and dried. A Kaiser test analyzed the efficiency of the labelling. CF is likely to polymerize during the coupling; therefore, a polymer cleavage was performed. The resin was swollen again in 1 mL DMF for 15 min and then incubated twice with 500 µl 20 % piperidine in DMF at room temperature for 20 min while shaking. Afterward, the resin was washed and dried under the fume hood.

2.7.9 Kaiser test

With the Kaiser test, it is possible to prove the presence of primary or secondary amines. Due to this, the test is used to check the coupling efficiency. A few beads of the resin were incubated with one drop of each solution 1 (1.0 g ninhydrin in 20 mL EtOH), 2 (80 g of phenol in 20 mL EtOH), and 3 (0.4 mL 1 mM KCN in 20 mL pyridine) at 95 °C for 5 min. Ethanolamine served as the positive control, whereby only solutions 1-3 were used as a negative control. Blue-colored beads after incubation time indicate free amino groups or incomplete coupling.

2.7.10 Sample cleavage

A sample cleavage was performed to determine the correctness of the sequence after the synthesis. Therefore, a few dry resin beads were transferred into a 1.5 mL reaction vessel. 2.5 µL MilliQ-water and 2.5 µL triisopropyl silane (TIS) served as scavengers, and finally, 95 µL trifluoroacetic acid (TFA) was added to the reaction vessel. When the sequence contains a Cys, Met, or Trp, a different scavenger mix containing 7 µl thioanisole, 3 µL 1,2-ethandithiol, and 90 µl TFA is used. The reaction was shaken for 3 h at rt. Afterward, 1 mL of ice-cold Et_2O was added, and the peptide precipitated for at least 20 min at -20 °C. After precipitation, the reaction vessel was centrifuged for 5 min at 10,000 x g and 4 °C. The supernatant was discarded, and the pellet was washed at least five times with 1 mL ice-cold Et_2O. Subsequently, the pellet was dried under the hood or dried in the SpeedVac and dissolved in 100 µL H_2O. The few resin beads were pelleted by centrifugation at max. speed for 1 min. The supernatant was diluted 1:2 in 10 % ACN/90 % H2O/0.1 % FA for LC-MS analysis.

2.7.11 Full cleavage

A sample cleavage was performed to determine the correctness of the sequence after the final synthesis. Therefore, the complete dry resin was incubated with 25 µL MilliQ-water and 25 µL TIS, which served as scavengers, and finally, 950 µL TFA was added to the reaction vessel. When the sequence contained Cys, Met, or Trp, a different scavenger mix containing 70 µl thioanisole, 30 µL 1,2 ethandithiol (EDT), and 900 µl TFA was used. The reaction was shaken for 3 h at rt. Afterward, the cleaved peptide was precipitated in 10 mL of ice-cold Et_2O for at least one night at -20 °C. After precipitation, the reaction vessel was centrifuged for 4 min at 4,696 x g and 4 °C. The supernatant was discarded, and the pellet was washed at least five times with 10 mL ice-cold Et_2O. Subsequently, the pellet was dried under the hood or in the SpeedVac and dissolved in 1-3 mL H_2O/tert-BuOH (3:1, v/v). The peptide solution was diluted 1:10 in 10 % ACN/90 % H_2O/0.1 % FA for LC-MS analysis. Finally, the peptide was transferred into a tared glass vessel and freeze-dried o/n under vacuum.

2.7.12 Preparative RP-HPLC

After the synthesis, the peptides were purified using reverse-phase HPLC (RP-HPLC). The previously lyophilized peptides were dissolved in 960 µl of the starting gradient of a mixture of H_2O/ACN and 0.1 % TFA, depending on the hydrophobicity. The solved peptide was centrifuged at maximum speed to eliminate particles in the solution. The supernatant was injected onto a C18-column running a gradient of increasing acetonitrile (ACN) with a flow rate of 6 mL min^{-1}. Hydrophilic peptides were purified using a gradient of 10-60 % ACN in H_2O supplemented with 0.1 % TFA in 45 or 60 min. In contrast, more hydrophobic peptides were purified using a gradient of 20-70 % or 30-80 % ACN in H_2O with 0.1 % TFA in 45 min. All peaks measured at 220 nm were collected and fractionated. After removing ACN from the collected fractions by vacuum concentration, they were analyzed by analytical LC-MS using a 1:5 dilution of the fraction solution in 10 % ACN/90 % H_2O and 0.1 % FA. The correct fractions were combined and finally lyophilized.

2.7.13 Analytical HPLC-MS

The quality of the peptides was analyzed using high-performance liquid chromatography-electrospray ionization mass spectrometry (HPLC-ESI-MS). Typically, a linear gradient from 10-60 % ACN or 20-70 % ACN is supplemented with 0.1 % FA in 15 min, depending on the hydrophobicity of the analyzed peptides. The flow rate of the gradient is set to 6 mL min^{-1}. The peptides were detected by measuring the absorption at 196 nm or 220 nm, whereby the identity was determined using a linear coupled electrospray ionization-mass spectrometer based on the corresponding quasi-molecular ions that are separated according to their m/z ratio. The spectra were analyzed using Xcalibur, and the purity was determined by integrating

the peptide peak in the UV-chromatogram at 220 nm relative to the total area of all peaks. All chromatograms were visualized using Origin.

2.8 Biophysical methods and *in vitro* characterization

2.8.1 Preparation of giant unilamellar vesicles (GUVs)

Giant unilamellar vesicles were used to investigate the interaction of the peptides with different cell membranes. Dextran buffer was prepared by dissolving 10 mM HEPES buffer, 50 mM KCl, 50 mM NaCl, and 1 mg mL^{-1} Dextran in 50 mL MilliQ-water and adjusting the pH value to 7.4 with NaOH.

Glass slides for the GUV generation were washed twice with water, soap, ethanol, and acetone, respectively. A thin, low-melting agarose layer is necessary to build GUVs. Therefore, 1 % low melting agarose was melted in MilliQ water by heating up in a microwave. Afterward, 200 µL were added per slide and distributed by a pipette tip. In the next step, slides were incubated at 50 °C for 30 min on a heating plate. Generation of the lipid mixture was performed by adding 1,2-dioleoyl-sn-glycero-3-phospho-rac-(1-glycerol) sodium salt (DOPG, 30 Mol %, 24 µL), 1,2-dioleoyl-sn-glycero-3-phosphocholine (DOPC, 40 Mol %, 31 µL) and 1,2-dioleoyl-sn-glycero-3-phosphoethanolamine (DOPE, 30 Mol %, 22 µL) in specific concentrations for negatively charged GUVs by using a Hamilton syringe and 920 µL chloroform. For staining the lipid phase, 3 µL Atto550 was added. To generate the neutral lipid composition, DOPC (50 Mol %, 50 µL) and DOPE (50 Mol %, 47.32 µL) and, for the red color, Atto550 (0.2 Mol %, 3.52 µL) were mixed. Afterward, 10 µL lipid solution was placed onto the thin agarose layer and subsequently distributed. The slides were dried under vacuum for 1 h to remove the chloroform. Afterward, a sealing ring was added around the pink lipid film. Lipids were hydrated with 297 µL dextran buffer and 3 µL Oyster405 (500 µM stock). Due to hydrophobic and hydrophilic forces, vesicles are formed. Afterward, slides were incubated for 2 h at rt in the dark. Subsequently, lipids were transferred into fresh PCR tubes and centrifuged for 10 min at maximum speed. The supernatant was removed, and the pellet was resuspended in 300 µL dextran buffer. 40 µL of the generated GUV solution was transferred into an Ibidi®. Finally, 1 µM of peptide concentration was used per well and filled up to 100 µL with dextran buffer. Incubation with peptides was performed for 30 min at rt. Afterward, GUVs were analyzed using the tabletop BZ-X800E microscope. The final analysis and processing were performed with Fiji.

2.8.2 Circular dichroism spectroscopy

Circular dichroism (CD) spectroscopy was used to determine the secondary structure of peptides. Therefore, the peptides were diluted either in 10 mM phosphate buffer (pH 7.0) or

10 mM phosphate buffer (pH 7.0) supplemented with various trifluoroethanol (TFE) concentrations (25-50 %) to a final concentration of 20 µM. The spectra were recorded from 260 – 180 nm at 20 °C in 0.5 or 1 nm intervals using a Jasco J-715 spectropolarimeter in an N_2-atmosphere. The measurement was done by following settings: sensitivity: 100 mdeg; scan mode: continuous; data pitch: 0.5 nm; speed: 50 nm min^{-1}; response: 2 sec; band width: 1.0 nm. A 1 mm quartz cell was used for the measurement. Each measurement was repeated five times, and the respective buffer was subtracted as a background signal. Afterward, the curves were smoothed. The molar ellipticity [θ] was calculated as $[\theta]\mathrm{calc} = \frac{[\theta]\mathrm{meas.}}{10*n*c*l}$; with n: number of residues, c: peptide concentration in mol $L^{-1,}$ and l: path length in cm. The quality of α-helical content was calculated from the molar ellipticity value at 222 nm. R-values were calculated as the ratio between the molar ellipticity values at 222 and 208 nm, with R = 1 defined as a reference for a completely built α-helix.

2.8.3 Stability assay

A stability test was performed in human and goat serum to investigate the proteolytic stability of the peptides. The peptides were diluted in each serum until the final concentration of 250 µM. Afterward, the samples were incubated at 37 °C under shaking conditions. Initially, 20 µL of the fresh peptide and serum mix were collected and used as time point zero. 20 µL of ice-cold 100 % ACN was added, and the sample was placed on ice. This procedure was repeated after 5, 15, 30, 45, 60, 90, 120, and 240 min. Samples were then centrifuged at 15,000 rpm for 15 min at 4 °C. 15 µL of supernatant was carefully removed, and 5 µL of 10 % ACN/H_2O containing 0.1 % formic acid was added. The peptide was analyzed by LC-MS. The peptide amount was determined by integrating the area under the curve. The first sample (t0) was set to 100 % of the peptide amount. The graphs were visualized using Origin.

2.9 Biological and biochemical methods

2.9.1 Cell lines and respective culturing media

Within this thesis, several human cell lines from ATCC were used, including HeLa (human cervix carcinoma), MCF-7 (Michigan Cancer Foundation 7), MCF-7-mCherryPTS1 (genetically modified cell line created by myself), HEK293 (human embryonic kidney), and HFF-1 (human foreskin fibroblast 1). The cell lines HeLa, MCF-7, and MCF-7-mCherryPTS1 were cultured in RPMI1640 medium supplemented with 10 % fetal bovine serum (FBS) and 4 mM L-glutamine. HEK-293 cells were cultured in MEM medium supplemented with 15 % FBS and 4 mM L-glutamine. HFF-1 cells were cultured in DMEM medium supplemented with 10 % FBS and 4 mM L-glutamine. All cell lines were cultured in 10 cm sterile petri dishes, except for HFF-1, which was cultured in T-75 culture flasks at 37 °C and 5 % CO_2 in a

humidified atmosphere. From now on, all media supplemented with FBS and L-glutamine will be referred to as complete medium.

2.9.2 Maintenance of cells and seeding

The cell culture work was generally performed under sterile conditions with autoclaved and cleaned materials. Cells were cultured in 10 mL complete medium at 37 °C, 5 % CO_2, and a humidified atmosphere until the cells reached ~80 % confluency. Afterward, cells must be split and seeded into a new sterile petri dish. The cells were usually split twice weekly, or the medium was exchanged if necessary. Before splitting and seeding, the old medium of the cells was removed, and the cells were washed twice with 5 mL PBS. Afterward, 1 mL trypsin-EDTA was added and incubated at 37 °C and 5 % CO_2 until the cells were detached. The reaction of this process can be stopped by adding 9 mL complete medium. Subsequently, cells were diluted depending on the cell line and transferred into new sterile petri dishes. If cells were needed for assays, 10 µL of the undiluted cell suspension was transferred into the hemocytometer (Neubauer chamber), and the total number of cells was counted. Afterward, depending on the assay, the required number of cells was transferred into an appropriate well plate filled with fresh complete medium and grown o/n to reach confluency.

2.9.3 Freezing and thawing cells

In general, cell lines were stored in liquid nitrogen. Freezing cells is a process in which they must be detached, as described above. Cells were transferred into a 15 mL falcon and spun down at 1,300 rpm at 30 °C for 5 min. After discarding the medium, cells were resuspended in 1.5 mL complete medium containing an additional 10 % sterile-filtered DMSO solution and transferred into cryogenic vials. The vials were placed in a cryo-freezing container at -80 °C. This container enables a freezing rate of 1 °C min^{-1}. On the next day, the vials were stored in the liquid nitrogen.

To thaw cells in culture, they were incubated for 10-20 sec in a water bath at 37 °C and then transferred to 8.5 mL complete medium in a 15 ml falcon. Cells were centrifuged at 1,300 rpm and 30 °C for 5 min, and after discarding the medium, cells were resuspended in 10 mL complete medium and transferred into a fresh 10 cm petri dish or T25 culture flask. Finally, cells were grown at 37 °C, 5 % CO_2 in a humidified atmosphere.

2.9.4 Cellular viability assay

To analyze the cellular viability, cells were seeded in a 96-well plate (HFF-1: 16,000 cells, MCF-7 and mCherryPTS1-MCF-7: 20,000 cells, HeLa: 16,000) and grown o/n to about 90 % confluency. Cells were incubated with 100 µL of various peptide concentrations, depending on the tested peptides/conjugates, in a serum-free medium at 37 °C and 5 % CO_2 for 24 h.

After the treatment, cells were washed once with 100 µL PBS and incubated with 100 µL of a 10 % resazurin solution (In-vitro toxicology assay kit) in serum-free medium at 37 °C for 45-90 min. Cells that served as positive control were treated beforehand with 70 % ethanol for 10 min, whereas untreated cells served as negative control and were set to 100 % viability. Viable cells can metabolize resazurin to resorufin, which is detectable at 595 nm after excitation at 550 nm. The detection was performed using the Tecan Infinite M200 plate reader.

2.9.5 Lactate dehydrogenase release assay

To analyze the lactate dehydrogenase release and, thus, the membrane integrity, cells were seeded in a 96-well plate (HFF-1: 16,000 cells, MCF-7 and mCherryPTS1-MCF-7: 20,000 cells, HeLa: 16,000) and grown o/n to about 90 % confluency. Cells were incubated with 100 µL of various peptide concentrations, depending on the tested peptides/conjugates, in serum-free medium at 37 °C and 5 % CO_2 for 30 min. Afterward, cells were equilibrated to rt. The positive control was treated with Triton X-100, whereas the negative control was left untreated. Subsequently, a volume of CytoTox-OneTM reagent (CytoTox-ONE^{TM} Homogeneous Membrane Integrity Assay) equal to the volume of the medium present in each well was added and incubated at rt for 10 min. Finally, the reaction was stopped by adding 50 µL stop solution. Cells with disrupted membrane integrity release lactate dehydrogenase (LDH), which enzymatically converts lactate and NAD^+ to pyruvate and NADH. Diaphorase then uses NADH to convert resazurin to resorufin, which can be detected at 595 nm after excitation at 550 nm. The LDH release of the positive control treated with Triton X-100 was defined as 100 % LDH release. The detection was performed using the Tecan Infinite M200 plate reader.

2.9.6 Hemolytic activity assay

Red blood cells (RBCs, SER-10MLRBC, Tebubio) were washed three times with PBS by centrifugation at 2,000 x g and 4 °C for 5 min and diluted 1:20 in PBS. In a 96-well plate, the RBC solution was mixed with 50 µL of different peptide concentrations (2:1, v/v) and incubated for 30 min or 24 h at 37 °C and 5 % CO_2. Untreated cells served as the negative control, while cells treated with 50 µL of 10 % Triton X-100 acted as the positive control, set at 100 % hemolytic activity. Afterward, the plate was centrifuged at 1,500 x g for 3 min, and the supernatant was transferred into a fresh 96-well plate and scanned for heme groups by measuring the absorption at 540 nm with a Tecan Infinite M200 plate reader.

2.9.7 Flow cytometry

The cellular uptake was analyzed using the Guava® easyCyte flow cytometer. All cells (MCF-7/mCherryPTS1-MCF-7: 120,000, HFF-1/HeLa/Hek293: 100,000) were seeded into a 24-well

plate and grown overnight at 37 °C and 5 % CO_2 until they reached ~90 % confluency. The CF-labelled peptides were diluted in 400 µL medium lacking FBS to a final concentration of 1 µM or 10 µM, respectively. Untreated cells served as negative control, and the signal was subtracted from all measurements. Afterward, the cells were incubated for 30-120 min, depending on the approach. After discarding the peptide solution, cells were washed once with PBS, and 150 µL trypsin-EDTA (without phenol red) was added. Cells started to detach, and the reaction was stopped by adding 850 µL complete medium (without phenol red), and cells were resuspended. After transferring 200 µL of the cell suspension into a fresh 96-well plate, the uptake quantity was determined using the mean fluorescence in 10,000 cells with a GRN-B (525/30) or laser using the Guava® easyCyte flow cytometer.

2.9.8 Fluorescence microscopy

Fluorescence microscopy was performed to visualize the cellular uptake of the peptides. Staining compartments and parts of the cell transiently or by a stable cell line helped to investigate the subcellular distribution and colocalization. For these analyses, MCF-7/mCherryPTS1-MCF-7: 30,000 cells were seeded into an ibidi® 8-well plate and grown at 37 °C and 5 % CO_2 overnight. When the cells reached a subconfluency of 60-70 %, cells were treated with 300 µL of different CF-labelled peptide concentrations in serum-free medium at 37 °C and 5 % CO_2 for 30 – 120 min. 10 min before the treatment ended, 0.6 µL Hoechst 33342 (1 mg ml^{-1}) was added to the cells to stain the nucleus in blue. After incubation, cells were washed twice with 200 µL PBS and incubated in 300 µL complete medium. Cells were imaged using a Keyence BZ-X810 microscope (Plan-Apo 60x/1,40 Oil, Keyence), UltraView VoX Spinning Disk confocal microscope (Plan-Apo Tirf 60x/1,49 Oil DIC, Nikon), or LSM 980 with Airyscan 2 and multiplex confocal laser scanning microscope, (Plan-Apo 63x/1.4 Oil DIC, Zeiss). The images were finally processed with Fiji.

2.9.9 Cell lysis

1,000,000 cells (MCF-7 cells) were seeded in a 6-well plate and grown at 37 °C and 5 % CO_2 o/n. After discarding the medium, cells were treated with 10 µM of peptides in a serum-free medium for 2 h at 37 °C. Untreated cells served as negative control. Afterward, cells were washed twice with PBS and placed on ice. 150 µL ice-cold lysis buffer (25 mM Tris, 150 mM NaCl, 1 mM TCEP, 2 mM EDTA, 1 % Triton X-100, 1X Halt™ Protease Inhibitor Cocktail) was added to the cells. Cells were placed on ice and subsequently abraded using a cell scraper. The cell suspension was transferred into fresh 1.5 mL Eppendorf tubes. The tubes were incubated on ice for 20 min. Afterward, the cell debris were pelleted by centrifugation at max speed at 4 °C for 30 min. The supernatant was transferred again into fresh 1.5 mL Eppendorf tubes and mixed with SDS-PAGE loading buffer (200 mM Tris-HCl pH 6.8, 400 mM DTT, 8 %

SDS, 0.4 % bromophenol blue and 40 % glycerol) in a ratio of 4:1 (v/v). The mix was heated at 95 °C for at least 5 min and then frozen at -20 °C until further use.

2.9.10 SDS-PAGE and Western blot analysis

SDS-PAGE is a process that separates the proteins of the cell lysates, followed by an immunoblot. SDS-PAGE gels consist of a 4 % stacking gel and a 10 % separating gel. (Tab. 6).

Table 6. Components of the 4% stacking gel and the 10% separating gel with appropriate volumes.

Component	4 % stacking gel	10 % separating gel
Acrylamide/bisacrylamide 30 % (37.5:1)	1.33 mL	4.16 mL
Gel buffer (3 M Tris, 0.3 % SDS, pH 8.45)	3 mL	4.165 mL
ddH_2O	5.6 mL	4 mL
10 % APS (ammonium persulfate)	90 µL	100 µL
TEMED	10 µL	15 µL

Proteins from cell lysates were analyzed using SDS-PAGE and immunoblotting techniques. Gels were assembled in the Mini-PROTEANT® Tetra Cell (Bio-Rad) with anode buffer (100 mM Tris, pH 8.9) and cathode buffer (100 mM Tris, pH 8.25, 100 mM tricine, 0.1 % SDS). Samples cooked and mixed with SDS-PAGE loading buffer were heated up again at 95 °C for a few minutes and were then loaded onto the SDS-PAGE gel and separated initially at 50 V for 10 min, then at 120 V for 1 h, alongside a protein size marker (PageRulerTM Plus Prestained Protein Ladder, Thermo Fisher Scientific).

Proteins were transferred onto a methanol-activated polyvinylidene fluoride membrane (PVDF) for immunoblotting using a semi-dry transfer method. The PVDF membrane was activated in methanol for 10 sec and assembled with six Whatman papers, the SDS-PAGE gel, and six more Whatman papers, all soaked in transfer buffer (25 mM Tris, pH 8.3, 192 mM glycine, 20 % methanol). The transfer was carried out at a constant current of 200 mA per membrane for 1.5 h.

Post-transfer, the membrane was blocked in 5 % BSA in PBS-T with gentle shaking for 1 h at rt. It was then incubated o/n at 4 °C with primary antibodies diluted in 5% BSA in PBS-T. The next day, the membrane was washed three times for 10 min each with PBS-T at room temperature, followed by a 1.5 h incubation with secondary antibodies diluted in 5% BSA in PBS-T. After another series of washes, the membrane was treated with enhanced

chemiluminescence solution (ECL) and visualized using a ChemiDoc system (Bio-Rad) to detect horseradish peroxidase (HRP)-conjugated antibodies.

2.9.11 Transient transfection

To perform transient transfection, cells were seeded (MCF-7/mCherryPTS1-MCF7: 30,000 cells per well) into an 8-well ibidi® in complete growth medium and grown to 70-90 % subconfluency. For the transfection, Lipofectamine2000 was used and equilibrated at rt 30 min before usage. 1 µg of the plasmid was mixed with 25 µl Opti-MEM, and 1 µL of Lipofectamine2000 was also mixed with Opti-MEM and filled up to 25 µL. Both mixtures were incubated for 5 min at rt. Afterward, they were combined by adding the plasmid-mix to the Lipofectamine2000-mix. The final mixture was incubated for 20 min at rt to form the DNA-Lipofectamine2000 complexes. Before the transfection mix was dropwise added to the 8-well ibidi®, the old medium was exchanged with medium without supplements. Afterward, the plate was incubated 4 h in a 37 °C CO_2 incubator. Then, the transfection medium was replaced by fresh complete medium. For protein expression, cells were incubated for 24 h. Cells were analyzed using a Keyence BZ-X810 microscope (Plan-Apo 60x/1,40 Oil, Keyence). The images were finally processed with Fiji.

2.9.12 Stable cell line bearing mCherry with PTS1

Plasmid construction was created to develop a stable cell line inductively expressing mCherry with peroxisomal-targeting signal 1(PTS1). In general, a PiggyBac system was used to create it. Therefore, the mCherry-PTS1 plasmid was ligated into the empty PiggyBac vector. After plasmid construction, the plasmids needed to be amplified and purified. 4-5 ng of PB-CuO-mCherry-Peroxisome-2-BGH 787 ng μl^{-1} (5.09 µL) and pCI-FLAG PiggyBac Transposase 1800 ng μL^{-1} (2.22 µL) were transformed into DH5α *E. coli*. The transformation was performed as follows: DH5α *E. coli* were thawed in a water bath directly mixed with the DNA and subsequently incubated on ice for 30 min. Afterward, cells were heat shocked at 42 °C for 45 sec, followed by incubation on ice for 2 min. Then, 500 µl fresh LB-medium was added, and the cells were incubated for 90 min under shaking conditions. Afterward, 200 µL of the suspension was distributed on LB-selection agar containing ampicillin. The next day, colonies were picked and inoculated in LB-medium containing ampicillin o/n at 37 °C and shaken with 180 rpm. The plasmids were purified using a midi prep (Carl Roth) as described in the manufacturer's instructions. The concentration of the plasmids was determined using the NanoDrop. Plasmid PCI-Flag-PB-TPase had a concentration of 896.8 ng μL^{-1} and the plasmid PB-CuO-mCherry-Peroxisome-2-BHG of 854.4 ng μL^{-1}. To ensure the correctness of the plasmids, they were sequenced using Sanger sequencing with appropriate primer.

On the first day, cells were seeded (MCF-7: 400,000 cells) into a 6-well plate and incubated in a 37 °C CO_2 incubator to reach 70-80 % subconfluency. For simultaneous transfection, Lipofectamine2000 was used and equilibrated at rt 30 min before usage. The plasmids, Lipofectamine2000, and the medium were mixed, as depicted in Tab. 7.

Table 7. Components of the transfection reagent with respective concentration and amount necessary to mix A and B.

Component	conc. [ng/µL]	amount [ng]	Tube A [µL]	Tube B [µL]
PCI-FLAG-PB-Tpase	896.8	500	0.6	-
PB-CuO-mCherry-Peroxisome-2-BHG	854.4	1300	1.5	-
Lipofectamine2000	-	-	-	5
Opti-MEME	-	-	247.9	245

Both mixes were incubated for 5 min at rt. Afterward, they were combined by adding Tube-A to Tube-B. The final mixture was incubated for 20 min at rt to form the DNA-Lipofectamine2000 complexes. Before the transfection mix was dropwise added to the 6-well plate, the old medium was exchanged for a medium without supplements.

Table 8. PCR-mix and the reaction steps used to amplify the oligonucleotides. PCR-mix consists of 5X Q5 buffer, 10 nM dNTPs, 10 µM forward primer, 10 µM reverse primer, Q5 polymerase, and nuclease-free water. The cycle of denaturation, annealing, and elongation was repeated 36 times.

Component	Volume [µL]
5X Q5 buffer	10
10 mM dNTPs	1
10 µM Forward primer	15
10 µM Reverse primer	15
Q5 Polymerase	0.5
Nuclease-free water	8.5

Reaction step	Temp. [°C]	Time [sec]	Cycle
Denaturation	95	60	1
Denaturation	95	5	36
Annealing	50	10	
Elongation	72	5	
Elongation	72	120	
Break	4	∞	

The transfection medium was replaced 24 h after transfection by a fresh, complete medium. After an additional 24 h, all cells were transferred using Trypsin/EDTA into 10 cm petri dishes in which they were treated with 2.5 µg mL^{-1} puromycin. Beforehand, a kill curve of puromycin was performed in MCF-7 cells, and the concentration of 2.5 µg/mL was set for further positive clone selection. Cells were grown for one week in a 37 °C CO_2 incubator in the selection medium containing the appropriate amount of puromycin. The medium was changed every two days to maintain the puromycin concentration in the medium. Afterward, cells were cultured in a complete medium without puromycin to recover successfully transfected cells. Few cells started to generate colonies in the dishes. The recovery time was around two weeks until the cells reached 70-80 % subconfluency. Cells were split into fresh petri dishes to freeze them in liquid nitrogen (as described in 2.9.3 Freezing and thawing cells). To determine whether the transfection worked, cells were induced with cumate in different concentrations to determine the best expression level of the mCherry-PTS1 protein. This analysis utilized the Keyence BZ-X810 microscope (Plan-Apo 60x/1,40 Oil, Keyence). The induction test revealed that 30 µg mL^{-1} cumate showed the best expression levels of mCherryPTS1 protein and subcellular distribution in a vesicular pattern labelling the peroxisomes.

2.9.13 Plasmid construction

For individual plasmid constructs, the constructs had to be designed beforehand. The Gehring Lab kindly provided the backbone plasmid 3407. This plasmid 3407 encodes a mGold protein with a multiple cloning site (MCS) at the *C*-terminus of this protein. The oligonucleotides for the insert were designed to contain the desired peptide and PTS, including the restriction enzyme sites for cloning into the plasmid 3407. The restriction sites of NotI and XhoI were chosen and included in the oligonucleotide sequences shown in Tab. 9. The oligonucleotides were designed to anneal with the reverse primer and amplify the oligonucleotides using polymerase chain reaction (PCR). The different oligonucleotides were industrially synthesized by metabion and shipped lyophilized. They were dissolved in appropriate nuclease-free water to a final concentration of 100 µM. Then, the forward and reverse primers were mixed with Q5 polymerase, dNTPs, Q5 buffer, and water. Afterward, the reaction was performed as described in Tab. 8. Afterward, the PCR product was purified via PCR clean-up from Roth. PCR products and the plasmid 3407 bearing the mGold protein were digested using NotI and XhoI restriction enzymes. The digest reaction mix was done as described in Tab. 10 and incubated for 1 h at 37 °C. To inactivate the enzymes, the digest mix was heated up to 65 °C for 20 min. The Plasmid constructs were purified via PCR clean-up from Machery Nagel, and the digested plasmid was purified using agarose gel electrophoresis. A 1 % agarose gel was used at 200 V for 1 h to separate the digested plasmid. Afterward, the plasmid was extracted using the NucleoSpin PCR and Gel Extraction Kit from Machery Nagel. The plasmid band was

cut out under UV light and melted at 60 °C in a buffer provided by the kit for 10 min. The purification was performed as described in manuals from Machery Nagel.

Table 9. Name and sequence of the engineered PCR constructs. The insert is highlighted in grey. All inserts have an XhoI and NotI restriction site, and behind the insert is a stop codon.

Name	Sequence
sC18*	AAA ACT CGA GGG CCT GAG AAA GCG GCT GCG GAA GTT CAG AAA CAA ATG AGC GGC CGC AAA A
sC18*^{R,L}	AAA ACT CGA GAG ACT GCG GAA GCT GCT GAG AAA GTT CCT GCG GAA ATG AGC GGC CGC AAA A
PX9	AAA ACT CGA GAG ACT GCG GAA GCT GCT GAG AAA GTT CCT GCG GAA GCC CGG CAA CGC CAA GCT CTG AGC GGC CGC AAA A
PX10	AAA ACT CGA GGG CCT GAG AAA GCG GCT GCG GAA GTT CAG AAA CAA GCC CGG CAA CGC CAA GCT CTG AGC GGC CGC AAA A
PX11	AAA ACT CGA GAG ACT GCG GAA GCT GCT GAG AAA GTT CCT GCG GAA AGG CGG AGG CAA GAG CAA GCT CTG AGC GGC CGC AAA A
PX12	AAA ACT CGA GGG CCT GAG AAA GCG GCT GCG GAA GTT CAG AAA CAA AGG CGG AGG CAA GAG CAA GCT CTG AGC GGC CGC AAA A
PTS1_1	AAA ACT CGA GCC TGG AAA CGC CAA GCT CTG AGC GGC CGC AAA A
PTS1_2	AAA ACT CGA GGG TGG CGG AAA GAG CAA GCT CTG AGC GGC CGC AAA A
Reverse Primer	TTT TGC GGC CGC

Table 10. Component and the respective volume of the restriction mix of the PCR products. Restriction mix consists of r3.1 10X buffer, PCR-product or plasmid, NotI, XhoI, and nuclease-free water.

Component	Volume [µL]
r3.1 10X Buffer	5
PCR-product/plasmid	19
NotI enzyme	1
XhoI enzyme	1
Nuclease-free water	24

The concentration of the purified digested plasmid was determined by analyzing the absorbance at 260 nm with a NanoDrop. To insert the digested PCR product into the digested plasmid, a ligation with the T4 ligase was performed. Therefore, the annealed oligonucleotides were mixed with the plasmid vector in a 1:3 molar ratio. The reaction mix is described in Tab. 11. The ligation was done at 16 °C in a thermocycler. Afterward, the T4 ligase is inactivated at 65 °C for 10 min.

Table 11. Component and respective volume of the ligation mix. The ligation mix is out of T4-ligase buffer, digested plasmid 3407, digested PCR product, T4 ligase, and nuclease-free water.

Component	Volume [µL]
T4-ligase buffer	2
Plasmid 3407	1
PCR construct	3
T4 Ligase	1
Nuclease-free water	13

The heat-shock method described above used 2 µL of ligation product to transform 50 µL chemically competent DH5α *E. coli* cells. After mixing the bacteria with the plasmids, the mixture is chilled on ice for 30 min. Afterward, cells were shocked at 42 °C for 30 sec and subsequently cooled down on ice for 2 min. The transformed cells were then incubated with 350 µL at 37 °C under shaking for 90 min. The transformation mix was distributed on AMP-LB-agar plates and incubated o/n at 37 °C for further selection. The next day, positive colonies were picked and incubated in AMP-LB-medium o/n at 37 °C. The plasmid DNA was extracted using a midi prep as described in the manufacturer's instructions. Finally, the sequence of the

plasmid and inserted oligos were analyzed by EuroFins, which performed sanger sequencing, for instance, using appropriate primers flanking the insert region.

2.9.14 Colocalization studies of CF-labelled peptides/mGold plasmid with stable cell line mCherryPTS1-MCF-7

For colocalization studies, 25,000 cells of mCherry-PTS1-MCF-7 per well were seeded into an ibidi with an appropriate complete medium and cultivated o/n at 37 °C, 5 % CO_2 under humidity conditions. Within the next day, cells were washed once with PBS. Afterward, they were induced with appropriate cumate concentration to produce the mCherry protein bearing the PTS1 and incubated again o/n at 37 °C, 5 % CO_2 under humidity conditions.

The transfection of the plasmid 3407 with individual insert was performed using Lipofectamine2000. For this, it was prewarmed at rt for 30 min. 1 µg of the plasmid was mixed with 25 µl Opti-MEM. Also, 1 µL of Lipofectamine2000 was mixed with Opti-MEM and filled to 25 µL. Both mixes were incubated for 5 min at rt. Afterward, they were combined by adding the plasmid mix to the Lipofectamine2000 mix. The final mixture was incubated for 20 min at rt to form the DNA-Lipofectamine2000 complexes. Before the transfection mix was added dropwise to the 8-well ibidi®, the old medium was exchanged for a medium without supplements. Afterward, the plate was incubated for 4 h in a 37 °C CO_2 incubator. Then, the transfection medium was replaced by the fresh, complete medium. Cells were incubated for 24 h for protein expression.

However, for the peptide co-localization assay, cells were treated with 300 µL of different CF-labelled peptide concentrations in serum-free medium at 37 °C and 5 % CO_2 for 15 min, 30 min, 60 min, or 120 min. 10 min before the end of the treatment, 0.6 µL Hoechst 33342 (1 mg ml^{-1}) was added to the cells to stain the nucleus in blue. After incubation, cells were washed twice with 200 µL PBS and placed in a 300 µL complete medium. Cells were imaged using a Keyence BZ-X810 microscope (Plan-Apo 60x/1,40 Oil, Keyence) or UltraView VoX Spinning Disk confocal microscope (Plan-Apo Tirf 60x/1,49 Oil DIC, Nikon). The images were processed with Fiji.

2.9.15 Bacterial cell culture

Within this thesis, several bacterial strains were used, including *Bacillus spizizenii (ATCC 6633)*, *Salmonella typhimurium (TA100)*, *Pseudomonas fluorescens (DSM 50090)*, *Micrococcus luteus (DSM 20030)*, *Neisseria gonorrhoeae* Ng196 (*pilE::cat, G4::acc*, S2), and methicillin-resistant *Staphylococcus aureus* (MRSA-43300, S2). All bacterial strains with biological safety level 1 (S1) were spread out of glycerol stock on LB-agar plates and incubated overnight at 37 °C. Bacteria were spread out monthly to avoid contamination. The

following day, one colony was selected, added to 5 mL of pre-warmed LB medium, and then incubated at 37°C under shaking at 180 rpm o/n. The preculture was diluted in 25 mL fresh LB-medium and grown to an optical density at 600 nm (OD_{600}) of more than 0.7. The bacterial culture was used for further experiments at the exact optical density.

N. gonorrhoeae was cultivated in the working group of Prof. Berenike Maier, whereas MRSA was cultivated in the working group of Prof. Andreas Klatt.

2.9.16 INT assay

The iodonitrotetrazolium chloride (INT) assay was used to analyze the bacterial viability. Bacterial cultures with an optical density of 0.7 at 600 nm were used. In a 96-well plate, 180 µL of minimal medium (10 mM Tris, 5 mM glucose) and for *N. gonorrhoeae* Gonococcal liquid medium was made from 5 g/L NaCl, 4 g/L K_2HPO_4, 1 g/L KH_2PO_4, and 15 g/L Proteose Peptone No. 3, supplemented with 1% IsoVitaleX (IVX). IVX was made from 1 g/L d-glucose, 0.1 g/L l-glutamine, 0.289 g/L l-cysteine-HCl·H_2O, 1 mg/L thiamine pyrophosphate, 0.2 mg/L $Fe(NO_3)_3$, 0.03 mg/L thiamine HCl, 0.13 mg/L 4-aminobenzoic acid, 2.5 mg/L β-nicotinamide adenine dinucleotide, and 0.1 mg/L vitamin B12. 10 µL of bacteria suspension (OD_{600}: 0.7) and 10 µL of peptide solution were mixed. All bacterial strains were tested against several concentrations. As the negative control, pure water was added, and ciprofloxacin was used as the positive control. All samples were incubated at 37 °C for 4 h under shaking conditions. Afterward, 10 µL of a 1 mg mL^{-1} solution of INT in pure DMSO was added to each well, and samples were further shaken for 15 min at 37 °C. Finally, the absorption of formazan at 560 nm was measured in each well using a Tecan Infinite M200 plate reader (Tecan Group AG). The EC_{50} value of the used peptides was calculated by a sigmoidal fit of the dose response using the computational program Origin. The fit of the graph is used for the following calculation:

$$EC_{50}=10^{LOG_x0}$$

The x values are supposed to be the logarithm of the dose; thereby, LOGx0 is the middle of the curve, representing the EC_{50} value.

2.9.17 Viable count assay

A viable count assay with methicillin-resistant Staphylococcus aureus (MRSA-43300) was performed at the University Clinic of Cologne with the working group of Prof. Andreas Klatt. Bacteria were cultivated in tryptic soy broth. Cells were diluted to an OD_{600} of 0.6. Bacteria were mixed with PG buffer (18.4 mM K_2HPO_4, 5 mM glucose, pH 7.4). Afterward, they were centrifuged and resuspended after discarding the supernatant again with 1 mL of PG buffer. The bacterial culture was diluted again at 1:10. Then, 500 µL of this dilution was mixed with

4.5 mL of PG buffer. Each well was prefilled with 50 µL of PG buffer. Peptides were mixed directly in each well. Afterward, 50 µL of bacterial solution was added, and the plate was incubated for 2 h at 37 °C. Bacterial cells were then diluted 1:10 and suspended again 1:8 in PG buffer. 50 µL of the desired solution was distributed onto prewarmed TSB agar plates and incubated o/n at 37 °C. On the next day, visible colonies were counted.

2.9.18 Transmission electron microscopy

For transmission electron microscopy (TEM), bacterial cells were cultured until they reached an OD_{600} of 1.0. Preparation was made by combining 100 µL of the bacterial culture, 490 µL of minimal medium (composed of 10 mM Tris and 5 mM glucose), and 10 µL of respective peptide solution to achieve a final peptide concentration of 5 µM. The mixture was incubated at 37 °C for 4 h under shaking conditions. Following incubation, the bacterial cells were centrifuged at 10,000 x g, and the supernatant was discarded. Afterward, the pellet was prepared for TEM analysis by the imaging facility of the CECAD as follows: The bacterial pellet was resuspended in 1 mL of a fixative solution containing 20 mM HEPES, 0.2 M Tris, and 3 % glutaraldehyde. Immersion fixation was performed using a solution of 2% glutaraldehyde, 2.5 % sucrose, and 3 mM $CaCl_2$ in 0.1 M HEPES buffer for 30 min at rt, followed by an additional 30 min at 4 °C. After fixation, the samples were washed with 0.1 M sodium cacodylate buffer and centrifuged at 1,000 g for 10 min. The supernatant was removed, and the pellet was mixed with 3 % low melting point agarose dissolved in 0.2 M sodium cacodylate buffer. The mixture was incubated at 37 °C for 10 min and hardened at 4 °C for 30 min. Small pieces of approximately 1 mm^3 were cut from the pellet and washed four times for 15 min each with 0.1 M sodium cacodylate buffer. Postfixation was done using 1 % osmium tetroxide (OsO_4), 1.25 % sucrose, and 1 % potassium ferricyanide in 0.1 M sodium cacodylate buffer at 4 °C for 2 h. The samples were washed four times with 0.1 M sodium cacodylate buffer and dehydrated using a graded ethanol series (50 %, 70 %, 90 %, and three times 100 %), with each step lasting 15 min. The samples were then treated sequentially with a 50 % ethanol/propylene oxide mixture, followed by two changes of pure propylene oxide, each for 15 min. Infiltration with Epon resin was performed in stages, starting with a mixture of 50 % Epon and 50 % propylene oxide, followed by 75 % Epon and 25 % propylene oxide, with each step lasting 2 h at 4 °C. Pure Epon resin was applied o/n at 4 °C. The next day, the resin was replaced with fresh Epon and incubated at rt for 2 h. Samples were then embedded in Epon blocks and polymerized at 60 °C for 72 h.

Ultrathin sections, approximately 70 nm thick, were prepared using an ultramicrotome with a diamond knife. The sections were stained with 1.5 % uranyl acetate at 37 °C for 15 min, followed by 3 % lead citrate for 4 min. TEM imaging was conducted in the CECAD imaging

facility using a JEM-2100 Plus Transmission Electron Microscope operating at 80 kV, with images captured using a OneView 4K camera (Gatan).

2.9.19 Statistical analysis

A paired Student's t-test was conducted using Microsoft Excel for statistical analysis of experiments comparing two groups. The paired t-test's significance levels were as follows: *p < 0.05, **p < 0.005, ***p < 0.0005, and ****p < 0.00005. When comparing data across more than two groups, the student-t test was performed in Microsoft Excel. The significance thresholds for one-way ANOVA were set as: *p < 0.05, **p < 0.01, ***p < 0.001, and ****p < 0.0001.

2.9.20 AlphaFold3

AlphaFold3 was used for in silico prediction of the interaction of PX1 with Pex7 protein or PX9 with Pex5 protein.[203] The predicted and generated model 0 was processed with Coot to form a cartoon of the peroxin (Pex5, Pex7) and the side chain animation of the PX peptides and their corresponding PTS. Further, Coot was used to generate a PDB file. The model's PDB file was used to generate images of PX peptides and their respective receptors using Pymol.

3. Results

In the following chapters, the results of my doctoral research are presented. The first chapter, “3.1 Comparing sC18 variants and synthesis of peptide-drug conjugates”, has already been published in the journal *Molecules* from MDPI in 2022 (Grabeck J, Lützenburg T, Frommelt P, Neundorf I. Comparing Variants of the Cell-Penetrating Peptide sC18 to Design Peptide-Drug Conjugates. *Molecules*. 2022 Oct 7;27(19):6656. doi: 10.3390/molecules27196656.)[204]

The second chapter, “3.2 Design of peroxisomal targeting sC18 variants”, has not been published yet. A manuscript about the achieved goals of this chapter is in preparation.

The last chapter, “3.3 Novel sC18* variants that display high antimicrobial activity” has already been published in *Infectious Diseases* from ACS in 2024 (Grabeck J, Mayer J, Miltz A, Casoria M, Quagliata M, Meinberger D, Klatt AR, Wielert I, Maier B, Papini AM, Neundorf I. Triazole-Bridged Peptides with Enhanced Antimicrobial Activity and Potency against Pathogenic Bacteria. *ACS Infect Dis*. 2024 Aug 9;10(8):2717-2727. doi: 10.1021/acsinfecdis.4c00078.)[205]. After this work was published, the retro-inverso peptides were synthesized and characterized. Thus, the structural examination of these peptides and preliminary data regarding their antimicrobial activity has not yet been published. A manuscript is submitted to ACS Biochemistry.

3.1 Comparing sC18 variants and synthesis of peptide-drug conjugates

Cancer remains one of the leading causes of mortality worldwide, and despite advances in treatment, many conventional therapies suffer from severe side effects and drug resistance.[148] To address these challenges, research in cancer therapy has increasingly focused on innovative approaches, such as peptide-drug conjugates (PDCs). By enhancing drug specificity and reducing systemic toxicity, PDCs represent a promising strategy in the fight against cancer.[151]

This chapter compares recently described sC18 variants regarding their activity towards artificial membranes, secondary structuring, cytotoxicity in cancerous and non-cancerous cells, and their ability to transport doxorubicin covalently. Dr. Tamara Sasse partly performed the experiments in chapter 3.1 as part of her Dissertation.

3.1.1 Synthesis of sC18 variants

Dr. Tamara Sasse synthesized and purified the sC18 variants.[206] These variants of this study included a truncated version of sC18 lacking the last four amino acids named sC18* and a modified variant thereof, as well as sC18ΔE, in which just the *C*-terminal glutamate residue of sC18 was deleted. The deletion of the glutamate in sC18ΔE at position 15 was done to

increase the peptide's net charge further and optimize the peptide interaction with negatively charged phospholipids at the plasma membrane. The eliminated negatively charged glutamate also led to less possible electrostatic repulsion between basic amino acids, as shown by the alanine scan.[207] The truncated version sC18* was already successfully used for drug delivery purposes.[96,208] To further improve the activity of sC18*, four amino acid substitutions were introduced at the first, fifth, tenth, and eleventh positions leading to peptide sC18*R,L. Indeed, the almost perfectly designed amphipathic character of this peptide might be able to interact even better with the cellular membrane and enable a higher cell entry of peptides. All peptides are listed in Tab. 12 and depicted in helical wheel projections in Fig. S1.

Table 12. Name, sequence, calculated molecular weight, experimental molecular weight, and net charge of synthesized peptides with amidated *C*-terminus.

Name	Sequence	MW_{calc} [g/mol]	MW_{exp} [g/mol]	Net charge
sC18	GLRKRLRKFRNKIKEK	2069.55	2069.87	+9
sC18ΔE	GLRKRLRKFRNKIKK	1940.44	1940.93	+10
sC18*	GLRKRLRKFRNK	1570.94	1571.33	+8
sC18*R,L	RLRKLLRKFLRK	1626.10	1626.46	+8

All peptides were synthesized by SPPS following the Fmoc/*t*-Bu strategy. The identity of synthesized peptides was confirmed by the mass spectra containing m/z signals corresponding to the respective peptide's calculated quasi-molecular ions. The purity of each peptide was determined by integrating the area under the peak in relation to the overall area of all peaks in the UV spectrum. The analytical spectra of the peptides are presented in the appendix, Fig. S1-S4. To enable the analysis of cellular uptake, the peptides were labelled with 5(6)-carboxyfluorescein. After successful synthesis, the peptides were analyzed using circular dichroism (CD) spectroscopy. As expected, all peptides showed an α-helical structure after adding 50 % TFE (see Fig. S6). TFE was characterized to replace the hydration shell via apolar interactions and dehydration entropy, subsequently forming bifurcated hydrogen bonds with peptide carbonyls, stabilizing secondary structures.[209]

3.1.2 Cytotoxicity and cellular uptake of sC18 variants

Then, the peptides were further tested regarding their cytotoxic activity toward cancerous HeLa and non-cancerous HEK-293 cells. Additionally, they were analyzed in terms of uptake efficacy and cellular distribution.

On the one hand, for sC18, sC18*, and sC18ΔE, no toxic effects were observed at concentrations up to 50 µM in HeLa cells, consistent with previously reported

findings.[197,210] However, increasing the concentration up to 100 µM reduced cell viability to 75 %, as depicted in Fig. 10. This observation supported the suggestion that CPPs generally increase their penetration capability with increasing concentrations, which is often accompanied by cytotoxicity caused by membrane destruction. [135]

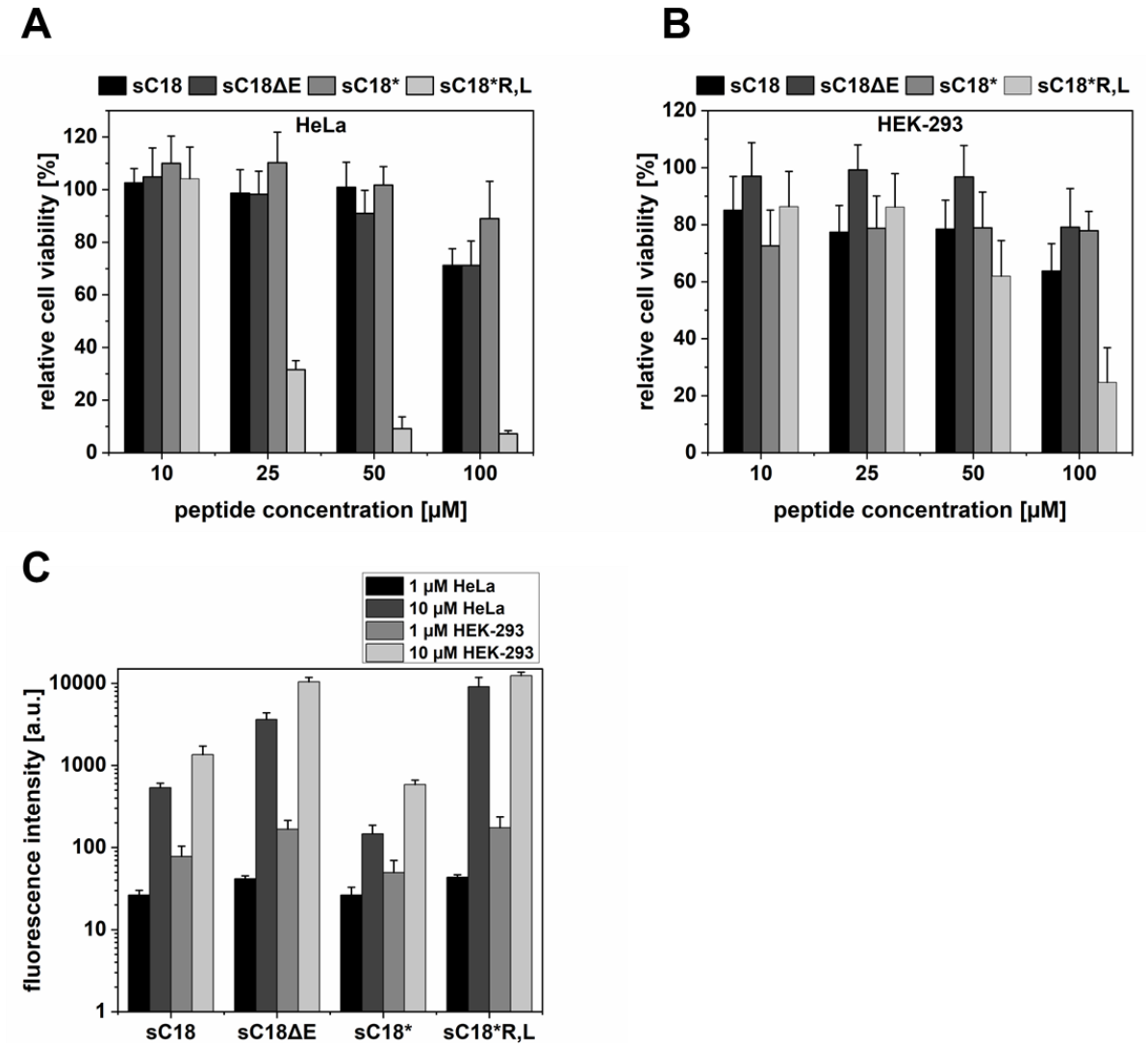

Figure 10. (A, B): Cytotoxicity profiles of peptides in HeLa and HEK-293 cells. Cells were incubated with varying concentrations of peptide solutions for 24 h. Untreated cells served as a negative control, while cells treated with 70% ethanol were used as the positive control. Values from the positive control were subtracted from all data, and the viability of untreated cells was set to 100%. Experiments were performed in triplicate with n=3. Dr. Tamara Sasse conducted these experiments in her dissertation. (C): Flow cytometry analysis of HeLa and HEK-293 cells after incubation with 1 µM and 10 µM peptide solutions for 30 min at 37 °C. Assays were performed in triplicate with n=3. These experiments were conducted as part of my master's thesis.

Interestingly, the newly modified peptide sC18*R,L exhibited markedly higher activity in HeLa cells, reducing cell viability to approximately 35 % at a concentration of 25 µM. In contrast, the cytotoxic effects of sC18*R,L in HEK-293 cells were less pronounced and became evident only at 50 µM or higher concentrations. The other variants, sC18, sC18*, and sC18ΔE, also

showed no toxic effects up to 50 µM. Only the parental peptide sC18 started to have slightly cytotoxic effects at a concentration of 100 µM, decreasing the cellular viability to ~75 %.

The enhanced cytotoxicity of sC18*R,L in HeLa cells may be attributed to its concentrated content of basic amino acids, which likely promoted strong electrostatic interactions with the more negatively charged plasma membrane of HeLa cells compared to HEK293 cells. The enhanced accumulation at the membrane surface may lead to membrane-disrupting effects, which is supported by a stronger interaction between peptide and membrane, which is further supported by a larger hydrophobic side of the peptide (see Fig. S5). The helical wheel projection supports this hypothesis, as the positively charged site is thoroughly separated from the hydrophobic part. To get more insights into the uptake mechanism, the peptides were further investigated regarding their uptake efficiency, measured by flow cytometry.

As mentioned, cellular uptake mechanisms and the ability to translocate the cell membrane often depend on the peptide concentration.[135] Therefore, the cellular uptake was tested at the non-toxic concentrations of 1 µM and 10 µM in both cell lines. As shown in Fig. 10, sC18 and its truncated version sC18* were taken up to a lower extent than their modified versions sC18ΔE and sC18*R,L at a used concentration of 10 µM. Analysis at lower peptide concentrations revealed less pronounced differences between the peptides, supporting the hypothesis of concentration-dependent uptake and efficiency. Notably, the uptake of the sC18ΔE and sC18*R,L was enhanced approximately 10-fold compared to the unmodified counterparts. These results align with the cytotoxicity assay findings, as high cellular uptake is often associated with increasing cytotoxicity, as mentioned, and suggest that the uptake of sC18ΔE lacking the glutamate is enhanced due to the reduced electrostatic countercharge. Therefore, the interaction of the peptide is no longer disturbed and supports the accumulation on cell surfaces. For sC18*R,L, the reordering of amino acids also demonstrated that precisely separating the hydrophilic and hydrophobic regions enhances cell-penetrating capacity. Overall, the results suggested that the internalization mechanism may be influenced by the peptide concentration, as uptake highly increased at higher concentrations.

3.1.3 Analyzing membrane interaction using giant unilamellar vesicles (GUVs)

Within the next chapter, the contact of these peptides with artificial membranes and the cellular uptake were investigated.

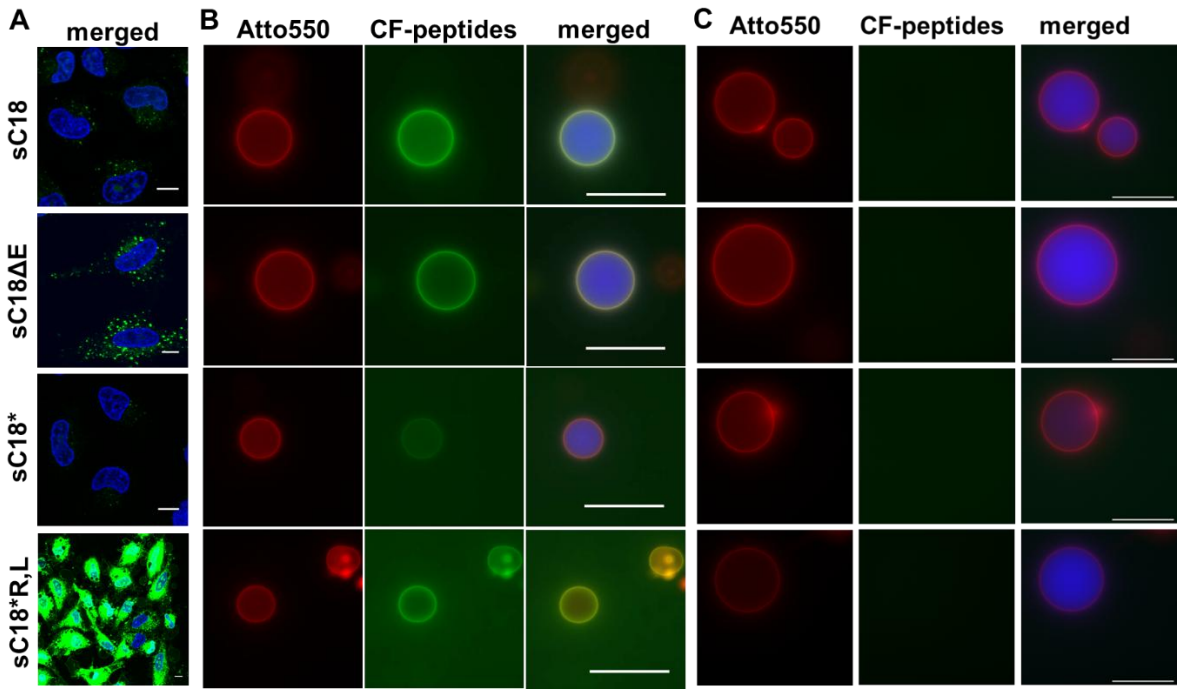

Figure 11. (A): Confocal fluorescence microscopy of HeLa cells after 10 µM CF-labelled peptide treatment for 30 min at 37 °C. Blue: Hoechst 33342 nuclear stain, Green: CF-labelled peptides. Dr. Tamara Sasse performed this experiment. Scale bar: 20 µm (B): Peptide interaction with negative giant lamellar vesicles (GUVs) composed of DOPC/DOPE/DOPG (40:30:30) treated with 1 µM solutions of CF-labelled peptides for 30 min and imaged using a fluorescence microscope (Keyence). Red: Atto550; green: CF-labelled peptides; blue: Oyster 405. Scale bar: 50 µm. (C): Peptide interaction with neutral giant lamellar vesicles (GUVs) composed of DOPC/DOPE (50:50) treated with 1 µM solutions of CF-labelled peptides for 30 min and imaged using a fluorescence microscope (Keyence). Red: Atto550; green: CF-labelled peptides; blue: Oyster 405. Scale bar: 50 µm. These experiments were performed as part of my master's thesis.

First, HeLa cells were treated with 10 µM CF-labelled peptides for 30 min. (Fig. 11A) As expected, the parental peptides sC18 and sC18* showed significantly lower uptake efficiency than the newly designed peptides. The pattern of uptake seemed to be different. The parental peptides were taken up punctually, suggesting they were taken up via endocytosis. This is also observable for the sC18ΔE. The uptake seemed to differ in efficiency. Interestingly, the pattern for sC18*R,L was different. The dot-like pattern was also visible, but the peptide was additionally diffusively distributed within the cell. This observation supports the suggestion that the peptide might be taken up both in an endocytic manner and by direct translocation. This may be attributed to the peptide's ideal amphipathic character, which also contributes to an α-helical structure and subsequent support embedding in the plasma membrane. Notably, sC18*R,L was also taken up into the nucleus, which may result from its highly positive net charge. So-called nuclear localization signals (NLS) are comprised primarily of basic amino acids and, therefore, favored for nuclear import. [169]

Next, the so-called lipid-peptide interaction with giant unilamellar vesicles (GUVs) was investigated. Anionic lipids (Fig. 11B) consisting of synthetic phosphatidylethanolamine,

phosphatidylcholine, and phosphatidylglycerol were used to mimic the plasma membrane composition of cancer cells. Lacking, the anionic phosphatidylglycerol was used to mimic the more balanced plasma membrane of healthy cells. Both vesicle types were treated with 1 µM of CF-labelled peptides for 30 min. In Fig. 11B, all peptides exhibited surface accumulation on vesicles mimicking the plasma membrane of cancer cells. However, sC18* showed the weakest accumulation signal, which was in line with previous studies.[197] Except for sC18*R,L, all peptides demonstrated intact vesicles confirmed by the Oyster405 dye within the vesicles. Interestingly, no interactions at all were observed for all tested peptides with zwitterionic vesicles at this concentration (Fig. 11C). The peptides could not accumulate on the artificial membrane, which may be due to the absence of anionic phospholipids. However, sC18*R,L showed high membrane interaction and penetration towards negatively charged GUVs. Due to its good amphipathic characteristics, it is likely that this peptide becomes embedded in the phospholipid bilayer and further builds temporary pores. This would result in cytosolic outflow, which leads to cell death.

In summary, the optimized peptides sC18ΔE and sC18*RL showed an enhanced internalization, which might correlate with an increased cytotoxicity. These findings suggest that sC18ΔE may be more suitable for future applications in drug delivery. It exhibits significantly improved uptake efficiency while remaining low cytotoxicity. Conversely, due to the high cytotoxicity of sC18R,L, this variant was excluded from further consideration in drug delivery.

3.1.4 Synthesis of peptide drug-conjugates

The peptides sC18, its truncated version sC18*, and the modified sC18ΔE were used for generating PDCs to investigate the capability of transporting Doxorubicin into the cell (Tab. 13).

Table 13. Name, sequence, calculated molecular weight, experimental molecular weight, and net charge of synthesized peptide-drug conjugates with amidated *C*-terminus. Dox: Doxorubicin, SMP: N-succinimidyl-3-maleimidopropionate.

Name	Sequence	MW_{calc} [g/mol]	MW_{exp} [g/mol]	Net charge
PDC-1	*Dox-SMP*-CGLRKRLRKFRNKIKEK	2868.43	2868.03	+8
PDC-2	*Dox-SMP*-CGLRKRLRKFRNKIKK	2738.31	2738.90	+9
PDC-3	*Dox-SMP*-CGLRKRLRKFRNK	2368.81	2368.95	+7

Adding an *N*-terminal cysteine to the peptides enabled PDC synthesis through the Michael addition with maleimide from the linker N-succinimidyl-3-maleimidopropionate (SMP). As

proof-of-principle, Doxorubicin, an anthracycline anti-cancer drug, was used. The effects of Doxorubicin are based on its intercalation into the DNA resulting in inhibition of nucleic acid synthesis. The goal of the PDCs was to investigate the uptake efficiency and capabilities of small-molecule transport of the used CPP. As Doxorubicin is known to be highly cytotoxic to healthy cells, minimizing these would be a goal. The synthesis of the PDCs is schematically shown in Fig. 12. First, Doxorubicin was coupled to SMP through its primary amino group. The success of the coupling reaction and the efficiency were monitored by thin-layer chromatography (TLC). To finalize the PDC, the building block Dox-SMP was covalently coupled to the added *N*-terminal cysteine of the peptides by Thiol-Michael addition.

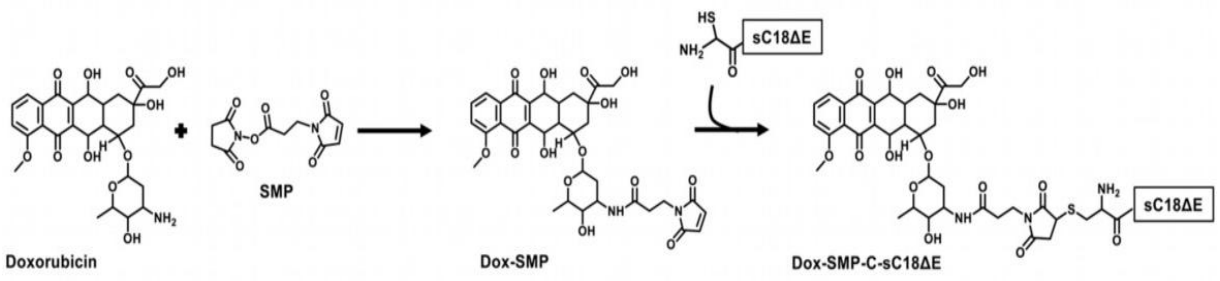

Figure 12. Exemplary synthesis scheme of PDC-2. Synthesis of PDCs is divided into the first building block, Dox-SMP, and finally, the Thiol-Michael addition with the cell-penetrating peptide.

The successful PDC synthesis was purified using RP-HPLC and analyzed analytically by LC-MS, as shown exemplarily for PDC-1 in Fig. 13. The calculated m/z ratios belonged to the detected values except for the peak 491.76. Some side products were visible after the synthesis, such as the hydrophobic side product with the m/z ratio of 397.19, which belonged to the anthracycline rings of Doxorubicin with a cleaved glycoside group.[211] It eluted at about 13-14 min retention time in all synthesized PDCs (Data not shown).

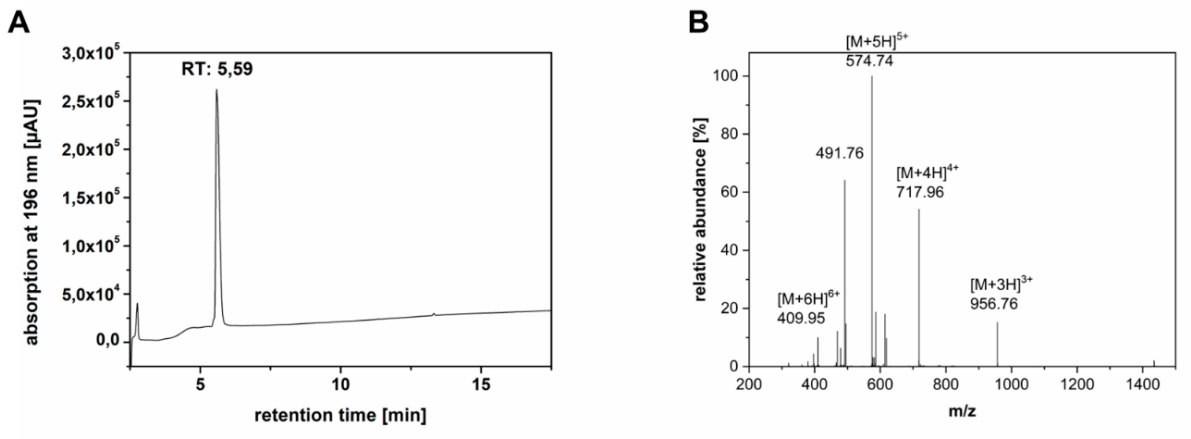

Figure 13. Final HPLC-ESI/MS analysis of purified PDC-1 (Dox-SMP-C-sC18). (A) A gradient of 10-60 % ACN with 0.1 % FA in 15 min was used for the HPLC analysis. UV-chromatogram of Dox-SMP-C-sC18. (B) Full scan of ESI/MS at a retention time of 5.25-5.71 min. In the peak of the UV chromatogram, the charged molecular ions are: $[M+3H]^{3+}$ = 956.76, $[M+4H]^{4+}$ = 717.96, $[M+5H]^{5+}$= 574.74 and $[M+6H]^{6+}$= 409.95.

3.1.5 Secondary structure of PDCs

Previous studies showed that the peptides sC18, sC18*, and sC18ΔE form an α-helical structure after adding 50 % TFE.[210] This structure might be influenced by conjugation with the Dox-SMP intermediate. Therefore, the secondary structure of the new PDCs was again analyzed using CD spectroscopy. The results in aqueous phosphate buffer and supplemented with 50 % TFE are shown in Fig. 14.

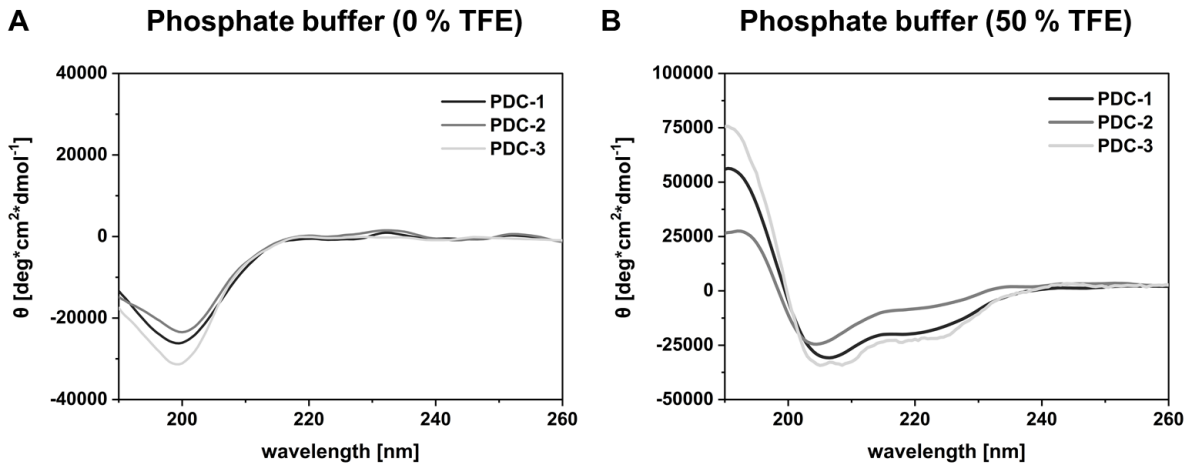

Figure 14. CD spectra of synthesized PDCs in phosphate buffer with and without adding TFE. PDCs were analyzed at a concentration of 20 µM in either (A) 10 mM phosphate buffer, pH 7.0 (A) or (B) 10 mM phosphate buffer, pH 7.0, with the addition of 50 % TFE. TFE: trifluorethanol.

All synthesized PDCs analyzed in phosphate buffer formed random coil structures as expected. Interestingly, the peptides formed an α-helical structure after adding TFE. This experiment supports that the additional building block did not affect the structuring of the

peptide. Since the interaction between simple CPPs and the membrane relies on electrostatic interactions, the PDCs, particularly PDC-2, may exhibit greater selectivity for cancer cells as the net charge of the PDC is +9. Cancer cells have a higher content of acidic phospholipids in their outer leaflet, like phosphatidylserine, which enhances the electrostatic attraction with the positively charged peptides.[22] In contrast, healthy cells maintain a more balanced and zwitterionic membrane composition, which may reduce the uptake of the designed PDCs.

3.1.6 Cytotoxicity and uptake of PDCs

In the next step, the cytotoxic activity and effectiveness of cellular uptake were examined exemplary in HeLa cells (cervical cancer cells) and in HFF-1 (human foreskin fibroblasts 1). A cell viability assay investigated the cytotoxic activity of the synthesized PDCs after 24 h of treatment with different concentrations (2.5 – 70 µM). In HeLa cells, a dose-response curve of the PDCs was measured, allowing the calculation of EC_{50} values. Interestingly, PDC-2 bearing sC18ΔE showed the lowest EC_{50} value with 14.47 µM. In contrast, PDC-3 containing sC18* showed a much higher value with 27.01 µM. Doxorubicin alone showed the highest cytotoxicity with an EC_{50} value of < 6 µM (data not shown).

Following, cytotoxicity assays performed in HFF-1 cells should determine if the PDCs would also be toxic in non-cancerous cells. (Fig. 15B) Remarkedly, no significant cytotoxic effects were detectable for up to 50 µM of the tested PDCs. Interestingly, Doxorubicin alone exhibited substantial toxicity in healthy cells already at a low micromolar range, resulting in decreased cell viability. Notably, the selectivity was markedly increased through the conjugation with the peptides, particularly by conjugation with sC18ΔE.

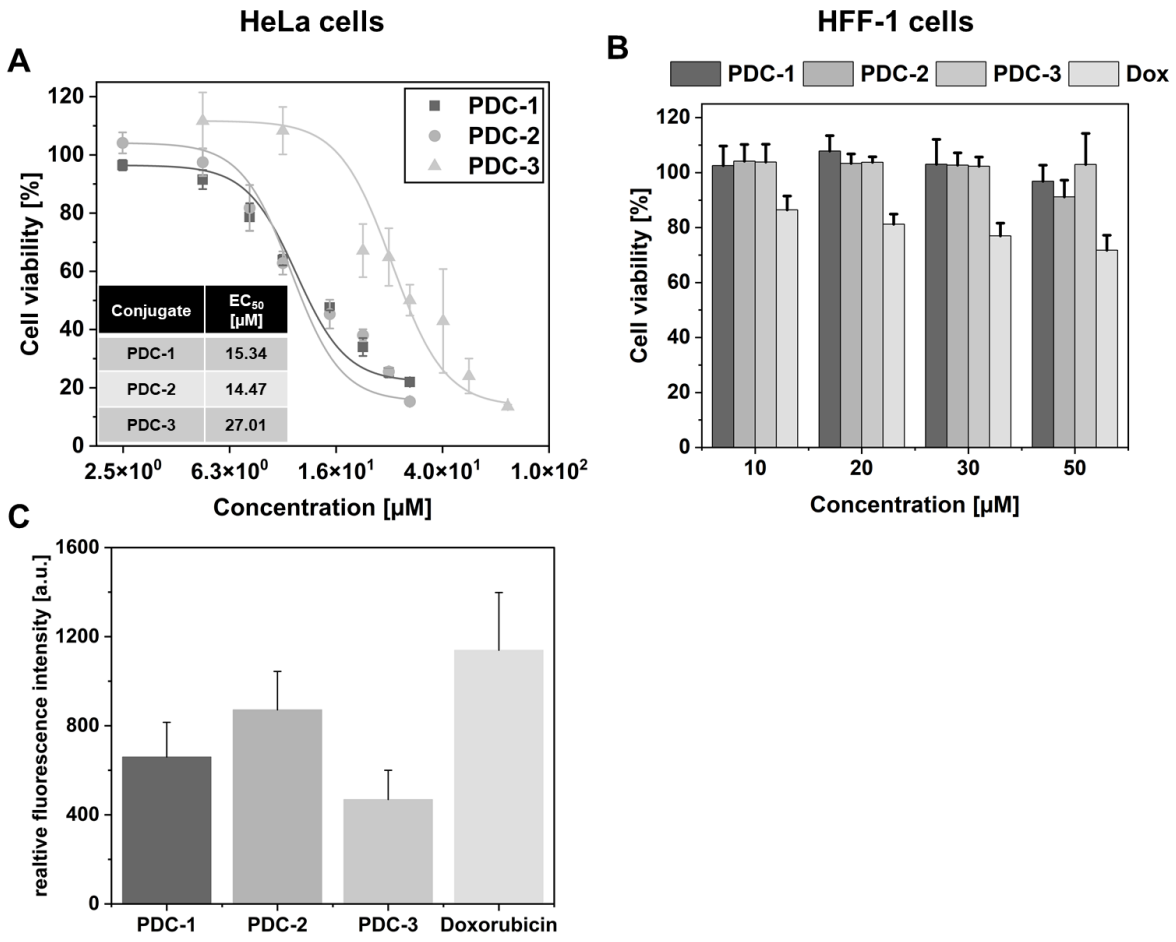

Figure 15. Cytotoxicity profiles and uptake efficiency of PDCs in HeLa and HFF-1 cells. (A) Dose-response curves for PDCs in HeLa cells: Cells were treated with PDC concentrations ranging from 2.5 – 70 µM for 24 h at 37 °C, and viability was measured using the resazurin-based assay. (B) Cytotoxicity assay in HFF-1 cells: Cells were incubated with varying concentrations (10 - 50 µM) of PDCs for 24 h at 37 °C, followed by resazurin-based viability assessment. (C) Quantification of PDC internalization in HeLa cells: Cells were incubated with 10 µM PDC solutions/Doxorubicin for 30 min at 37 °C, and the uptake was analyzed via flow cytometry. All experiments were performed in triplicate (n = 3).

Doxorubicin enables intrinsic absorption and fluorescence within the visible spectrum (excitation and emission wavelengths of 470 and 560 nm). Therefore, no additional fluorophore was necessary to analyze the uptake efficiency of the PDCs. The cytotoxic results align with the cellular uptake efficiencies of these PDCs, depicted in Fig. 15C. PDC-2 demonstrated the highest uptake efficiency, 2-fold higher than PDC-3, followed by PDC-1, with 1.5-fold increased uptake compared to PDC-3. However, the uptake of PDC-3 is 3-fold decreased compared to the drug alone. The difference in cytotoxicity compared to Doxorubicin alone could be explained by the good penetration properties of Doxorubicin instead of possibly endocytosis-mediated uptake mediated by the PDCs. Thus, the observed lower cytotoxicity of the conjugates might be associated with the lower uptake compared to the free drug. However, the uptake and cytotoxic activity data support the hypothesis that sC18ΔE exhibits enhanced

cellular uptake, likely because of reduced electrostatic counter-interactions and a greater net charge than the other PDCs.

The mechanism of action of Doxorubicin primarily involves nuclear DNA intercalation, leading to double-strand breaks. Therefore, the long-term effects of Doxorubicin on healthy cells would be even greater as the uptake of the drug alone was higher. The use of peptides as carrier molecules notably decreased the uptake of Doxorubicin. This reduced uptake paradoxically proved beneficial, enhancing selectivity for unbalanced anionic membranes, such as those found in many cancer membranes. Compared to the cytotoxicity of the unconjugated peptides, the overall cytotoxic effect of the PDCs was significantly enhanced, highlighting the potential of PDC in targeted cancer therapy.

3.1.7 Localization studies of PDCs

Lastly, the PDCs were analyzed using a fluorescence microscope to get further insights into the cellular distribution of Doxorubicin. The cellular uptake was elucidated after 30 min incubation with 5 µM PDCs or Doxorubicin, respectively, as shown in Fig. 16. These internalization studies also supported the already observed lower uptake of PDC-3, whereas the uptake of PDC-1 and PDC-2 appeared punctate and in aggregates. This might indicate an endocytic uptake mechanism or PDC aggregation. Otherwise, the red fluorescence of Doxorubicin would be more distributed within the cytosol or localized in the nucleus. However, it remained unclear if the endosomal uptake ended in the endosomes or lysosomes. Nevertheless, Doxorubicin is known to be undegradable, but it is sequestered by lysosomal enzymes in the lysosome to reduce the drug efficiency.[212] This might also be an advantage, as the drug was likely cleaved off from the peptide after proteolytic digestion to be effective. PDC-1 exhibited a more cytosolic distribution, suggesting that the peptide was less entrapped in endosomes and began to reach the nucleus, as indicated by colocalization with the nucleus, stained in blue. Interestingly, Doxorubicin alone started co-localizing with the nucleus directly after incubation. The analysis of uptake efficiency and localization of the PDCs and Doxorubicin in HFF-1 cells revealed distinct differences in both quantity and intracellular distribution. The reduced uptake of PDCs in HFF-1 cells may be due to the more zwitterionic nature of the plasma membrane, which lacks an unbalanced membrane composition and might influence peptide accumulation. This observation aligns with previous findings using artificial membrane systems. In contrast, Doxorubicin uptake in healthy cells occurred independently of such interactions and was quite equal with cancerous cells.

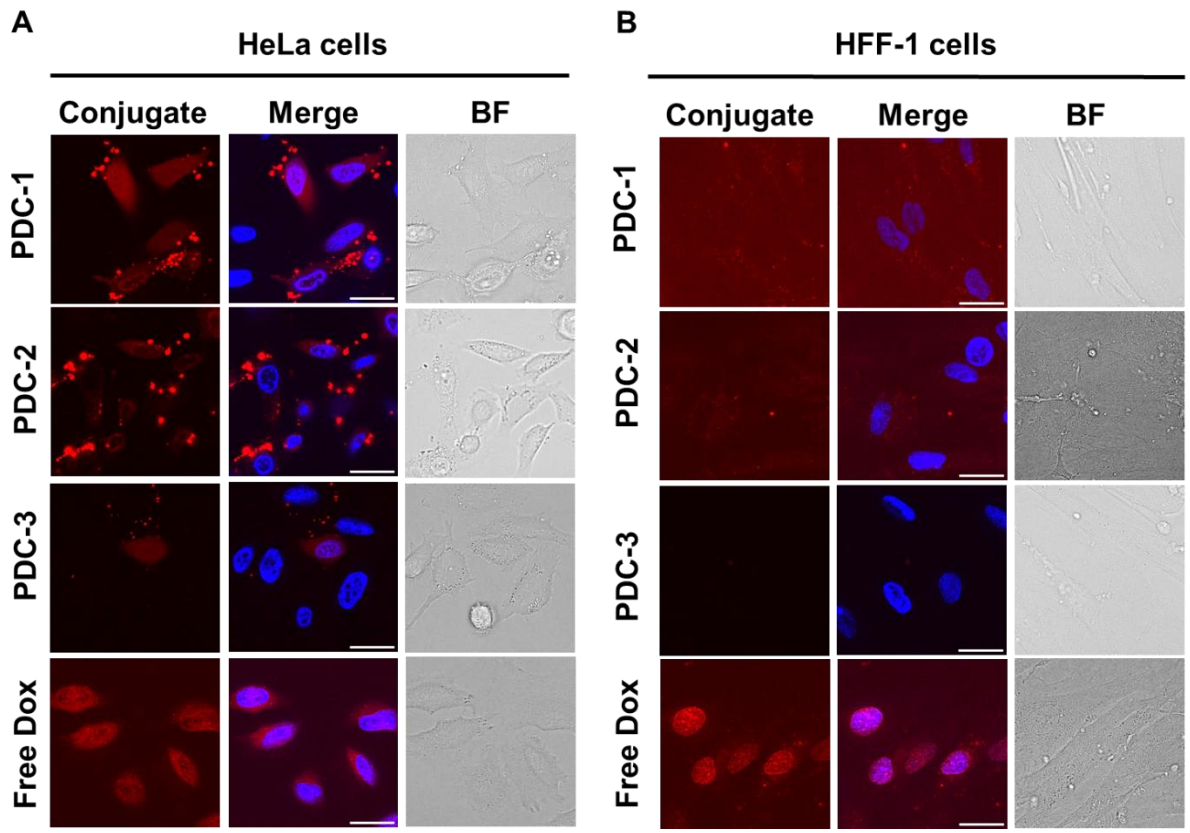

Figure 16. Fluorescence microscopy was performed after treatment of HeLa (A) and HFF-1 (B) cells with 5 µM PDCs and Doxorubicin after 30 min of incubation at 37 °C. Red: peptides coupled to red fluorophore Doxorubicin; blue: Hoechst 33342 nuclear stain; BF: brightfield to identify cell structure; scale bar represents 20 µm.

In summary, these findings support the hypothesis that PDCs are able to transport small molecules into cells such as Doxorubicin. Further, they might reduce cytotoxic effects in healthy cells due to diminished electrostatic interactions. However, further investigation is warranted to optimize the drug release mechanism by exploring alternative linker chemistries for controlled release. The developed PDCs, especially sC18ΔE, showed a potential base for future research in targeted drug delivery to cancer cells.

3.2 Design of peroxisomal targeting sC18 variants

Peroxisomes are key metabolic organelles that are essential in scavenging reactive oxygen species (ROS), controlling cellular lipid metabolism, and β-oxidation fatty acids.[178] For example, the lack of protein import into the peroxisome leads to the well-known Zellweger syndrome, while the upregulation of certain enzymes leads to aggressive types of cancer.[177,213] Only a few drugs have been developed to treat peroxisomal diseases. Therefore, research focuses on developing drugs that reach peroxisomes by using antibodies or peroxisomal targeting sequences (PTS).

A simple and effective approach for cell-specific delivery involves using specific targeting sequences within CPP. Some variants of sC18 were already equipped with organelle-targeting moieties, confirming its ability to target organelles.[197,214] This chapter describes the design and biological evaluation of peroxisomal targeting sC18 peptides. Under my supervision, Philipp Holz partly performed the experiments in chapter 3.2 as part of his bachelor's thesis.

3.2.1 Design and synthesis of sC18* peptides bearing PTS1 and PTS2 sequences

The chimeric peptides consist of a CPP and an intracellular targeting signal. Based on previous studies of uptake efficiency and chimeric properties, the CPPs selected were sC18* and sC18*R,L.[204] sC18*R,L is most likely taken up both via endocytosis and direct translocation, whereas sC18* may be used only via endocytosis.

The added PTS sequence should be recognized in the cytosol and facilitate the transport to the peroxisome. Therefore, either PTS1 or PTS2 signals were used. PTS1 signals are the most common *C*-terminal signal sequence recognized by the Pex5 receptor, whereas the Pex7 receptor recognizes *N*-terminal PTS2 sequences. Different well-known PTS sequences were used, derived from peroxisomal proteins, which are discussed and used in literature to date.[185–187] All peptides were labelled with 5(6)-carboxyfluorescein (CF) to follow the uptake efficiency and investigate cellular distribution. In particular, for peptides containing PTS2 at the *N*-terminus, CF was incorporated into the sequence via a lysine side chain residue. Instead of having an amidated *C*-terminus, peptides with PTS1 signals at the *C*-terminus utilized Wang-resin to create a natural *C*-terminus necessary for recognition by the peroxisomal import protein Pex5. CF was then introduced at the *N*-terminus.

Table 14. Peptide, name, sequence, calculated molecular weight, experimental molecular weight, and the net charge of the synthesized peptides. PX1-PX5 have an amidated *C*-terminus. Different PTS2 are marked in red, different PTS1 are marked in blue, and the 5(6)-carboxyfluorescein is marked in green. Under my supervision, Philipp Holz synthesized the peptides PX1-4 and PX6-7 as part of his bachelor's thesis.

Name	Peptide	Sequence	Mw_{calc} [g/mol]	Mw_{exp} [g/mol]	Net charge
sC18*	sC18*	CF-GLRKRLRKFRNK	1929.3	1930.0	+7
PX1	PTS2_1-sC18*	RLQVVLGHLGLRK(-CF)RLRKFRNK	2945.5	2946.8	+8
PX2	PTS2_2-sC18*	RVQVVLGHAGLRK(-CF)RLRKFRNK	2889.4	2890.6	+8
PX3	PTS2_3-sC18*	KIQVVLGHLGLRK(-CF)RLRKFRNK	2917.5	2918,6	+8
PX4	PTS2_4-sC18*	KLQVVLGHAGLRK(-CF)RLRKFRNK	2875.4	2876.7	+8
PX5	PTS2_1-sC18*R,L	RLQVVLGHLRLRK(-CF)LLRKFLRK	3000.7	3001.6	+8
PX6	sC18*-PTS1	CF-GLRKRLRKFRNKKL	2171.6	2172.2	+7
PX7	sC18*-PTS1	CF-GLRKRLRKFRNKSKL	2258.7	2259.4	+7
PX8	sC18*R,L-PTS1	CF-RLRKLLRKFLRKGGGSKL	2483.9	2485.7	+7
PX9	sC18*R,L-PTS1_1	CF-RLRKLLRKFLRKPGNAKL	2566.1	2566.9	+6
PX10	sC18*-PTS1_1	CF-GLRKRLRKFRNKPGNAKL	2510.9	2511.7	+7
PX11	sC18*R,L-PTS1_2	CF-RLRKLLRKFLRKGGGKSKL	2613.2	2614.0	+7
PX12	sC18*-PTS1_2	CF-GLRKRLRKFRNKGGGKSKL	2558.0	2558.9	+8

Except for the fluorophore labelling, the synthesis was performed using automated SPPS. The final analytical HPLC-UV-chromatogram and the respective mass spectrum are exemplarily shown for CF-PX9 in Fig. 17. The analytical data for the other successfully synthesized peptides are attached in Fig. S7-S19. All peptides were purified and obtained in a high purity, which was determined by integrating the area under the respective peak concerning the total area of all peaks. The identity was confirmed by mass spectrometry. All synthesized peptides are listed in Tab. 14 with the respective sequence, calculated and experimentally evaluated molecular weight, and the resulting net charge. The synthesized peptides were differentiated into PTS2 (peptides PX1-PX5) and PTS1 (PX6-PX12) bearing peptides. Analysis of the secondary structure confirmed by CD spectroscopy that all tested peptides adopted an α-helical structure after adding 50 % TFE (Fig. S19).

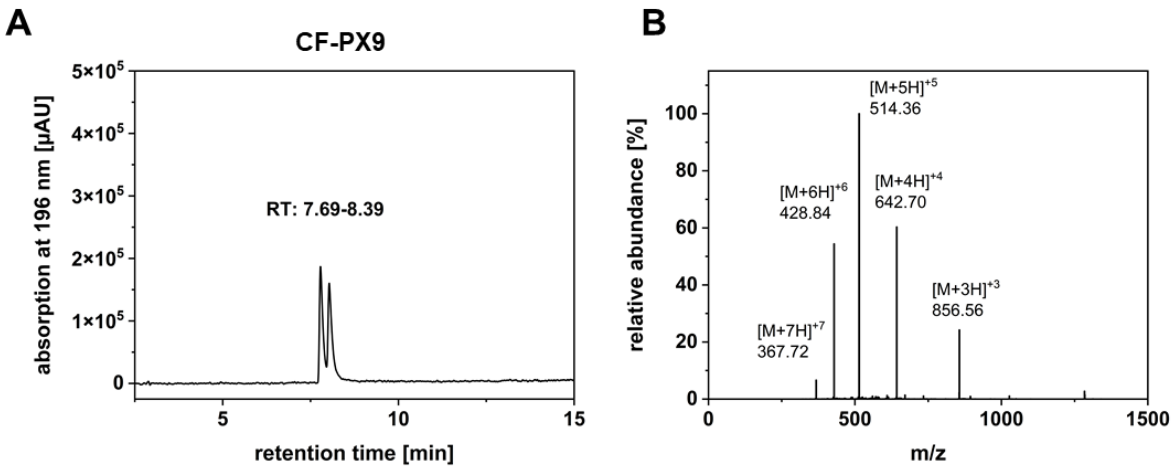

Figure 17. Final HPLC-ESI/MS analysis of CF-PX9 after purification. (A) UV-chromatogram of CF-labelled PX9 with a double peak at a retention time from 7.69-8.39 min. (B) Mass spectrum of the peak at the retention time of 7.69-8.39 min showing m/z ratios that correspond to the quasi-molecular ions of CF-PX9: $[M+7H]^{7+}$ 376.72, $[M+6H]^{6+}$ 428.84, $[M+5H]^{5+}$ 514.36, $[M+4H]^{4+}$ 642.70, $[M+3H]^{3+}$ 856.56.

3.2.2 Cytotoxicity and uptake efficacy of PX-peptides

First, the cytotoxicity of peptides was analyzed using MCF-7 cells (Michigan Cancer Foundation-7). Since the cytotoxicity of sC18*R,L in different cell lines was studied in previous work, it was not used as a control here.[206,215] Thus, only sC18* was a peptide control for cytotoxicity and uptake assays. (Fig. 18, Fig. 19)

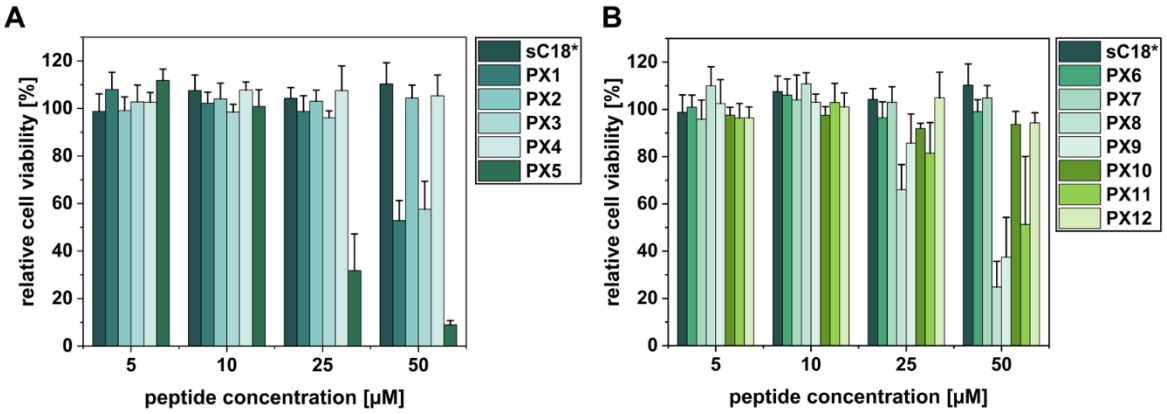

Figure 18. Cytotoxicity assay of CF-labelled PX peptides., (A) PTS2 bearing peptides and PTS1 (B) PTS1 bearing peptides. MCF-7 cells were treated for 24 h, and peptide concentrations varied between 5 to 50 µM. The assay was conducted in triplicates (n=3). Error bars represent standard deviations. Under my supervision, Philipp Holz performed the cytotoxic profile of sC18*, PX1-4, and PX6-7 as part of his bachelor's thesis.

MCF-7 cells were treated with various concentrations of the PX-peptides. After 24 h, the cell viability was determined using a resazurin-based cytotoxicity assay (Fig. 18). The investigation of cytotoxicity is necessary, as the chimeric peptides should be able to translocate across the membrane and pass through the peroxisome without causing any damage to the cells. Interestingly, peptides bearing PTS2 showed no cytotoxicity at a

concentration of up to 25 µM, except for PX5. The peptides PX1 and PX3 reduced cell viability at 50 µM to about 50 %, while PX2, PX4, and the control peptide sC18* showed no cytotoxicity at the highest concentration. Here, it was unexpected that similar signal sequences led to different cytotoxicity at higher concentrations. The leucine at the *C*-terminal end of PTS2_1 and PTS2_3 of PX1 and PX3 is probably responsible for a larger hydrophobic side. The increased hydrophobic side favors the insertion of the peptide into the plasma membrane and possible pore formation, which results in increased cytotoxicity. However, using the PTS2 and the highly membrane-active peptide sC18*R,L, as seen in PX5, markedly increased cytotoxic behavior and reduced cell viability to below 40 % at a peptide concentration of just 25 µM. The peptides sC18* with the shorter PTS1 at the *C*-terminus (PX6-7, PX10, and PX12) showed no cytotoxicity. As expected, exchanging the CPP to sC18*R,L led to a further increase in cytotoxicity, highlighting that the toxicity of these chimera likely results from this particular CPP. However, PX8, PX9, and PX11 exhibited cytotoxic effects in MCF-7 cells at a concentration of 25 µM, while the cell viability of PX9 and PX11 was still above 80 %.

In summary, the PX-peptides compromise the CPP sC18*R,L generally exhibited higher toxicity, with the smaller PTS1 sequence contributing less to this effect. Basic and hydrophobic amino acids increased the peptides' cytotoxicity compared to the other signal sequences, which contained fewer amino acids overall. All peptides have a high net charge above +7, supporting the interaction with negatively charged plasma membranes of many cancerous cells. The increased toxicity of the peptides could be further explained by higher internalization efficiency, which might lead to direct translocation of the plasma membrane and, thus, to an increased lytic effect. Therefore, the peptides were investigated concerning their cellular uptake using a lower and probably harmless concentration. For the uptake analysis, cells were incubated for 30 min with a peptide concentration of 10 µM (Fig. 19). PX1-4 peptides showed highly increased uptake. Especially the peptides PX1 (33-fold higher) and PX3 (22-fold higher) showed excellent cellular uptake compared to sC18*. These findings are consistent with the increasing cytotoxic behavior at higher concentrations and support the assumption that the high uptake of these peptides is associated with increased cytotoxicity. Interestingly, the peptide PX5 with the CPP sC18*R,L showed an even higher uptake efficiency (80-fold higher). This supports the hypothesis that the transport vehicle coupled to the hydrophobic signal sequence is highly membrane-active and agrees with former observations. The uptake quantity is more than doubled compared to the peptide PX1. For further investigations, the highly active peptide PX5 was excluded, as the peptide was too membrane-active and toxic. PX1 and PX3 bearing PTS2 showed cytotoxic activity only at the highest concentration but exhibited a high uptake efficiency, so they were investigated further.

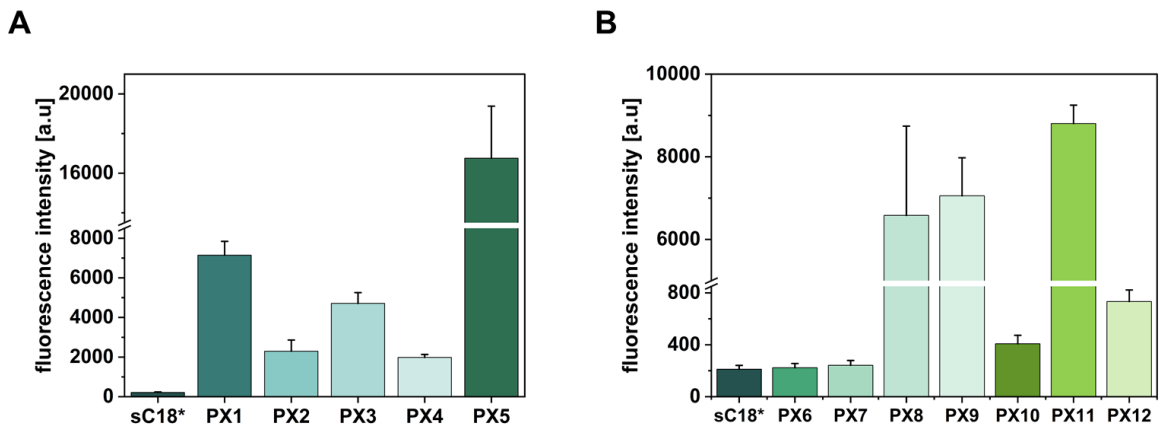

Figure 19. Internalization studies of CF-labelled PX peptides in MCF-7 cells. MCF-7 cells were treated with 10 µM of the respective CF-labelled peptide for 2 h, and the internalization was measured by flow cytometry. (A) PTS2 and (B) PTS1 containing PX peptides. The experiment was conducted in triplicates (n=3). Error bars represent standard deviations.

In contrast, the peptides PX6/7 comprising PTS1 and sC18* showed marginally increased uptake efficiencies than sC18* alone. Interestingly, the other PTS1 in PX10 and PX12 increased the uptake compared to sC18*. These findings for PX6, PX7, PX10, and PX12 also aligned with the cytotoxic behavior tested in MCF-7 cells. However, exchanging the peptide to sC18*R,L highly increased the uptake efficiency into MCF-7 cells again. The efficacy of PX8 (31-fold higher), PX9 (33-fold higher), and PX11 (41-fold higher) was significantly increased compared to sC18* while remaining non-toxic at low concentrations. The increased net charge for PX11 could explain the differences between these peptides. However, these peptides showed minor cytotoxicity starting at higher concentrations around 25 µM. Therefore, further investigations of PX-peptide comprising sC18*R,L were performed at a lower concentration.

3.2.3 Intracellular localization of PX-peptides

The selected peptides PX1, PX3, PX8, PX9, and PX11 were further clarified concerning their intracellular distribution and localization to ascertain whether they were transported into the peroxisome. Therefore, a stable cell line was generated by permanently implementing a gene by the PiggyBac system into MCF-7 cells using transposase. The PiggyBac vector encodes mCherry bearing a *C*-terminal PTS1 for peroxisomal uptake and has a promoter inducible by cumate. Generally, the gene is on standby and can be activated by inducing the expression of this protein by adding a certain amount of cumate. Within the induction time of around 24 h, mCherry_PTS1 is expressed and recognized by Pex5 and gets imported into the peroxisome. After induction, mCherry is mainly located in the peroxisome with low cytosolic levels (Fig. 20). The idea was to co-incubate the stable cell line with the respective CF-labelled peptides to investigate colocalization signals using live cell imaging.

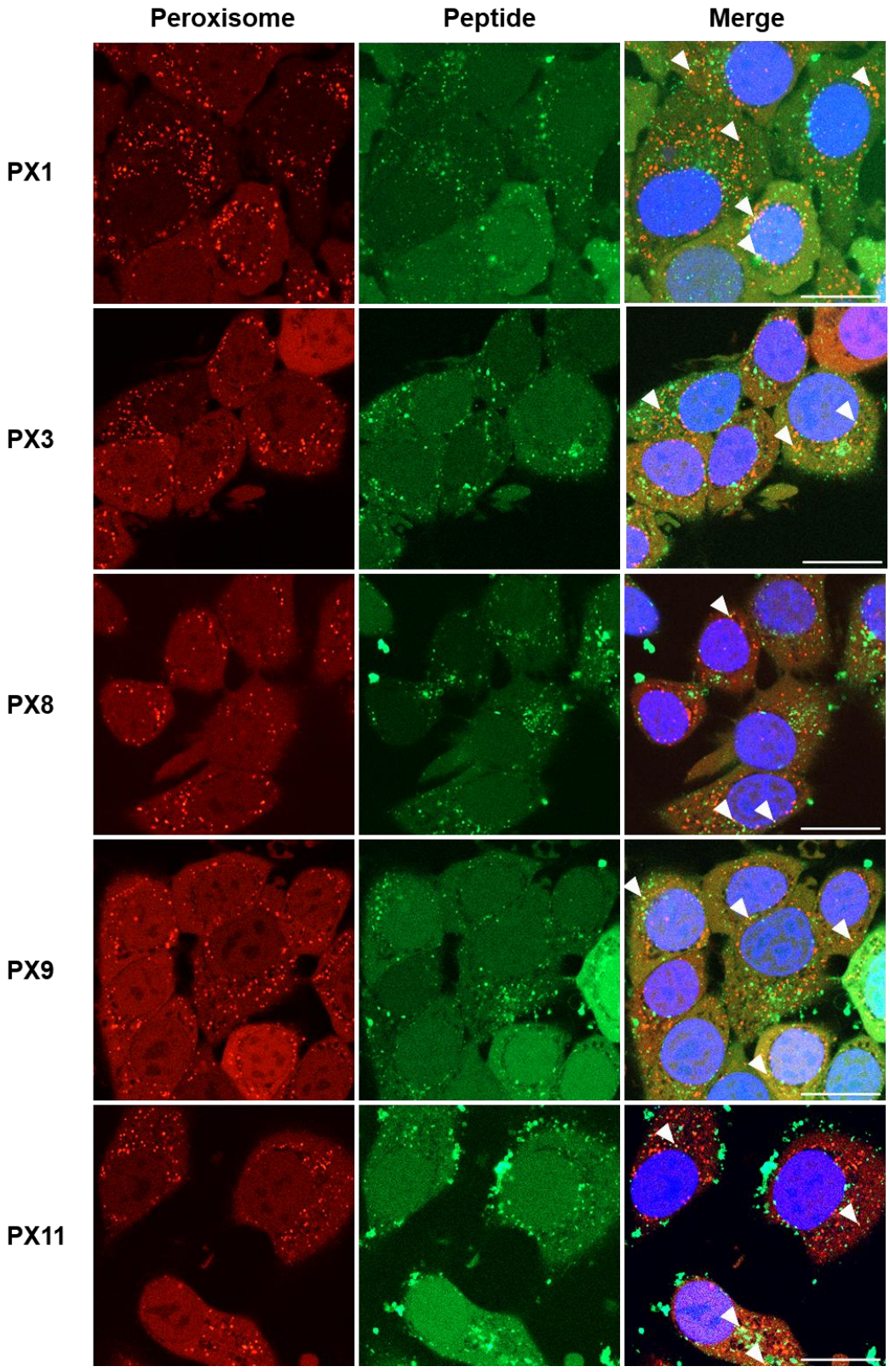

Figure 20. Colocalization studies of PX1, PX3, PX8, and PX9 using a stable transfected MCF-7 cell line. The stable cell line expressing mCherry_PTS1 was induced with cumate for 24 h, followed by peptide incubation with a concentration of 10 µM (PX1, PX3) or 5 µM (PX8, PX9, and PX11) for 2 h. Nuclei were stained with Hoechst 33342. Cells were imaged using the confocal Airy Scan microscope and processed with Fiji. The scale bar represents 20 µm. (n=3)

For colocalization studies, stable MCF-7 cells were treated after appropriate cumate induction with 5 µM (PX8, PX9, PX11) or 10 µM (PX1, PX3) peptide concentration for 2 h and analyzed with a confocal Airy Scan fluorescence microscope. The results are shown in Fig. 20.

The general cellular uptake of the peptides was in a punctuated pattern. Therefore, it was assumed that the peptides were taken up through endocytic processes or were already transported to the peroxisome through the peroxisomal uptake machinery. All tested peptides showed some colocalization signals (indicated by a white arrow). However, the extent of these signals was low, and almost the whole peptide was still in a punctuate pattern but not overlaying with the peroxisomes. Analysis of the colocalization signals using the Fiji tool "JACoP" indicated that the colocalized peptides with the peroxisome were entirely localized within the peroxisome (data not shown). However, the total number of colocalization signals was quite low. Additionally, it was observed that the peptides exhibited significantly higher mobility compared to the peroxisomes, indicating insufficient peroxisomal import. Furthermore, the peroxisomal export mechanism may be particularly rapid for unstructured peptides. Typically, folded proteins are imported into peroxisomes, whereby the cargo bearing the PTS1/PTS2 signal is stripped off.[182,189] Due to the short length of the peptides, the Pex5 receptor might be quickly recycled, preventing the retention of the PX-peptides within the peroxisome. As the colocalization study did not fully confirm the successful uptake of the peptide into the peroxisomes, the incubation time of the peptides was adjusted. PX1 and PX9 were chosen to investigate the time-dependent localization, as they showed the most colocalization signals in the former study. As new time points, the peptides were analyzed after a treatment of 15 min, 30 min, and 60 min, as depicted in Fig. 21.

The overall uptake of the peptides seems to be time-dependent, as after a short incubation time, less peptide was internalized into the cells. Interestingly, after 30 min, both a punctate pattern and a cytosolic distribution were observed for the peptide PX1. No efficient overlap was identified in terms of colocalization, even when considering different points in time. This could be because the peptides are taken up by the peroxisome import machinery but are exported subsequently through the export mechanism. This phenomenon could be explained by the fact that the peptide itself might not have been released appropriately during export. Thus, the idea emerged to investigate whether the peptide alters the recognition of the signal sequence, whether its size is insufficient for effective release in the peroxisomal export process, and whether the transport might occur co-translationally.

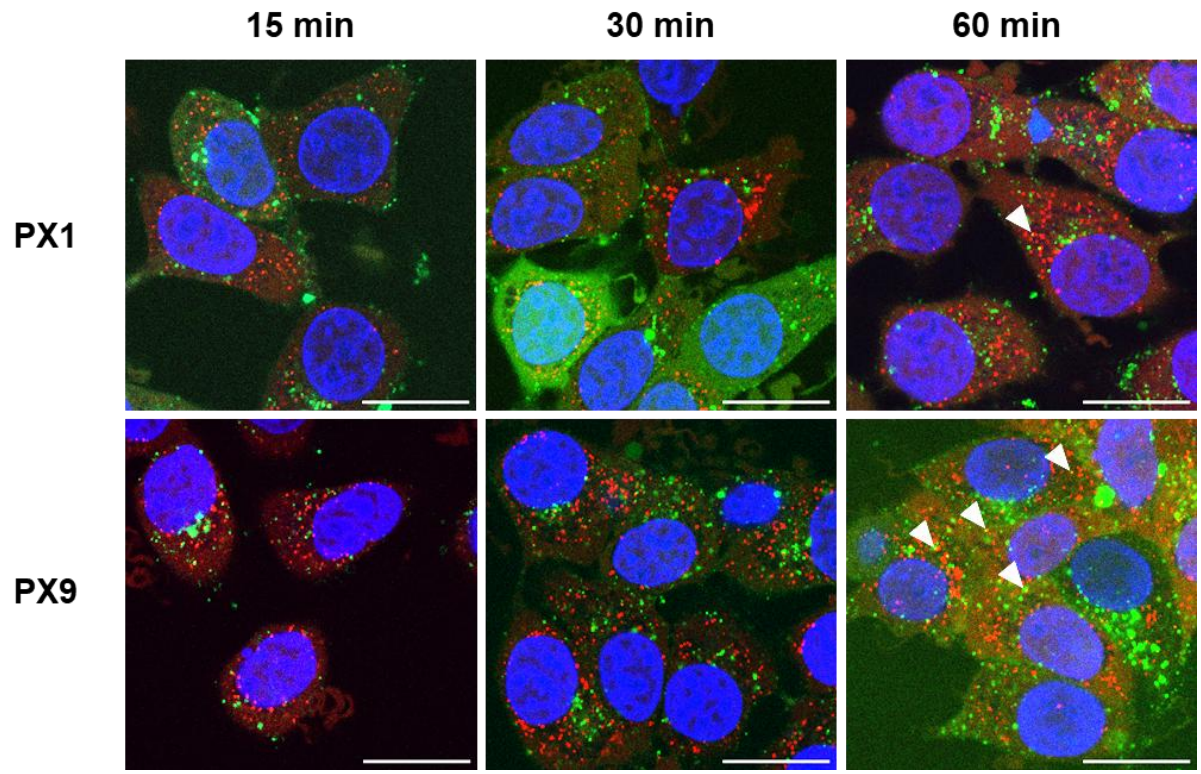

Figure 21. Colocalization studies of PX1 and PX9 within stable MCF-7 cells. Stable cell line MCF-7 expressing mCherry_PTS1 was induced with cumate for 24 h followed by peptide incubation with a concentration of 10 µM (PX1) and 5 µM (PX9) for 15, 30, and 60 min. Nuclei were stained with Hoechst 33342. Cells were imaged using the confocal Airy Scan microscope and processed with Fiji. White arrows indicate colocalization signals. The scale bar represents 20 µm. (n=2)

3.2.4 Generation of recombinant mGold-PX peptide chimeras

To explore if the CPPs might affect the accurate recognition of the PTS, fusion proteins containing the PX-peptides were created. First, plasmids, including the mGold fluorophore and a *C*-terminal multiple cloning site (MCS), were developed to insert DNA encoding the PX-peptides with PTS1 signals. The peptides PX9-12 were each incorporated into the *C*-terminal end by subcloning. The design of the plasmids is shown in Fig. S20. As control plasmids, the mGold protein was combined with PTS1_1 signal from PX9-10, PTS1_2 from PX11-12, or solely the peptide sC18*R,L.

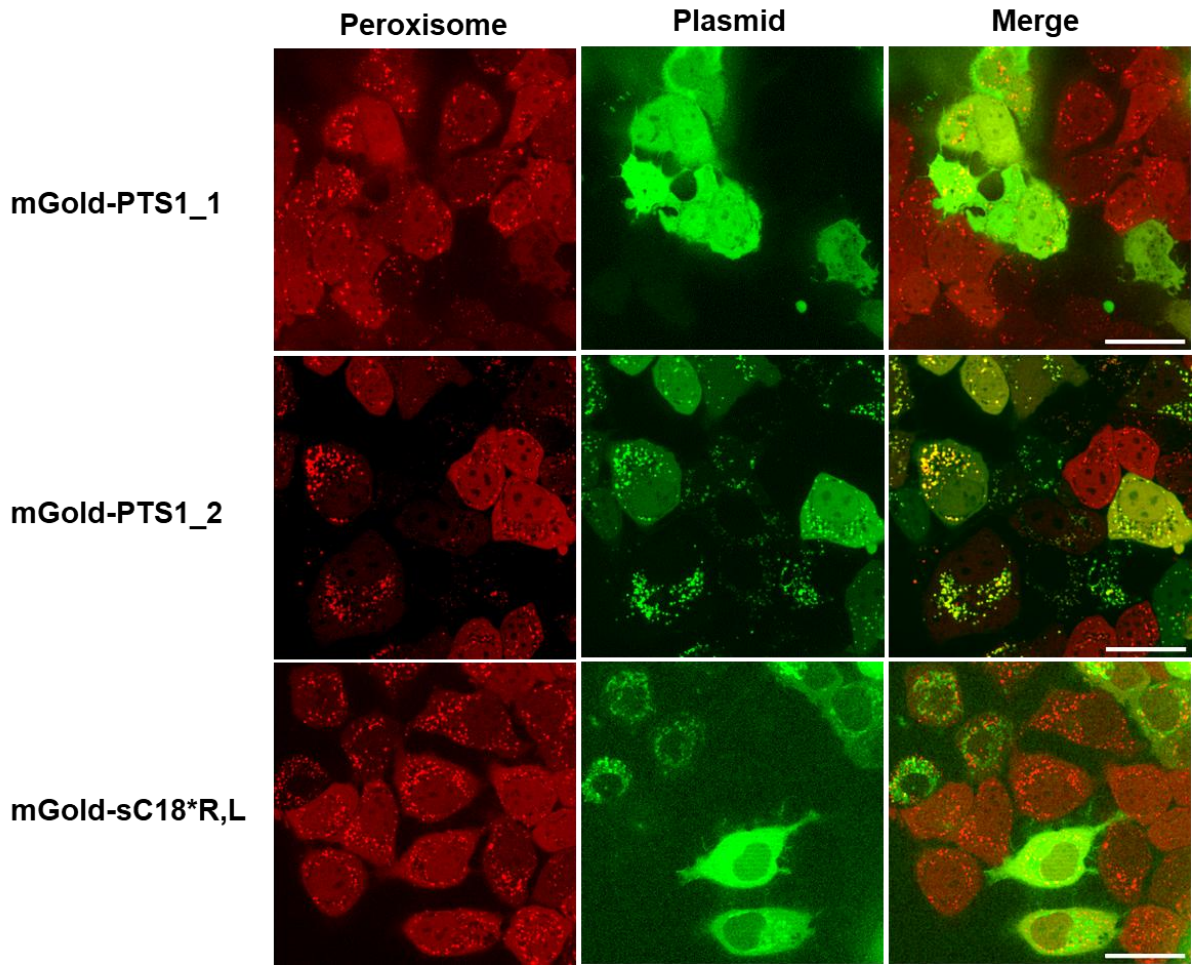

Figure 22. Colocalization studies of control plasmids mGold-PTS1_1, mGold-PTS1_2, and mGold-sC18*R,L transfected into stable MCF-7 cells. MCF-7 cells expressing mCherry-PTS1 were induced with Cumate for 24 h, followed by transfection with 1 µg plasmid for 24 h, respectively. Cells were imaged using a Keyence tabletop fluorescence microscope. Images were processed with Fiji. The scale bar represents 20 µm. (n=2)

After transfecting the mCherry-PTS1-MCF-7 cells with the unmodified mGold, it was distributed all over the cytosol (data not shown). These data confirmed that mGold is not interfering with the fluorescence signal of mCherry-PTS1. However, the protein was still cytosolically distributed using the mGold plasmid with incorporated PTS1_1 sequence (PGNAKL). Potentially, *C*-terminal amino acids or tertiary structure of the mGold protein are hindering the recognition of the signal sequence. However, using mGold fused to PTS1_2 sequence (KSKL), a punctate pattern of the protein was observed, which fully overlapped with the peroxisomes. It could be assumed that the protein was recognized by Pex5 co-translationally or post-translationally and successfully imported into the peroxisome. The negative control, mGold, fused to the peptide sC18*R,L, showed again a cytosolic distribution but somehow also an accumulation pattern. The overlay of the peroxisomes showed no colocalization signals for these accumulations. These controls demonstrated that the signal sequence is necessary for peroxisomal protein import, that recognition of PTS1 depends on

the *C*-terminal end of the protein or peptide, and that the PTS or the peptide sC18*R,L does not substantially alter the distribution of the mGold protein. [184]

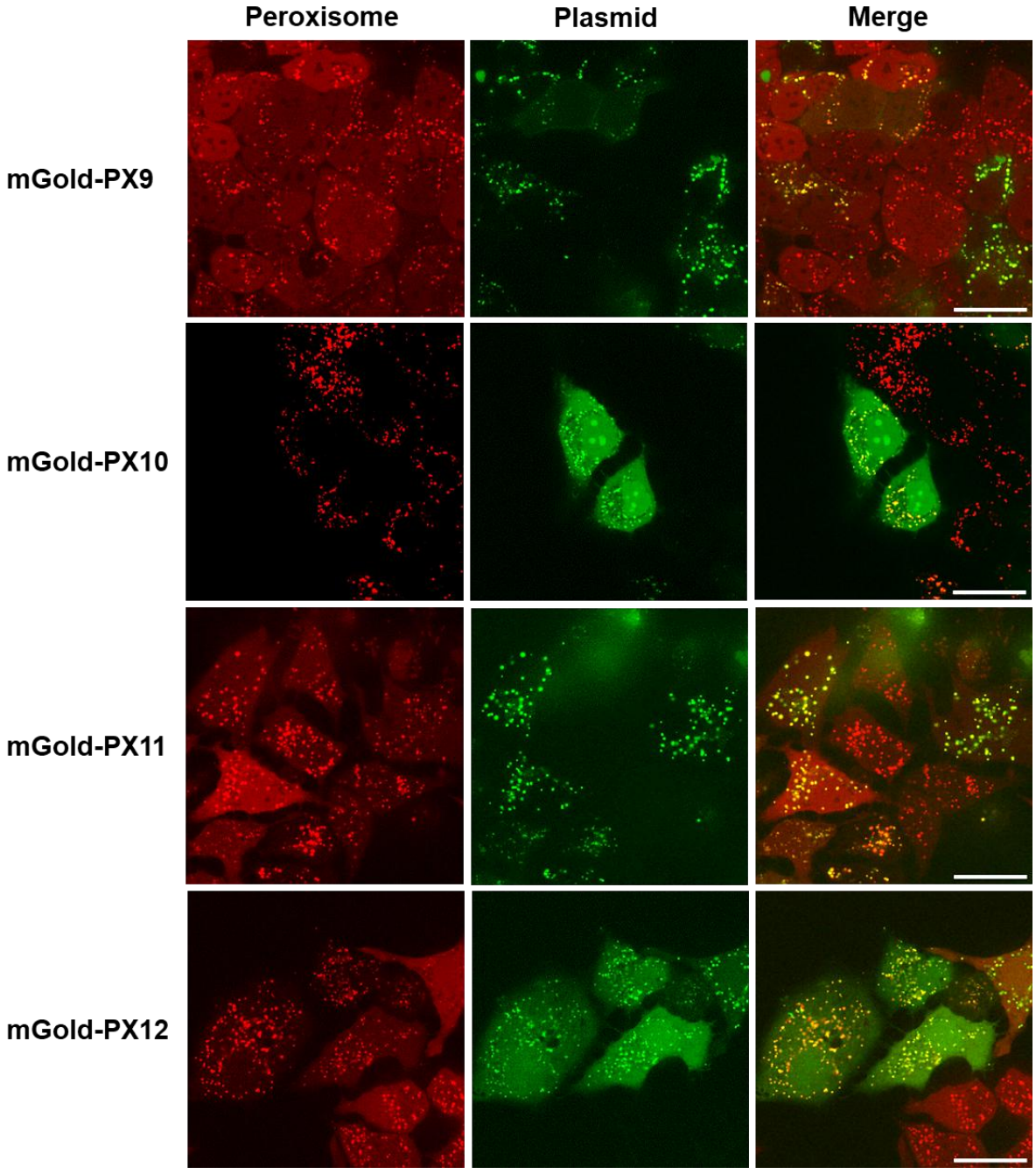

Figure 23. Colocalization studies of the plasmids mGold-PX9, mGold-PX10, mGold-PX11, and mGold-PX12 in stable MCF-7 cells. MCF-7 cells expressing mCherry-PTS1 were induced with cumate for 24 h, followed by transfection with 1 µg plasmid for 24 h. Cells were imaged using a Keyence tabletop fluorescence microscope. Images were processed with Fiji. The scale bar represents 20 µm. (n=2)

Next, new plasmids were designed to investigate whether the peptides would alter the recognition. As the MCS of mGold is located at the *C*-terminus, the peptides PX9-12 were selected. Indeed, mGold fused to respective PX-peptides showed an interesting distribution within the cells (Fig. 23), as almost the whole fluorescence signal was in a punctate pattern

suggesting that the protein got transported into the peroxisomes. The peroxisome staining confirmed this, as it fully overlapped with the mGold-PX variants. Interestingly, the mGold protein bearing PTS1_1 of PX9 or PX10 was colocalized with the peroxisome. Beforehand, mGold with PTS1_1 of PX9 and PX10 was distributed within the cytosol and not localized in the peroxisomes. The signal sequence was somehow recognized for mGold-PX9 and mGold-PX10, and the fusion construct might be correctly imported into the peroxisome. These results showed that the mGold protein altered the recognition efficiency of PTS1_1, but the added peptide sequence again achieved recognition by the receptor Pex5.

In summary, these results indicated that the *C*-terminal amino acids of the peptides enabled the recognition of the signal sequence. However, the recognition efficiency was somehow altered by the CPP. Differences in distribution were detected as the peptides PX9 and PX11, which comprise the CPP sC18*R,L were less present in the cytosol than PX10 and PX12 with sC18* as CPP. This might indicate enhanced recognition efficiency of the proteins with PX9/11 by the receptor Pex5.

With these findings in hand, proteins' peroxisomal import might depend on the translation machinery of peroxisomal proteins on ribosomes. They might be recognized during the translation or post-translationally by receptor proteins Pex5 or Pex7. However, these findings do not support or explain why the peptides were taken up to such a low extent. It may be that the size of the peptides is too small for proper peroxisomal release.

3.2.5 Investigating changes in peroxisomal protein levels

To gain more insights into the efficacy of PX-peptides, the expression level of the peroxisomal protein Pex5 was analyzed using Western blot. To assess changes in protein levels, MCF-7 cells were treated for 2 h with a peptide concentration of 10 µM. Peptides PX1, PX3, PX8, PX9, and PX11 were studied due to their observed colocalization signals. The Western blot results were quantified using the untreated control set to 1.

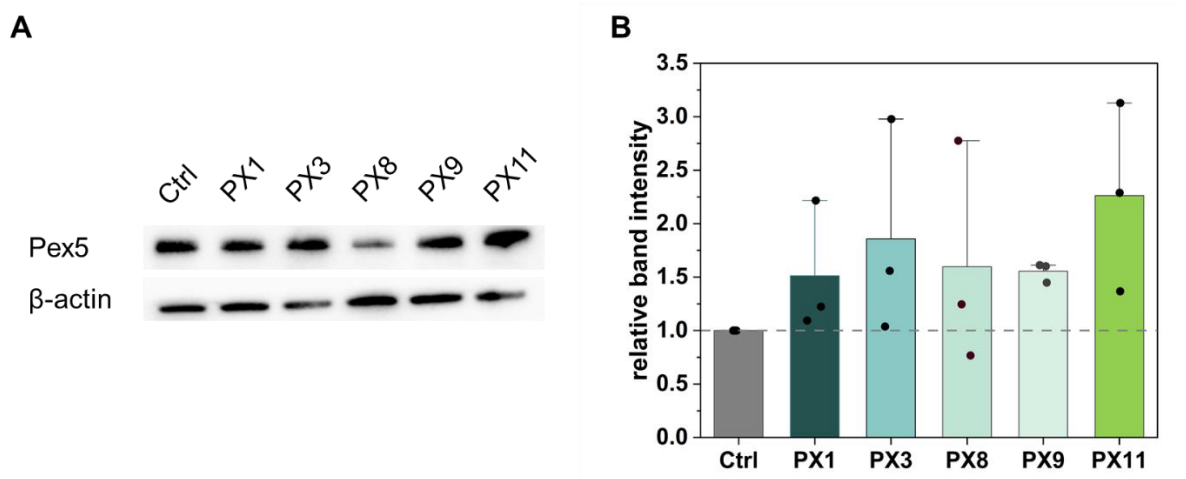

Figure 24. Western blot analysis of Pex5 protein in MCF-7 cells. Cells were analyzed after 2h incubation with 10 µM PX peptide. The band intensities normalized to beta-actin were set in relation to the control. The Western blot was conducted in triplicates (n=3).

Fig. 24 showed that cells treated with peptides had higher levels of the peroxisomal import receptor Pex5 than untreated cells. Cells treated with PX1 and PX3 containing a PTS2 signal also showed increased Pex5 levels. This observation aligns with the import mechanism, as the PTS2 signal is initially recognized by Pex7, followed by recruitment of the Pex5L isoform.[195] Thus, the upregulation of Pex5 levels appears to be directly associated with PTS2 recognition. Furthermore, PX peptides (PX8, PX9, and PX11) containing a PTS1 signal also demonstrated increased Pex5 levels, suggesting that these peptides might be recognized by Pex5, leading to elevated Pex5 levels.

With these results in hand, the question arose whether the altered receptor level depends on the peptide treatment. Therefore, AlphaFold3 was used to predict how the peptides would interact with the respective receptor. The prediction shown in Fig. 25 confirmed that the exemplary peptide PX9 bearing PTS1 may be able to interact with Pex5 with a high interface predicted template modeling (ipTM) score above 0.74. However, exemplary the peptide PX1 bearing PTS2 may also interact with the receptor Pex7 with a high ipTM score above 0.86. Scores above 0.8 represent confident predictions.[203] This prediction further underlines that the peptide can interact with the respective receptor and that the low extent of the colocalization might be due to other reasons.

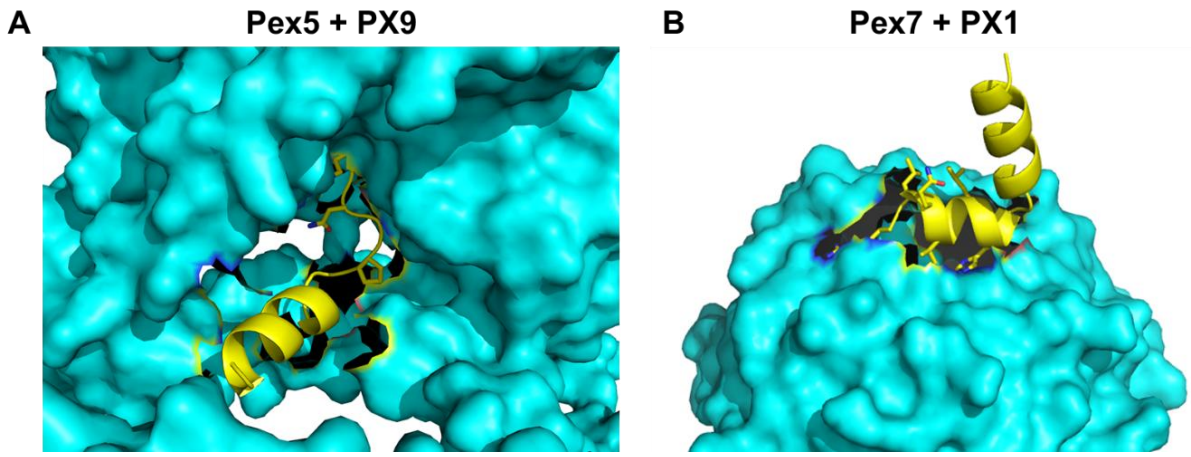

Figure 25. AlphaFold3 prediction of PX peptides with the respective peroxisomal targeting signal receptor. (A) Predicted interaction of Pex5 protein with PX9 peptide. (B) Predicted interaction of Pex7 protein with PX1 peptide. Protein structures were illustrated using PyMol.

In summary, either the PTS2 sequence or the sC18*R,L peptide significantly increased the cytotoxicity of synthesized PX-peptides. PX1, PX3, PX8, PX9, and PX11 were taken up efficiently into MCF-7 cells without harming the cells at lower concentrations, making them potent candidates for further studies on peroxisomal uptake. However, the colocalization study of potent peptides showed that small amounts of the peptides reached the peroxisome. It is hypothesized that the receptors Pex5 or Pex7 may recognize the peptides, which could explain the observed increase in Pex5 levels. Predictions from AlphaFold3 supported that at least PX1 and PX9 are likely recognized by the receptor. The peptides PX1, PX3, PX8, PX9, and PX11 showed a potential base for future research in peroxisomal targeting.

3.3 Novel sC18* variants that display high antimicrobial activity

A growing global issue is the increasing resistance of various bacterial strains to common antibiotics. To date, research in antimicrobial drug development focuses on addressing the antibiotic resistance crisis. However, the creation of new antibiotics is lagging behind the development of resistant bacteria. Innovative antimicrobial peptides that exhibit strong antimicrobial activity may assist in combating this crisis.[123]

Previous studies showed that changing the physicochemical properties of the CPP sC18 leads to antimicrobial activity.[215] Chapters 3.1 and 3.2 already presented the modified peptide sC18*R,L, which displayed significant lytic activity, anti-cancer activity, and overall strong membrane interaction. Therefore, it indicates its effectiveness in disrupting microbial membranes as well.[196,210] Under my supervision, Axel Miltz and Jacob Mayer partly conducted the experiments in chapter 3.3 during their laboratory module and master's thesis. Isabelle Wielert performed the cytotoxicity assay in *N. gonorrhoeae*.

3.3.1 Synthesis of sC18*RL variants

A screen was performed to analyze the effects of up to four amino acid exchanges at specific positions of the peptide sC18* regarding the antimicrobial activity. In Fig. 26, the screen's principle was depicted to increase either the hydrophobic part or the basic part in the α-helix of the peptides. This was achieved by exchanging at a single position or up to four positions at once in the first, fifth, tenth, or eleventh amino acid leading to 15 peptides RL-1 - RL-15, listed in Tab. 15 and additionally depicted in the helical wheel projection in the appendix. (Fig. S21) The synthesis of the 15 RL-peptides was performed using automated SPPS on a Rink amide resin with an overall purity of above 85 %.

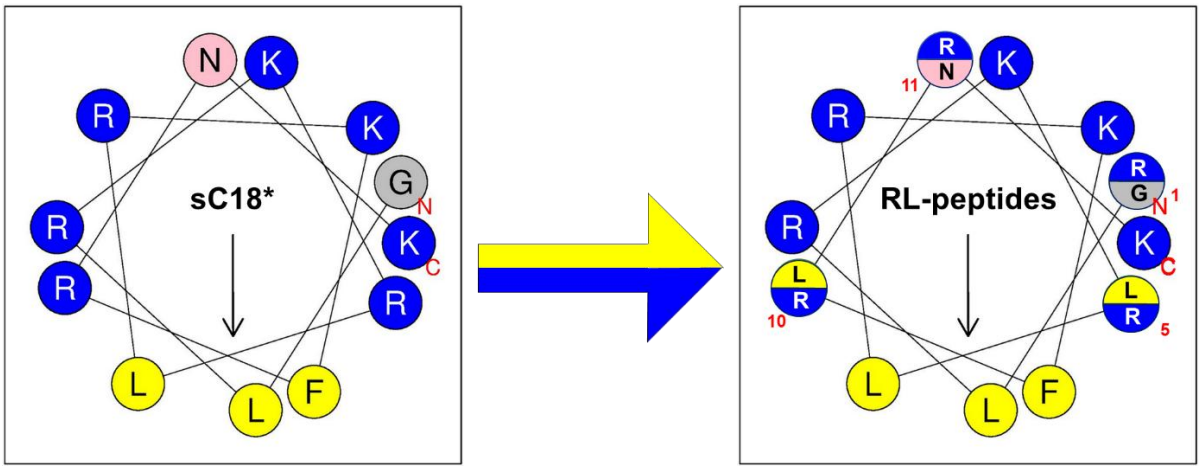

Figure 26. Helical wheel projection of designed RL-peptides originating from sC18* with indicated exchanged amino acids at the first, fifth, tenth, and eleventh position either at a single position or at up to four positions at once.

Table 15. Name, sequence, calculated molecular weight, net charge, and hydrophobicity. The hydrophobicity value was determined using HPLC by measuring the acetonitrile content at the retention time where the synthesized peptides eluted. Peptides marked in blue were tested in detail. All peptides are *C*-terminally amidated.

Name	Sequence	$Mw_{calc.}$ [g/mol]	Net charge	Hydrophobicity
RL-1	**R**LRKRLRKFRNK	1671.08	+9	16.3
RL-2	GLRK**L**LRKFRNK	1528.91	+7	19.5
RL-3	GLRKRLRKF**L**NK	1528.91	+7	19.5
RL-4	GLRKRLRKFR**R**K	1614.03	+9	16.2
RL-5	**R**LRK**L**LRKFRNK	1628.05	+8	17.4
RL-6	**R**LRKRLRKF**L**NK	1628.05	+8	17.6
RL-7	**R**LRKRLRKFR**R**K	1713.16	+10	16.2
RL-8	GLRK**L**LRKF**L**NK	1485.89	+6	31.5
RL-9	GLRK**L**LRKFR**R**K	1571.00	+8	19.5
RL-10	GLRKRLRKF**L**RK	1571.00	+8	26.8
RL-11	**R**LRK**L**LRKF**L**NK	1585.02	+7	26.1
RL-12	**R**LRK**L**LRKFR**R**K	1670.13	+9	17.1
RL-13	**R**LRKRLRKF**LR**K	1670.13	+9	19.4
RL-14	GLRK**L**LRKF**LR**K	1527.97	+7	29.7
RL-15	**R**LRK**L**LRKF**LR**K	1627.11	+8	25.5

3.3.2 Cytotoxic screening of peptides in bacteria

At first, all 15 RL-peptides were screened regarding their antimicrobial activity against the Gram-positive bacterium *Bacillus spizizenii* at five concentrations ranging from 0.5 to 50 µM in LB-medium, as shown in Fig. 27. The bacterial cultures were grown to an OD_{600} of 0.7, followed by a 1:20 dilution. The diluted cultures were then treated with the respective peptide concentrations and incubated for 4 h at 37 °C to assess their efficacy. The screen revealed the four blue-marked peptides RL-1, RL-8, RL-14, and RL-15 as the most potent peptides with enhanced antimicrobial activity. Based on the helical wheel projections shown in Fig. S21, the results demonstrated that the RL-1 peptide differed from the others. Enriching the basic amino acids decreased the hydrophobic part of the peptide. In contrast, the other hit compounds

exhibit an enlarged hydrophobic part consisting of at least five hydrophobic amino acids. In view of the net charge, the antimicrobial activity was not related to the number of cationic amino acids in the sequence. Since RL-7 has the highest net charge of +10, it showed no antimicrobial activity. The balance between hydrophobic and basic amino acids seems to be important. Comparing the peptides RL-13 and RL-14, it was observed that a reduction of the hydrophobicity by one hydrophobic amino acid led to significantly decreased antimicrobial activity.

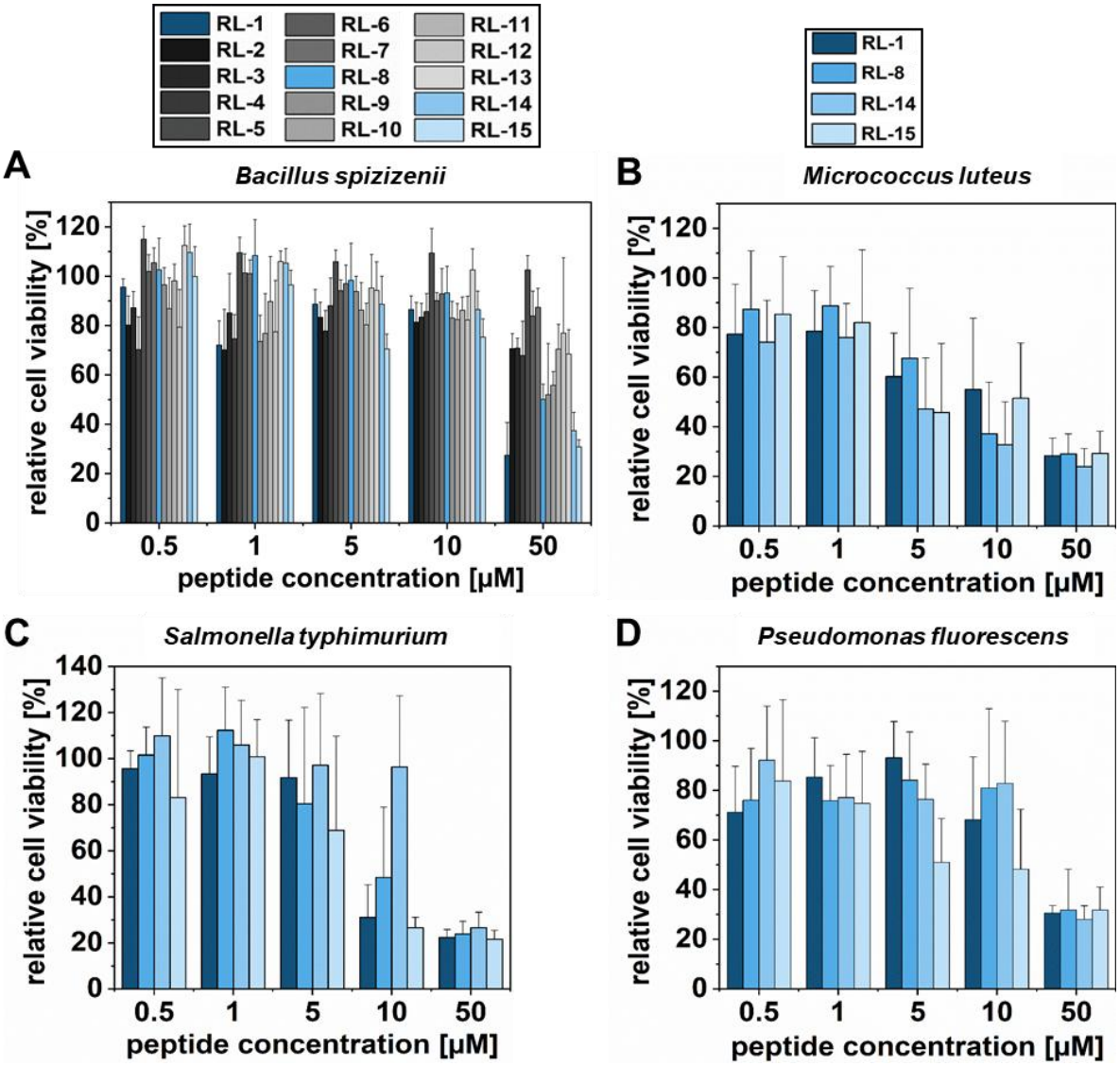

Figure 27. Antimicrobial profile of RL-peptides tested against Gram-positive and Gram-negative bacteria. (A) Screening the antimicrobial activity of the RL-peptides against *B. spizizenii* in complete medium and against *P. fluorescens* (B), *M. luteus* (C), and *S. typhimurium* (D) in minimal medium (H_2O, 5 mM glucose, 10 mM Tris). Untreated bacteria served as negative control and were set to 100 % viability. The assays were performed in triplicates (n=3). Error bars represent standard deviations. Jacob Mayer and Axel Miltz conducted the experiment. Reprinted with permission from Grabeck J,et al. Triazole-Bridged Peptides with Enhanced Antimicrobial Activity and Potency against Pathogenic Bacteria. *ACS Infect Dis*. 2024 Aug 9;10(8):2717-2727. doi: 10.1021/acsinfecdis.4c00078. © 2024 American Chemical Society.

However, the RL-1 peptide does not align with this hypothesis, as it has almost the lowest hydrophobicity. An interesting observation is that it contains the amino acid Asn. This amino acid is present in RL-1 and RL-8, known to play a role in intermolecular helix-helix interactions through the interaction of polar residues of the side chains from Asn.[216,217] This interaction might also influence the antimicrobial activity of the peptides after accumulation on the plasma membrane.

Ongoing assays were performed with the four most potent peptides, RL-1, RL-8, RL-14, and RL-15, in a Gram-positive and two Gram-negative bacterial species. In addition, it was observed that the bacteria in the complete medium somehow recovered too quickly, which led to restored cell viability. Consequently, ongoing assays were performed in a minimal medium composed of 5 mM glucose and 10 mM Tris in H_2O, in which the bacteria were still viable, but the dividing rate was decreased. Through this change, the immediate antimicrobial activity of the peptides could be examined in detail. This experimental procedure was also repeated in *B. spizizenii* (Fig. S22). With the data of the assays, the half maximal concentration EC_{50} was calculated (see Tab. 16).

Table 16. Calculated half maximal effective concentration EC_{50} of RL-1, RL-8, RL-14, and RL-15 in µM against *B. spizizenii*, *M. Luteus*, *S. Typhimurium*, *P. fluorescens*. Adapted with permission from Grabeck J,et al. Triazole-Bridged Peptides with Enhanced Antimicrobial Activity and Potency against Pathogenic Bacteria. *ACS Infect Dis*. 2024 Aug 9;10(8):2717-2727. doi: 10.1021/acsinfecdis.4c00078. © 2024 American Chemical Society.

	B. spizizenii	***M. luteus***	***S. typhimurium***	***P. fluorescens***
Peptide	**EC_{50} [µM]**			
RL-1	20	15	7.5	20
RL-8	30	7.5	10	25
RL-14	25	5	25	25
RL-15	7.5	10	7.5	10

The EC_{50} values showed an antimicrobial effect of RL-peptides in the lower micromolar range of 5-25 µM in all tested bacteria. Interestingly, the values showed the highest activity for RL-15, previously known for its lytic activity (sC18*R,L), followed by RL-1, RL-8, and RL-14. The differences in the cell walls of the tested bacteria did not influence the antimicrobial activity. However, it was observed that the peptides were individually more or less active against certain bacteria. Therefore, developing individual peptides against a selective bacteria strain would be greatly interesting. However, it is well established that most AMPs interact with the membrane to form temporary pores and translocate the membranes directly. This would be

favorable in clinical application because bacteria develop resistance to cell wall disruption more slowly and require several generations. For example, resistance development could emerge by increased efflux pumps within the bacterial envelopes.[128,218] To circumvent rapid resistance development, an additional chemical modification was clarified.

3.3.3 Synthesis of triazolyl-bridged peptides

It was assumed that the distribution of the hydrophobic and hydrophilic parts in the α-helical formation is helpful in embedding the peptides in plasma membranes, leading to increased membrane activity. Therefore, the idea was to force the secondary structuring of the peptides via a triazolyl-bridge between two amino acids within the sequence. The peptide RL-8 was chosen for this modification as it was one of the four most potent peptides regarding antimicrobial activity. This triazolyl-bridge was formed at different positions and directions between introduced L-propargylglycine (Pra) and L-azidolysine (Aza) either in the hydrophobic part or the hydrophilic part, as displayed in Tab. 17 and in the helical wheel projection in Fig. S23. Pra and Aza introduced at positions four and eight, results in peptides 8A and 8B. In contrast, the triazolyl bridge introduced at positions two and six, leads to peptides 8C and 8D. The synthesis was performed by the working group of Prof. Anna-Maria Papini (University of Florence) following the scheme depicted in Fig. 28.

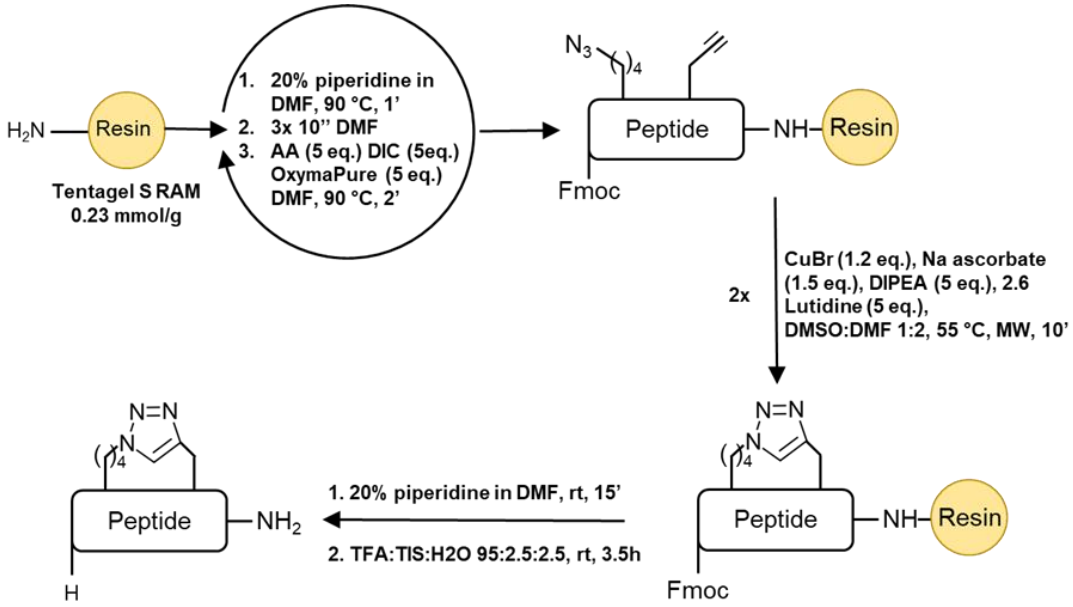

Figure 28. Synthesis scheme of triazolyl-bridged peptides. The synthesis was performed on a Tentagel S RAM resin with a heat-inducted automated synthesis robot. Click reaction of L-propargylglycine (Pra) and L-azidolysine (Aza) to generate triazolyl moiety was catalyzed by Cu(I)-catalyzed azide−alkyne cycloaddition (CuAAC). After the click reaction, the last Fmoc group was removed, followed by full cleavage with scavenger-TFA mix. The peptide was cleaved off with an amidated *C*-terminus. The group of Prof. Papini performed the synthesis, and I performed the re-synthesis in Florence. Adapted with permission from Grabeck J,et al. Triazole-Bridged Peptides with Enhanced Antimicrobial Activity and Potency against Pathogenic Bacteria. *ACS Infect Dis*. 2024 Aug 9;10(8):2717-2727. doi: 10.1021/acsinfecdis.4c00078. © 2024 American Chemical Society.

Previously performed assays by the group of Prof. Anna-Maria Papini elucidated the best length of the methylenes (in total five) to promote the formation of helix-like secondary structure.[219] After SPPS, the last Fmoc-group was retained. Reaction attempts without the Fmoc-protecting group yielded high impurities (data not shown). Following, a Cu(I)-catalyzed azide-alkyne cycloaddition (CuAAC) reaction was performed using microwave irradiation adapted from the Nobel prize winner Morten Meldal.[220] Then, the last Fmoc group was cleaved off, followed by full cleavage of the peptides from the solid support and subsequent purification using RP-HPLC. HPLC measurements showed that hydrophobicity increased for 8A and 8B, and decreased for 8C and 8D.

Table 17. Name, sequence, calculated molecular weight, experimental molecular weight, net charge, and hydrophobicity. The hydrophobicity value was determined using HPLC by measuring the acetonitrile content at the retention time when the synthesized peptides RL-8 8A-8D eluted. Adapted with permission from Grabeck J,et al. Triazole-Bridged Peptides with Enhanced Antimicrobial Activity and Potency against Pathogenic Bacteria. *ACS Infect Dis*. 2024 Aug 9;10(8):2717-2727. doi: 10.1021/acsinfecdis.4c00078. © 2024 American Chemical Society.

Name	Sequence	$MW_{calc.}$ [Da]	$MW_{exp.}$ [Da]	Net charge	Hydro-phobicity
RL-8	GLRKLLRKFLNK	1485.9	1485.3	+6	31.5
8A	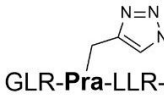 GLR-**Pra**-LLR-**Aza**-FLNK	1478.8	1478.2	+4	42.5
8B	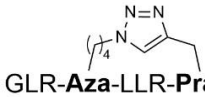 GLR-**Aza**-LLR-**Pra**-FLNK	1478.8	1478.2	+4	41.8
8C	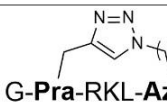 G-**Pra**-RKL-**Aza**-RKFLNK	1508.8	1508.2	+6	21.5
8D	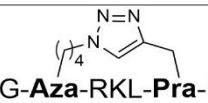 G-**Aza**-RKL-**Pra**-RKLNK	1508.8	1508.2	+6	19.3

3.3.4 Structural analysis

The secondary structure of peptides 8A-8D was analyzed using CD spectroscopy. Previous studies of the group of Prof. Papini revealed the impact of triazolyl-bridge in supporting the secondary structure.[221] CD-spectroscopy demonstrated that the linear peptide RL-8 exhibited a random coil structure in an aqueous solution (Fig. 29), whereas it formed an α-helical structure in a phosphate buffer containing 50 % TFE.[204] Interestingly, the triazolyl-bridged peptides already displayed α-helical structures in aqueous solution.

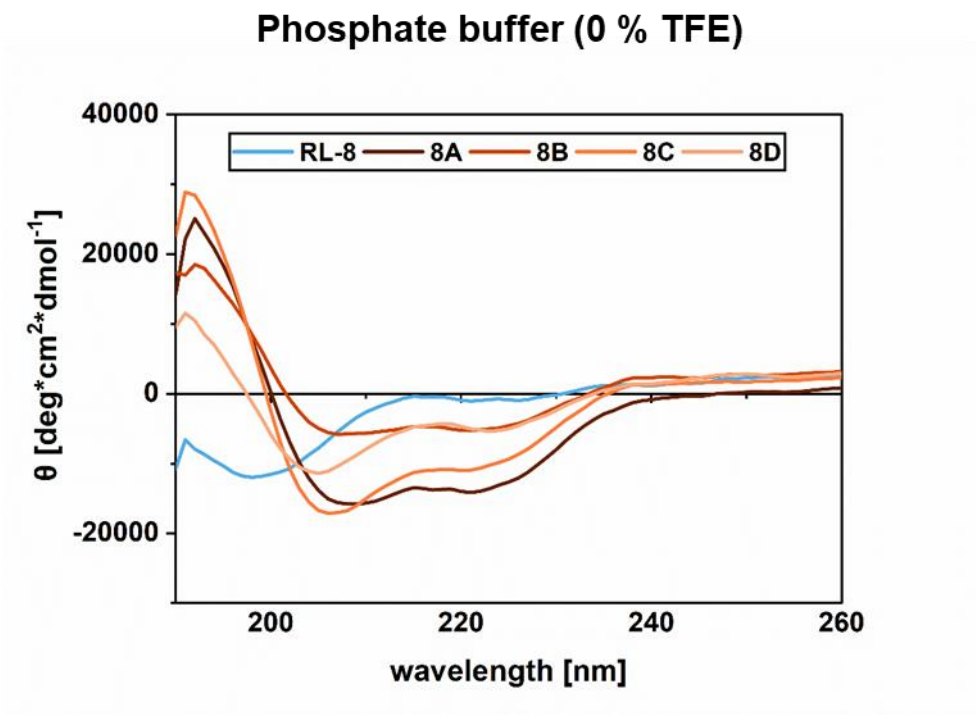

Figure 29. CD spectra of triazolyl-bridged RL-peptides and linear peptide RL-8 in aqueous phosphate-buffered solution. Reprinted with permission from Grabeck J,et al. Triazole-Bridged Peptides with Enhanced Antimicrobial Activity and Potency against Pathogenic Bacteria. *ACS Infect Dis*. 2024 Aug 9;10(8):2717-2727. doi: 10.1021/acsinfecdis.4c00078. © 2024 American Chemical Society.

In summary, introducing the triazolyl-bridge immediately stabilized the peptide's secondary structure in an aqueous solution. Based on these findings, the peptides may exhibit enhanced biological activity, which was elucidated in subsequent studies.

3.3.5 Antimicrobial activity against non-pathogenic and pathogenic bacteria

To prove the above-mentioned hypothesis of increased antimicrobial activity, the peptides were tested in non-pathogenic Gram-positive (*B. spizizenii*) and Gram-negative (*S. typhimurium*) bacteria (Fig. 30A, B). Indeed, significantly enhanced antimicrobial activity was observed for 8A and 8B at 5 µM. Interestingly, the novel peptides 8C and 8D did not show antimicrobial activity at the highest concentration tested (10 µM). Therefore, the position of the triazolyl-bridge within the peptide sequence led to significant differences in antimicrobial activity. While the position of the triazolyl-bridge did not affect the secondary structures, it did influence antimicrobial activity. Introducing the bridge into the hydrophobic region (8C and 8D) decreased the hydrophobicity, resulting in diminished antimicrobial activity. Conversely, enhancing hydrophobicity through the triazolyl-bridge in the area of the basic amino acids significantly increased the antimicrobial activity. For peptides 8A and 8B, a dose-response curve against both bacteria was measured, and the calculated EC_{50} values can be found in Tab. 8.

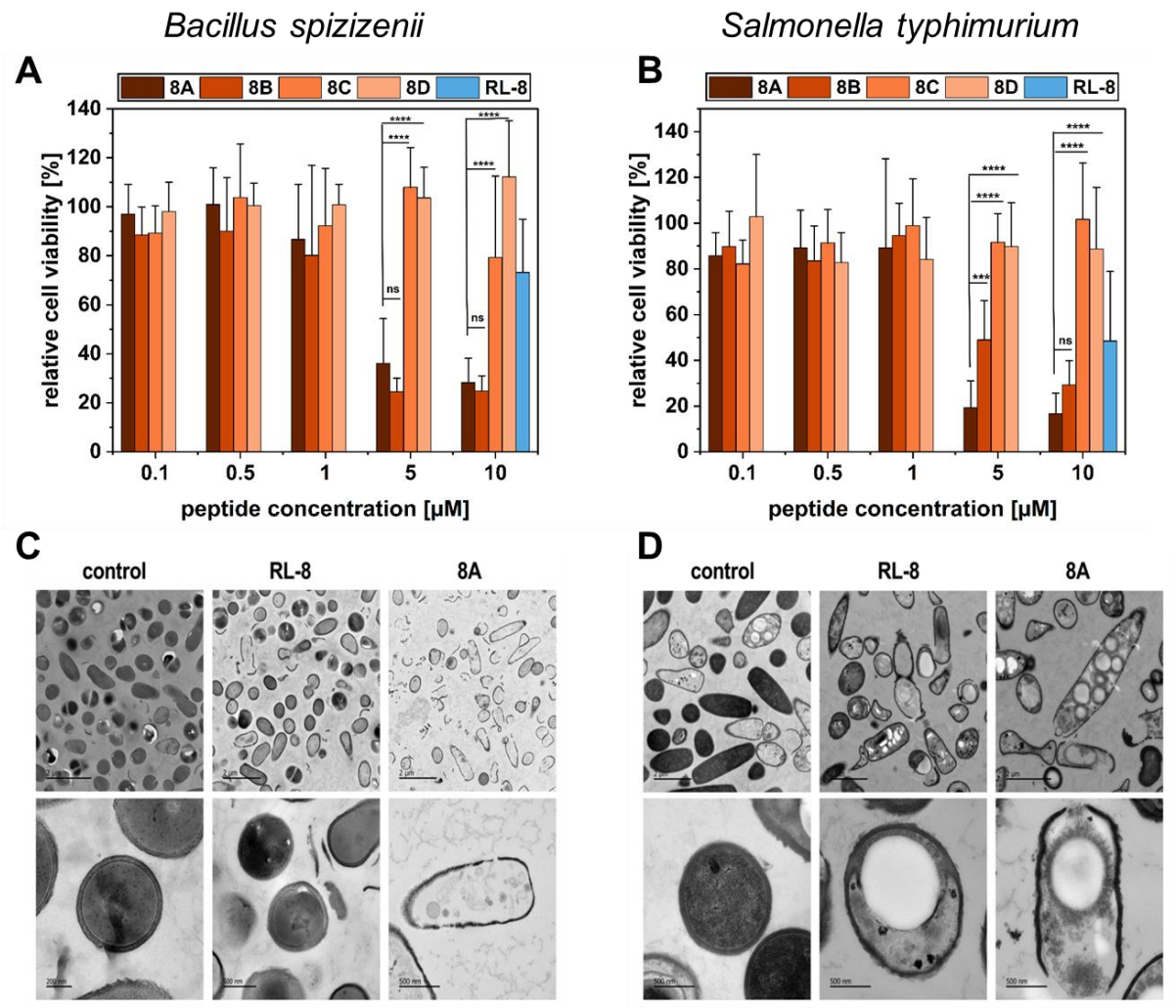

Figure 30. Antimicrobial activity and membrane interaction of novel triazolyl-bridged peptides compared to RL-8. (A) Antimicrobial profile against Bacillus spizizenii and (B) Salmonella typhimurium after 4 h incubation in minimal medium. Experiments were conducted in triplicates (n=3). Statistical analyses were performed using a one-way ANOVA test (****p < 0.00001, ***p < 0.0001, ns p > 0.05). This experiment was performed together with Jacob Mayer during his Master's module. Observation of membrane interaction of new peptides in (C) Bacillus spizizenii and (D) Salmonella spizizenii via Transmission Electron Microscopy (TEM). Bacteria were treated for 4h with 5 µM of the respective peptide. The conditions, control (no treatment), RL-8, and 8A, were captured zoomed out at 5,000X (upper row) and zoomed in at 25,000-40,000X (lower row). This experiment was performed at the imaging facility of the CECAD. The assay was performed once as a preliminary data set (n=1). Reprinted with permission from Grabeck J,et al. Triazole-Bridged Peptides with Enhanced Antimicrobial Activity and Potency against Pathogenic Bacteria. *ACS Infect Dis*. 2024 Aug 9;10(8):2717-2727. doi: 10.1021/acsinfecdis.4c00078. © 2024 American Chemical Society.

The low values for both 8A and 8B (<2.5 µM) confirmed their great potent antimicrobial activity, and it was also observable that the Gram-negative bacteria were more sensitive. The increased antimicrobial activity might probably be explained by a stabilized secondary structure supporting direct membrane interaction and potential transient pore formation.[222] Furthermore, the stabilized secondary structure may allow the peptide to interact more strongly with the bacterial membrane through electrostatic interaction, which is additionally

supported by the hydrophobic part that can be easily inserted into the hydrophobic part of the lipid bilayer, supporting pore formation.

Nevertheless, bacteria are able to build resistance to these lytic functions.[218] Higher peptide stability could also indicate longer efficiencies after treatment. Less proteolytic degradation by prokaryotic proteases may lead to increased efficiencies of the triazolyl-bridged peptides. Another explanation for the increased EC_{50}-values in Gram-negative S. typhimurium could be the distinct structure of the bacterial cell wall, which lacks the thick peptidoglycan layer. It may be favored by amphiphilic peptides to accumulate on negatively charged surfaces, such as LPS. However, the EC_{50} of 8A was slightly more effective against both tested bacterial strains.

Table 18. Half maximal effective concentration, EC_{50} [µM], of the triazolyl-bridged peptides 8A and 8B for *B. spizizenii* and *S. typhimurium.* Reprinted with permission from Grabeck J,et al. Triazole-Bridged Peptides with Enhanced Antimicrobial Activity and Potency against Pathogenic Bacteria. *ACS Infect Dis*. 2024 Aug 9;10(8):2717-2727. doi: 10.1021/acsinfecdis.4c00078. © 2024 American Chemical Society.

	EC_{50} [µM]	
Peptide	***B. Spizizenii***	***S. Typhimurium***
8A	1.35 ± 0.12	0.75 ± 0.09
8B	2.39 ± 0.20	1.28 ± 0.12

8A and RL-8 were exemplarily analyzed with transmission electron microscopy (TEM) to investigate the uptake mechanism and the membrane interaction in more detail. The bacteria *B. spizizenii* and *S. Typhimurium* were treated with 5 µM peptide for 4 h and prepared for TEM analysis, respectively. As shown in Fig. 30C and D, bacteria treated with RL-8 showed a mixed phenotype of mostly intact cell membranes and bacteria with visibly interrupted cell walls, while untreated bacteria were predominantly intact. When the bacteria were treated with the triazolyl-bridged peptide 8A, it was observed that the membrane integrity was heavily influenced, and almost all cells were lysed. A large intracellular efflux was visible, and the light-colored structure suggested that these bacteria were almost or already dead. These findings confirmed that the novel peptides were highly membrane-active and lysed the bacterial cell wall, leading to cell death in both bacteria types, most likely via the formation of permanent or temporary pores. Encouraged by these findings, the newly synthesized peptides were also tested against pathogenic bacteria.

The peptides 8C and 8D were excluded in the following assays because they did not show promising antimicrobial activity. RL-8 and peptides 8A and 8B were tested against both pathogenic Gram-positive (methicillin-resistance *S. Aureus,* MRSA) and Gram-negative

bacteria (*N. gonorrhoeae*) as shown in Fig. 31. Interestingly, in MRSA, the linear peptide RL-8 demonstrated activity comparable to that of 8B. However, 8B showed slightly enhanced potency, as no colonies of MRSA were observed after treatment with 2.5 µM, whereas for RL-8, colony growth was thoroughly inhibited only at 6 µM peptide concentration. Additionally, 8A exhibited a decreased response in reducing colony growth. However, it remained effective at low micromolar concentrations. The working group of Prof. Andreas Klatt used the peptide LL-37 as a positive control because it is already well-described and used in clinical trials, e.g., against venous leg ulcers.[223,224] As expected, the activity of LL-37 was high and efficiently reduced the viable colonies at low micromolar concentrations.

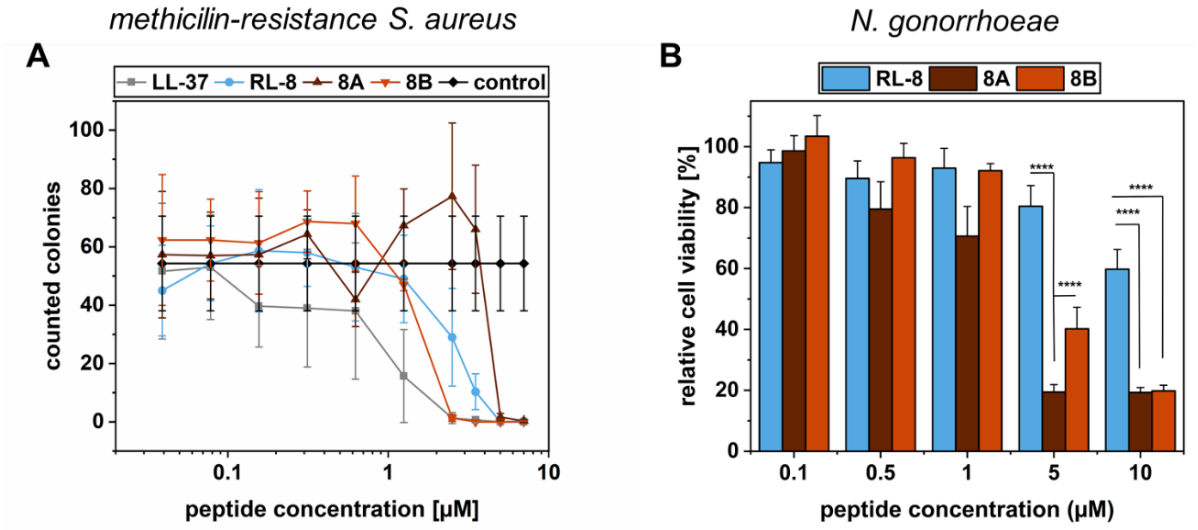

Figure 31. Antimicrobial profile of LL-37, RL-8, 8A, and 8B in pathogenic bacteria. (A) Viable count assay against methicillin-resistant *S. aureus* (B) Antimicrobial assay against *N. gonorrhoeae*. Assays were performed in triplicates (n=3). Values were normalized against the untreated control. Error bars represent standard deviation. Statistical analyses were performed using a one-way ANOVA test (****p < 0.00001, ***p < 0.0001, ns p > 0.05). Peptides tested in *N. gonorrhoeae* were kindly performed by Isabelle Wielert. Reprinted with permission from Grabeck J,et al. Triazole-Bridged Peptides with Enhanced Antimicrobial Activity and Potency against Pathogenic Bacteria. *ACS Infect Dis*. 2024 Aug 9;10(8):2717-2727. doi: 10.1021/acsinfecdis.4c00078. © 2024 American Chemical Society.

The more flexible peptide might better penetrate the thick peptidoglycan layer and favor interaction with the predominant present negatively charged phosphatidylglycerol in the membrane and wall teichoic acid on the peptidoglycan layer.[225] This might be supported by the increased net charge of the linear peptide compared to the triazolyl-bridged peptides. These observations are of great interest for future therapeutic applications of the peptide RL-8 and the novel triazolyl-bridged peptides as they showed antimicrobial activity in pathogenic MRSA in low micromolar concentration. Thus, it would be interesting to test further pathogenic Gram-positive bacteria like Enterococcus faecium, which is known to be responsible for sepsis after infection.[44]

When testing the activity against *N. gonorrhoeae,* the INT assay was used, in which the peptide 8A exhibited the highest activity, consistent with previous studies. At a concentration of 5 µM, 8A significantly reduced bacterial cell viability to approximately 20 %, outperforming RL-8 and 8B. Although 8B also showed great antimicrobial activity, a similar reduction was observed at twice the concentration at 10 µM. In contrast, RL-8 demonstrated lower efficacy, reducing bacterial cell viability to approximately 60 % at the highest tested concentration of 10 µM. The enhanced activity of the triazolyl-bridged peptides might be attributed to the structural characteristics of Gram-negative bacterial cell walls bearing two membranes instead of the thick peptidoglycan layer. The high membrane activity of the triazolyl-bridged peptides might be facilitated by interactions with both the outer and inner membranes. These findings highlight the critical role of secondary structures, particularly α-helices, in their mechanism of action. Basic amino acids might initially interact with negatively charged LPS on the outer membrane, inducing membrane perturbation and transient or permanent pore formation. This is followed by penetration of the inner membrane, leading to bacterial leakage, membrane destruction, and cell death. However, the cell viability of another pathogenic Gram-negative bacterium, *P. aeruginosa,* remained unaffected even at peptide concentrations of up to 10 µM (data not shown). This highlights the importance of developing tailored peptides targeting specific bacterial infections, offering a focused approach to combating resistant pathogens.

3.3.6 Activity of newly designed AMPs in human cells

Antimicrobial peptides often exhibit simultaneous anti-cancer activity.[226] In previous studies, other peptide variants of sC18 also demonstrated anti-cancer effects.[200,204,210] Peptides with anti-cancer properties are proposed to interact with enriched negatively charged phospholipids of the plasma membrane through their basic amino acid residues. Moreover, these peptides frequently adopt secondary structures that enable them to embed themselves within the membrane and to form transient pores. This disruption might ultimately lead to cell death through cell lysis.

To explore their potential anti-cancer properties, the triazolyl-bridged peptides 8A and 8B, as well as the linear RL-8, were tested on HeLa cells at different concentrations (Fig. 32). Furthermore, the peptides were tested on healthy human foreskin fibroblast 1 (HFF-1) cells to assess their potential suitability and safety in clinical application.

After 24 h incubation with HeLa cells, the peptides 8A and 8B revealed significant cytotoxicity compared to RL-8 at a concentration of around 10 µM. After treatment with 25 µM of 8A and 8B, the cancerous HeLa cells were not viable anymore, respectively. In contrast, with the linear peptide RL-8, almost 100 % of the cells were viable at this concentration. Finally, doubling the concentration led to an increase in cytotoxic activity. Interestingly, no cytotoxicity was

observed when testing the peptides in equal concentration against HFF-1 up to 25 µM. Only at the highest concentration (50 µM), 8A showed significantly reduced cell viability to around 30 %.

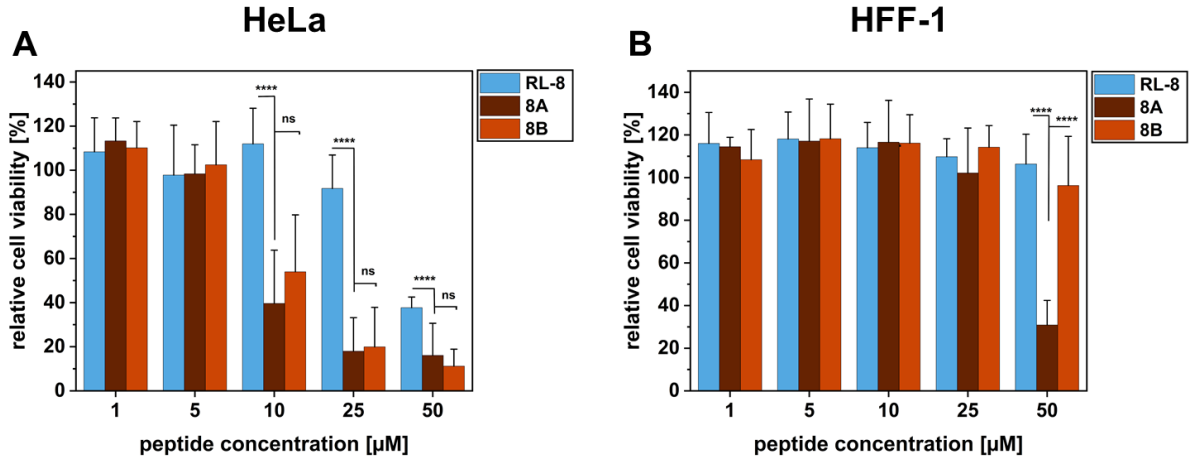

Figure 32. Cell viability assays using HeLa (A) and HFF-1 (B) cells. A cell viability assay was performed, where cells were incubated for 24 h at the indicated concentrations. All assays were conducted in triplicates (n=3). Values were normalized against the untreated control. Error bars represent standard deviation. Statistical analyses were performed using a one-way ANOVA test (****p < 0.00001, ***p < 0.0001, ns p > 0.05). Jacob Mayer conducted the experiments in triplicates (n=3) under my supervision as part of his Master's thesis. Reprinted with permission from Grabeck J,et al. Triazole-Bridged Peptides with Enhanced Antimicrobial Activity and Potency against Pathogenic Bacteria. *ACS Infect Dis*. 2024 Aug 9;10(8):2717-2727. doi: 10.1021/acsinfecdis.4c00078. © 2024 American Chemical Society.

Based on these results, further clinical application of the peptides should be in the lower micromolar range, which should not harm healthy cells. These findings suggest that the developed peptides might predominantly interact with the cell membrane via electrostatic interaction. The more balanced zwitterionic phospholipids and lower levels of acidic phospholipids in healthy cells like HFF-1 might markedly reduce the cytotoxicity. These data were further supported by the LDH-release assay (Fig. S24), in which the direct effect of the peptides on the membrane integrity was tested. The membrane integrity was highly impaired at lower concentrations tested in HeLa cells, whereas in healthy HFF-1 cells, LDH release started after treatment with 8A at a concentration of 25 µM. Interestingly, this effect was already detectable after 30 min. These findings may provide further insights into the cellular uptake mechanism of the peptide RL-8 and especially the triazolyl-bridged peptides 8A and 8B. The forced secondary structure appears to enhance the interaction with the membrane. It potentially allows the peptides to be better embedded into the plasma membrane independently of the organism if the membrane consists of negatively charged parts such as LPS or acidic phospholipids. Losing this electrostatic affinity in balanced zwitterionic phospholipid layers or neutrally charged envelopes might correlate with lower attractive force, as shown in HFF-1 cells.

Next, the synthesized peptides were tested in red blood cells (RBCs) according to the hypothesis that the synthesized peptides act more “selectively” on membranes with negatively charged phospholipids. RBCs must remain thoroughly neutrally charged; otherwise, the electrostatic interaction with the cell walls could have an effect on the bloodstream.[227] , It was expected that the membrane activity of the peptides in RBCs should be correspondingly low. As shown in Fig. S25, it was observed in RBCs that the peptides Rl-8 and 8B, except 8A, exhibited no lytic activity after 30 min and 24 h. The lytic activity of 8A started at 25 µM. However, at the highest concentration (50 µM), 50 % of the cells were still not lysed. Strikingly, peptide 8B demonstrated significantly lower lytic activity in RBCs and reduced cytotoxicity against HFF-1 cells while maintaining high antimicrobial and anti-cancer activity. Therefore, this peptide would still be reasonable for further therapeutic application.

3.3.7 Synthesizing retro-inverso peptides

To further improve the performance of the novel peptides RL-8, 8A, and 8B, their structure was modified using amino acids in the D-configuration and synthesizing the peptides as retro-inverso variant (Tab. 19.) The design of the retro-inverso peptides might increase the proteolytic resistance and, therefore, the antimicrobial activity further.

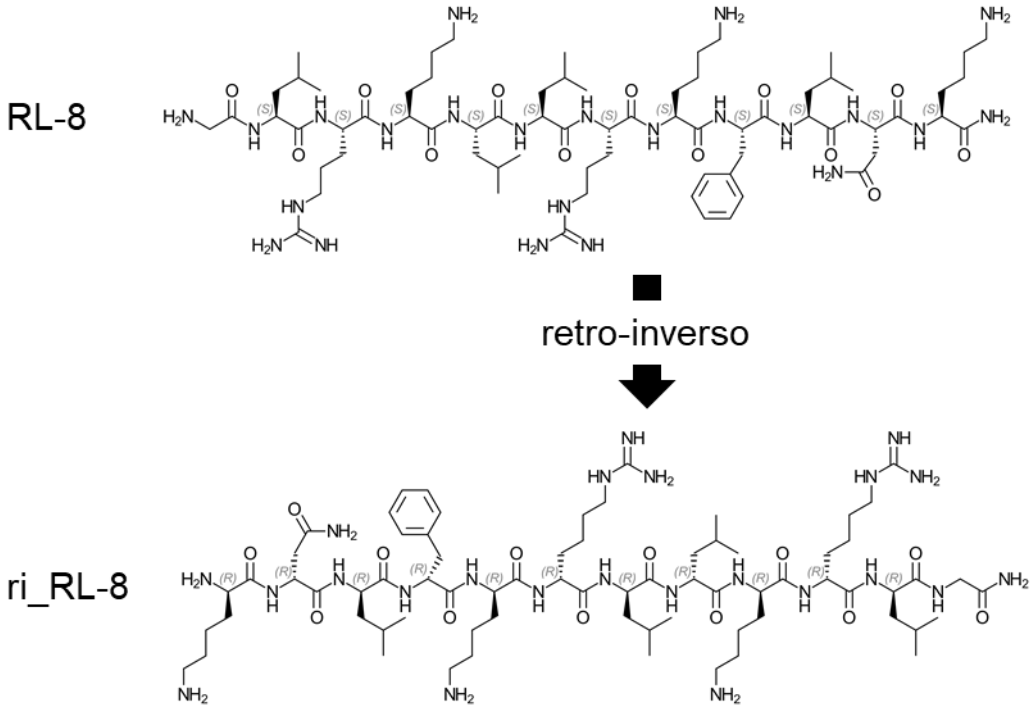

Figure 33. The design of the retro-inverso peptide RL-8 serves as an example. The original peptide sequence is inverted, utilizing only the D-configuration for the amino acid.

Fig. 33 shows the exemplary design of the peptide ri_RL-8 using D-amino acids and an inverted sequence. Thereby, the chirality and, simultaneously, the sequence is inverted. This should not be detectable by proteases or the organism.[228] Nevertheless, the changes in

chirality might also lead to changes in membrane interaction behavior and, therefore, antimicrobial activity. This will be tested in further studies using exemplary one Gram-positive and one Gram-negative bacteria strain.

Table 19. Name, sequence, calculated molecular weight, experimental molecular weight, net charge, and hydrophobicity. Hydrophobicity was assessed by measuring the acetonitrile content at the retention time of the synthesized retro-inverso peptides using HPLC. Small letters stand for D-amino acids.

Name	Sequence	$MW_{calc.}$ [Da]	$MW_{exp.}$ [Da]	Net charge	Hydro-phobicity
ri_RL-8	knlfkrllkrlg	1485.9	1485.3	+6	32.37
ri_8A	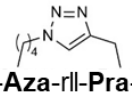 knlf-**Aza**-rll-**Pra**-rlg	1478.8	1478.2	+4	43.63
ri_8B	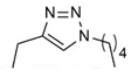 knlf-**Pra**-rll-**Aza**-rlg	1478.8	1478.2	+4	39.40

The synthesis was performed using SPPS with a synthesis robot. Afterward, the triazolyl-bridge of the peptides was again realized by using click chemistry with incorporated amino acids Pra and Aza, as described in the previous chapter, 3.3.3. The number of methylene groups flanking the triazolyl moiety remained unchanged. The synthesis and subsequent purification by RP-HPLC were performed as described and shown. Exemplary, purified ri_8A is depicted in Fig. 34. The other spectra of ri_RL-8 and ri_8B are attached in Fig. S26-27.

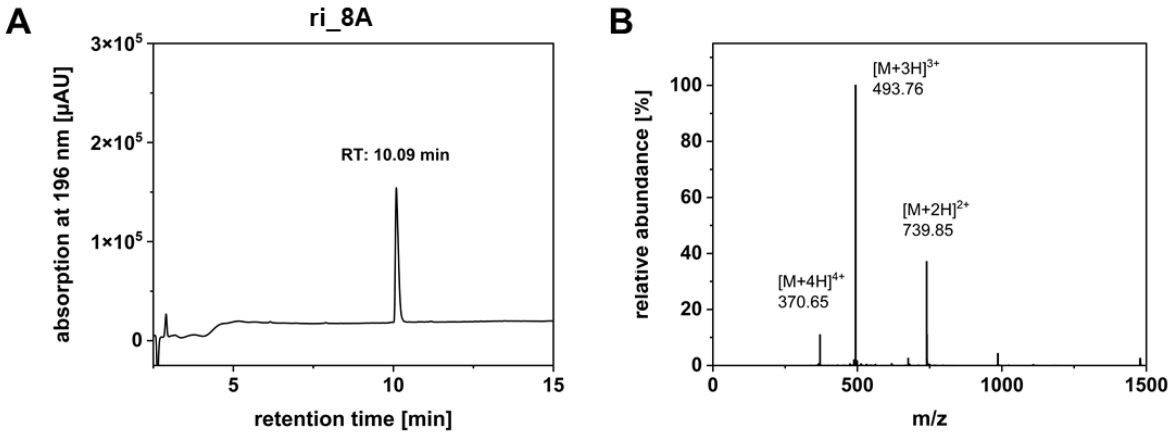

Figure 34. HPLC-ESI/MS analysis of ri_8A after purification. (A) UV-chromatogram of ri_8A (retention time of 10.09 min). (B) The mass spectrum of the peak at the retention time of 10.09 min shows m/z ratios that correspond to the quasi-molecular ions of ri_8A: $[M+4H]^{4+}$ = 370.65, $[M+3H]^{3+}$= 493.76 and $[M+2H]^{2+}$= 739.85.

3.3.8 Proteolytic stability of retro-inverso peptides

The triazolyl-bridge and the incorporated amino acids (Pra, Aza) are non-natural and could influence the stability against proteases.[229] Before synthesizing the retro-inverso peptides, the stability of triazolyl-bridged peptides 8A and 8B was tested in goat serum, attached in Fig. S28. The linear peptide RL-8 underwent rapid degradation within 60 min, with a calculated half-life of approximately 15 min. Beyond 60 min, RL-8 was undetectable by LC, indicating complete proteolytic degradation. In contrast, the triazolyl-bridged peptides demonstrated significantly enhanced stability, retaining approximately 50 % of their initial concentration after 120 min. The degradation of the triazolyl-bridged peptides was slower, so a final concentration of approximately 40 % remained after 240 min. The orientation of the triazolyl-bridge could potentially favor protease recognition, explaining the observed differences in stability for 8A and 8B. However, these experiments could not conclusively demonstrate this.

In comparison, the stability of novel peptides will be analyzed after incubation in human serum at 37 °C for 240 min. The presence of D-amino acids should further enhance protection against enzymatic degradation. The peptide stability was determined at the same time points using the UV detector of the LC. The results are depicted in Fig. 35.

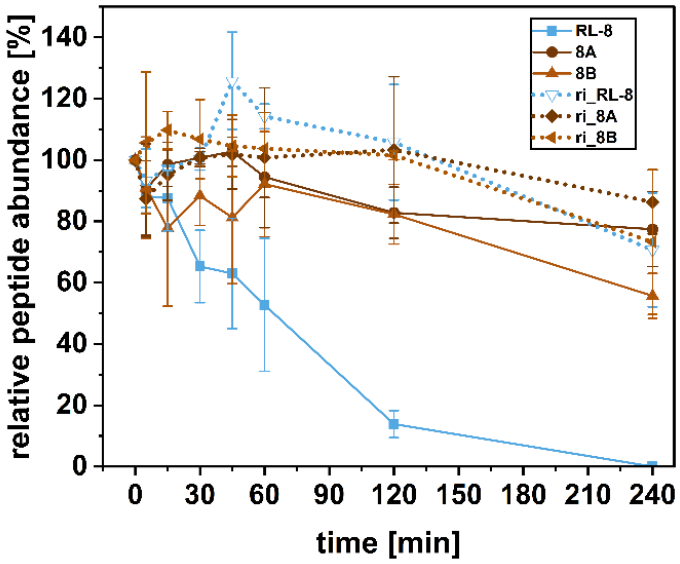

Figure 35. Stability analysis in human serum of triazolyl-bridged and retro-inverso peptides. Peptides were incubated with a concentration of 250 µM for 240 min, with aliquots collected at designated time points (5, 15, 30, 45, 60, 90, 120 and 240 min). Samples were precipitated using acetonitrile, and peptide abundance was quantified via LC-MS. Abundance values were normalized to the initial measurement at time point zero. Error bars represent standard deviation. The stability assay was conducted in triplicates (n=3).

Testing the stability in human serum showed that the linear peptide RL-8 exhibited slower degradation compared to goat serum, with over 50 % abundance detected after 60 min. However, RL-8 was degraded by approximately 80 % after 120 min and thoroughly after

240 min. The retro-inverso variant (ri_RL-8) demonstrated significantly increased stability, retaining ~75 % abundance even after 240 min. These findings underline the enhanced proteolytic stability reached by D-amino acids. Similarly, the triazolyl-bridged peptides displayed improved stability in both goat and human serum, with over 60 % abundance remaining after 240 min. The retro-inverso variants of 8A and 8B were detected in even higher abundance, highlighting that incorporating D-amino acids into triazolyl-bridged peptides further enhanced their stability.

3.3.9 Antimicrobial activity of retro-inverso peptides

Next, the antimicrobial activity was elucidated for the retro-inverso peptides using *B. spizizenii* (Gram-positive) and *S. typhimurium* (Gram-negative) to compare the data with the previous results.

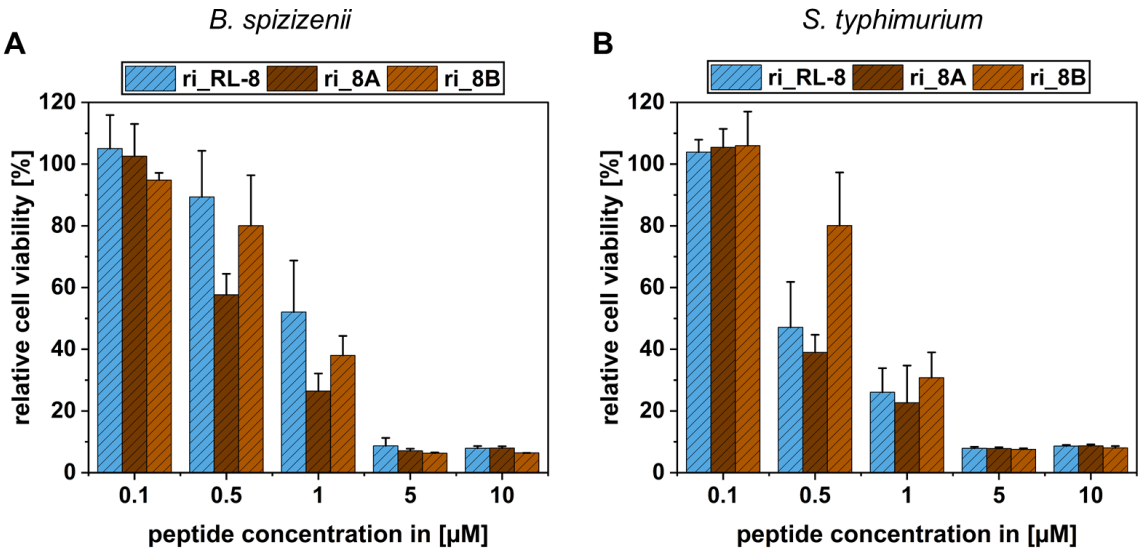

Figure 36. Antimicrobial profile of novel retro-inverso peptides after 4 h incubation in minimal medium. (A) *Bacillus spizizenii* and (B) *Salmonella typhimurium*. Error bars represent standard deviation. Experiments were conducted in triplicates (n=3). These experiments were performed together with Michael Quagliata.

The assay shown in Fig. 36 revealed that the retro-inverso peptides exhibited high efficacy against both *B. spizizenii* and *S. Typhimurium* already at 0.5-1 µM peptide concentration. In contrast, the parental peptides started to be antimicrobial around 5 µM peptide concentration, shown in Fig. 30. Interestingly, the retro-inverso linear variant displayed comparable antimicrobial activity to the retro-inverso triazolyl-bridged peptides. The activity of RL-8 was significantly higher than that of the linear RL-8 peptide (10 µM: >70 % cell viability), indicating that retro-inverso properties contribute to bacterial toxicity.

In summary, the synthesis of retro-inverso peptides confirmed that the stability has increased further. The first results in Gram-negative and Gram-positive bacteria showed increased

antimicrobial activity of all peptides, especially for the linear peptide RL-8. It would be interesting to test the novel retro-inverso peptides in pathogenic bacteria, and the developed AMPs are of great interest for future therapeutic applications.

4. Conclusion and outlook

The discovery of peptides has opened numerous opportunities for clinical applications. Over the past decades, peptides have been utilized to treat antimicrobial, anti-cancer, and metabolic diseases.[230] For instance, many CPPs have already been used for carrying anti-cancer drugs. Besides the worldwide prominent cancer disease, intracellular diseases dependent on organelle dysfunction are the focus of current research. In most cases, the treatment focuses not on the diseases themselves but on the symptoms resulting from the dysfunction of the organelles. Consequently, numerous research groups are interested in creating drugs that target diseases in organelles after uptake into the cells through signal sequences. Furthermore, antibiotic resistance is a growing global health crisis. Antibiotics have been used incorrectly or too much in healthcare, agriculture, and animal husbandry, promoting the development of resistant pathogens.[123] Nowadays, conventional antibiotics become less effective, and some infections are untreatable, leading to increased mortality and higher healthcare costs. In the last decades, the research has focused on developing novel antimicrobial agents, and global teams are collaborating to combat this rising topic.

In this thesis, all these topics mentioned above were addressed and tackled using the peptide sC18 and its variants to advance research in the respective areas.

1. *Comparing sC18 variants and synthesis of peptide-drug conjugates*

In this part of the thesis, the anti-cancer and drug-delivery properties of sC18 variants, namely sC18*, sC18ΔE, and sC18*R,L, were investigated. Exploring the secondary structure of these variants revealed that they were randomly coiled in an aqueous solution. Interestingly, adding TFE led to the α-helix formation of all analyzed peptides. This was somewhat expected, and the former data was agreed upon.[109] The analysis showed that deleting the glutamate in the *C*-terminal part of sC18 led to an increased amphipathic character and, thus, promoted the uptake efficiency of sC18ΔE compared to the other peptides. When these variants were tested in healthy and cancerous cells, it was shown that the plasma membrane composition likely influenced the membrane interaction of the peptides. The increased quantity of acidic phospholipids in cancer cells might improve the ability of the peptides to accumulate on the surface. They might have led to the formation of α-helices, which simultaneously trigger the cellular uptake mechanisms. May be due to this improved accumulation, the cytotoxicity against cancerous HeLa cells of all tested peptides was markedly increased compared to their interaction with “healthy” HEK-293 cells. These findings are supported by the analysis of negatively charged GUVs, in which the membrane accumulation of all peptides was visible. Of particular interest was the almost “perfect” amphipathic peptide sC18*R,L, where the hydrophobic and the basic amino acids were arranged oppositely, resulting in two perfectly

separated sites. This peptide showed the ability to disrupt the artificial membrane of the tested negatively charged GUVs. That effect was probably the reason for the increased cytotoxicity in HeLa cells and HEK293 cells at quite lower micromolar concentrations. As sC18ΔE has the highest net charge, the internalization efficacy was, as expected, enhanced. Interestingly, the mechanism of this peptide might be different compared to sC18*R,L, as the cytotoxicity was not increased. Instead of a direct translocation mechanism, this peptide seems to be taken up by endocytosis. The fluorescence microscopy showed the punctate pattern, indicating endocytic uptake.

To further test the ability of the sC18, sC18*, and sC18ΔE variants to function as carriers for drug delivery, PDCs containing the respective CPP and the anti-cancer drug Doxorubicin were synthesized and investigated. The sC18*R,L peptide was excluded in PDC synthesis, as it was too membrane-active and harmful to healthy cells in the lower micromolar range. The bifunctional SMP linker enhances the stability of the PDC. However, the drug is attached through an amide bond with the succinyl moiety, which is likely hydrolyzed by amidases in the lysosomes, potentially allowing for the release of the unmodified drug.[154] Additionally, the maleimide moiety was coupled with the peptide through a Thiol-Michael addition, a reversible reaction. For example, high levels of glutathione could trigger a retro Michael addition.[231] After PDC synthesis, the cytotoxicity and the uptake quantity were investigated and compared to Doxorubicin. The cytotoxicity and the amount of PDCs internalized into the HeLa cells were reduced, as Doxorubicin already has good uptake properties.[232] In general, the cytotoxicity of the coupled drug could be influenced by the added linker at the topoisomerase II interaction domain. After a possible retro-Michael reaction the peptide would be cleaved off and release the Dox-SMP intermediate. Side residues attached to Doxorubicin could have altered the interaction efficacy of the drug, and only the ability to intercalate DNA might still be active. It was not analyzed where and when the drug was cleaved off. Further studies of these PDCs regarding their cytotoxicity mechanism would elucidate the cleavage mechanism inside the cell. Therefore, the cells could be analyzed regarding their proliferation ability, and the marker γH2AX could be used to detect double-strand breaks.[233] These indications could show if the anthracycline drug works correctly or is altered by the linkage.

Interestingly, the uptake of PDC-2 appeared to be endocytic, which might have affected the drug's efficacy as it probably hindered its uptake in the nucleus. Further extension of the incubation period would help to investigate the long-term benefits of this PDC. To date, conjugation of Dox might be favored for therapeutic use, as Dox has, when applied in clinical chemotherapy, an 8-fold increase in lethal cardiotoxicity.[234] The minimization of cardiotoxicity through the use of PDCs could be analyzed as a proof of principle for PDC-2 in healthy cardiomyocyte cells. Further optimization of the PDCs could involve incorporating

another linker system, such as a cathepsin B-sensitive linker, which would enhance selective release in cancer cells where this particular enzyme is highly expressed.[235]

In summary, this thesis identified the peptide sC18ΔE as an efficient transporter for the anthracycline drug Doxorubicin. This PDC minimized the drug's side effects on healthy HFF-1 cells while largely preserving its cytotoxic activity in HeLa cells.

2. *Design of peroxisomal targeting sC18 variants*

In the second part of the thesis, the organelle-targeting properties of sC18 were investigated. CPPs can translocate the plasma membrane by various mechanisms and can be modified to reach specific organelles through targeting sequences. Due to this precise targeting, potential drug delivery may be more efficient. Therefore, the CPPs sC18* and sC18*R,L were combined with either *N*-terminal PTS2 or *C*-terminal PTS1 sequences for peroxisomal import. The 12 resulting PX-peptides were successfully synthesized and labelled with 5(6)-carboxyfluorescein. First, their cytotoxicity in MCF-7 cells was investigated. It was observed that the longer and hydrophobic PTS-2 sequences increased the overall cytotoxicity. However, the carrying peptide was also responsible for cytotoxic activity. In former studies, sC18*R,L already showed lytic activity in higher micromolar ranges, which was in line with the results when combined with the PTS2 or PTS1 signals. Thus, the following assays used a lower micromolar range to avoid harming the cells. Peptides were then analyzed for their uptake efficiency, which showed that they correlate with cytotoxic activity. Interestingly, all peptides bearing PTS2 were taken up significantly better than the sC18* alone, which might be attributed to the added hydrophobic amino acids of the signal sequence. sC18* combined with PTS1 did not show increased uptake efficiency. As expected, only sC18*R,L combined with PTS1 showed enhanced internalization levels that might depend on the internalization efficiency of the used CPP. In total, PX1, PX3, PX5, PX8, PX9, and PX11 were taken up very efficiently. PX5 exhibited high cytotoxic activity at lower micromolar concentrations, excluding it from subsequent colocalization experiments.

To perform colocalization studies, MCF-7 cells were generated that stably expressed the fusion protein mCherry_PTS1 (SKL) upon cumate induction. Afterward, cells were treated for 2 h with PX-peptides. To sum up, a small number of all tested peptides were colocalized in the peroxisome, but the movement of the peptides during imaging was very high, which probably influenced the localization signals. To discriminate if the peptides were transported into the peroxisome at other time points, the colocalization assays were repeated with the most promising peptides, PX1 and PX9, with earlier time points: 15 min, 30 min, and 60 min. However, different time points also did not show more effective peroxisome targeting by the PX1 and PX9 peptides. To exclude the possibility that the peptide sequence altered the signal

sequence's recognition, a plasmid was generated that expressed a mGold_PX9-PX12 protein. These plasmids were transfected into the inducible mCherry-PTS1-MCF-7 cells. As expected, mGold alone and combined with sC18*R,L showed random cytosolic distribution for the controls. mGold with only targeting sequence PTS1_1 was surprisingly distributed randomly in the cytosol. In contrast, the distribution of mGold with targeting sequence PTS1_2 showed almost perfect co-localization with peroxisomes. This might be due to the tertiary structure or the last amino acids of the mGold protein influencing the recognition of the PTS1_1 signal. Proline acts as a helix breaker, which might have altered the structure.[236] However, all plasmids with mGold_PX9-PX12 showed an almost perfect overlay with the peroxisomes. Concluding that the peptides bearing both PTS were recognized and might be transported into the peroxisome. These findings exclude the hypothesis that the peptide influenced the PTS recognition itself. Instead, it might be that the export of the peptides occurred quite fast through the recycling mechanism of the Pex5 protein. To analyze the levels of the Pex5 receptor, MCF-7 cells were treated with the peptides for 2 h, followed by Western blot analysis, since both PTS1 and PTS2 sequences were imported directly or indirectly through the Pex5 protein. Indeed, the peptides containing PTS1 or PTS2 increased the Pex5 levels. These findings suggested that the Pex5 protein is able to recognize the PX-peptides. However, the confirmation of successful import was not possible.

Different methods could be used to underline further that the peptides can successfully be imported into the peroxisome. First, another stable cell line could be generated expressing the peroxisomal receptor Pex5, usually located within cytosol but fused to the PTS1 signal, and with an additional part of a split-GFP.[237] The other part of the split-GFP will be added to the peptide sequence. Green fluorescence can only be observed in this system if the peptides get transported into peroxisomes and bind to the recombinant Pex5 with the PTS1 sequence. Moreover, it can be determined in a time-dependent manner when and with what efficiency the peptides were imported into the peroxisome. Beforehand, it would be interesting to see if binding with Pex5 occurs properly. Therefore, the PX-peptides bearing PTS1 must be tagged with a biotin followed by a pull-down after incubation. Then, the interaction with Pex5 will be investigated using Western blot. Additionally, it would be possible to examine the interactomics of PX-peptides in MCF-7 cells. Another proof of principle could be a newly designed PDC consisting of a potent PX-peptide (PX1 or PX9) coupled with an inhibitor of a peroxisomal protein such as alkyl dihydroxyacetone phosphate synthase (AGPS), which is responsible for ether lipid synthesis. This enzyme is highly upregulated in some cancerous cell lines (MCF-7), favoring fast cell division and tumor growth.[177] A research group discovered an inhibitor that can inhibit this enzyme, which could be used for conjugation.[238]

In summary, the peptides PX1, PX3, PX9, and PX11 found so far are candidates for further modifications, as promising colocalization signals and increased receptor protein levels of Pex5 support the overall functionality. Therefore, they could be the basis for additional modification and improvement of peroxisomal targeting peptides with the ability to inhibit proteins or metabolic pathways localized within the peroxisome.

3. *Novel sC18 variants that display high antimicrobial activity*

In the final section of this work, the increased antimicrobial activity of the peptide sC18* was examined by swapping specific amino acids and conducting further chemical modifications. In the foregoing studies, the almost “perfect” amphipathic peptide sC18*R,L showed high membrane interaction, lytic activity, and increased cytotoxicity against cancerous and healthy cell lines.[204,210,215] As this peptide showed potent properties for membrane perturbation, it would be interesting to see if this would also be useful regarding antimicrobial aspects. Cell wall disruption often leads to cell death due to lacking membrane integration and functionality. Thus, a screen of the parental sC18* was created with up to four mutations, varying the overall amphipathicity and the net charge of the peptides to identify the optimal physicochemical properties of the peptides. After successful synthesis, these peptides were tested in Gram-positive and Gram-negative bacteria to determine their general antimicrobial activity. The outcome showed that the peptides do not inhibit cell division and growth. Instead, the primary activity appears to be the destruction of the membrane. To obtain precise information on the efficiency of cell wall destruction, the bacteria were tested against the peptides incubated in a minimal medium in which the bacteria can no longer recover, thus making the lytic effect more visible. Within the first screen in *B. spizizenii*, the peptides RL-1, RL-8, RL-14, and RL-15 (sC18*R,L) were chosen for further examination in Gram-negative and Gram-positive bacteria. The other peptides were less active in tested bacteria, which might be due to the decrease in basic amino acids and the unbalanced amphipathic character. Furthermore, the Asn within the sequence might be responsible for helix-helix interaction, increasing the efficiency of membrane interaction due to higher peptide accumulation. For further peptide designs, it might be interesting to investigate the position of the Asn further to increase the membrane interaction through a stronger helix-helix interaction.

Despite the highest activity of RL-15 in all tested bacteria, the less modified peptide RL-8 was selected for further chemical modification, as the antimicrobial activity was high, and the cytotoxicity for mammals might be lower in comparison to RL-15. A triazolyl-bridge was used as a chemical modification to support the rigid structure of the peptide and, at the same time, increase the membrane interaction of the peptides with microbes and further enhance stability to enzymatic degradation.[229,239] The triazolyl-bridge was incorporated by the incorporation

of the amino acids Pra and Aza. These amino acids were bridged by Cu(I)-catalyzed click chemistry. The novel peptides 8A-D were analyzed regarding their secondary structure, which showed that the triazolyl-bridged peptides already forced an α-helix in an aqueous phosphate-buffered solution. This might further enhance the membrane interaction.

The four peptides were tested against the same bacteria as the linear ones. Indeed, the antimicrobial activity was significantly increased for the peptides 8A and 8B, whereas the peptides with the triazolyl-bridge in the hydrophobic region, 8C and 8D, showed decreased antimicrobial activity. These findings again demonstrated the importance of the hydrophobic part of the synthesized peptides. Detailed analysis of the peptides RL-8 and 8A using TEM after treatment in both *B. spizizenii* and *S. typhimurium* revealed that the clicked peptide 8A exhibited much higher bacterial membrane lysis, releasing intracellular contents. Further studies showed increased antimicrobial activity of the chemically modified peptides in two prominent pathogenic bacteria, methicillin-resistant *S. Aureus* and *N. gonorrhoeae*. Further investigating the antimicrobial activity against more pathogenic bacteria of these novel peptides is of great interest.

Interestingly, the peptides showed very similar activity in the human cancerous cell line HeLa. However, when testing them in the HFF-1, cytotoxic activity was only observed in the higher micromolar range. These results were confirmed by LDH-release assay after peptide treatment. It was observed that LDH was released at higher micromolar concentrations, but the cells can recover again, as confirmed with cell viability assay in HFF-1 cells. This was supported by testing them in fully neutral RBC, revealing that higher micromolar concentrations were needed to harm uncharged phospholipids. In these studies, it was shown that triazolyl-bridged peptides showed significantly increased antimicrobial and anti-cancer activity. Additionally, they were quite stable in goat serum against protease and peptidases. Testing in human cells revealed cytotoxic and lytic activity but far from the concentration that might be used for application in bacterial infections. Due to the significantly enhanced activity of the triazolyl-bridged peptides, the idea arose to incorporate unnatural amino acids further. Therefore, the peptides were synthesized using D-amino acids and using retro-inverso synthesis. The stability in the human serum of the retro-inverso peptides ri_RL-8, ri_8A, and ri_8B was markedly increased. In particular, ri_RL-8 was highly stable compared to its parental peptide RL-8. The other variants were slightly more stable but similar to 8A/B. Furthermore, the peptides were preliminarily tested in both *B. spizizenii* and S*. typhimurium,* and enhanced antimicrobial activity was observed. Another interesting aspect would be to evaluate the potential for circumventing the resistance development of bacteria against the tested peptides. Therefore, a long-term experimental approach can be employed. Pathogenic strains like *N. gonorrhoeae* or MRSA will be treated with half of the EC_{50} value peptide concentration.

Bacteria will be re-inoculated several times (20-30 generations). The EC_{50} value must be checked several times to prevent the starting concentration from becoming too low. Afterward, the bacteria can be analyzed using genome sequencing to identify mutations, membrane modifications, or similar. Slow resistance development would further increase the interest of these peptides in clinical applications. However, additional *in vitro* screening would have to be carried out beforehand to circumvent harming mammalian cells. After additional *in vitro* screening, animal infection models could be used to test efficacy *in vivo*. Simultaneously, the pharmacokinetics and -dynamics of the novel antimicrobial peptides could be determined.[240]

In summary, variants of sC18* were synthesized and chemically modified with triazolyl-bridges. Antimicrobial activity was significantly enhanced, particularly against pathogenic bacteria; stability in human serum improved, and the interaction with negatively charged plasma membranes became better. Especially, the novel peptide 8B exhibited good antimicrobial and anti-cancer properties with lower lytic activity in tested healthy cells, making it a promising candidate for clinical applications, alongside its retro-inverso variant showing enhanced serum stability.

In total, this work demonstrated the versatility of sC18 through systematic amino acid substitutions, deletions, truncations, insertions, and modifications. Conjugating sC18ΔE with the anti-cancer drug Doxorubicin produced a functional PDC with potentially greater selectivity for cancer cells. Inserting the PTS into sC18 variants provided initial indications of an impact on the peroxisomal import machinery, establishing a promising foundation for optimizing peroxisomal targeting peptides with potential applications. Additionally, chemical modifications of sC18* variants, including triazolyl-bridge formation, significantly enhanced their antimicrobial activity against pathogenic bacteria. Further optimization through incorporating D-amino acids and sequence inversion may enhance the overall activity even more. These diverse strategies, stemming from the parental peptide sC18, emphasize its broad potential for therapeutic applications.

5. References

1. Seantier, B.; Giocondi, M.C.; Grimellec, C. Le; Milhiet, P.E. Probing Supported Model and Native Membranes Using AFM. *Curr Opin Colloid Interface Sci* **2008**, *13*, 326–337, doi:10.1016/J.COCIS.2008.01.003.
2. Dias, C.; Nylandsted, J. Plasma Membrane Integrity in Health and Disease: Significance and Therapeutic Potential. *Cell Discovery 2020 7:1* **2021**, *7*, 1–18, doi:10.1038/s41421-020-00233-2.
3. Cooper, G.M. Structure of the Plasma Membrane. **2000**.
4. Alberts, B.; Johnson, A.; Lewis, J.; Raff, M.; Roberts, K.; Walter, P. The Lipid Bilayer. **2002**.
5. Hilton, K.L.F.; Manwani, C.; Boles, J.E.; White, L.J.; Ozturk, S.; Garrett, M.D.; Hiscock, J.R. The Phospholipid Membrane Compositions of Bacterial Cells, Cancer Cell Lines and Biological Samples from Cancer Patients. *Chem Sci* **2021**, *12*, 13273–13282, doi:10.1039/D1SC03597E.
6. Chiricozzi, E.; Aureli, M.; Mauri, L.; Di Biase, E.; Lunghi, G.; Fazzari, M.; Valsecchi, M.; Carsana, E.V.; Loberto, N.; Prinetti, A.; et al. Glycosphingolipids. *Adv Exp Med Biol* **2021**, *1325*, 61–102, doi:10.1007/978-3-030-70115-4_3/FIGURES/13.
7. Drescher, S.; van Hoogevest, P. The Phospholipid Research Center: Current Research in Phospholipids and Their Use in Drug Delivery. *Pharmaceutics* **2020**, *12*, 1235, doi:10.3390/PHARMACEUTICS12121235.
8. Harayama, T.; Riezman, H. Understanding the Diversity of Membrane Lipid Composition. *Nat Rev Mol Cell Biol* **2018**, *19*, 281–296, doi:10.1038/NRM.2017.138.
9. Li, J.; Wang, X.; Zhang, T.; Wang, C.; Huang, Z.; Luo, X.; Deng, Y. A Review on Phospholipids and Their Main Applications in Drug Delivery Systems. *Asian J Pharm Sci* **2015**, *10*, 81–98, doi:10.1016/J.AJPS.2014.09.004.
10. Ridgway, N.D. Phospholipid Synthesis in Mammalian Cells. *Biochemistry of Lipids, Lipoproteins and Membranes: Sixth Edition* **2016**, 209–236, doi:10.1016/B978-0-444-63438-2.00007-9.
11. Quinville, B.M.; Deschenes, N.M.; Ryckman, A.E.; Walia, J.S. A Comprehensive Review: Sphingolipid Metabolism and Implications of Disruption in Sphingolipid Homeostasis. *International Journal of Molecular Sciences 2021, Vol. 22, Page 5793* **2021**, *22*, 5793, doi:10.3390/IJMS22115793.
12. Shorthouse, D.; Hedger, G.; Koldsø, H.; Sansom, M.S.P. Molecular Simulations of Glycolipids: Towards Mammalian Cell Membrane Models. *Biochimie* **2016**, *120*, 105–109, doi:10.1016/J.BIOCHI.2015.09.033.
13. Dufourc, E.J. Sterols and Membrane Dynamics. *J Chem Biol* **2008**, *1*, 63, doi:10.1007/S12154-008-0010-6.
14. Simons, K.; Ehehalt, R. Cholesterol, Lipid Rafts, and Disease. *J Clin Invest* **2002**, *110*, 597–603, doi:10.1172/JCI16390.
15. Ibarguren, M.; López, D.J.; Encinar, J.A.; González-Ros, J.M.; Busquets, X.; Escribá, P. V. Partitioning of Liquid-Ordered/Liquid-Disordered Membrane Microdomains Induced by the Fluidifying Effect of 2-Hydroxylated Fatty Acid Derivatives. *Biochim Biophys Acta* **2013**, *1828*, 2553–2563, doi:10.1016/J.BBAMEM.2013.06.014.
16. Antimicrobial Peptides. **2019**, *1117*, doi:10.1007/978-981-13-3588-4.
17. Van Meer, G.; Voelker, D.R.; Feigenson, G.W. Membrane Lipids: Where They Are and How They Behave. *Nat Rev Mol Cell Biol* **2008**, *9*, 112, doi:10.1038/NRM2330.

18. Bucci, M. Leaflets out of Order. *Nature Chemical Biology 2013 9:2* **2013**, *9*, 67–67, doi:10.1038/nchembio.1175.
19. Phosphatidylserine, X.; Alunni-Fabbroni, M.; Nahum Goldberg, S.; Wildgruber, M.; Kaynak, A.; Davis, H.W.; Kogan, A.B.; Lee, J.-H.; Narmoneva, D.A.; Qi, X. Phosphatidylserine: The Unique Dual-Role Biomarker for Cancer Imaging and Therapy. *Cancers (Basel)* **2022**, *14*, 2536, doi:10.3390/CANCERS14102536.
20. Pomorski, T.; Menon, A.K. Lipid Flippases and Their Biological Functions. *Cell Mol Life Sci* **2006**, *63*, 2908, doi:10.1007/S00018-006-6167-7.
21. Sebastian, T.T.; Baldridge, R.D.; Xu, P.; Graham, T.R. Phospholipid Flippases: Building Asymmetric Membranes and Transport Vesicles. *Biochim Biophys Acta* **2012**, *1821*, 1068–1077, doi:10.1016/J.BBALIP.2011.12.007.
22. Desai, T.J.; Toombs, J.E.; Minna, J.D.; Brekken, R.A.; Udugamasooriya, D.G. Identification of Lipid-Phosphatidylserine (PS) as the Target of Unbiasedly Selected Cancer Specific Peptide-Peptoid Hybrid PPS1. *Oncotarget* **2016**, *7*, 30678–30690, doi:10.18632/ONCOTARGET.8929.
23. Preta, G. New Insights Into Targeting Membrane Lipids for Cancer Therapy. *Front Cell Dev Biol* **2020**, *8*, 571237, doi:10.3389/FCELL.2020.571237/BIBTEX.
24. Hosonuma, M.; Yoshimura, K. Association between PH Regulation of the Tumor Microenvironment and Immunological State. *Front Oncol* **2023**, *13*, 1175563, doi:10.3389/FONC.2023.1175563.
25. Mollinedo, F.; Gajate, C. Lipid Rafts as Signaling Hubs in Cancer Cell Survival/Death and Invasion: Implications in Tumor Progression and Therapy: Thematic Review Series: Biology of Lipid Rafts. *J Lipid Res* **2020**, *61*, 611–635, doi:10.1194/JLR.TR119000439.
26. Cheng, C.; Geng, F.; Cheng, X.; Guo, D. Lipid Metabolism Reprogramming and Its Potential Targets in Cancer. *Cancer Communications 2018 38:1* **2018**, *38*, 1–14, doi:10.1186/S40880-018-0301-4.
27. Chimento, A.; Casaburi, I.; Avena, P.; Trotta, F.; De Luca, A.; Rago, V.; Pezzi, V.; Sirianni, R. Cholesterol and Its Metabolites in Tumor Growth: Therapeutic Potential of Statins in Cancer Treatment. *Front Endocrinol (Lausanne)* **2019**, *10*, 425869, doi:10.3389/FENDO.2018.00807/BIBTEX.
28. Chang, W.; Fa, H.; Xiao, D.; Wang, J. Targeting Phosphatidylserine for Cancer Therapy: Prospects and Challenges. *Theranostics* **2020**, *10*, 9214, doi:10.7150/THNO.45125.
29. Imtiyaz, Z.; He, J.; Leng, Q.; Agrawal, A.K.; Mixson, A.J. PH-Sensitive Targeting of Tumors with Chemotherapy-Laden Nanoparticles: Progress and Challenges. *Pharmaceutics* **2022**, *14*, 2427, doi:10.3390/PHARMACEUTICS14112427.
30. Carey, A.B.; Ashenden, A.; Köper, I. Model Architectures for Bacterial Membranes. *Biophys Rev 1*, 3, doi:10.1007/s12551-021-00913-7.
31. Strahl, H.; Errington, J. Bacterial Membranes: Structure, Domains, and Function. *Annu Rev Microbiol* **2017**, *71*, 519–538, doi:10.1146/ANNUREV-MICRO-102215-095630.
32. Hilton, K.L.F.; Manwani, C.; Boles, J.E.; White, L.J.; Ozturk, S.; Garrett, M.D.; Hiscock, J.R. The Phospholipid Membrane Compositions of Bacterial Cells, Cancer Cell Lines and Biological Samples from Cancer Patients. *Chem Sci* **2021**, *12*, 13273, doi:10.1039/D1SC03597E.
33. Bogdanov, M.; Pyrshev, K.; Yesylevskyy, S.; Ryabichko, S.; Boiko, V.; Ivanchenko, P.; Kiyamova, R.; Guan, Z.; Ramseyer, C.; Dowhan, W. Phospholipid Distribution in the Cytoplasmic Membrane of Gram-Negative Bacteria Is Highly Asymmetric, Dynamic,

and Cell Shape-Dependent. *Sci Adv* **2020**, *6*, doi:10.1126/SCIADV.AAZ6333/SUPPL_FILE/AAZ6333_SM.PDF.
34. Sáenz, J.P.; Grosser, D.; Bradley, A.S.; Lagny, T.J.; Lavrynenko, O.; Broda, M.; Simons, K. Hopanoids as Functional Analogues of Cholesterol in Bacterial Membranes. *Proc Natl Acad Sci U S A* **2015**, *112*, 11971–11976, doi:10.1073/PNAS.1515607112/SUPPL_FILE/PNAS.201515607SI.PDF.
35. Rohmer, M.; Bouvier-Nave, P.; Ourisson, G. Distribution of Hopanoid Triterpenes in Prokaryotes. *J Gen Microbiol* **1984**, *130*, 1137–1150, doi:10.1099/00221287-130-5-1137/CITE/REFWORKS.
36. Malott, R.J.; Steen-Kinnaird, B.R.; Lee, T.D.; Speert, D.P. Identification of Hopanoid Biosynthesis Genes Involved in Polymyxin Resistance in Burkholderia Multivorans. **2012**, doi:10.1128/AAC.00602-11.
37. Itzhak Fishov; Vic Norris Membrane Structure and Heterogeneity. **2012**, doi:10.13140/RG.2.1.3736.3285.
38. Silhavy, T.J.; Kahne, D.; Walker, S. The Bacterial Cell Envelope. *Cold Spring Harb Perspect Biol* **2010**, *2*, a000414, doi:10.1101/CSHPERSPECT.A000414.
39. Lithgow, T.; Stubenrauch, C.J.; Stumpf, M.P.H. Surveying Membrane Landscapes: A New Look at the Bacterial Cell Surface. *Nature Reviews Microbiology 2023 21:8* **2023**, *21*, 502–518, doi:10.1038/s41579-023-00862-w.
40. Pokhrel, R.; Shakya, R.; Baral, P.; Chapagain, P. Molecular Modeling and Simulation of the Peptidoglycan Layer of Gram-Positive Bacteria Staphylococcus Aureus. *J Chem Inf Model* **2022**, *62*, 4955–4962, doi:10.1021/ACS.JCIM.2C00437/SUPPL_FILE/CI2C00437_SI_002.MP4.
41. Silhavy, T.J. Classic Spotlight: Gram-Negative Bacteria Have Two Membranes. *J Bacteriol* **2015**, *198*, 201, doi:10.1128/JB.00599-15.
42. Brown, S.; Santa Maria, J.P.; Walker, S. Wall Teichoic Acids of Gram-Positive Bacteria. *Annu Rev Microbiol* **2013**, *67*, 10.1146/annurev-micro-092412–155620, doi:10.1146/ANNUREV-MICRO-092412-155620.
43. Nguyen, M.T.; Matsuo, M.; Niemann, S.; Herrmann, M.; Götz, F. Lipoproteins in Gram-Positive Bacteria: Abundance, Function, Fitness. *Front Microbiol* **2020**, *11*, 582582, doi:10.3389/FMICB.2020.582582/FULL.
44. Miller, W.R.; Arias, C.A. ESKAPE Pathogens: Antimicrobial Resistance, Epidemiology, Clinical Impact and Therapeutics. *Nature Reviews Microbiology 2024 22:10* **2024**, *22*, 598–616, doi:10.1038/s41579-024-01054-w.
45. Bos, M.P.; Tommassen, J. Biogenesis of the Gram-Negative Bacterial Outer Membrane. *Curr Opin Microbiol* **2004**, *7*, 610–616, doi:10.1016/J.MIB.2004.10.011.
46. Farhana, A.; Khan, Y.S. Biochemistry, Lipopolysaccharide. *StatPearls* **2023**.
47. Gurvic, D.; Zachariae, U. Multidrug Efflux in Gram-Negative Bacteria: Structural Modifications in Active Compounds Leading to Efflux Pump Avoidance. *npj Antimicrobials and Resistance 2024 2:1* **2024**, *2*, 1–11, doi:10.1038/s44259-024-00023-w.
48. Melander, R.J.; Mattingly, A.E.; Nemeth, A.M.; Melander, C. Overcoming Intrinsic Resistance in Gram-Negative Bacteria Using Small Molecule Adjuvants. *Bioorg Med Chem Lett* **2023**, *80*, 129113, doi:10.1016/J.BMCL.2022.129113.
49. Scott, D.A.; Best, C.H. The Preparation of Insulin. *Ind Eng Chem* **1925**, *17*, 238–240, doi:10.1021/ie50183a004.
50. Merrifield, R.B. Solid Phase Peptide Synthesis. I. The Synthesis of a Tetrapeptide. *J Am Chem Soc* **1963**, *85*, 2149–2154, doi:10.1021/ja00897a025.

51. Mathieu, C.; Gillard, P.; Benhalima, K. Insulin Analogues in Type 1 Diabetes Mellitus: Getting Better All the Time. *Nat Rev Endocrinol* **2017**, *13*, 385–399, doi:10.1038/nrendo.2017.39.
52. Keen, H.; Pickup, J.C.; Bilous, R.W.; Glynne, A.; Viberti, G.C.; Jarrett, R.J.; Marsden, R. HUMAN INSULIN PRODUCED BY RECOMBINANT DNA TECHNOLOGY: SAFETY AND HYPOGLYCÆMIC POTENCY IN HEALTHY MEN. *The Lancet* **1980**, *316*, 398–401, doi:https://doi.org/10.1016/S0140-6736(80)90443-2.
53. Lau, J.L.; Dunn, M.K. Therapeutic Peptides: Historical Perspectives, Current Development Trends, and Future Directions. *Bioorg Med Chem* **2018**, *26*, 2700–2707, doi:https://doi.org/10.1016/j.bmc.2017.06.052.
54. Hermesch, A.C.; Kernberg, A.S.; Layoun, V.R.; Caughey, A.B. Oxytocin: Physiology, Pharmacology, and Clinical Application for Labor Management. *Am J Obstet Gynecol* **2024**, *230*, S729–S739, doi:10.1016/J.AJOG.2023.06.041.
55. Dyke, P.C.; Tobias, J.D. Vasopressin: Applications in Clinical Practice. *J Intensive Care Med* **2004**, *19*, 220–228, doi:10.1177/0885066604265246.
56. Wilson, A.C.; Meethal, S.V.; Bowen, R.L.; Atwood, C.S. Leuprolide Acetate: A Drug of Diverse Clinical Applications. *Expert Opin Investig Drugs* **2007**, *16*, 1851–1863, doi:10.1517/13543784.16.11.1851.
57. Wang, J.; Dou, X.; Song, J.; Lyu, Y.; Zhu, X.; Xu, L.; Li, W.; Shan, A. Antimicrobial Peptides: Promising Alternatives in the Post Feeding Antibiotic Era. *Med Res Rev* **2019**, *39*, 831–859, doi:https://doi.org/10.1002/med.21542.
58. Kang, H.-K.; Kim, C.; Seo, C.H.; Park, Y. The Therapeutic Applications of Antimicrobial Peptides (AMPs): A Patent Review. *Journal of Microbiology* **2017**, *55*, 1–12, doi:10.1007/s12275-017-6452-1.
59. Lei, J.; Sun, L.; Huang, S.; Zhu, C.; Li, P.; He, J.; Mackey, V.; Coy, D.H.; He, Q. *The Antimicrobial Peptides and Their Potential Clinical Applications*; 2019; Vol. 11;.
60. Roudi, R.; Syn, N.L.; Roudbary, M. Antimicrobial Peptides as Biologic and Immunotherapeutic Agents against Cancer: A Comprehensive Overview. *Front Immunol* 2017, *8*.
61. Cerrato, C.P.; Langel, Ü. An Update on Cell-Penetrating Peptides with Intracellular Organelle Targeting. *Expert Opin Drug Deliv* **2022**, *19*, 133–146, doi:10.1080/17425247.2022.2034784.
62. Li, C.H.O.H.H.; F~, P.; Nss-Bech,); Geschwind, I.I.; Hayashida, T.; Hungerford, G.F.; Lostroh, A.J.; Lyons, W.R.; Moon, Y.D.; Reinhardt, W.O.; et al. *(ACTH) X. BIOLOGICAL INVESTIGATIONS ON u-CoRTICOTROPIN*;
63. HABENER, J.F.; SINGER, F.R.; DEFTOS, L.J.; NEER, R.M.; POTTS, J.T. Explanation for Unusual Potency of Salmon Calcitonin. *Nat New Biol* **1971**, *232*, 91–92, doi:10.1038/newbio232091a0.
64. du Vigneaud, V.; Ressler, C.; Swan, J.M.; Roberts, C.W.; Katsoyannis, P.G. The Synthesis of Oxytocin1. *J Am Chem Soc* **1954**, *76*, 3115–3121, doi:10.1021/ja01641a004.
65. Glavaš, M.; Gitlin-Domagalska, A.; Dębowski, D.; Ptaszyńska, N.; Łęgowska, A.; Rolka, K. Vasopressin and Its Analogues: From Natural Hormones to Multitasking Peptides. *Int J Mol Sci* 2022, *23*.
66. Chrisp, P.; Sorkin, E.M.; Crawford, ; E D; Murphy, ; G P *DRUG EVALUATION ~~~_~~~_~_~~~~~_~~~~ Leuprorelin A Review of Its Pharmacology and Therapeutic Use in Prostatic Disorders*; 1991;

67. Al Musaimi, O.; Al Shaer, D.; Albericio, F.; de la Torre, B.G. 2022 FDA TIDES (Peptides and Oligonucleotides) Harvest. *Pharmaceuticals (Basel)* **2023**, *16*, doi:10.3390/PH16030336.
68. Rossino, G.; Marchese, E.; Galli, G.; Verde, F.; Finizio, M.; Serra, M.; Linciano, P.; Collina, S. Peptides as Therapeutic Agents: Challenges and Opportunities in the Green Transition Era. *Molecules* **2023**, *28*, doi:10.3390/MOLECULES28207165.
69. Wang, L.; Wang, N.; Zhang, W.; Cheng, X.; Yan, Z.; Shao, G.; Wang, X.; Wang, R.; Fu, C. Therapeutic Peptides: Current Applications and Future Directions. *Signal Transduct Target Ther* **2022**, *7*, doi:10.1038/S41392-022-00904-4.
70. Apostolopoulos, V.; Bojarska, J.; Chai, T.T.; Elnagdy, S.; Kaczmarek, K.; Matsoukas, J.; New, R.; Parang, K.; Lopez, O.P.; Parhiz, H.; et al. A Global Review on Short Peptides: Frontiers and Perspectives. *Molecules* **2021**, *26*, doi:10.3390/MOLECULES26020430.
71. Gori, A.; Lodigiani, G.; Colombarolli, S.G.; Bergamaschi, G.; Vitali, A. Cell Penetrating Peptides: Classification, Mechanisms, Methods of Study, and Applications. *ChemMedChem* **2023**, *18*, e202300236, doi:10.1002/CMDC.202300236.
72. Copolovici, D.M.; Langel, K.; Eriste, E.; Langel, Ü. Cell-Penetrating Peptides: Design, Synthesis, and Applications. *ACS Nano* **2014**, *8*, 1972–1994, doi:10.1021/NN4057269/ASSET/IMAGES/LARGE/NN-2013-057269_0004.JPEG.
73. Ruseska, I.; Zimmer, A. Internalization Mechanisms of Cell-Penetrating Peptides. *Beilstein Journal of Nanotechnology* **2020**, *11*, 101, doi:10.3762/BJNANO.11.10.
74. Tsuchiya, K.; Horikoshi, K.; Fujita, M.; Hirano, M.; Miyamoto, M.; Yokoo, H.; Demizu, Y. Development of Hydrophobic Cell-Penetrating Stapled Peptides as Drug Carriers. *Int J Mol Sci* **2023**, *24*, 11768, doi:10.3390/IJMS241411768/S1.
75. Bottens, R.A.; Yamada, T. Cell-Penetrating Peptides (CPPs) as Therapeutic and Diagnostic Agents for Cancer. *Cancers (Basel)* **2022**, *14*, doi:10.3390/CANCERS14225546.
76. CPP, Cell-Penetrating Peptides., doi:10.1007/978-981-13-8747-0.
77. Gräslund, A.; Madani, F.; Lindberg, S.; Langel, Ü.; Futaki, S. Mechanisms of Cellular Uptake of Cell-Penetrating Peptides. *Journal of Biophysics* **2011**, *2011*, doi:10.1155/2011/414729.
78. Frankel, A.D.; Pabo, C.O. Cellular Uptake of the Tat Protein from Human Immunodeficiency Virus. *Cell* **1988**, *55*, 1189–1193, doi:10.1016/0092-8674(88)90263-2.
79. Flinterman, M.; Farzaneh, F.; Habib, N.; Malik, F.; Gäken, J.; Tavassoli, M. Delivery of Therapeutic Proteins as Secretable TAT Fusion Products. *Molecular Therapy* **2009**, *17*, 334–342, doi:10.1038/MT.2008.256.
80. Lichtenstein, M.; Zabit, S.; Hauser, N.; Farouz, S.; Melloul, O.; Hirbawi, J.; Lorberboum-Galski, H. TAT for Enzyme/Protein Delivery to Restore or Destroy Cell Activity in Human Diseases. *Life* **2021**, *11*, doi:10.3390/LIFE11090924.
81. Rapoport, M.; Lorberboum-Galski, H. TAT-Based Drug Delivery System--New Directions in Protein Delivery for New Hopes? *Expert Opin Drug Deliv* **2009**, *6*, 453–463, doi:10.1517/17425240902887029.
82. Dupont, E.; Prochiantz, A.; Joliot, A. Penetratin Story: An Overview. *Methods in Molecular Biology* **2011**, *683*, 21–29, doi:10.1007/978-1-60761-919-2_2.
83. Derakhshankhah, H.; Jafari, S. Cell Penetrating Peptides: A Concise Review with Emphasis on Biomedical Applications. *Biomedicine & Pharmacotherapy* **2018**, *108*, 1090–1096, doi:10.1016/J.BIOPHA.2018.09.097.

84. Weller, K.; Lauber, S.; Lerch, M.; Renaud, A.; Merkle, H.P.; Zerbe, O. Biophysical and Biological Studies of End-Group-Modified Derivatives of Pep-1. *Biochemistry* **2005**, *44*, 15799–15811, doi:10.1021/BI051535D/SUPPL_FILE/BI051535DSI20051011_094251.PDF.
85. Elmquist, A.; Lindgren, M.; Bartfai, T.; Langel, Ü. Ve-Cadherin-Derived Cell-Penetrating Peptide, PVEC with Carrier Functions. *Exp Cell Res* **2001**, *269*, 237–244, doi:10.1006/excr.2001.5316.
86. Neundorf, I.; Rennert, R.; Hoyer, J.; Schramm, F.; Löbner, K.; Kitanovic, I.; Wölfl, S. Fusion of a Short HA2-Derived Peptide Sequence to Cell-Penetrating Peptides Improves Cytosolic Uptake, but Enhances Cytotoxic Activity. *Pharmaceuticals (Basel)* **2009**, *2*, 49–65, doi:10.3390/PH2020049.
87. Crombez, L.; Aldrian-Herrada, G.; Konate, K.; Nguyen, Q.N.; McMaster, G.K.; Brasseur, R.; Heitz, F.; Divita, G. A New Potent Secondary Amphipathic Cell-Penetrating Peptide for SiRNA Delivery into Mammalian Cells. *Mol Ther* **2009**, *17*, 95–103, doi:10.1038/MT.2008.215.
88. Benincasa, M.; Scocchi, M.; Podda, E.; Skerlavaj, B.; Dolzani, L.; Gennaro, R. Antimicrobial Activity of Bac7 Fragments against Drug-Resistant Clinical Isolates. *Peptides (N.Y.)* **2004**, *25*, 2055–2061, doi:10.1016/J.PEPTIDES.2004.08.004.
89. Zaro, J.L.; Shen, W.C. Cationic and Amphipathic Cell-Penetrating Peptides (CPPs): Their Structures and in Vivo Studies in Drug Delivery. *Frontiers of Chemical Science and Engineering 2015 9:4* **2015**, *9*, 407–427, doi:10.1007/S11705-015-1538-Y.
90. Fernández-Carneado, J.; Kogan, M.J.; Pujals, S.; Giralt, E. Amphipathic Peptides and Drug Delivery. *Peptide Science* **2004**, *76*, 196–203, doi:10.1002/BIP.10585.
91. Rádis-Baptista, G.; Campelo, I.S.; Morlighem, J.É.R.L.; Melo, L.M.; Freitas, V.J.F. Cell-Penetrating Peptides (CPPs): From Delivery of Nucleic Acids and Antigens to Transduction of Engineered Nucleases for Application in Transgenesis. *J Biotechnol* **2017**, *252*, 15–26, doi:10.1016/J.JBIOTEC.2017.05.002.
92. Bui Thi Phuong, H.; Doan Ngan, H.; Le Huy, B.; Vu Dinh, H.; Luong Xuan, H. The Amphipathic Design in Helical Antimicrobial Peptides. *ChemMedChem* **2024**, *19*, e202300480, doi:10.1002/CMDC.202300480.
93. Drexelius, M.; Reinhardt, A.; Grabeck, J.; Cronenberg, T.; Nitsche, F.; Huesgen, P.F.; Maier, B.; Neundorf, I. Multistep Optimization of a Cell-Penetrating Peptide towards Its Antimicrobial Activity. *Biochem J* **2021**, *478*, 63–78, doi:10.1042/BCJ20200698.
94. Klimpel, A.; Stillger, K.; Wiederstein, J.L.; Krüger, M.; Neundorf, I. Cell-Permeable CaaX-Peptides Affect K-Ras Downstream Signaling and Promote Cell Death in Cancer Cells. *FEBS J* **2021**, *288*, 2911–2929, doi:10.1111/FEBS.15612.
95. Lützenburg, T.; Neundorf, I.; Scholz, M. Direct Carborane-Peptide Conjugates: Synthesis and Evaluation as Non-Natural Lipopeptide Mimetics. *Chem Phys Lipids* **2018**, *213*, 62–67, doi:10.1016/J.CHEMPHYSLIP.2018.03.009.
96. Gronewold, A.; Horn, M.; Ranđelović, I.; Tóvári, J.; Muñoz Vázquez, S.; Schomäcker, K.; Neundorf, I. Characterization of a Cell-Penetrating Peptide with Potential Anticancer Activity. *ChemMedChem* **2017**, *12*, 42–49, doi:10.1002/CMDC.201600498.
97. Reichart, F.; Horn, M.; Neundorf, I. Cyclization of a Cell-Penetrating Peptide via Click-Chemistry Increases Proteolytic Resistance and Improves Drug Delivery. *J Pept Sci* **2016**, *22*, 421–426, doi:10.1002/PSC.2885.
98. Pujals, S.; Giralt, E. Proline-Rich, Amphipathic Cell-Penetrating Peptides. *Adv Drug Deliv Rev* **2008**, *60*, 473–484, doi:10.1016/J.ADDR.2007.09.012.

99. Tabujew, I.; Lelle, M.; Peneva, K. Cell-Penetrating Peptides for Nanomedicine-How to Choose the Right Peptide. *BioNanoMaterials* **2015**, *16*, 59–72, doi:10.1515/BNM-2015-0001/ASSET/GRAPHIC/J_BNM-2015-0001_FIG_003.JPG.
100. Choi, Y.; David, A. Cell Penetrating Peptides and the Mechanisms for Intracellular Entry. *Curr Pharm Biotechnol* **2014**, *15*, 192–199, doi:10.2174/1389201015666140617093331.
101. Guo, Z.; Peng, H.; Kang, J.; Sun, D. Cell-Penetrating Peptides: Possible Transduction Mechanisms and Therapeutic Applications (Review). *Biomed Rep* **2016**, *4*, 528–534, doi:10.3892/BR.2016.639/HTML.
102. Jiao, C.Y.; Delaroche, D.; Burlina, F.; Alves, I.D.; Chassaing, G.; Sagan, S. Translocation and Endocytosis for Cell-Penetrating Peptide Internalization. *J Biol Chem* **2009**, *284*, 33957, doi:10.1074/JBC.M109.056309.
103. Bechara, C.; Sagan, S. Cell-Penetrating Peptides: 20 Years Later, Where Do We Stand? *FEBS Lett* **2013**, *587*, 1693–1702, doi:10.1016/J.FEBSLET.2013.04.031.
104. Porosk, L.; Langel, Ü. Approaches for Evaluation of Novel CPP-Based Cargo Delivery Systems. *Front Pharmacol* **2022**, *13*, doi:10.3389/FPHAR.2022.1056467.
105. Kauffman, W.B.; Fuselier, T.; He, J.; Wimley, W.C. Mechanism Matters: A Taxonomy of Cell Penetrating Peptides. *Trends Biochem Sci* **2015**, *40*, 749–764, doi:10.1016/J.TIBS.2015.10.004.
106. Conner, S.D.; Schmid, S.L. Regulated Portals of Entry into the Cell. *Nature* **2003**, *422*, 37–44, doi:10.1038/NATURE01451.
107. Teo, S.L.Y.; Rennick, J.J.; Yuen, D.; Al-Wassiti, H.; Johnston, A.P.R.; Pouton, C.W. Unravelling Cytosolic Delivery of Cell Penetrating Peptides with a Quantitative Endosomal Escape Assay. *Nature Communications 2021 12:1* **2021**, *12*, 1–12, doi:10.1038/s41467-021-23997-x.
108. Kondow-Mcconaghy, H.M.; Muthukrishnan, N.; Erazo-Oliveras, A.; Najjar, K.; Juliano, R.L.; Pellois, J.P. Impact of the Endosomal Escape Activity of Cell-Penetrating Peptides on the Endocytic Pathway. *ACS Chem Biol* **2020**, *15*, 2355, doi:10.1021/ACSCHEMBIO.0C00319.
109. Di Pisa, M.; Chassaing, G.; Swiecicki, J.M. Translocation Mechanism(s) of Cell-Penetrating Peptides: Biophysical Studies Using Artificial Membrane Bilayers. *Biochemistry* **2015**, *54*, 194–207, doi:10.1021/BI501392N/ASSET/IMAGES/LARGE/BI-2014-01392N_0006.JPEG.
110. Morishita, T.; Aburai, K.; Sakai, K.; Abe, M.; Nakase, I.; Futaki, S.; Sakai, H.; Sakamoto, K. Key Process and Factors Controlling the Direct Translocation of Cell-Penetrating Peptide through Bio-Membrane. *Int J Mol Sci* **2020**, *21*, 1–18, doi:10.3390/IJMS21155466.
111. Takechi, Y.; Mizuguchi, C.; Tanaka, M.; Kawakami, T.; Aimoto, S.; Okamura, E.; Saito, H. Physicochemical Mechanism for the Lipid Membrane Binding of Polyarginine: The Favorable Enthalpy Change with Structural Transition from Random Coil to α-Helix. *Chem Lett* **2012**, *41*, 1374–1376, doi:10.1246/CL.2012.1374.
112. Rothbard, J.B.; Jessop, T.C.; Lewis, R.S.; Murray, B.A.; Wender, P.A. Role of Membrane Potential and Hydrogen Bonding in the Mechanism of Translocation of Guanidinium-Rich Peptides into Cells. *J Am Chem Soc* **2004**, *126*, 9506–9507, doi:10.1021/JA0482536/SUPPL_FILE/JA0482536SI20040610_011835.PDF.
113. Herce, H.D.; Garcia, A.E.; Litt, J.; Kane, R.S.; Martin, P.; Enrique, N.; Rebolledo, A.; Milesi, V. Arginine-Rich Peptides Destabilize the Plasma Membrane, Consistent with a

Pore Formation Translocation Mechanism of Cell-Penetrating Peptides. *Biophys J* **2009**, *97*, 1917–1925, doi:10.1016/J.BPJ.2009.05.066.
114. Yang, L.; Harroun, T.A.; Weiss, T.M.; Ding, L.; Huang, H.W. Barrel-Stave Model or Toroidal Model? A Case Study on Melittin Pores. *Biophys J* **2001**, *81*, 1475, doi:10.1016/S0006-3495(01)75802-X.
115. Sengupta, D.; Leontiadou, H.; Mark, A.E.; Marrink, S.J. Toroidal Pores Formed by Antimicrobial Peptides Show Significant Disorder. *Biochimica et Biophysica Acta (BBA) - Biomembranes* **2008**, *1778*, 2308–2317, doi:10.1016/J.BBAMEM.2008.06.007.
116. Xie, J.; Bi, Y.; Zhang, H.; Dong, S.; Teng, L.; Lee, R.J.; Yang, Z. Cell-Penetrating Peptides in Diagnosis and Treatment of Human Diseases: From Preclinical Research to Clinical Application. *Front Pharmacol* **2020**, *11*, doi:10.3389/FPHAR.2020.00697/FULL.
117. Ruseska, I.; Zimmer, A. Internalization Mechanisms of Cell-Penetrating Peptides. *Beilstein Journal of Nanotechnology* **2020**, *11*, 101, doi:10.3762/BJNANO.11.10.
118. Kawamoto, S.; Takasu, M.; Miyakawa, T.; Morikawa, R.; Oda, T.; Futaki, S.; Nagao, H. Inverted Micelle Formation of Cell-Penetrating Peptide Studied by Coarse-Grained Simulation: Importance of Attractive Force between Cell-Penetrating Peptides and Lipid Head Group. *J Chem Phys* **2011**, *134*, doi:10.1063/1.3555531.
119. LeCher, J.C.; Nowak, S.J.; McMurry, J.L. Breaking in and Busting out: Cell-Penetrating Peptides and the Endosomal Escape Problem. *Biomol Concepts* **2017**, *8*, 131–141, doi:10.1515/BMC-2017-0023/ASSET/GRAPHIC/J_BMC-2017-0023_FIG_002.JPG.
120. Wadia, J.S.; Stan, R. V.; Dowdy, S.F. Transducible TAT-HA Fusogenic Peptide Enhances Escape of TAT-Fusion Proteins after Lipid Raft Macropinocytosis. *Nature Medicine 2004 10:3* **2004**, *10*, 310–315, doi:10.1038/nm996.
121. Lönn, P.; Kacsinta, A.D.; Cui, X.S.; Hamil, A.S.; Kaulich, M.; Gogoi, K.; Dowdy, S.F. Enhancing Endosomal Escape for Intracellular Delivery of Macromolecular Biologic Therapeutics. *Sci Rep* **2016**, *6*, doi:10.1038/SREP32301.
122. Sahni, A.; Qian, Z.; Pei, D. Cell-Penetrating Peptides Escape the Endosome by Inducing Vesicle Budding and Collapse. *ACS Chem Biol* **2020**, *15*, 2485, doi:10.1021/ACSCHEMBIO.0C00478.
123. Chen, C.H.; Lu, T.K. Development and Challenges of Antimicrobial Peptides for Therapeutic Applications. *Antibiotics* **2020**, *9*, 24, doi:10.3390/ANTIBIOTICS9010024.
124. Rima, M.; Rima, M.; Fajloun, Z.; Sabatier, J.M.; Bechinger, B.; Naas, T. Antimicrobial Peptides: A Potent Alternative to Antibiotics. *Antibiotics (Basel)* **2021**, *10*, doi:10.3390/ANTIBIOTICS10091095.
125. Huan, Y.; Kong, Q.; Mou, H.; Yi, H. Antimicrobial Peptides: Classification, Design, Application and Research Progress in Multiple Fields. *Front Microbiol* **2020**, *11*, 582779, doi:10.3389/FMICB.2020.582779/BIBTEX.
126. Harris, F.; Dennison, S.; Phoenix, D. Anionic Antimicrobial Peptides from Eukaryotic Organisms. *Curr Protein Pept Sci* **2009**, *10*, 585–606, doi:10.2174/138920309789630589.
127. Cole, J.N.; Nizet, V. Bacterial Evasion of Host Antimicrobial Peptide Defenses. *Microbiol Spectr* **2016**, *4*, 10.1128/microbiolspec.VMBF-0006–2015, doi:10.1128/MICROBIOLSPEC.VMBF-0006-2015.
128. Bechinger, B.; Gorr, S.U. Antimicrobial Peptides: Mechanisms of Action and Resistance. *J Dent Res* **2016**, *96*, 254, doi:10.1177/0022034516679973.

129. K R, G.; Balenahalli Narasingappa, R.; Vishnu Vyas, G. Unveiling Mechanisms of Antimicrobial Peptide: Actions beyond the Membranes Disruption. *Heliyon* **2024**, *10*, e38079, doi:10.1016/J.HELIYON.2024.E38079.
130. Mangano, K.; Florin, T.; Shao, X.; Klepacki, D.; Chelysheva, I.; Ignatova, Z.; Gao, Y.; Mankin, A.S.; Vázquez-Laslop, N. Genome-Wide Effects of the Antimicrobial Peptide Apidaecin on Translation Termination in Bacteria. *Elife* **2020**, *9*, e62655, doi:10.7554/ELIFE.62655.
131. Zhang, Q.Y.; Yan, Z. Bin; Meng, Y.M.; Hong, X.Y.; Shao, G.; Ma, J.J.; Cheng, X.R.; Liu, J.; Kang, J.; Fu, C.Y. Antimicrobial Peptides: Mechanism of Action, Activity and Clinical Potential. *Military Medical Research 2021 8:1* **2021**, *8*, 1–25, doi:10.1186/S40779-021-00343-2.
132. Travkova, O.G.; Moehwald, H.; Brezesinski, G. The Interaction of Antimicrobial Peptides with Membranes. *Adv Colloid Interface Sci* **2017**, *247*, 521–532, doi:10.1016/J.CIS.2017.06.001.
133. Espeche, J.C.; Varas, R.; Maturana, P.; Cutro, A.C.; Maffía, P.C.; Hollmann, A. Membrane Permeability and Antimicrobial Peptides: Much More than Just Making a Hole. *Peptide Science* **2024**, *116*, e24305, doi:10.1002/PEP2.24305.
134. Mookherjee, N.; Anderson, M.A.; Haagsman, H.P.; Davidson, D.J. Antimicrobial Host Defence Peptides: Functions and Clinical Potential. *Nature Reviews Drug Discovery 2020 19:5* **2020**, *19*, 311–332, doi:10.1038/s41573-019-0058-8.
135. Hadjicharalambous, A.; Bournakas, N.; Newman, H.; Skynner, M.J.; Beswick, P. Antimicrobial and Cell-Penetrating Peptides: Understanding Penetration for the Design of Novel Conjugate Antibiotics. *Antibiotics* **2022**, *11*, 1636, doi:10.3390/ANTIBIOTICS11111636.
136. Bensch, K.W.; Raida, M.; Mägert, H.J.; Schulz-Knappe, P.; Forssmann, W.G. HBD-1: A Novel β-Defensin from Human Plasma. *FEBS Lett* **1995**, *368*, 331–335, doi:10.1016/0014-5793(95)00687-5.
137. Larrick, J.W.; Hirata, M.; Shimomoura, Y.; Yoshida, M.; Zheng, H.; Zhong, J.; Wright, S.C. Antimicrobial Activity of Rabbit CAP18-Derived Peptides. *Antimicrob Agents Chemother* **1993**, *37*, 2534–2539, doi:10.1128/AAC.37.12.2534.
138. Jung, Y.; Kong, B.; Moon, S.; Yu, S.H.; Chung, J.; Ban, C.; Chung, W.J.; Kim, S.G.; Kweon, D.H. Envelope-Deforming Antiviral Peptide Derived from Influenza Virus M2 Protein. *Biochem Biophys Res Commun* **2019**, *517*, 507–512, doi:10.1016/J.BBRC.2019.07.088.
139. Munshi, T.; Sparrow, A.; Wren, B.W.; Reljic, R.; Willcocks, S.J. The Antimicrobial Peptide, Bactenecin 5, Supports Cell-Mediated but Not Humoral Immunity in the Context of a Mycobacterial Antigen Vaccine Model. *Antibiotics* **2020**, *9*, 926, doi:10.3390/ANTIBIOTICS9120926.
140. Wang, G. Structures of Human Host Defense Cathelicidin LL-37 and Its Smallest Antimicrobial Peptide KR-12 in Lipid Micelles. *Journal of Biological Chemistry* **2008**, *283*, 32637–32643, doi:10.1074/JBC.M805533200.
141. Fernandez-Rojo, M.A.; Deplazes, E.; Pineda, S.S.; Brust, A.; Marth, T.; Wilhelm, P.; Martel, N.; Ramm, G.A.; Mancera, R.L.; Alewood, P.F.; et al. Gomesin Peptides Prevent Proliferation and Lead to the Cell Death of Devil Facial Tumour Disease Cells. *Cell Death Discovery 2018 4:1* **2018**, *4*, 1–11, doi:10.1038/s41420-018-0030-0.
142. Kravchenko, S. V.; Domnin, P.A.; Grishin, S.Y.; Zakhareva, A.P.; Zakharova, A.A.; Mustaeva, L.G.; Gorbunova, E.Y.; Kobyakova, M.I.; Surin, A.K.; Poshvina, D. V.; et al. Optimizing Antimicrobial Peptide Design: Integration of Cell-Penetrating Peptides,

Amyloidogenic Fragments, and Amino Acid Residue Modifications. *Int J Mol Sci* **2024**, *25*, 6030, doi:10.3390/IJMS25116030/S1.

143. Ma, X.; Aminov, R.; Franco, O.L.; de la Fuente-Nunez, C.; Wang, G.; Wang, J. Editorial: Antimicrobial Peptides and Their Druggability, Bio-Safety, Stability, and Resistance. *Front Microbiol* **2024**, *15*, doi:10.3389/FMICB.2024.1425952.
144. Chen, E.H.L.; Weng, C.W.; Li, Y.M.; Wu, M.C.; Yang, C.C.; Lee, K.T.; Chen, R.P.Y.; Cheng, C.P. De Novo Design of Antimicrobial Peptides With a Special Charge Pattern and Their Application in Combating Plant Pathogens. *Front Plant Sci* **2021**, *12*, 753217, doi:10.3389/FPLS.2021.753217/BIBTEX.
145. Lu, J.; Xu, H.; Xia, J.; Ma, J.; Xu, J.; Li, Y.; Feng, J. D- and Unnatural Amino Acid Substituted Antimicrobial Peptides With Improved Proteolytic Resistance and Their Proteolytic Degradation Characteristics. *Front Microbiol* **2020**, *11*, 563030, doi:10.3389/FMICB.2020.563030/FULL.
146. López-Sanmartín, M.; Rengel, R.; López-López, M.; Lebrón, J.A.; Molina-Márquez, A.; de la Rosa, I.; López-Cornejo, P.; Cuesta, A.; Vigara, J.; León, R. D-Amino Acid Peptides as Antimicrobial Agents against Vibrio-Associated Diseases in Aquaculture. *Aquaculture* **2023**, *569*, 739362, doi:10.1016/J.AQUACULTURE.2023.739362.
147. Han, Y.; Zhang, M.; Lai, R.; Zhang, Z. Chemical Modifications to Increase the Therapeutic Potential of Antimicrobial Peptides. *Peptides (N.Y.)* **2021**, *146*, 170666, doi:10.1016/J.PEPTIDES.2021.170666.
148. Chunarkar-Patil, P.; Kaleem, M.; Mishra, R.; Ray, S.; Ahmad, A.; Verma, D.; Bhayye, S.; Dubey, R.; Singh, H.N.; Kumar, S. Anticancer Drug Discovery Based on Natural Products: From Computational Approaches to Clinical Studies. *Biomedicines 2024, Vol. 12, Page 201* **2024**, *12*, 201, doi:10.3390/BIOMEDICINES12010201.
149. Nejadmoghaddam, M.R.; Minai-Tehrani, A.; Ghahremanzadeh, R.; Mahmoudi, M.; Dinarvand, R.; Zarnani, A.H. Antibody-Drug Conjugates: Possibilities and Challenges. *Avicenna J Med Biotechnol* **2019**, *11*, 3.
150. Mckertish, C.M.; Kayser, V. Advances and Limitations of Antibody Drug Conjugates for Cancer. *Biomedicines* **2021**, *9*, doi:10.3390/BIOMEDICINES9080872.
151. Wang, M.; Liu, J.; Xia, M.; Yin, L.; Zhang, L.; Liu, X.; Cheng, Y. Peptide-Drug Conjugates: A New Paradigm for Targeted Cancer Therapy. *Eur J Med Chem* **2024**, *265*, 116119, doi:10.1016/J.EJMECH.2023.116119.
152. Singh, T.; Kim, T.W.; Murthy, A.S.N.; Paul, M.; Sepay, N.; Jeong Kong, H.; Sung Ryu, J.; Rim Koo, N.; Yoon, S.; Song, K.H.; et al. Tumor–Homing Peptide IRGD-Conjugate Enhances Tumor Accumulation of Camptothecin for Colon Cancer Therapy. *Eur J Med Chem* **2024**, *265*, 116050, doi:10.1016/J.EJMECH.2023.116050.
153. Kondo, E.; Iioka, H.; Saito, K. Tumor-homing Peptide and Its Utility for Advanced Cancer Medicine. *Cancer Sci* **2021**, *112*, 2118, doi:10.1111/CAS.14909.
154. Alas, M.; Saghaeidehkordi, A.; Kaur, K. Peptide-Drug Conjugates with Different Linkers for Cancer Therapy. *J Med Chem* **2020**, *64*, 216, doi:10.1021/ACS.JMEDCHEM.0C01530.
155. Weissman, M.R.; Winger, K.T.; Ghiassian, S.; Gobbo, P.; Workentin, M.S. Insights on the Application of the Retro Michael-Type Addition on Maleimide-Functionalized Gold Nanoparticles in Biology and Nanomedicine. *Bioconjug Chem* **2016**, *27*, 586–593, doi:10.1021/ACS.BIOCONJCHEM.5B00600/ASSET/IMAGES/LARGE/BC-2015-00600N_0002.JPEG.

156. Hossein-Nejad-Ariani, H.; Althagafi, E.; Kaur, K. Small Peptide Ligands for Targeting EGFR in Triple Negative Breast Cancer Cells. *Sci Rep* **2019**, *9*, 2723, doi:10.1038/S41598-019-38574-Y.
157. Lingasamy, P.; Tobi, A.; Kurm, K.; Kopanchuk, S.; Sudakov, A.; Salumäe, M.; Rätsep, T.; Asser, T.; Bjerkvig, R.; Teesalu, T. Tumor-Penetrating Peptide for Systemic Targeting of Tenascin-C. *Scientific Reports 2020 10:1* **2020**, *10*, 1–13, doi:10.1038/s41598-020-62760-y.
158. Okur, A.C.; Erkoc, P.; Kizilel, S. Targeting Cancer Cells via Tumor-Homing Peptide CREKA Functional PEG Nanoparticles. *Colloids Surf B Biointerfaces* **2016**, *147*, 191–200, doi:10.1016/J.COLSURFB.2016.08.005.
159. Gayraud, F.; Klußmann, M.; Neundorf, I. Recent Advances and Trends in Chemical CPP–Drug Conjugation Techniques. *Molecules* **2021**, *26*, 1591, doi:10.3390/MOLECULES26061591.
160. Rinaldi, A.; Caraffi, R.; Grazioli, M.V.; Oddone, N.; Giardino, L.; Tosi, G.; Vandelli, M.A.; Calzà, L.; Ruozi, B.; Duskey, J.T. Applications of the ROS-Responsive Thioketal Linker for the Production of Smart Nanomedicines. *Polymers (Basel)* **2022**, *14*, 687, doi:10.3390/POLYM14040687.
161. Corrie, P.G. Cytotoxic Chemotherapy: Clinical Aspects. *Medicine* **2008**, *36*, 24–28, doi:10.1016/J.MPMED.2007.10.012.
162. Noble, S.; Goa, K.L. Gemcitabine. A Review of Its Pharmacology and Clinical Potential in Non-Small Cell Lung Cancer and Pancreatic Cancer. *Drugs* **1997**, *54*, 447–472, doi:10.2165/00003495-199754030-00009.
163. Kaveh Zenjanab, M.; Alimohammadvand, S.; Doustmihan, A.; Kianian, S.; Sadeghzadeh Oskouei, B.; Mazloomi, M.; Akbari, M.; Jahanban-Esfahlan, R. Paclitaxel for Breast Cancer Therapy: A Review on Effective Drug Combination Modalities and Nano Drug Delivery Platforms. *J Drug Deliv Sci Technol* **2024**, *95*, 105567, doi:10.1016/J.JDDST.2024.105567.
164. Linders, A.N.; Dias, I.B.; López Fernández, T.; Tocchetti, C.G.; Bomer, N.; Van der Meer, P. A Review of the Pathophysiological Mechanisms of Doxorubicin-Induced Cardiotoxicity and Aging. *npj Aging 2024 10:1* **2024**, *10*, 1–9, doi:10.1038/s41514-024-00135-7.
165. Hulst, M.B.; Zhang, L.; van der Heul, H.U.; Du, C.; Elsayed, S.S.; Koroleva, A.; Grocholski, T.; Wander, D.P.A.; Metsä-Ketelä, M.; Neefjes, J.J.C.; et al. Metabolic Engineering of Streptomyces Peucetius for Biosynthesis of N,N-Dimethylated Anthracyclines. *Front Bioeng Biotechnol* **2024**, *12*, 1363803, doi:10.3389/FBIOE.2024.1363803/BIBTEX.
166. Huang, C.; Guo, Y.; Li, T.; Sun, G.; Yang, J.; Wang, Y.; Xiang, Y.; Wang, L.; Jin, M.; Li, J.; et al. Pharmacological Activation of GPX4 Ameliorates Doxorubicin-Induced Cardiomyopathy. *Redox Biol* **2024**, *70*, 103024, doi:10.1016/J.REDOX.2023.103024.
167. Stillger, K.; Neundorf, I. Cell-Permeable Peptide-Based Delivery Vehicles Useful for Subcellular Targeting and Beyond. *Cell Signal* **2023**, *109*, 110796, doi:10.1016/J.CELLSIG.2023.110796.
168. Kardani, K.; Milani, A.; H. Shabani, S.; Bolhassani, A. Cell Penetrating Peptides: The Potent Multi-Cargo Intracellular Carriers. *Expert Opin Drug Deliv* **2019**, *16*, 1227–1258, doi:10.1080/17425247.2019.1676720.
169. Lu, J.; Wu, T.; Zhang, B.; Liu, S.; Song, W.; Qiao, J.; Ruan, H. Types of Nuclear Localization Signals and Mechanisms of Protein Import into the Nucleus. *Cell*

Communication and Signaling **2021**, *19*, 1–10, doi:10.1186/S12964-021-00741-Y/FIGURES/1.

170. Makkerh, J.P.S.; Dingwall, C.; Laskey, R.A. Comparative Mutagenesis of Nuclear Localization Signals Reveals the Importance of Neutral and Acidic Amino Acids. *Curr Biol* **1996**, *6*, 1025–1027, doi:10.1016/S0960-9822(02)00648-6.
171. Suomalainen, A.; Battersby, B.J. Mitochondrial Diseases: The Contribution of Organelle Stress Responses to Pathology. *Nature Reviews Molecular Cell Biology 2017 19:2* **2017**, *19*, 77–92, doi:10.1038/nrm.2017.66.
172. Russell, O.M.; Gorman, G.S.; Lightowlers, R.N.; Turnbull, D.M. Mitochondrial Diseases: Hope for the Future. *Cell* **2020**, *181*, 168–188, doi:10.1016/J.CELL.2020.02.051.
173. Taanman, J.W. The Mitochondrial Genome: Structure, Transcription, Translation and Replication. *Biochimica et Biophysica Acta (BBA) - Bioenergetics* **1999**, *1410*, 103–123, doi:10.1016/S0005-2728(98)00161-3.
174. Schmidt, O.; Pfanner, N.; Meisinger, C. Mitochondrial Protein Import: From Proteomics to Functional Mechanisms. *Nature Reviews Molecular Cell Biology 2010 11:9* **2010**, *11*, 655–667, doi:10.1038/nrm2959.
175. Klimpel, A.; Neundorf, I. Bifunctional Peptide Hybrids Targeting the Matrix of Mitochondria. *Journal of Controlled Release* **2018**, *291*, 147–156, doi:10.1016/J.JCONREL.2018.10.029.
176. Khan, T.; Waseem, R.; Zehra, Z.; Aiman, A.; Bhardwaj, P.; Ansari, J.; Hassan, Md.I.; Islam, A. Mitochondrial Dysfunction: Pathophysiology and Mitochondria-Targeted Drug Delivery Approaches. *Pharmaceutics 2022, Vol. 14, Page 2657* **2022**, *14*, 2657, doi:10.3390/PHARMACEUTICS14122657.
177. Benjamin, D.I.; Cozzo, A.; Ji, X.; Roberts, L.S.; Louie, S.M.; Mulvihill, M.M.; Luo, K.; Nomura, D.K. Ether Lipid Generating Enzyme AGPS Alters the Balance of Structural and Signaling Lipids to Fuel Cancer Pathogenicity. *Proc Natl Acad Sci U S A* **2013**, *110*, 14912–14917, doi:10.1073/PNAS.1310894110/SUPPL_FILE/SD01.XLSX.
178. Kumar, R.; Islinger, M.; Worthy, H.; Carmichael, R.; Schrader, M. The Peroxisome: An Update on Mysteries 3.0. *Histochemistry and Cell Biology 2024 161:2* **2024**, *161*, 99–132, doi:10.1007/S00418-023-02259-5.
179. Alberts, B.; Johnson, A.; Lewis, J.; Raff, M.; Roberts, K.; Walter, P. Peroxisomes. **2002**.
180. Smith, J.J.; Aitchison, J.D. Peroxisomes Take Shape. *Nat Rev Mol Cell Biol* **2013**, *14*, 803, doi:10.1038/NRM3700.
181. Titorenko, V.I.; Rachubinski, R.A. The Life Cycle of the Peroxisome. *Nature Reviews Molecular Cell Biology 2001 2:5* **2001**, *2*, 357–368, doi:10.1038/35073063.
182. Kim, P.K.; Hettema, E.H. Multiple Pathways for Protein Transport to Peroxisomes. *J Mol Biol* **2015**, *427*, 1176, doi:10.1016/J.JMB.2015.02.005.
183. Kempiński, B.; Chełstowska, A.; Poznański, J.; Król, K.; Rymer, Ł.; Frydzińska, Z.; Girzalsky, W.; Skoneczna, A.; Erdmann, R.; Skoneczny, M. The Peroxisomal Targeting Signal 3 (PTS3) of the Budding Yeast Acyl-CoA Oxidase Is a Signal Patch. *Front Cell Dev Biol* **2020**, *8*, 198, doi:10.3389/FCELL.2020.00198/FULL.
184. Olivier, L.M.; Krisans, S.K. Peroxisomal Protein Targeting and Identification of Peroxisomal Targeting Signals in Cholesterol Biosynthetic Enzymes. *Biochimica et Biophysica Acta (BBA) - Molecular and Cell Biology of Lipids* **2000**, *1529*, 89–102, doi:10.1016/S1388-1981(00)00139-6.
185. Williams, C.P.; Schueller, N.; Thompson, C.A.; Van Den Berg, M.; Van Haren, S.D.; Erdmann, R.; Bond, C.S.; Distel, B.; Schliebs, W.; Wilmanns, M.; et al. The Peroxisomal

Targeting Signal 1 in Sterol Carrier Protein 2 Is Autonomous and Essential for Receptor Recognition. *BMC Biochem* **2011**, *12*, 1–8, doi:10.1186/1471-2091-12-12/TABLES/5.
186. Kunze, M. The Type-2 Peroxisomal Targeting Signal. *Biochimica et Biophysica Acta (BBA) - Molecular Cell Research* **2020**, *1867*, 118609, doi:10.1016/J.BBAMCR.2019.118609.
187. Johnson, T.L.; Olsen, L.J. Import of the Peroxisomal Targeting Signal Type 2 Protein 3-Ketoacyl-Coenzyme A Thiolase into Glyoxysomes. *Plant Physiol* **2003**, *133*, 1991, doi:10.1104/PP.103.028217.
188. Gao, Y.; Skowyra, M.L.; Feng, P.; Rapoport, T.A. Protein Import into Peroxisomes Occurs through a Nuclear Pore-like Phase. *Science* **2022**, *378*, eadf3971, doi:10.1126/SCIENCE.ADF3971.
189. Lanyon-Hogg, T.; Warriner, S.L.; Baker, A. Getting a Camel through the Eye of a Needle: The Import of Folded Proteins by Peroxisomes. *Biol Cell* **2010**, *102*, 245–263, doi:10.1042/BC20090159.
190. Carvalho, A.F.; Pinto, M.P.; Grou, C.P.; Alencastre, I.S.; Fransen, M.; Sá-Miranda, C.; Azevedo, J.E. Ubiquitination of Mammalian Pex5p, the Peroxisomal Import Receptor. *Journal of Biological Chemistry* **2007**, *282*, 31267–31272, doi:10.1074/JBC.M706325200.
191. Platta, H.W.; El Magraoui, F.; Bäumer, B.E.; Schlee, D.; Girzalsky, W.; Erdmann, R. Pex2 and Pex12 Function as Protein-Ubiquitin Ligases in Peroxisomal Protein Import. *Mol Cell Biol* **2009**, *29*, 5505, doi:10.1128/MCB.00388-09.
192. Wang, W.; Subramani, S. Role of PEX5 Ubiquitination in Maintaining Peroxisome Dynamics and Homeostasis. *Cell Cycle* **2017**, *16*, 2037–2045, doi:10.1080/15384101.2017.1376149.
193. Gardner, B.M.; Castanzo, D.T.; Chowdhury, S.; Stjepanovic, G.; Stefely, M.S.; Hurley, J.H.; Lander, G.C.; Martin, A. The Peroxisomal AAA-ATPase Pex1/Pex6 Unfolds Substrates by Processive Threading. *Nature Communications 2018 9:1* **2018**, *9*, 1–15, doi:10.1038/s41467-017-02474-4.
194. Rodrigues, T.A.; Francisco, T.; Carvalho, A.F.; Pinto, M.P.; Grou, C.P.; Azevedo, J.E. Factors Involved in Ubiquitination and Deubiquitination of PEX5, the Peroxisomal Shuttling Receptor. *Molecular Machines Involved in Peroxisome Biogenesis and Maintenance* **2014**, 371–388, doi:10.1007/978-3-7091-1788-0_16.
195. Rodrigues, T.A.; Grou, C.P.; Azevedo, J.E. Revisiting the Intraperoxisomal Pathway of Mammalian PEX7. *Scientific Reports 2015 5:1* **2015**, *5*, 1–12, doi:10.1038/srep11806.
196. Reinhardt, A.; Horn, M.; Pieper Gen Schmauck, J.; Bröhl, A.; Giernoth, R.; Oelkrug, C.; Schubert, A.; Neundorf, I. Novel Imidazolium Salt--Peptide Conjugates and Their Antimicrobial Activity. *Bioconjug Chem* **2014**, *25*, 2166–2174, doi:10.1021/BC500510C.
197. Gronewold, A.; Horn, M.; Neundorf, I. Design and Biological Characterization of Novel Cell-Penetrating Peptides Preferentially Targeting Cell Nuclei and Subnuclear Regions. *Beilstein Journal of Organic Chemistry* **2018**, *14*, 1378, doi:10.3762/BJOC.14.116.
198. Feni, L.; Parente, S.; Robert, C.; Gazzola, S.; Arosio, D.; Piarulli, U.; Neundorf, I. Kiss and Run: Promoting Effective and Targeted Cellular Uptake of a Drug Delivery Vehicle Composed of an Integrin-Targeting Diketopiperazine Peptidomimetic and a Cell-Penetrating Peptide. *Bioconjug Chem* **2019**, *30*, 2011–2022, doi:10.1021/ACS.BIOCONJCHEM.9B00292/SUPPL_FILE/BC9B00292_LIVESLIDES.MP4.

199. Hoyer, J.; Schatzschneider, U.; Schulz-Siegmund, M.; Neundorf, I. Dimerization of a Cell-Penetrating Peptide Leads to Enhanced Cellular Uptake and Drug Delivery. *Beilstein journal of organic chemistry* **2012**, *8*, 1788–1797, doi:10.3762/BJOC.8.204.
200. Gronewold, A.; Horn, M.; Ranđelović, I.; Tóvári, J.; Muñoz Vázquez, S.; Schomäcker, K.; Neundorf, I. Characterization of a Cell-Penetrating Peptide with Potential Anticancer Activity. *ChemMedChem* **2016**, *12*, 42, doi:10.1002/CMDC.201600498.
201. Haseloer, A.; Lützenburg, T.; Strache, J.P.; Neudörfl, J.; Neundorf, I.; Klein, A. Building up PtII−Thiosemicarbazone−Lysine−sC18 Conjugates. *ChemBioChem* **2021**, *22*, 694–704, doi:10.1002/CBIC.202000564.
202. Drexelius, M.; Arnold, R.; Meinberger, D.; Wilhelm, M.; Mathur, S.; Neundorf, I. Rational Design of Bifunctional Chimeric Peptides That Combine Antimicrobial and Titanium Binding Activity. *Journal of Peptide Science* **2023**, *29*, e3481, doi:10.1002/PSC.3481.
203. Abramson, J.; Adler, J.; Dunger, J.; Evans, R.; Green, T.; Pritzel, A.; Ronneberger, O.; Willmore, L.; Ballard, A.J.; Bambrick, J.; et al. Accurate Structure Prediction of Biomolecular Interactions with AlphaFold 3. *Nature 2024 630:8016* **2024**, *630*, 493–500, doi:10.1038/s41586-024-07487-w.
204. Grabeck, J.; Lützenburg, T.; Frommelt, P.; Neundorf, I. Comparing Variants of the Cell-Penetrating Peptide SC18 to Design Peptide-Drug Conjugates. *Molecules* **2022**, *27*, doi:10.3390/MOLECULES27196656.
205. Grabeck, J.; Mayer, J.; Miltz, A.; Casoria, M.; Quagliata, M.; Meinberger, D.; Klatt, A.R.; Wielert, I.; Maier, B.; Papini, A.M.; et al. Triazole-Bridged Peptides with Enhanced Antimicrobial Activity and Potency against Pathogenic Bacteria. *ACS Infect Dis* **2024**, *10*, 2717–2727, doi:10.1021/ACSINFECDIS.4C00078.
206. Lützenburg, T. Intrinsic and Extrinsic Approaches to Modulate the Structure-Activity Relationship of Cell-Penetrating Peptides. **2021**.
207. Gessner, I.; Klimpel, A.; Klußmann, M.; Neundorf, I.; Mathur, S. Interdependence of Charge and Secondary Structure on Cellular Uptake of Cell Penetrating Peptide Functionalized Silica Nanoparticles. *Nanoscale Adv* **2020**, *2*, 453–462, doi:10.1039/C9NA00693A.
208. Klimpel, A.; Stillger, K.; Wiederstein, J.L.; Krüger, M.; Neundorf, I. Cell-Permeable CaaX-Peptides Affect K-Ras Downstream Signaling and Promote Cell Death in Cancer Cells. *FEBS J* **2021**, *288*, 2911–2929, doi:10.1111/FEBS.15612.
209. Rajan, R.; Balaram, P. A Model for the Interaction of Trifluoroethanol with Peptides and Proteins. *Int J Pept Protein Res* **1996**, *48*, 328–336, doi:10.1111/J.1399-3011.1996.TB00849.X.
210. Drexelius, M.; Reinhardt, A.; Grabeck, J.; Cronenberg, T.; Nitsche, F.; Huesgen, P.F.; Maier, B.; Neundorf, I. Multistep Optimization of a Cell-Penetrating Peptide towards Its Antimicrobial Activity. *Biochemical Journal* **2021**, *478*, 63–78, doi:10.1042/BCJ20200698.
211. Wang, X.; Hui, R.; Chen, Y.; Wang, W.; Chen, Y.; Gong, X.; Jin, J. Discovery of Novel Doxorubicin Metabolites in MCF7 Doxorubicin-Resistant Cells. *Front Pharmacol* **2019**, *10*, 1434, doi:10.3389/FPHAR.2019.01434.
212. Halaby, R. Influence of Lysosomal Sequestration on Multidrug Resistance in Cancer Cells. *Cancer Drug Resistance* **2019**, *2*, 31, doi:10.20517/CDR.2018.23.
213. Braverman, N.E.; Raymond, G. V.; Rizzo, W.B.; Moser, A.B.; Wilkinson, M.E.; Stone, E.M.; Steinberg, S.J.; Wangler, M.F.; Rush, E.T.; Hacia, J.G.; et al. Peroxisome Biogenesis Disorders in the Zellweger Spectrum: An Overview of Current Diagnosis,

Clinical Manifestations, and Treatment Guidelines. *Mol Genet Metab* **2015**, *117*, 313, doi:10.1016/J.YMGME.2015.12.009.
214. Klimpel, A.; Neundorf, I. Bifunctional Peptide Hybrids Targeting the Matrix of Mitochondria. *Journal of Controlled Release* **2018**, *291*, 147–156, doi:10.1016/J.JCONREL.2018.10.029.
215. Drexelius, M.G. Development and Application of Antimicrobial Peptides Based on SC18 to Fight Antibiotic Resistance and Bacterial Adhesion. **2023**.
216. Meindl-Beinker, N.M.; Lundin, C.; Nilsson, I.M.; White, S.H.; von Heijne, G. Asn- and Asp-Mediated Interactions between Transmembrane Helices during Translocon-Mediated Membrane Protein Assembly. *EMBO Rep* **2006**, *7*, 1111, doi:10.1038/SJ.EMBOR.7400818.
217. Thomas, F.; Niitsu, A.; Oregioni, A.; Bartlett, G.J.; Woolfson, D.N. Conformational Dynamics of Asparagine at Coiled-Coil Interfaces. *Biochemistry* **2017**, *56*, 6544–6554, doi:10.1021/ACS.BIOCHEM.7B00848/ASSET/IMAGES/LARGE/BI-2017-00848K_0005.JPEG.
218. Assoni, L.; Milani, B.; Carvalho, M.R.; Nepomuceno, L.N.; Waz, N.T.; Guerra, M.E.S.; Converso, T.R.; Darrieux, M. Resistance Mechanisms to Antimicrobial Peptides in Gram-Positive Bacteria. *Front Microbiol* **2020**, *11*, 593215, doi:10.3389/FMICB.2020.593215.
219. Scrima, M.; Le Chevalier-Isaad, A.; Rovero, P.; Papini, A.M.; Chorev, M.; D'Ursi, A.M. CuI-Catalyzed Azide–Alkyne Intramolecular i-to-(I+4) Side-Chain-to-Side-Chain Cyclization Promotes the Formation of Helix-Like Secondary Structures. *European J Org Chem* **2010**, *2010*, 446–457, doi:10.1002/EJOC.200901157.
220. Meldal, M.; Tomøe, C.W. Cu-Catalyzed Azide - Alkyne Cycloaddition. *Chem Rev* **2008**, *108*, 2952–3015, doi:10.1021/CR0783479/ASSET/IMAGES/MEDIUM/CR-2007-083479_0069.GIF.
221. Nuti, F.; Larregola, M.; Staśkiewicz, A.; Retzl, B.; Tomašević, N.; Macchia, L.; Street, M.E.; Jewgiński, M.; Lequin, O.; Latajka, R.; et al. Design, Synthesis, Conformational Analysis, and Biological Activity of Cα1-to-Cα6 1,4- and 4,1-Disubstituted 1 H-[1,2,3]Triazol-1-Yl-Bridged Oxytocin Analogues. *J Enzyme Inhib Med Chem* **2023**, *38*, doi:10.1080/14756366.2023.2254019.
222. Hassan, M.F.; Qutb, A.M.; Dong, W. Prediction and Activity of a Cationic α-Helix Antimicrobial Peptide ZM-804 from Maize. *Int J Mol Sci* **2021**, *22*, 2643, doi:10.3390/IJMS22052643.
223. Mahlapuu, M.; Sidorowicz, A.; Mikosinski, J.; Krzyżanowski, M.; Orleanski, J.; Twardowska-Saucha, K.; Nykaza, A.; Dyaczynski, M.; Belz-Lagoda, B.; Dziwiszek, G.; et al. Evaluation of LL-37 in Healing of Hard-to-Heal Venous Leg Ulcers: A Multicentric Prospective Randomized Placebo-Controlled Clinical Trial. *Wound Repair Regen* **2021**, *29*, 938–950, doi:10.1111/WRR.12977.
224. Lin, X.; Wang, R.; Mai, S. Advances in Delivery Systems for the Therapeutic Application of LL37. *J Drug Deliv Sci Technol* **2020**, *60*, 102016, doi:10.1016/J.JDDST.2020.102016.
225. Wölk, C.; Youssef, H.; Guttenberg, T.; Marbach, H.; Vizcay-Barrena, G.; Shen, C.; Brezesinski, G.; Harvey, R.D. Phase Diagram for a Lysyl-Phosphatidylglycerol Analogue in Biomimetic Mixed Monolayers with Phosphatidylglycerol: Insights into the Tunable Properties of Bacterial Membranes. *ChemPhysChem* **2020**, *21*, 702–706, doi:10.1002/CPHC.202000026.

226. Tornesello, A.L.; Borrelli, A.; Buonaguro, L.; Buonaguro, F.M.; Tornesello, M.L. Antimicrobial Peptides as Anticancer Agents: Functional Properties and Biological Activities. *Molecules* **2020**, *25*, 2850, doi:10.3390/MOLECULES25122850.
227. Fernandes, H.P.; Cesar, C.L.; Barjas-Castro, M. de L. Electrical Properties of the Red Blood Cell Membrane and Immunohematological Investigation. *Rev Bras Hematol Hemoter* **2011**, *33*, 297, doi:10.5581/1516-8484.20110080.
228. Doti, N.; Mardirossian, M.; Sandomenico, A.; Ruvo, M.; Caporale, A. Recent Applications of Retro-Inverso Peptides. *Int J Mol Sci* **2021**, *22*, 8677, doi:10.3390/IJMS22168677.
229. Staśkiewicz, A.; Ledwoń, P.; Rovero, P.; Papini, A.M.; Latajka, R. Triazole-Modified Peptidomimetics: An Opportunity for Drug Discovery and Development. *Front Chem* **2021**, *9*, 674705, doi:10.3389/FCHEM.2021.674705/BIBTEX.
230. Wang, L.; Wang, N.; Zhang, W.; Cheng, X.; Yan, Z.; Shao, G.; Wang, X.; Wang, R.; Fu, C. Therapeutic Peptides: Current Applications and Future Directions. *Signal Transduction and Targeted Therapy 2022 7:1* **2022**, *7*, 1–27, doi:10.1038/s41392-022-00904-4.
231. Weissman, M.R.; Winger, K.T.; Ghiassian, S.; Gobbo, P.; Workentin, M.S. Insights on the Application of the Retro Michael-Type Addition on Maleimide-Functionalized Gold Nanoparticles in Biology and Nanomedicine. *Bioconjug Chem* **2016**, *27*, 586–593, doi:10.1021/ACS.BIOCONJCHEM.5B00600/ASSET/IMAGES/LARGE/BC-2015-00600N_0002.JPEG.
232. Lee, J.; Choi, M.K.; Song, I.S. Recent Advances in Doxorubicin Formulation to Enhance Pharmacokinetics and Tumor Targeting. *Pharmaceuticals 2023, Vol. 16, Page 802* **2023**, *16*, 802, doi:10.3390/PH16060802.
233. Valdiglesias, V.; Giunta, S.; Fenech, M.; Neri, M.; Bonassi, S. ΓH2AX as a Marker of DNA Double Strand Breaks and Genomic Instability in Human Population Studies. *Mutation Research/Reviews in Mutation Research* **2013**, *753*, 24–40, doi:10.1016/J.MRREV.2013.02.001.
234. Mozaffari, S.; Salehi, D.; Mahdipoor, P.; Beuttler, R.; Tiwari, R.; Aliabadi, H.M.; Parang, K. Design and Application of Hybrid Cyclic-Linear Peptide-Doxorubicin Conjugates as a Strategy to Overcome Doxorubicin Resistance and Toxicity. *Eur J Med Chem* **2021**, *226*, 113836, doi:10.1016/J.EJMECH.2021.113836.
235. Bryden, F.; Martin, C.; Letast, S.; Lles, E.; Viéitez-Villemin, I.; Rousseau, A.; Colas, C.; Brachet-Botineau, M.; Allard-Vannier, E.; Larbouret, C.; et al. Impact of Cathepsin B-Sensitive Triggers and Hydrophilic Linkers on in Vitro Efficacy of Novel Site-Specific Antibody-Drug Conjugates. *Org Biomol Chem* **2018**, *16*, 1882–1889, doi:10.1039/C7OB02780J.
236. Li, S.C.; Goto, N.K.; Williams, K.A.; Deber, C.M. Alpha-Helical, but Not Beta-Sheet, Propensity of Proline Is Determined by Peptide Environment. *Proc Natl Acad Sci U S A* **1996**, *93*, 6676, doi:10.1073/PNAS.93.13.6676.
237. Romei, M.G.; Boxer, S.G. Split Green Fluorescent Proteins: Scope, Limitations, and Outlook. *Annu Rev Biophys* **2019**, *48*, 19, doi:10.1146/ANNUREV-BIOPHYS-051013-022846.
238. Piano, V.; Benjamin, D.I.; Valente, S.; Nenci, S.; Marrocco, B.; Mai, A.; Aliverti, A.; Nomura, D.K.; Mattevi, A. Discovery of Inhibitors for the Ether Lipid-Generating Enzyme AGPS as Anti-Cancer Agents. *ACS Chem Biol* **2015**, *10*, 2589–2597, doi:10.1021/ACSCHEMBIO.5B00466/ASSET/IMAGES/LARGE/CB-2015-00466U_0006.JPEG.

239. Saffour, S.; AL-Sharabi, A.A.; Evren, A.E.; Cankiliç, M.Y.; Yurttaş, L. Antimicrobial Activity of Novel Substituted 1,2,4-Triazole and 1,3-Thiazole Derivatives. *J Mol Struct* **2024**, *1295*, 136675, doi:10.1016/J.MOLSTRUC.2023.136675.
240. Rodríguez-Gascón, A.; Solinís, M.Á.; Isla, A. The Role of PK/PD Analysis in the Development and Evaluation of Antimicrobials. *Pharmaceutics* **2021**, *13*, 833, doi:10.3390/PHARMACEUTICS13060833.

6. Appendix

6.1 Supplementary figures

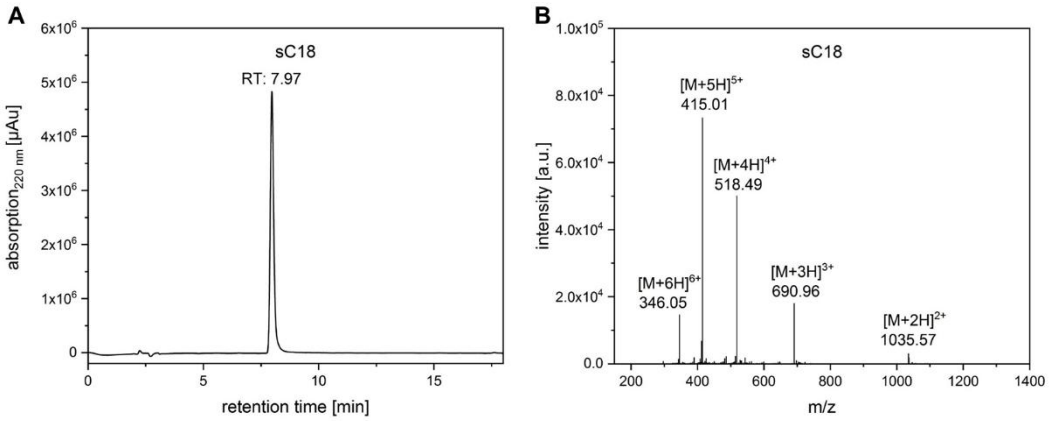

Figure S1. HPLC-ESI/MS analysis of purified sC18. A gradient of 10-60 % ACN with 0.1 % FA in 15 min was used for the HPLC. (A) UV-chromatogram of sC18. (B) Full scan of ESI/MS at a retention time of 7.97 min. Dr. Tamara Sasse kindly provided this analysis.[206]

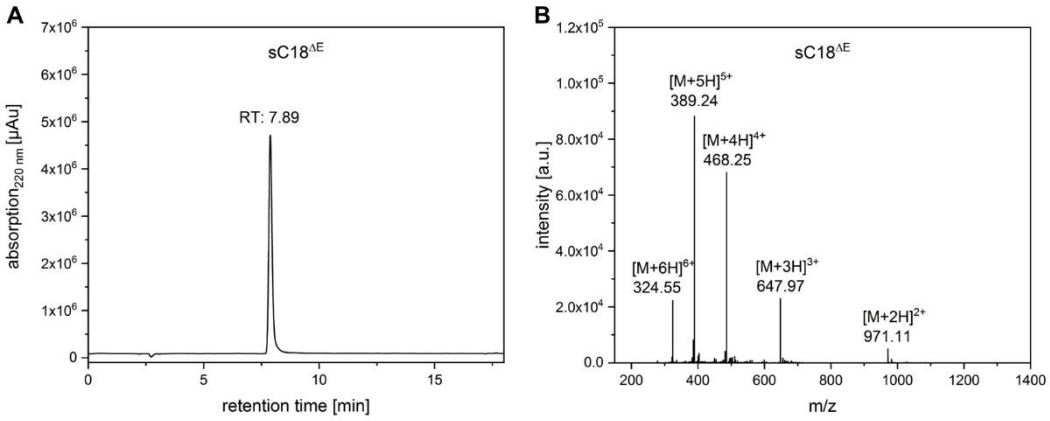

Figure S2. HPLC-ESI/MS analysis of purified sC18ΔE. A gradient of 10-60 % ACN with 0.1 % FA in 15 min was used for the HPLC. (A) UV-chromatogram of sC18ΔE. (B) Full scan of ESI/MS at a retention time of 7.89 min. Dr. Tamara Sasse kindly provided this analysis.[206]

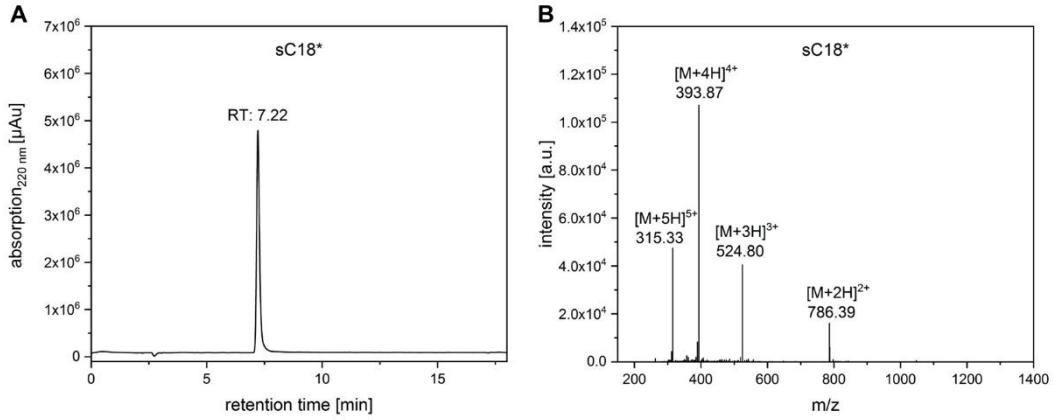

Figure S3. HPLC-ESI/MS analysis of purified sC18*. A gradient of 10-60 % ACN with 0.1 % FA in 15 min was used for the HPLC. (A) UV-chromatogram of sC18*. (B) Full scan of ESI/MS at a retention time of 7.22 min. Dr. Tamara Sasse kindly provided this analysis.[206]

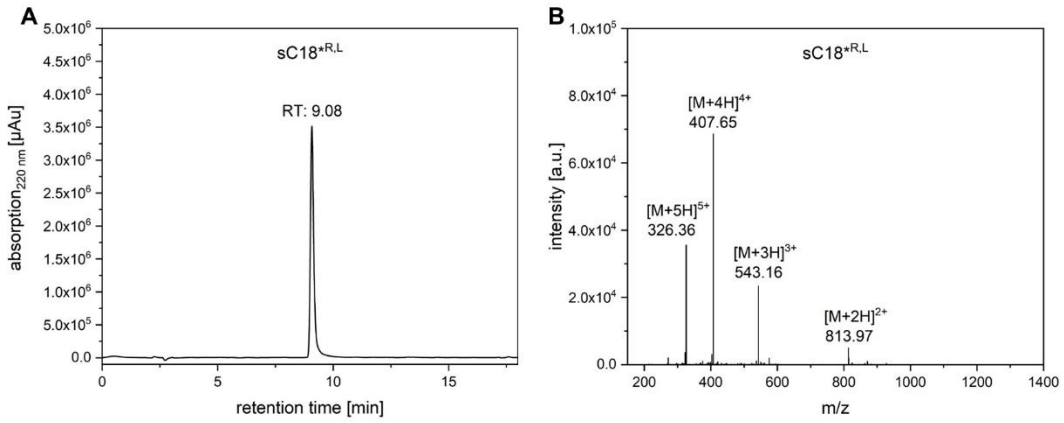

Figure S4. HPLC-ESI/MS analysis of purified sC18*R,L. A gradient of 10-60 % ACN with 0.1 % FA in 15 min was used for the HPLC. (A) UV-chromatogram of sC18*R,L. (B) Full scan of ESI/MS at a retention time of 9.08 min. Dr. Tamara Sasse kindly provided this analysis.[206]

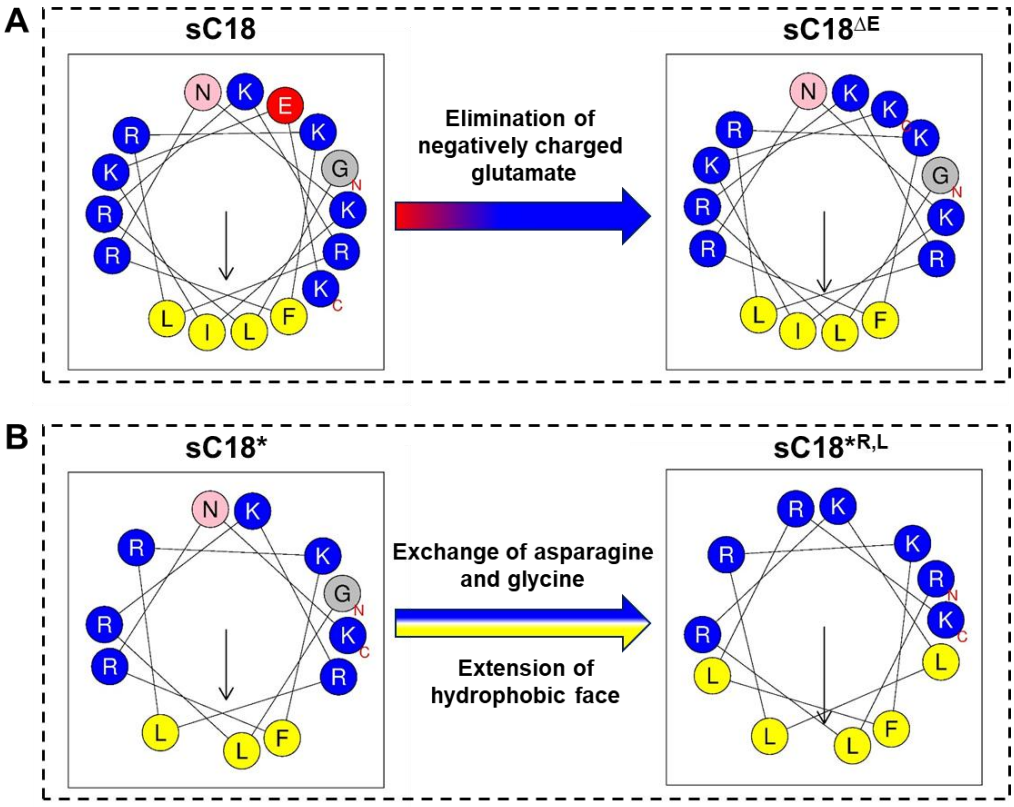

Figure S5. Helical Wheel projection of either (A) glutamate deletion in sC18 or (B) amino acid exchange of truncated version sC18* leading to sC18ΔE and sC18*R,L kindly provided by Dr. Tamara Sasse.[206]

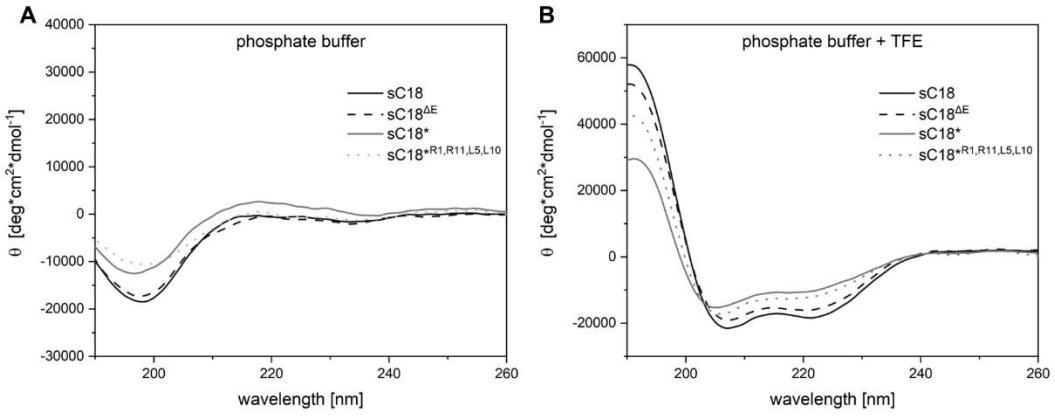

Figure S6. CD spectra of sC18 variants were analyzed at a peptide concentration of 20 µM in either (A) 10 mM phosphate buffer, pH 7.0 (A) or (B) 10 mM phosphate buffer, pH 7.0 with the addition of 50 % TFE. This experiment was kindly provided by Dr. Tamara Sasse.[206]

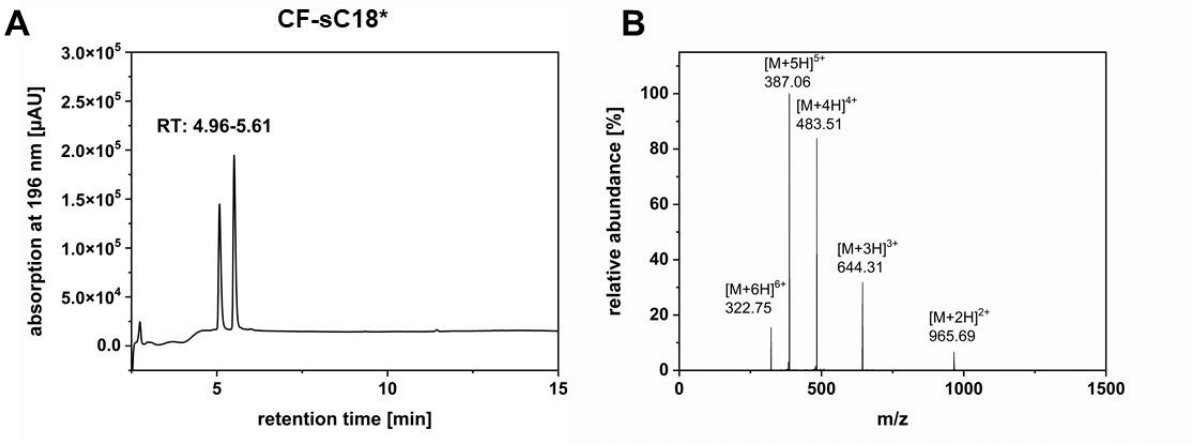

Figure S7. HPLC-ESI/MS analysis of purified CF-sC18. A gradient of 10-60 % ACN with 0.1 % FA in 15 min was used for the HPLC. (A) UV-chromatogram of CF-sC18*. (B) Full scan of ESI/MS at a retention time of 4.96-5.61 min.

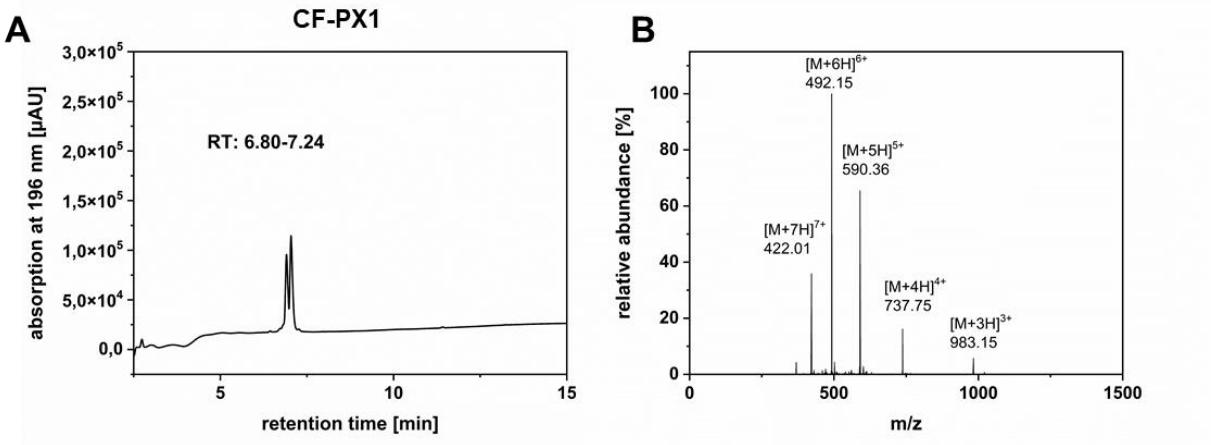

Figure S8. HPLC-ESI/MS analysis of purified CF-PX1. A gradient of 10-60 % ACN with 0.1 % FA in 15 min was used for the HPLC. (A) UV-chromatogram of CF-PX2. (B) Full scan of ESI/MS at a retention time of 6.80-7.24 min. This peptide was synthesized by Philipp Holz during his bachelor's thesis under my supervision.

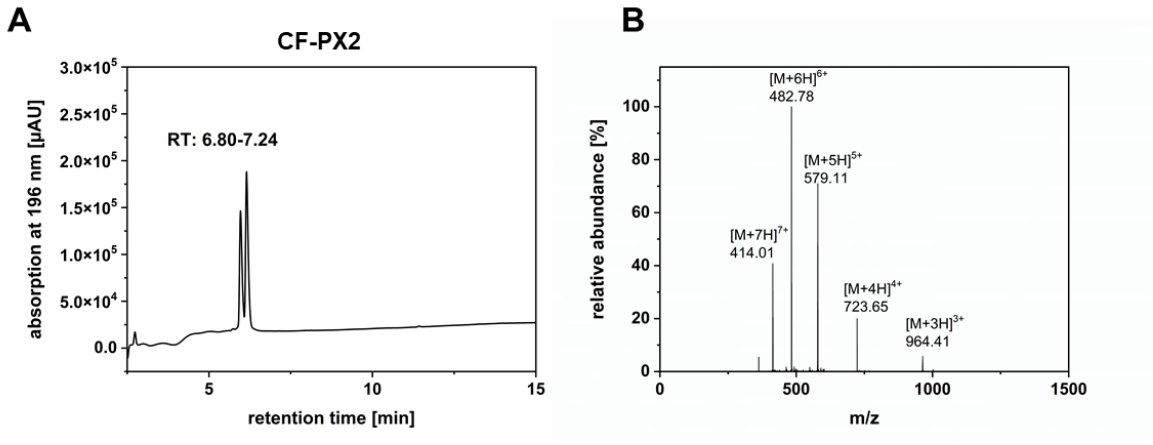

Figure S9. HPLC-ESI/MS analysis of purified CF-PX2. A gradient of 10-60 % ACN with 0.1 % FA in 15 min was used for the HPLC. (A) UV-chromatogram of CF-PX2. (B) Full scan of ESI/MS at a retention time of 6.80-7.24 min. This peptide was synthesized by Philipp Holz during his bachelor's thesis under my supervision.

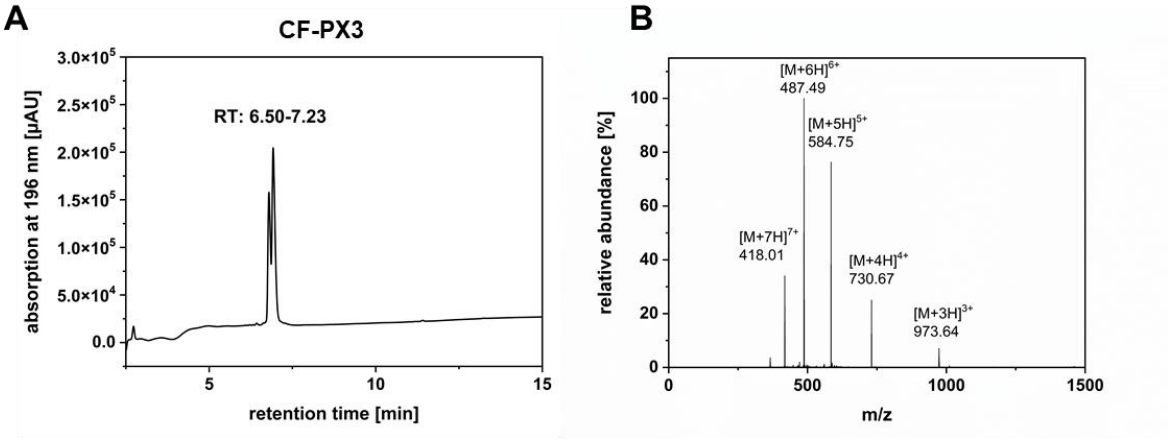

Figure S10. HPLC-ESI/MS analysis of purified CF-PX3. A gradient of 10-60 % ACN with 0.1 % FA in 15 min was used for the HPLC. (A) UV-chromatogram of CF-PX3. (B) Full scan of ESI/MS at a retention time of 6.50-7.23 min. This peptide was synthesized by Philipp Holz during his bachelor's thesis under my supervision.

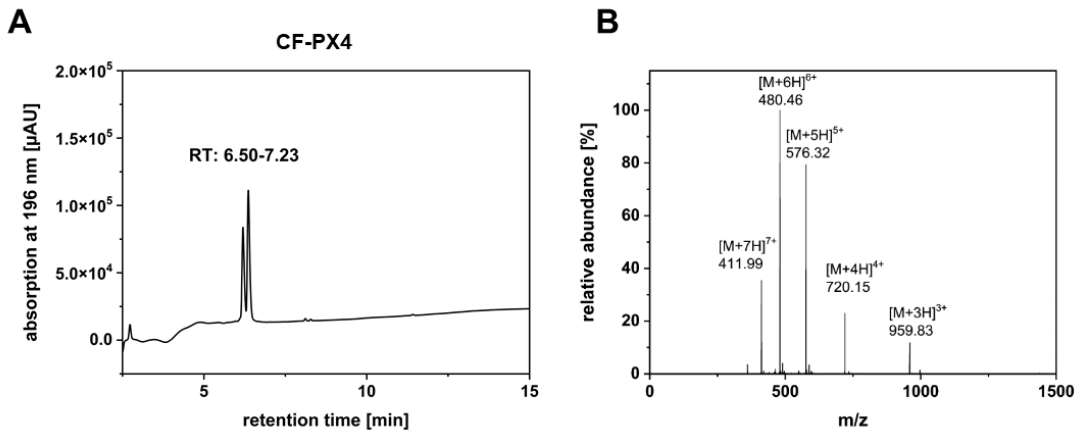

Figure S11. HPLC-ESI/MS analysis of purified CF-PX4. A gradient of 10-60 % ACN with 0.1 % FA in 15 min was used for the HPLC. (A) UV-chromatogram of CF-PX4. (B) Full scan of ESI/MS at a retention time of 6.50-7.23 min. This peptide was synthesized by Philipp Holz during his bachelor's thesis under my supervision.

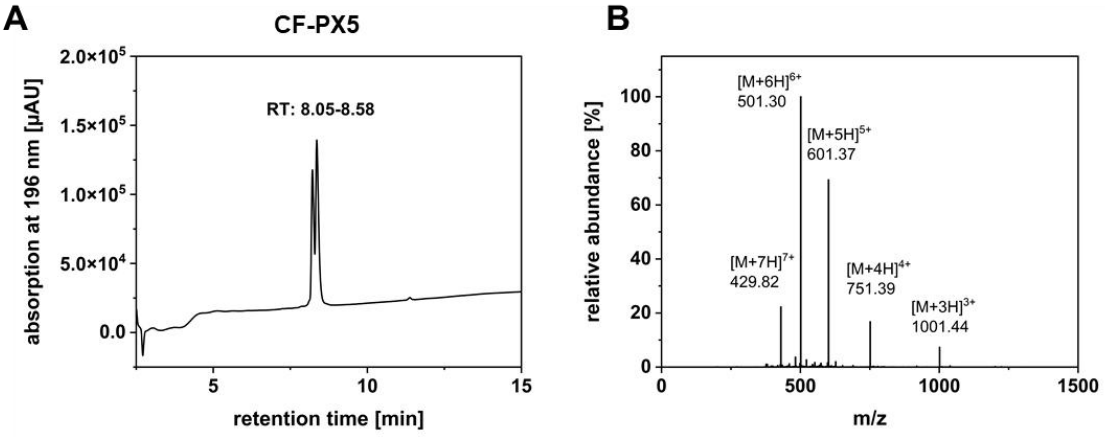

Figure S12. HPLC-ESI/MS analysis of purified CF-PX5. A gradient of 10-60 % ACN with 0.1 % FA in 15 min was used for the HPLC. (A) UV-chromatogram of CF-PX5. (B) Full scan of ESI/MS at a retention time of 8.05-8.58 min.

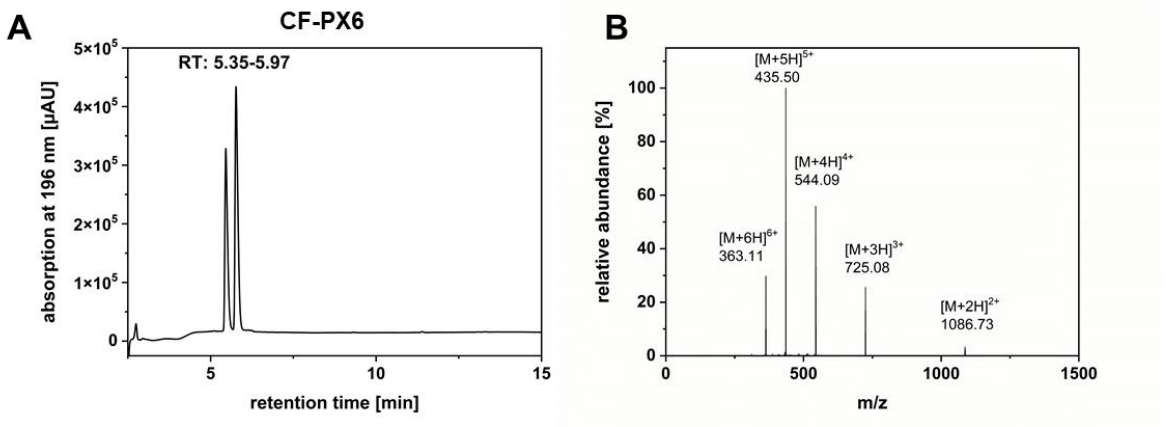

Figure S13. HPLC-ESI/MS analysis of purified CF-PX6. A gradient of 10-60 % ACN with 0.1 % FA in 15 min was used for the HPLC. (A) UV-chromatogram of CF-PX6. (B) Full scan of ESI/MS at a retention time of 5.35-5.97 min. This peptide was synthesized by Philipp Holz during his bachelor's thesis under my supervision.

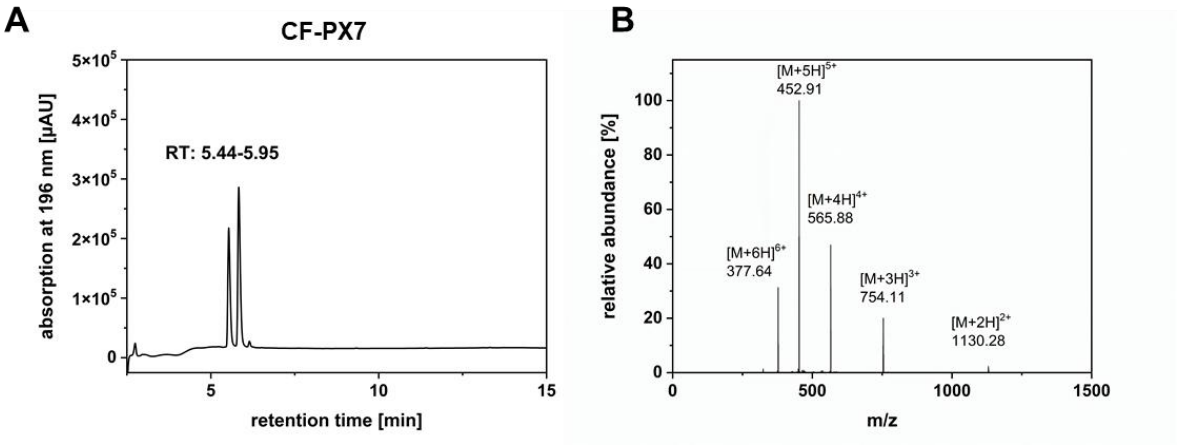

Figure S14. HPLC-ESI/MS analysis of purified CF-PX7. A gradient of 10-60 % ACN with 0.1 % FA in 15 min was used for the HPLC. (A) UV-chromatogram of CF-PX7. (B) Full scan of ESI/MS at a retention time of 5.44-5.95 min. This peptide was synthesized by Philipp Holz during his bachelor's thesis under my supervision.

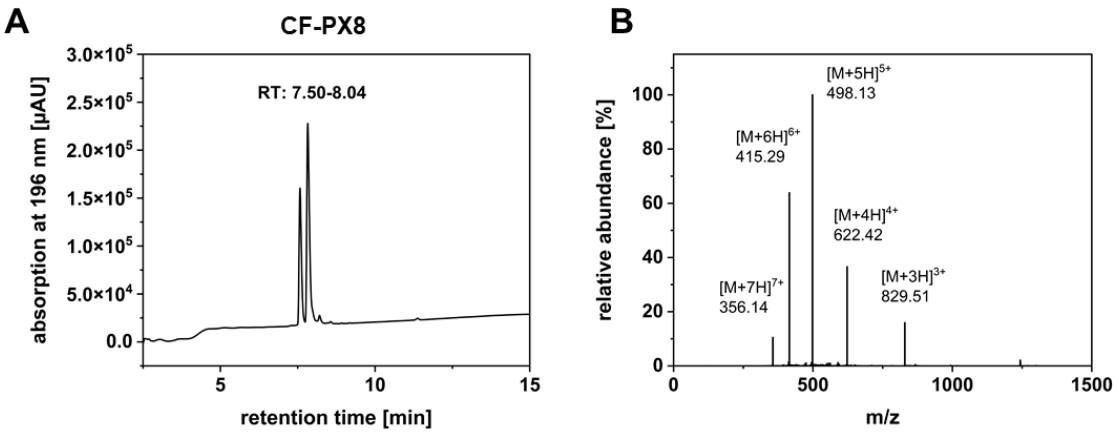

Figure S15. HPLC-ESI/MS analysis of purified CF-PX8. A gradient of 10-60 % ACN with 0.1 % FA in 15 min was used for the HPLC. (A) UV-chromatogram of CF-PX8. (B) Full scan of ESI/MS at a retention time of 7.50-8.04 min.

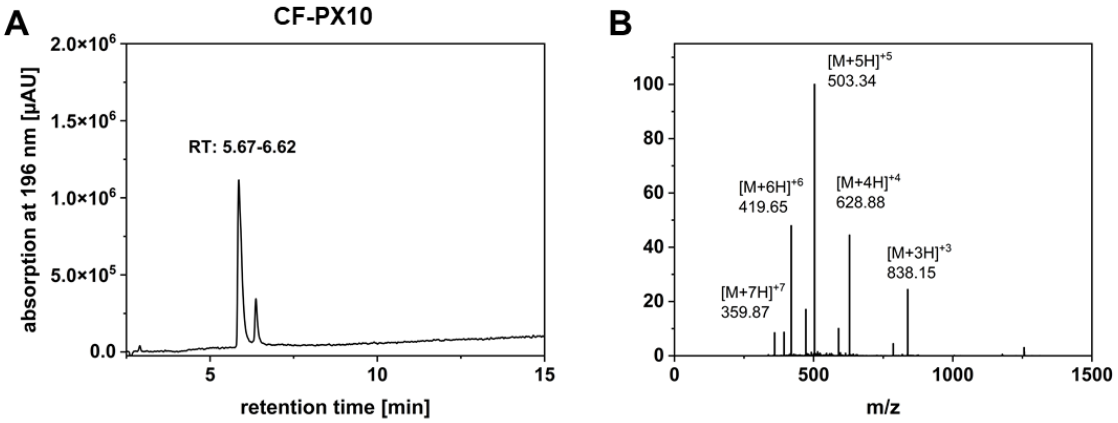

Figure S16. HPLC-ESI/MS analysis of purified CF-PX10. A gradient of 10-60 % ACN with 0.1 % FA in 15 min was used for the HPLC. (A) UV-chromatogram of CF-PX10. (B) Full scan of ESI/MS at a retention time of 5.67-6.62min.

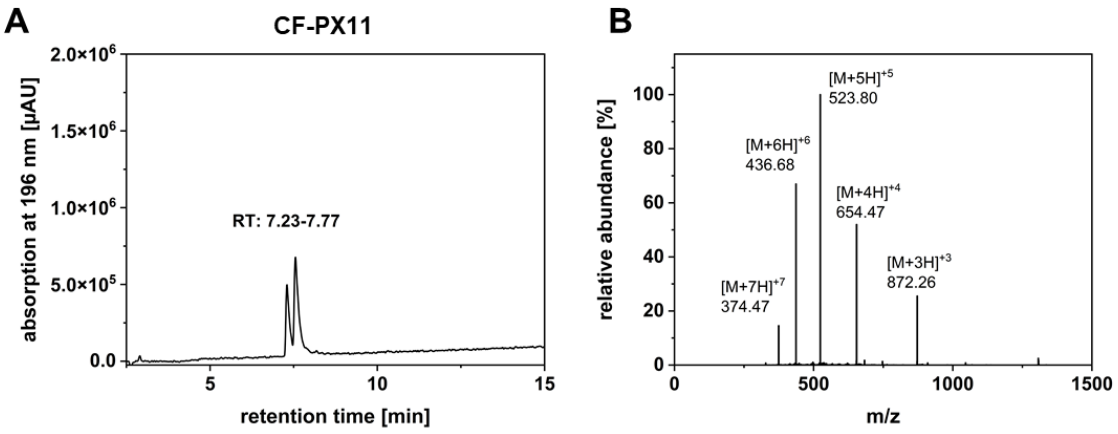

Figure S17. HPLC-ESI/MS analysis of purified CF-PX11. A gradient of 10-60 % ACN with 0.1 % FA in 15 min was used for the HPLC. (A) UV-chromatogram of CF-PX11. (B) Full scan of ESI/MS at a retention time of 7.23-7.77 min.

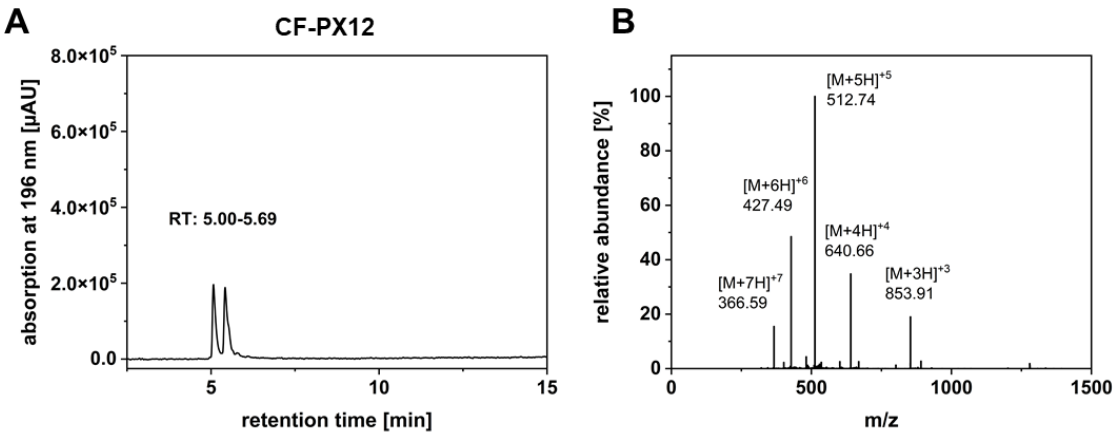

Figure S18. HPLC-ESI/MS analysis of purified CF-PX12. A gradient of 10-60 % ACN with 0.1 % FA in 15 min was used for the HPLC. (A) UV-chromatogram of CF-PX12. (B) Full scan of ESI/MS at a retention time of 5.00-5.69 min.

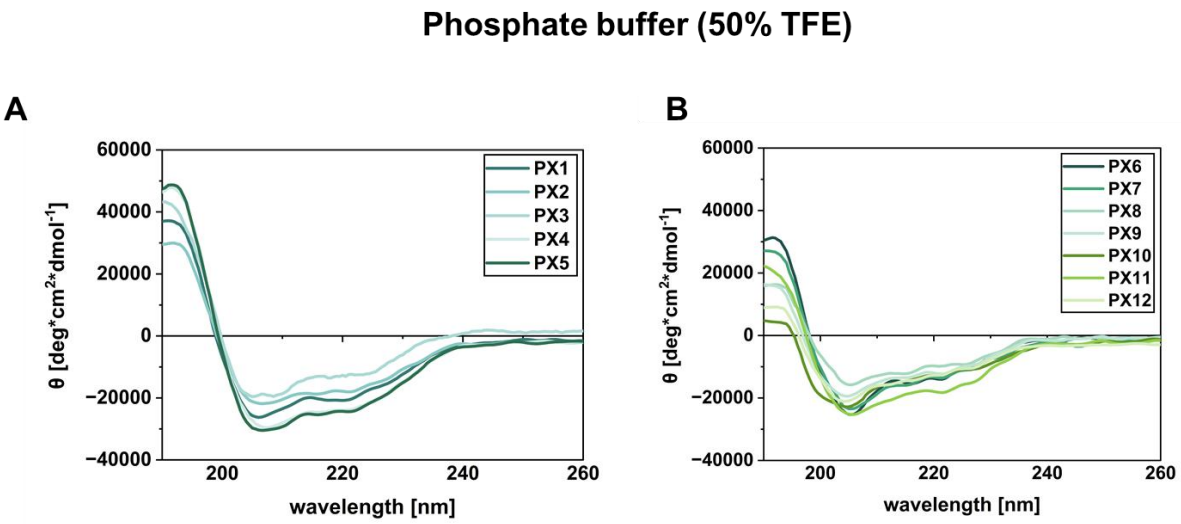

Figure S19. CD spectra of PX peptides in Phosphate buffer containing 50 % TFE. Graphs are discriminated into PTS2 (A) and PTS1 (B) bearing PX peptides.

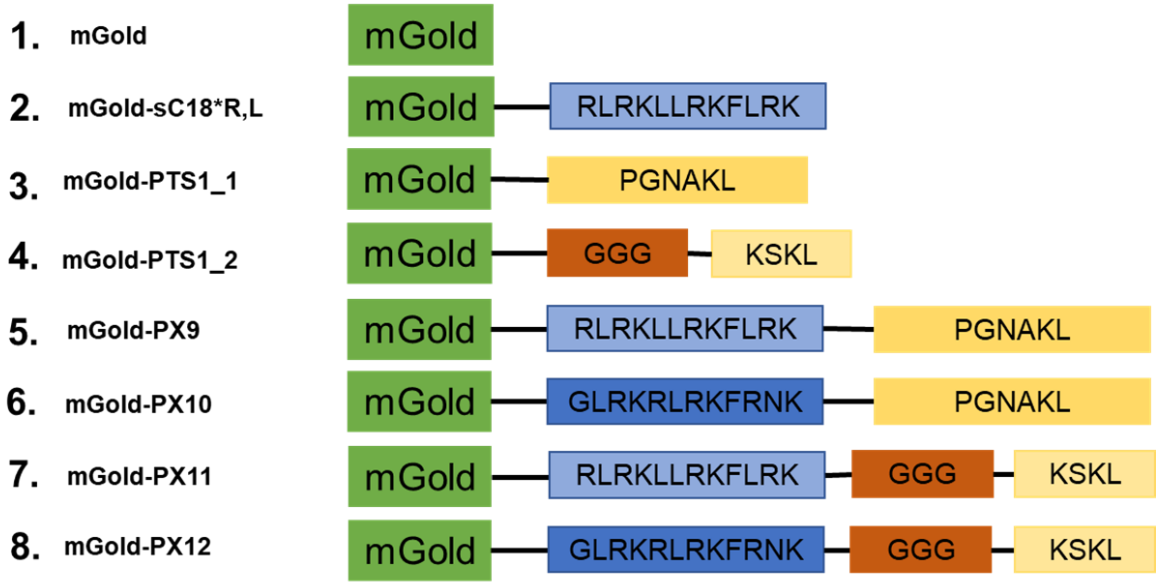

Figure S20. Plasmid design with mGold as green fluorophore and the respective insert.

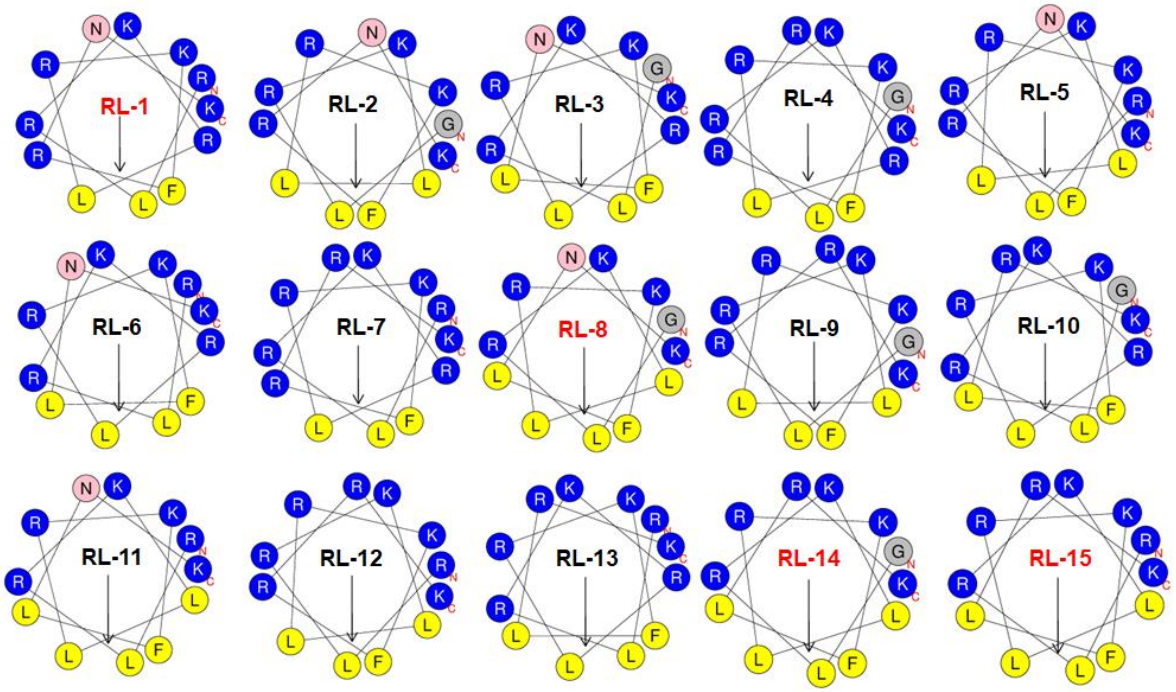

Figure S21. Helical wheel projection of all 15 synthesized R,L variants of sC18* created with HeliQuest. Reprinted with permission from Grabeck J,et al. Triazole-Bridged Peptides with Enhanced Antimicrobial Activity and Potency against Pathogenic Bacteria. *ACS Infect Dis*. 2024 Aug 9;10(8):2717-2727. doi: 10.1021/acsinfecdis.4c00078. © 2024 American Chemical Society.

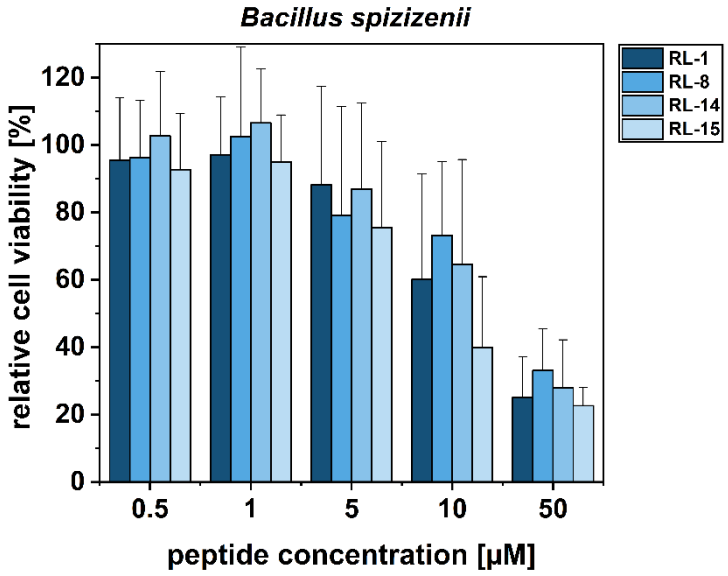

Figure S22. Adapted assay with minimal medium containing H_2O, 5 mM glucose, 10 mM Tris against *B. spizizenii*. Untreated bacteria served as negative control. The assays were performed in triplicates (n = 3). Values were normalized against the untreated control. Error bars represent standard deviations. The experiment was performed together and under my supervision with my master students Jacob Mayer and Axel Miltz. Reprinted with permission from Grabeck J,et al. Triazole-Bridged Peptides with Enhanced Antimicrobial Activity and Potency against Pathogenic Bacteria. *ACS Infect Dis*. 2024 Aug 9;10(8):2717-2727. doi: 10.1021/acsinfecdis.4c00078. © 2024 American Chemical Society.

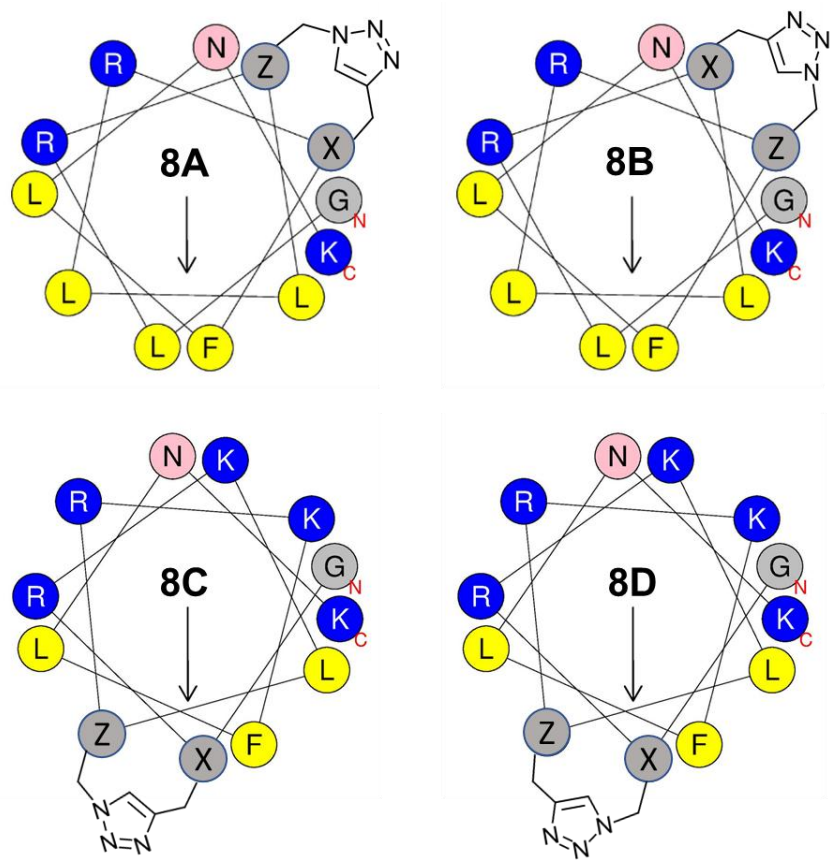

Figure S23. Helical wheel projection of triazolyl-bridged RL-8 peptide variants; 8A, 8B, 8C and 8D created with HeliQuest. X: Pra, Y: Aza.

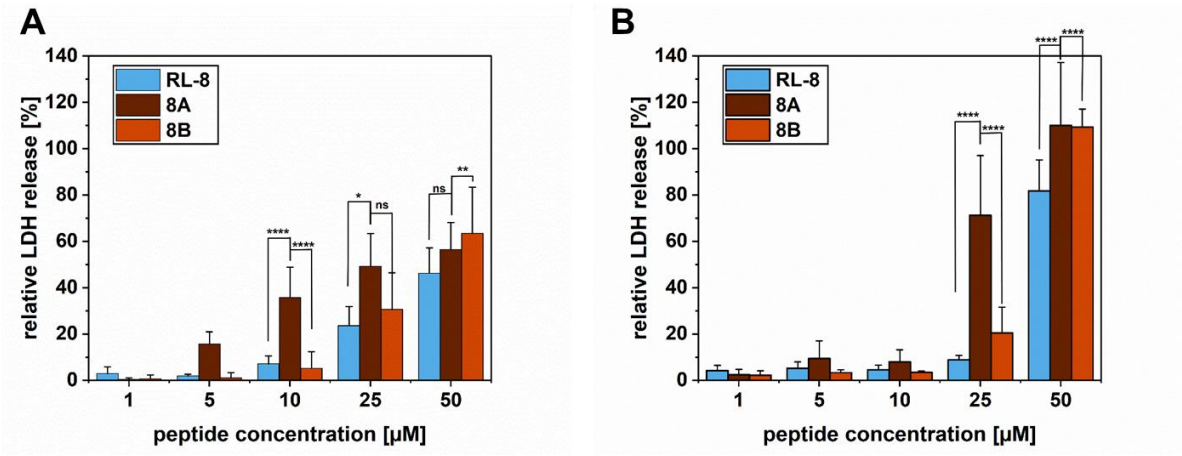

Figure S24. LDH-release assay in either (A) HeLa cells or (B) HFF-1 cells. Assays were performed in triplicates (n = 3). Values were normalized against the untreated control. Error bars represent standard deviation. Statistical analyses were performed using a one-way ANOVA test (****p < 0.00001, ***p < 0.0001, ns p > 0.05). Jacob Mayer performed this experiment during his master's thesis under my supervision. Reprinted with permission from Grabeck J,et al. Triazole-Bridged Peptides with Enhanced Antimicrobial Activity and Potency against Pathogenic Bacteria. *ACS Infect Dis*. 2024 Aug 9;10(8):2717-2727. doi: 10.1021/acsinfecdis.4c00078. © 2024 American Chemical Society.

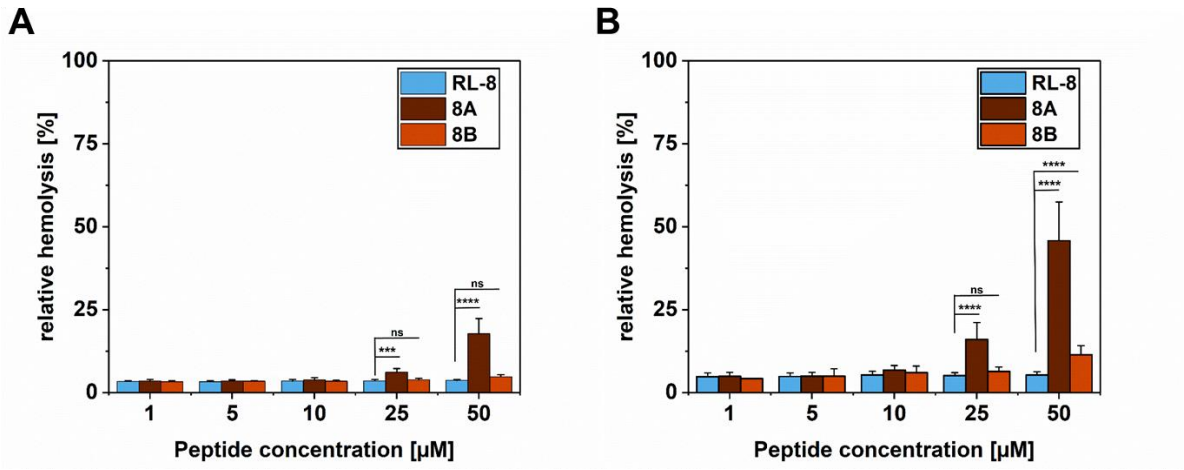

Figure S 25. Hemolysis assay for either (A) 30 min or (B) 24 h treatment. Assays were performed in triplicates (n = 3). Values were normalized against the untreated control. Error bars represent standard deviation. Statistical analyses were performed using a one-way ANOVA test (****p < 0.00001, ***p < 0.0001, ns p > 0.05). Jacob Mayer performed this experiment during his master's thesis under my supervision. Reprinted with permission from Grabeck J,et al. Triazole-Bridged Peptides with Enhanced Antimicrobial Activity and Potency against Pathogenic Bacteria. *ACS Infect Dis*. 2024 Aug 9;10(8):2717-2727. doi: 10.1021/acsinfecdis.4c00078. © 2024 American Chemical Society.

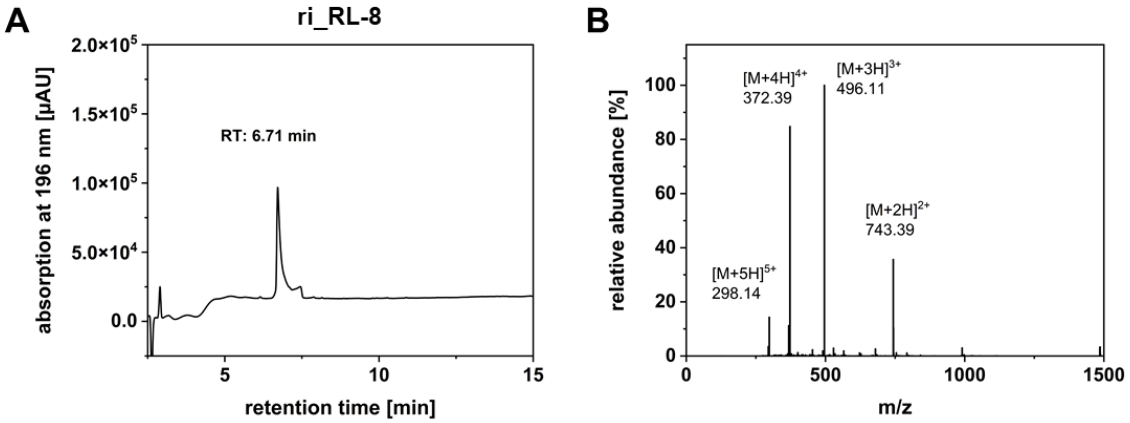

Figure S26. HPLC-ESI/MS of purified ri_RL-8. (A) UV-chromatogram with a retention time at 6.71 min. (B) Mass spectrum of the peak at the retention time of 6.71 min showing m/z ratios that correspond to the quasi-molecular ions.

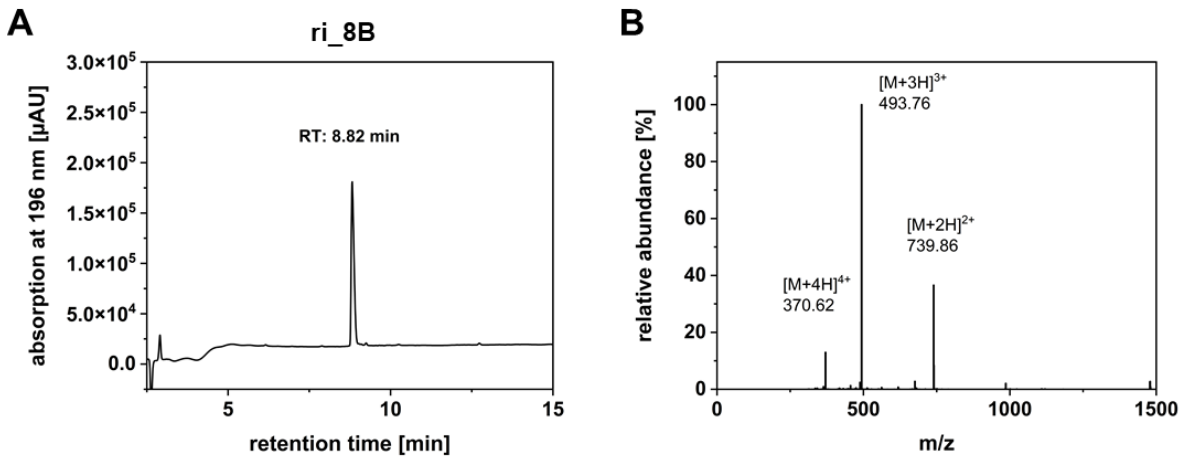

Figure S27. HPLC-ESI/MS of purified ri_8B. (A) UV-chromatogram with a retention time at 6.71 min. (B) Mass spectrum of the peak at the retention time of 6.71 min showing m/z ratios that correspond to the quasi-molecular ions.

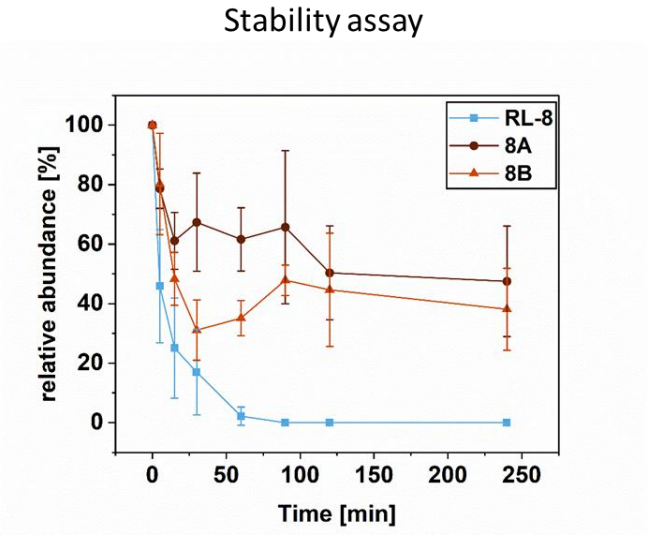

Figure S28. Stability assay using 250 µM peptide solutions in goat serum. Peptides were incubated for 240 min, with aliquots collected at designated time points (5, 15, 30, 45, 60, 90, 120 and 240 min). Samples were precipitated using acetonitrile, and peptides were quantified via LC-MS. Values were normalized to the initial measurement at time point zero. This experiment was performed by the master's student Jacob Mayer. The assay was performed in triplicates (n = 3). Error bars represent standard deviations. Reprinted with permission from Grabeck J,et al. Triazole-Bridged Peptides with Enhanced Antimicrobial Activity and Potency against Pathogenic Bacteria. *ACS Infect Dis*. 2024 Aug 9;10(8):2717-2727. doi: 10.1021/acsinfecdis.4c00078. © 2024 American Chemical Society.

6.2 List of abbreviations

ACN	acetonitrile
AMP	antimicrobial peptide
APS	ammonium persulfate
ATP	adenosine triphosphate
Aza	L-azidolysine
Boc	tert-butyloxycarbonyl
BSA	bovine albumin serum
B. spizizenii	*Bacillus spizizenii*
CAP18	cationic antimicrobial protein 18
CD	circular dichroism
CF	5(6)-carboxyfluorescein
CO_2	carbon dioxide
CPP	cell-penetrating peptide
CTP	cell-targeting peptide
CuAAC	Cu(I)-catalyzed azide−alkyne cycloaddition
Da	Dalton
DCM	dichloromethane
Dde	1-(4,4-dimethyl-2,6-dioxocyclohex-1-ylidene)ethyl
DIC	N,N'-diisopropylcarbodiimide
DIPEA	N,N'-diisopropylethylamine
DMEM	Dulbeco's Modified Eagle Medium
DMF	dimethylformamide
DMSO	dimethyl sulfoxide
DNA	deoxyribonucleic acid
DTT	dithiothreitol
ECL	enhanced chemiluminescence
E. coli	*Escherichia coli*
EC_{50}	half maximal effective concentration
EED	endosomal escape domain
EDT	1,2-ethandithiol
EDTA	ethylenediaminetetraacetic acid
Eq	equivalents
ESI	electrospray ionization

ESKAPE	*Enterococcus faecium, Staphylococcs aureus, Klebsiella pneumoniae, Acinetobacter baumannii, Pseudomonas aeruginosa, Enterobacter-Spezies*
ET_2O	diethyl ether
EtOH	Ethanol
FA	formic acid
FBS	fetal bovine serum
FDA	federal drug administration
Fig.	Figure
Fmoc	fluorenyl methoxycarbonyl
GUV	giant unilamellar vesicles
HATU	hexafluorophosphate azabenzotriazole tetramethyl uranium
HEK293	human embryonic kidney cells
HeLa	human cercal carcinoma cells
HFF-1	human foreskin fibroblasts
HIV	human immunodeficiency virus
H_2O	water
H_2O_2	hydrogen peroxide
HPLC	high-performance liquid chromatography
INT	iodonitrotetrazolium chloride
LC-MS	liquid chromatography-mass spectroscopy
LDH	lactate dehydrogenase
LPS	lipopolysaccharides
MCF-7	Michigan Cancer Foundation 7
MCS	multiple cloning site
MeOH	methanol
$MgCl_2$	magnesium chloride
M. luteus	*Micrococcus luteus*
MPP	mitochondrial processing peptidase
MRSA	methicillin-resistant *Staphylococcus aureus*
MTS	mitochondrial targeting sequence
MW	molecular weight
MW_{calc}	calculated molecular weight
MW_{exp}	experimental molecular weight
m/z	mass to charge ratio
NaCl	sodium chloride
N. gonorrhoeae	*Neisseria gonorrhoeae*

NLS	nuclear localization signal
NMP	*N*-methyl-2-pyrrolidone
Oxyma	ethyl canohydroxyiminoacetate
P. aeruginosa	*Pseudomonas aeruginosa*
PAGE	polyacrylamide gel electrophoresis
PCR	polymerase chain reaction
PBS	phosphate-buffered saline
PBS-T	phosphate-buffered saline with 0.05% Tween20
P. fluorescens	*Pseudomonas fluorescens*
PDC	peptide-drug conjugate
Pra	L-propargylglycine
RNA	ribonucleic acid
ROS	reactive oxygen species
rpm	rounds per minute
RPMI-1640	Roswell Park Memorial Institute, cell culture medium
rt	room temperature
RT	retention time
SDS	sodium dodecyl sulfate
SMP	N-succinimyl-3 maleimideproppionate
SPPS	solid phase peptide synthesis
S. typhimurium	*Salmonella typhimurium*
TAT	trans activator of transcription
*t*Bu	*tert*-butyl
t-BuOH	*tert*-butanol
Tab.	Table
TEM	transmission electron microscopy
TEMED	tetramethylethylenediamine
TFA	trifluoroacetic acid
TIM23	translocase inner membrane 23
TIS	triisopropylsilane
TLC	thin-layer chromatography
TOM	translocase outer membrane
UV	ultraviolet

6.3 Amino acids:

A	Ala	alanine
C	Cys	cysteine
D	Asp	aspartate
E	Glu	glutamate
F	Phe	phenylalanine
G	Gly	glycine
H	His	histidine
I	Ile	isoleucine
K	Lys	lysine
L	Leu	leucine
M	Met	methionine
N	Asn	asparagine
P	Pro	proline
Q	Gln	glutamine
R	Arg	arginine
S	Ser	serine
T	Thr	threonine
V	Val	valine
W	Trp	tryptophan
Y	Tyr	tyrosine

6.4 Lists of figures

6.5 List of supplementary figures

6.6 Lists of tables

Teilpublikationen:

- Marco Drexelius, Andre Reinhardt, **Joshua Grabeck**, Tom Cronenberg, Frank Nitsche, Pitter F. Huesgen, Berenike Maier, Ines Neundorf; Multistep optimization of a cell-penetrating peptide towards its antimicrobial activity. Biochem J 15 January 2021; 478 (1): 63–78. doi: https://doi.org/10.1042/BCJ20200698
- **Joshua, Grabeck**, Tamara Lützenburg, Pia Frommelt, and Ines Neundorf. 2022. "Comparing Variants of the Cell-Penetrating Peptide sC18 to Design Peptide-Drug Conjugates" *Molecules* 27, no. 19: 6656. https://doi.org/10.3390/molecules27196656
- Denise, Meinberger, Marco G. Drexelius, **Joshua Grabeck**, Gabriele Hermes, Annika Roth, Dzemal Elezagic, Ines Neundorf, Thomas Streichert, and Andreas R. Klatt. 2023. "Modified CLEC3A-Derived Antimicrobial Peptides Lead to Enhanced Antimicrobial Activity against Drug-Resistant Bacteria" Antibiotics 12, no. 10: 1532. https://doi.org/10.3390/antibiotics12101532
- **Joshua Grabeck**, Jacob Mayer, Axel Miltz, Michele Casoria, Michael Quagliata, Denise Meinberger, Andreas R. Klatt, Isabelle Wielert, Berenike Maier, Anna Maria Papini, and Ines Neundorf *ACS Infectious Diseases* **2024** *10* (8), 2717-2727 DOI: 10.1021/acsinfecdis.4c00078
- Michael Quagliata, **Joshua Grabeck**, Kathrin König, Anna Maria Papini, Paolo Rovero, Ines Neundorf and Daniel Friedrich. α-Helical structure of antimicrobial peptides enhances their activity through molecular surface signatures. ACS Biochemistry, *manuscript in preparation*.

Posterpräsentationen:

- **Joshua Grabeck**, Tamara Lützenburg, Merlin Klußmann, Ines Neundorf, Improving cellular uptake, cell selectivity and cargo delivery of the cell-penetrating peptide sC18. *PhD Symposium Graduate School Chemistry Cologne 2022, 36th European Peptide Symposium, Sitges 2022*
- **Joshua Grabeck**, Tamara Lützenburg, Merlin Klußmann, Ines Neundorf, Creating peptide-drug conjugates with doxorubicin by coupling to a variant of the carrier peptide sC18. *Magic Bullet retreat for Drug-conjugates, Darmstadt 2023*
- **Joshua Grabeck**, Philipp Holz, Ines Neundorf, *Directing cell-penetrating peptides to the peroxisome for a targeted drug delivery, 16th German Peptide Symposium, Jena 2023*
- **Joshua Grabeck**, Jacob Mayer, Axel Miltz, Michele Casoria, Michael Quagliata, Denise Meinberger, Andreas R. Klatt, Isabelle Wielert, Berenike Meier, Anna Maria Papini, Ines Neundorf, *Triazolyl-bridged peptides with enhanced antimicrobial activitiy and potency against pathogenic bacteria, 37th European Peptide Symposium, Florenz 2024*

6.7. Curriculum vitae

Persönliche Daten

Name:	Joshua Christian Grabeck
Geburtsdatum:	28.05.1997
Geburtsort:	Bergisch Gladbach
Staatsangehörigkeit:	deutsch

Ausbildung

Seit 10/2021	Promotion am Institut für Biochemie, Universität zu Köln bei Frau Prof. Dr. Ines Neundorf
10/2019 - 10/2021	Universität zu Köln, Mathematisch-Naturwissenschaftliche Fakultät, Studium Biological Sciences in Biology, Abschluss: Master of Science
19/2015 – 09/2019	Universität zu Köln, Mathematisch-Naturwissenschaftliche Fakultät, Studium Bachelor of Science in Biologie, Abschluss: Bachelor of Science
08/2007 – 06/2015	Dietrich-Bonhoeffer Gymnasium, Wiehl, Abschluss: Abitur
08/2003 – 06/2007	GGS Gemeinschaftsgrundschule Oberwiehl